

TECHNISCHE UNIVERSITÄT
CHEMNITZ

Development, Implementation, and Analysis of a Multiple-Input Multiple-Output Concept for Spaceborne High-Resolution Wide-Swath Synthetic Aperture Radar

von der Fakultät für Elektrotechnik und Informationstechnik

der Technischen Universität Chemnitz

genehmigte
Dissertation
zur Erlangung des akademischen Grades

DOKTOR-INGENIEUR

Dr.-Ing.

vorgelegt

von **Dipl.-Ing. (FH) Tobias Rommel**

geboren am 16.12.1987 in Bad Kissingen

eingereicht am 16.11.2017

Gutachter: Prof. Dr. rer. nat. Madhukar Chandra
Prof. Dr.-Ing. habil. Alberto Moreira

Tag der Verleihung: 28.08.2018

Rommel, Tobias
Development, Implementation, and Analysis of a Multiple-Input Multiple-Output Concept for Spaceborne High-Resolution Wide-Swath Synthetic Aperture Radar
Dissertation, Fakultät für Elektrotechnik und Informationstechnik
Technische Universität Chemnitz, August 2018
265 Seiten, 103 Abbildungen, 8 Tabellen, 133 Literaturquellen

Danksagung

Die vorliegende Dissertation enstand während meiner Tätigkeit als Doktorand sowie als wissenschaftlicher Mitarbeiter am Institut für Hochfrequenztechnik und Radarsysteme des Deutschen Zentrums für Luft- und Raumfahrt e.V. (DLR) in Oberpfaffenhofen. Im Rahmen eines Kooperationsvertrags mit der Fakultät für Elektrotechnik und Informationstechnik der Technischen Universität in Chemnitz erfolgte die Betreuung durch den dort ansässigen Lehrstuhl für Hochfrequenztechnik und Theoretische Elektrotechnik.

Mein ganz besonderer Dank gilt meinem Doktorvater Prof. Dr. rer. nat. Madhukar Chandra von der Technischen Universität in Chemnitz. Er ist nicht nur der Hauptreferent der Arbeit, sondern er ermöglichte mir außerdem wertvolle Lehrerfahrung an seinem Lehrstuhl zu sammeln. Bei unseren gemeinsamen Arbeitssitzungen führten wir immer interessante Gespräche, bei denen ich viel gelernt habe. Selbstverständlich möchte ich mich auch bei meinem Institutsleiter, Prof. Dr.-Ing. habil. Alberto Moreira, für die Annahme des Korreferats und die Korrektur der Arbeit bedanken. Sein Einsatz und Engagement für die Doktoranden am Institut ist ohnegleichen. Auch ohne meinen Abteilungsleiter, Dr.-Ing. Gerhard Krieger, hätte die vorliegende Arbeit erst gar nicht entstehen können. Sein unglaubliches Maß an Fachwissen half signifikant bei fachlichen Diskussionen nebst wertvollen Kommentaren während der letzten sechs Jahre. Bei dieser Gelegenheit bedanke ich mich auch bei meinem Gruppenleiter, Prof. Dr.-Ing. Marwan Younis. Seine fachliche Unterstüzung während der gesamten Promotionsphase leistete einen großen Beitrag zum Gelingen.

Auch allen meinen jederzeit hilfsbereiten Kollegen aus meinem direkten Arbeitsumfeld bin ich zu Dank verpflichtet. Ich möchte insbesondere Dr.-Ing. Sigurd Huber, Dr.-Ing. Federica Bordoni, Christopher Laux, Markus Limbach, Bernd Gabler, Dr.-Ing. Alberto Di Maria, Dr.-Ing. Eric Schreiber und Stephan Dill für Ihre Unterstützung danken. Dabei sind meine ehemaligen Kollegen, Dr.-Ing. Jung-Hyo Kim, Anton Patyuchenko und Piotr Laskowski, nicht zu vergessen, die mir bei der Startphase mit der Radarhardware geholfen haben. Sie alle waren mir eine sehr große Hilfe! Nicht nur mit wertvollen fachlichen Diskussionen haben sie zu einer angenehmen Arbeitsatmophäre beigetragen, sodass ich mich jeden Morgen auf die Arbeit freuen durfte. Von den Resultaten meiner beiden fleißigen Werksstudenten und Praktikanten, Adithya Madanahalli und Sören Marahrens, konnte ich ganz besonders profitieren. Sie beide haben wesentlich zur Benutzerfreundlichkeit bei der Bedienung des Radar Demonstrators sowie dessen Qualitätsverbesserung beigetragen. Im kollegialen Umfeld richte ich abschließend einen großen Dank an die Institutswerkstatt von Peter Heitzer für die mecha-

nischen Aufbauten, und an Sibylle Radzuweit, welche meine zahlreichen Dienstreisen organisiert und gebucht hat.
Selbstverständlich hat auch mein privates Umfeld zum Gelingen der Arbeit beigetragen. Beginnend bei meinen Eltern, welche mir den Weg geebnet und überhaupt ermöglicht haben. Von ihnen habe ich permanent volle Unterstützung erhalten. Meine ehemaligen und gegenwärtigen WG-Mitbewohner, Lars, Felix, Susi und Lukas, hatten immer ein offenes Ohr und sorgten für das richtige Maß an Ablenkung. Der durchaus notwendige Ausgleich war mir des öfteren sehr willkommen. Eine ebenfalls wichtige Rolle hat meine ehemalige Arbeitskollegin und gute Freundin, Dr.-Ing. Carolina Tienda, eingenommen. Unsere Gespräche waren eine gute Kombination von Beruf und Privatem. Meinem Großmeister, Alfred Gehlen, danke ich für die Weitergabe der richtigen Philosophie und Lebenseinstellung – insbesondere in Bezug auf Zielsetzung und Zielerreichung. Er hat mein Leben zum richtigen Zeitpunkt positiv und nachhaltig beeinflusst.
Zuallerletzt danke ich allen weiteren Personen aus meinem Umfeld, welche indirekt zu meinem Erfolg beigetragen haben. Ohne eure Unterstützung wäre es zu all dem nicht gekommen.

München, im November 2017

Tobias Rommel

Abstract

Since the development of the first Synthetic Aperture Radar (SAR), radar has become an important sensor for imaging applications. Manifold fields of application ranging from climate change research, over change-detection, and 4-D mapping up to earthquake and flood monitoring are covered by SAR. Especially high-resolution, day- and night-, as well as weather-independent imaging capabilities led to the success of recent spaceborne SAR missions. However, due to a high demand for global SAR data sets, state-of-the-art sensors reach their limits in terms of resolution, swath-width, repeat cycle, and flexibility.

To solve SAR-inherent limitations, in this dissertation, a new generation of SAR sensors with multiple transmit and multiple receive channels (MIMO) and Digital Beam-Forming (DBF) capabilities is proposed. Apart from an increased flexibility, this enables a large variety of new operation- and acquisition-modes for high-resolution wide-swath SAR imaging.

To separate the individual channels in the post-processing, established processing techniques can not be applied, since SAR is highly sensitive to interferences. Hence, the Space-Time-Frequency Adaptive Processing (STFAP) algorithm is derived, which allows channel separation without any interferences. Basically, STFAP forms frequency- and time-variant antenna beams, which follow the echo signals of each transmitted waveform individually. However, this method demands waveforms of certain structures, which are described and suitable waveform types are compared in detail.

STFAP and other DBF-SAR techniques need very sharp antenna beams in elevation. In presence of unknown topography, when the assumed geometrical model of the Earth surface is complex, antenna pointing might be mismatched with the surface geometry. To handle this issue, it is suggested to apply an additional algorithm prior to DBF, which determines the angle of the incident echo signal on the antenna array. The algorithm, which is proposed in this dissertation, is based on the matrix pencil method and allows a highly accurate and signal-adaptive DBF in real-time.

For an experimental verification of new imaging modes and STFAP, a ground-based MIMO-SAR demonstrator in X-band has been developed. The dissertation concludes with its description and promising experimental results, which proof that the suggested concepts have the potential to enhance the capabilities of state-of-the-art SAR sensors significantly.

Keywords:

synthetic aperture radar (SAR), digital beam-forming (DBF), waveforms, multiple-input multiple-output (MIMO), matrix pencil, direction of arrival estimation, radar development

Referat

Seit Entwicklung des ersten Radars mit synthetischer Apertur (SAR) hat sich Radar zu einem wichtigen Sensor für bildgebende Anwendungen entwickelt. Vielfältige Anwendungsgebiete, von der Forschung am Klimawandel, über die Veränderungsdetektion und 4-D-Kartierung, bis hin zu Erdbeben- und Hochwasserschutz werden von SAR abgedeckt. Insbesondere die hochauflösende und wetterunabhängige Bildgebung bei Tag und Nacht führte zum Erfolg der jüngsten Satelliten-SAR-Missionen. Aufgrund der hohen Nachfrage nach globalen SAR-Datensätzen gelangen modernste Sensoren jedoch hinsichtlich Auflösung, Streifenbreite, Wiederholungszyklus und Flexibilität an ihre Grenzen.

Zur Behebung von SAR-inhärenten Limitationen, wird in dieser Arbeit eine neue Generation von SAR-Sensoren mit mehreren Sende- und Empfangskanälen (MIMO) und der Fähigkeit digitaler Strahlformung (DBF) vorgeschlagen. Abgesehen von einer erhöhten Flexibilität ermöglicht dies eine Vielzahl von neuen Betriebs- und Aufzeichnungsmodi für hochauflösende SAR-Abbildungen mit großer Streifenbreite.

Etablierte Prozessierungstechniken können in der Nachprozessierung nicht zur Kanaltrennung angewendet werden, da SAR höchst empfindlich gegenüber Interferenzen ist. Daher wird ein Raum-Zeit-Frequenz-adaptiver Algorithmus (STFAP) hergeleitet, welcher eine Kanaltrennung ohne jegliche Interferenzen ermöglicht. Im Wesentlichen formt STFAP frequenz- und zeitvariante Antennenrichtdiagramme, die den Echosignalen jeder gesendeten Wellenform individuell folgen. Dieses Verfahren erfordert jedoch Wellenformen mit bestimmten Strukturen. Die Anforderungen daran werden beschrieben und geeignete Wellenformtypen werden im Detail verglichen.

STFAP und andere DBF-SAR-Techniken benötigen Antennen mit sehr hoher Richtwirkung in Elevation. In Gegenwart von unbekannter Topographie, wenn das zugrundeliegende geometrische Modell der Erde nicht passt, kann die Antenne in eine falsche Richtung zeigen. Um dieses Problem zu umgehen, wird vorgeschlagen, vor DBF einen zusätzlichen Algorithmus anzuwenden, welcher den Winkel des einfallenden Echosignals auf dem Antennenarray bestimmt. Der Algorithmus, der in dieser Arbeit vorgeschlagen wird, basiert auf dem Matrizenbüschelverfahren und ermöglicht ein hochgenaues und signaladaptives DBF in Echtzeit.

Zur experimentellen Verifikation neuer Bildgebungsmodi und STFAP, wurde ein bodenbasierter MIMO-SAR-Demonstrator im X-Band entwickelt. Die Arbeit schließt mit dessen Beschreibung und vielversprechenden Messergebnissen ab, welche beweisen, dass die vorgeschlagenen Konzepte das Potenzial besitzen, die Leistungsfähigkeiten von modernen SAR-Sensoren erheblich zu verbessern.

Schlagwörter:

Radar mit synthetischer Apertur (SAR), digitale Strahlenformung (DBF), Wellenformen, mehrere Sende- und Empfangskanäle (MIMO), Matrizenbüschel, Richtungsschätzung, Radarentwicklung

Contents

1. Introduction 25
   1.1. State-of-the-Art and Motivation for new Imaging Modes 25
   1.2. Outline and Contributions of this Work 27

2. Fundamentals and Principles of SAR and MIMO-SAR 31
   2.1. Conventional SAR Principle 31
   2.2. Analytic MIMO-SAR Signal Model 36
      2.2.1. Transmitter 37
      2.2.2. Channel and Target 38
      2.2.3. Receiver 41
   2.3. Fundamental Limitations of SAR 42
      2.3.1. Range Ambiguities 42
      2.3.2. Azimuth Ambiguities 44
   2.4. Multi-Channel SAR Signal Processing 45
      2.4.1. DBF in Elevation 45
      2.4.2. DBF in Azimuth 47
      2.4.3. Range Compression 48
      2.4.4. Range Cell Migration Correction 49
      2.4.5. Azimuth Compression 50
      2.4.6. MIMO-SAR Processing Tool 51
   2.5. Advanced DBF and MIMO Modes 51
      2.5.1. Fully Polarimetric SAR Imaging by Simultaneous Measurement of the Scattering Matrix 51
      2.5.2. Interferometric Modes 53
      2.5.3. Forward- and Nadir-Looking SAR 54
      2.5.4. Hybrid SAR Modes 54
      2.5.5. Multistatic SAR 54
      2.5.6. MIMO-SAR Tomography 55
      2.5.7. MIMO Circular SAR for Holographic SAR Tomography with High Altitude Pseudo-Satellites 57

3. Orthogonal MIMO-SAR Waveforms 61
   3.1. Orthogonality Condition 63
   3.2. MIMO-SAR Waveforms 67
      3.2.1. Standard Chirp Waveform 67

3.2.2. OFDM-Chirp Waveforms 69
3.2.3. Multiple Sub-Pulse Mode 72
3.2.4. Segmentally-Shifted Chirp Waveforms 76
3.2.5. Further Waveforms 78
3.3. Ambiguity Function 82
3.3.1. Description of the Ambiguity Function 82
3.3.2. Ambiguity Function Analysis 85
3.4. Waveform Performance Parameters 88
3.4.1. Range Resolution 88
3.4.2. Integrated Sidelobe Ratio 89
3.4.3. Transmit Energy 94
3.4.4. Doppler Tolerance 97
3.4.5. Practical Implementation 99
3.4.6. Maximum Number of Transmit Signals 100
3.4.7. Summary 101

4. Elevation Beam-Forming and Waveform Separation 103
4.1. Adaption of the MIMO-SAR Signal Model for Waveform Separation Techniques 104
4.2. Antenna Design Requirements 108
4.2.1. Optimum Size in Elevation 109
4.2.2. Minimum Number of Antenna Elements 114
4.3. Digital Beam-Forming on Receive - Single Transmit Waveform . . . 115
4.3.1. Time-Variant Beam-Forming 115
4.3.2. Frequency- and Time-Variant Beam-Forming 122
4.4. Waveform Separation of Sub-Pulses 128
4.4.1. Time-Variant Beam-Forming for Waveform Separation . . . 130
4.4.2. Time- and Frequency-Variant Beam-Forming for Waveform Separation 134
4.4.3. Time- and Frequency-Variant Beam-Forming with Null-Steering for Waveform Separation 139
4.5. Waveform Separation of Segmentally-Shifted Chirp Waveforms . . 142
4.6. Waveform Separation of OFDM Chirp Waveforms 143

5. Topography-Adaptive Elevation Beam-Forming on Receive 147
5.1. Problem Formulation 149
5.2. Matrix Pencil Method 151
5.2.1. Adapted Signal Model for Direction of Arrival Estimation . 151
5.2.2. Angle of Arrival Estimation via the Matrix Pencil 152
5.2.3. Total Least Squares Matrix Pencil 155
5.2.4. Forward-Backward Matrix Pencil 157
5.2.5. Modification of the Matrix Pencil Method for Extended Angular Coverage 159
5.2.6. Moving Window Average 161

5.2.7. Practical Implementation 165
5.3. Performance Analysis 167
5.3.1. Evaluation of the Computational Complexity 168
5.3.2. Basic Angular Estimation for a Single Point Target 170
5.3.3. Multiple Individual Targets 173
5.3.4. Targets with Spatial Extension 174
5.3.5. Concluding Remarks 174

6. Ground-Based MIMO-SAR Demonstrator 177
6.1. Architecture of the Radar System 177
6.1.1. Transmit Path 178
6.1.2. Receive Path 182
6.1.3. Calibration Crate 184
6.2. Hardware Synchronization and Coherent System Design 187
6.3. Nonlinear Signal Distortions 190
6.4. Antennas 193
6.5. SAR Configuration 194
6.5.1. SAR Platform 194
6.5.2. Step-Motor 195
6.6. Signal Pre-Conditioning and Pre-Processing 197
6.7. Signal Calibration 199

7. Experimental Results of DBF and MIMO Measurements 203
7.1. Digital Beam-Forming on Receive with a Reflector Antenna for Suppression of Signal Ambiguities 203
7.1.1. Description of the Experiment 204
7.1.2. Processing and Measurement Results 206
7.2. Demonstration of Digital Beam-Forming in Azimuth 208
7.2.1. Description of the Experiment 208
7.2.2. Measurement Results 208
7.3. Detection of Multipath Propagation Effects in SAR-Tomography . . 209
7.3.1. Description of the Experiment 209
7.3.2. Calibration 214
7.3.3. Processing and Measurement Results 215
7.3.4. Conclusions of the Experiment 218
7.4. Fully Polarimetric SAR Imaging by Simultaneous Measurement of the Scattering Matrix 218
7.4.1. Fully Polarimetric SAR Imaging with Orthogonal Waveforms 218
7.4.2. Measurement Scenario and Signal Processing 219
7.4.3. Measurement Results 219
7.4.4. Conclusions of the Experiment 222

8. Discussion 225

A. Mathematical Solution of the Basic Matrix Pencil 229

B. Computational Complexity of Angular Estimators 231

Bibliography 237

Abbreviations

Abbreviation	Description
ADC	analog-to-digital converter
ADSL	asymmetric digital subscriber line
AoA	angle of arrival
AS	auto synchronous
ASIC	application-specific integrated circuit
AWG	arbitrary waveform generator
CDM	code division multiplex
CL	conversion loss
cPCI	compact peripheral component interconnect
CPU	central processing unit
CRLB	Cramer-Rao lower bound
CSAR	circular synthetic aperture radar
CSC	circular shifted chirp
DAB	digital audio broadcasting
DBF	digital beam-forming
DEM	digital elevation model
DVB	digital video broadcasting
ESPRIT	estimation of signal parameters using rotational invariance techniques
FB	forward-backward
FDM	frequency division multiplex
FIR	finite impulse response
FPGA	field programmable gate array
GMTI	ground moving target indication
HAPS	high altitude pseudo-satellites
HPA	high-power amplifier
HPBW	half-power beam-width
HRWS	high-resolution wide-swath
ICI	inter-carrier-to-interference
IDL	interactive data language
IF	intermediate frequency
IIR	infinite impulse response
IL	insertion loss
ISLR	integrated sidelobe ratio
LCMV	linear constraint minimum variance
LED	light emitting diode
LEO	low-Earth orbit
LNA	low-noise amplifier
LO	local oscillator
LTE	long term evolution

Abbreviation	Description
MIMO	multiple-input multiple-output
MP	matrix pencil
MS	multiple-snapshot
MSP	multiple sub-pulse
MTI	moving target indication
MUSIC	multiple signal classification
MVDR	minimum variance distortionless response
NBW	null-to-null beam-width
OFDM	orthogonal frequency division multiplexing
OXO	ovenized crystal oscillator
PLL	phase-locked loop
PM	polarization multiplex
PSD	power spectral density
PSLR	peak sidelobe ratio
PXIe	PCI extensions for instrumentation
radar	radio detection and ranging
RAM	random-access memory
RASR	range ambiguity to signal ratio
RF	radio frequency
RMS	Root-Mean-Square
RMSE	Root-Mean-Square Error
SAR	synthetic aperture radar
SCORE	scan on receive
SDM	space division multiplex
SSD	solid-state drive
STAP	space-time adaptive processing
STFAP	space-time-frequency adaptive processing
STFT	short-time-Fourier-transform
STSO	short-term shift-orthogonal
SVD	singular value decomposition
TDM	time division multiplex
TLS	total least squares
ToA	time of arrival
ULA	uniform linear array
USB	universal serial bus
USV	uninterruptable power supply
VNA	vector network analyzer

Mathematical Operators and Functions

Operator	Description
$+$	addition
$-$	subtraction
$\cdot$	multiplication
$/$	division
$*$	convolution
$\odot$	Hadamard product (elementwise multiplication)
*	complex conjugate
$^{\mathrm{H}}$	Hermitian (complex conjugate + transpose)
$^{\mathrm{T}}$	transpose
†	Moore-Penrose pseudo inverse
δ	Dirac delta
$\lvert\,\rvert$	absolute value of a quantity
$\lVert\,\rVert$	Euclidean norm
$\lfloor\,\rfloor$	floor function
$\lceil\,\rceil$	ceiling function
$\lfloor\,\rceil$	nearest integer function
DFT	discrete Fourier transform
DFT^{-1}	inverse discrete Fourier transform
E	expectation value of a random variable
$\mathcal{F}$	Fourier transform
$\mathcal{F}^{-1}$	inverse Fourier transform
$\mathcal{O}$	Landau symbol
sin	sine function
cos	cosine function
tan	tangent function
sinc	cardinal sine function ($\mathrm{sinc}(x) = \sin(x)/x$)
exp	exponential function
rect	rectangular window function
$\sum$	sum
$\int$	integral
$\prod$	product symbol

Mathematical and Physical Constants

Symbol	Value	Description
e	2.718281	Euler's constant
j	$\sqrt{-1}$	complex constant
π	3.141592	pi
c_0	$2.997925 \cdot 10^8$ m/s	speed of light in vacuum
c	$< 2.997925 \cdot 10^8$ m/s	speed of light in corresponding medium
R_E	6371.001 km	mean Earth radius
$\mathbf{0}$	0	zero matrix
$\boldsymbol{E}$		exchange matrix
$\boldsymbol{I}$		identity matrix

Capital Latin Symbols

Symbol	Unit	Description
$\boldsymbol{A}$		DBF steering matrix
$\overline{\boldsymbol{A}}$		simplified DBF steering matrix
A	V	amplitude of IF transmit signal
A_amp		amplification factor of transmit signal
A_out	V	amplitude of transmit signal after last amplifier
AR		ambiguity ratio
B	Hz	signal bandwidth
B_BP	Hz	analog filter bandwidth
B_FIR	Hz	FIR filter bandwidth
C		joint weighting factor involving $\boldsymbol{C}_\mathrm{Rx}$, $\boldsymbol{C}_\mathrm{Tx}$ and σ_κ
$\boldsymbol{C}_\mathrm{Rx}$		receive antenna beam pattern
$\boldsymbol{C}_\mathrm{Tx}$		transmit antenna beam pattern
E_tot	Ws	total transmit energy
E_k	Ws	energy of transmit waveform
$ENOB$		effective number of bits
F		noise figure
F_cas		noise figure of cascade
G		gain
$H_{\mathrm{FIR},l}$		filter transfer function frequency domain
$ISLR$		integrated sidelobe ratio
K_r		chirp modulation rate
$K_\mathrm{r,sub}$		sub-chirp modulation rate
L		pencil parameter
M_FIR		filter order of FIR filters
N_0	V	noise level
N_az		number of samples in azimuth

Symbol	Unit	Description
N_{c}		number of sub-carriers
N_{cas}		number of components in a cascade
N_{dig}		number of significant digits
N_{el}		number of samples in elevation
N_{FIR}		number of FIR filter
N_{Rx}		total number of receive channels
$N_{\mathrm{Rx,az}}$		number of receive channels in azimuth
$N_{\mathrm{Rx,el}}$		number of receive channels in elevation
$N_{\mathrm{Rx,min}}$		minimum number of receive channels
N_{sn}		number of snapshots
$N_{\mathrm{sn,sub}}$		number of samples in fast-time within a sub-swath
N_{subsw}		number of sub-swathes
$N_{\mathrm{Tar,max}}$		maximum number of point-like targets
N_{Tx}		number of transmit channels
NBW	rad	null-to-null pattern width
OIP_3	W	3$^{\mathrm{rd}}$ order intercept point at amplifier output
PEL		pulse extension loss
PRF	Hz	pulse repetition frequency
PRF_{sub}	Hz	pulse repetition frequency used for sub-sampling
PRI	s	pulse repetition interval
PRI_{sub}	Hz	pulse repetition interval used for sub-sampling
$\boldsymbol{R}$		noise covariance matrix
$SFDR$		spurious-free dynamic range
SNR		signal-to-noise ratio
T_{NBW}	s	null-beam-width of impulse response
T_{ob}	s	observation time
TB		time-bandwidth product
W_{g}	m	swath-width
$\boldsymbol{W}_{\mathrm{Tx}}$		transmit beam-forming weighting matrix
$\boldsymbol{Y}$	V	Hankel matrix with receive signal
$\boldsymbol{Y}_0$	V	left sub-matrix of Hankel matrix $\boldsymbol{Y}$
$\boldsymbol{Y}_1$	V	right sub-matrix of Hankel matrix $\boldsymbol{Y}$

Lower Case Latin Symbols

Symbol	Unit	Description
$\boldsymbol{a}_k$		DBF steering vector
$\overline{a}_{k,i}$		channel dependent attenuation factor
$\widehat{\boldsymbol{a}}_{k,l}$		band-discrete steering vector
b		arbitrary count variable
d	m	antenna element spacing
$\boldsymbol{f}_{\mathrm{d}}$	Hz	discrete frequency vector

Symbol	Unit	Description
f	Hz	frequency along range
$\acute{f}$	Hz	frequency along azimuth
f_0	Hz	carrier frequency
f_{Dop}	Hz	Doppler frequency
f_{IF}	Hz	center frequency of IF signal
f_{S}	Hz	sampling frequency
f_k	Hz	instantaneous signal frequency
f_v	Hz	Doppler shift in Ambiguity Function
h	m	orbit height over the Earth's surface
$h_{\mathrm{az},k,i}$		channel dependent azimuth response function
$\widehat{h}_{\mathrm{az}}$		filter function used for azimuth compression
$h_{\mathrm{el},k,i}$		channel dependent elevation response function
$h_{\mathrm{FIR},l}$		filter transfer function time domain
h_{Hil}		Hilbert transfer function
i		count variable receive channels
k		count variable transmit channels
l		count variable taps of FIR filter
$l_{\mathrm{ant,az}}$	m	effective antenna length in azimuth
$l_{\mathrm{ant,el}}$	m	effective antenna height in elevation
l_{cell}	m	cell size azimuth on ground
l_{min}	m	minimum antenna height
l_{sa}	m	length of synthetic aperture
m		arbitrary count variable
$\boldsymbol{n}$	V	Additive White Gaussian Noise (AWGN) of all receive channels
n	V	Additive White Gaussian Noise (AWGN)
$\boldsymbol{p}$	m	target position
$\boldsymbol{p}_{\mathrm{Rx},i}$	m	receive antenna position
$\boldsymbol{p}_{\mathrm{Tx},k}$	m	transmit antenna position
p		counting variable of time samples
$\tilde{p}_l$		specific time sample
q		counting variable of frequency samples
$r_{k,i}$	m	equivalent range radar - target
$r_{0,k,i}$	m	slant range distance of closest approach
$\boldsymbol{s}$	V	set of transmit waveforms
$\boldsymbol{s}_{\mathrm{BB}}$	V	set of transmit waveforms in base-band
$s_{\mathrm{BB,chirp}}$	V	chirp waveform in base-band
$s_{\mathrm{BB},k}$	V	transmit waveform in base-band
s_k	V	transmit waveform
t	s	continuous fast-time variable
$\acute{t}$	s	continuous slow-time variable
$t_{\mathrm{c},k}$	s	center of sub-pulse

Symbol	Unit	Description
$t_{\mathrm{c1},k}$	s	center of first part of k-th CSC waveform
$t_{\mathrm{c2},k}$	s	center of second part of k-th CSC waveform
$\boldsymbol{t}_{\mathrm{d}}$	s	discrete fast-time vector
t_{horpos}	s	time shift for calibration
$\boldsymbol{u}$	V	set of receive signals
$\check{\boldsymbol{u}}_{\mathrm{d}}$	V	set of simplified receive signals time-discrete
u_{az}	V	focused raw data
u_{DBF}	V	raw-data after DBF
$\check{u}_{\mathrm{FIR},l,i}$	V	filtered receive signal
u_{rcm}	V	range migrated data
u_{rec}	V	reconstructed raw data
u'_{rec}	V	reconstructed raw data at certain time
u_{rg}	V	range compressed raw data
u_i	V	receive signal
$\check{u}_i$	V	simplified form of receive signal
v_{E}	m/s	velocity of projected antenna beam on Earth
v_{sat}	m/s	velocity of SAR platform
$\boldsymbol{w}_{\mathrm{Rx},k}$		DBF weight for receive
w_{Tx}		DBF weight for transmit
$\widehat{\boldsymbol{w}}_{\mathrm{sub},l,k}$		discrete DBF weight
w_{win}		window function
x	m	Cartesian coordinate
y	m	Cartesian coordinate
z	m	Cartesian coordinate
z_k,z_m		signal poles

Capital Greek Symbols

Symbol	Unit	Description
Γ		generalized eigenvectors
ΔR	m	range-variation due to sensor movement
ΔT	s	observation time interval
Δf	Hz	sub-carrier distance
Δf_{Dop}	rad	effective Doppler bandwidth
Δh	m	height offset
Δt	s	time-variation due to range cell migration
$\Delta\Theta_{\mathrm{3dB}}$	rad	half-power beam-width in elevation
$\Delta\phi_{\mathrm{3dB}}$	rad	half-power beam-width in azimuth
$\Delta\varphi_k$	rad	differential phase delay of receive signal
Θ	rad	elevation angle
Θ_Δ	rad	angular offset between two antenna beams
$\widehat{\Theta}_k$	rad	angle of arrival vs. nadir

Symbol	Unit	Description
Θ_{ambig}	rad	separation of grating lobes
Θ_{d}	rad	discrete elevation angle
Θ_{inc}	rad	incidence angle
Θ_{mis}	rad	antenna mis-pointing
Θ_{tilt}	rad	antenna tilt angle vs. nadir
Θ_{true}	rad	actual antenna steering angle
$\boldsymbol{\Lambda}_{\text{L}}$		left singular vector after SVD
$\boldsymbol{\Lambda}_{\text{R}}$		right singular vector after SVD
$\boldsymbol{\Xi}$	V	matrix containing singular values of $\boldsymbol{Y}_0$
$\boldsymbol{\Sigma}$	V	matrix containing singular values of $\boldsymbol{Y}$
$\boldsymbol{\Psi}$		generalized eigenvalues
Ω_l	Hz	angular center frequency of filter

Lower Case Greek Symbols

Symbol	Unit	Description
γ		parameter for shaping Gaussian window
δ_{MP}	rad	angular accuracy limit
δ_{rg}	m	ground range resolution
δ_{sa}	m	azimuth resolution
ϵ	s	margin for orthogonal limits
η		shifting factor
$\vartheta_{\text{d},0}$	rad	discrete angle of arrival vs. tilt
$\widehat{\vartheta}_k$	rad	angle of arrival vs. tilt
$\check{\vartheta}_m$	rad	estimated angle of arrival vs. tilt
κ		polarization state
$\widehat{\lambda}_l$	m	wavelength of filter signal
λ_0	m	carrier wavelength
λ_k	m	instantaneous signal wavelength
μ		threshold value
μ_{max}		real part of largest estimated singular value
ξ		MUSIC pseudo-spectrum
$\wp_b$		spectrogram
σ_κ^0		differential target scattering coefficient
$\varsigma_{k,b}$		cross-correlation interferences
$\tau_{\text{c},k}$	s	center of sub-pulse
$\tau_{\text{c1},k}$	s	first center of circular shifted chirp
$\tau_{\text{c2},k}$	s	second center of circular shifted chirp
τ_{echo}	s	duration of recorded echo-window
τ_{p}	s	pulse duration
τ_{s}	s	gap between two sub-pulses

Symbol	Unit	Description
τ_{sub}	s	sub-pulse duration
$\tau_{\text{sub1},k}$	s	duration of first part of k-th CSC waveform
$\tau_{\text{sub2},k}$	s	duration of second part of k-th CSC waveform
$\tau_{k,i}$	s	round-trip signal delay
υ^2	W	noise power
ϕ	rad	azimuth angle
φ	rad	signal phase shift along azimuth
χ_{MIMO}	rad	unambiguous slant range interval
χ_k		ambiguity function
$\chi'_{k,b}$		cross ambiguity function
χ_Θ	rad	angular pulse extent
$\chi_{\Theta,\text{MIMO}}$	rad	angular extent of unambiguous swath
$\chi_{\Theta,\text{max}}$	rad	maximum acceptable angular pulse extent
χ_ρ	rad	slant range extent
ω_0	Hz	angular carrier frequency

1. Introduction

Radar is an acronym and stands for RAdio Detection And Ranging. The first radar system was invented by Christian Hülsmeyer in 1904 for detection of ships on the river Rhine [1, 2]. The radar principle is based on transmission of an electromagnetic wave, which is reflected by an object and backscattered to the receiver. Using the known propagation speed of light, the distance between radar and target can be determined.

Many years later, in 1951, the mathematician Carl A. Wiley invented the first Synthetic Aperture Radar (SAR), which is an imaging sensor [3]. By using advanced signal processing methods, imaging radar systems allow for two-dimensional and in case of tomographic systems even three-dimensional imaging of the observed area. From the backscattered signal key information, e.g. roughness, geometrical structure and electromagnetic characteristics of the surface, and depending on the penetration, the area directly below the surface can be extracted. The penetration depth is dependent on the signal wavelength and the electrical characteristics of the illuminated area. In contrast to passive sensors, a radar system has its own illumination source, which allows for imaging independent of external illumination sources. In addition, signals with a wavelength of greater than 1 cm are usually used, which leads almost to an all-weather capability. In the meantime, SAR systems have evolved to a versatile technique for remote sensing of our planet.

1.1. State-of-the-Art and Motivation for new Imaging Modes

Since the first developments of SAR, radar for imaging applications and Earth observation has become an important sensor. Manifold applications, ranging from climate change research over change detection and 4-D mapping up to security-related applications are now common. Not only the aforementioned weather-independent imaging capabilities, but also the high-resolution and the day-and-night operation led to the success of SAR. An example for a high-resolution SAR image, acquired with the airborne F-SAR system [4] of the German Aerospace

Center (DLR) is given in Fig. 1.1. It was acquired in X-band at a center frequency of 9.6 GHz and has a spatial resolution of 0.25 m. The colors indicate different scattering mechanisms, which could be separated by different polarization states of the transmitted and received electromagnetic waves. Apart from airborne SAR systems there exists a large number of spaceborne SAR missions, like COSMO-SkyMed, TerraSAR-X / TanDEM-X, Radarsat-2 or Sentinel-1 [5–7]. In the meantime, more than 30 spaceborne SARs have been launched. However, the steady demand for observations with higher resolutions, wider coverage, increased flexibility and shorter retake intervals, stretches the state-of-the-art SAR sensors to their maximum limits.

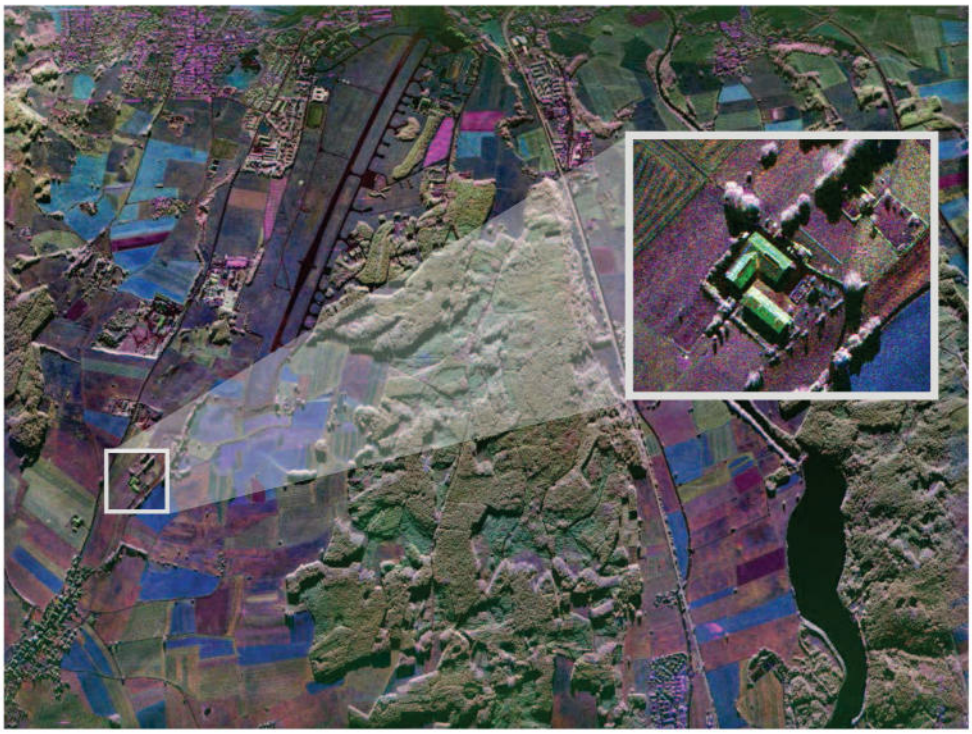


Figure 1.1. An example for a fully polarimetric SAR image acquired with DLR's F-SAR sensor in X-band.

A consideration of various studies [8–10] shows that SAR sensors with Digital Beam-Forming (DBF) capabilities have promising properties to overcome these limitations. The overall idea is to tailor the radiation characteristics of an antenna array within the digital part of the hardware and to apply thereby a spatial filtering. Since the filtering is done in the digital part, the raw data are still available and no information is lost. This allows a great flexibility and various algorithms for signal processing and antenna beam-forming can be applied.

If multiple receivers, along with multiple transmitters are used within the same radio channel, the Multiple-Input Multiple-Output (MIMO) technique offers a new field of operation in SAR. To separate the transmit signals in the digital receiver, advanced modulation and multiplex techniques are used, which exploit the characteristics of the individual signals and channels. This offers an increase in the information rate, because multiple information can be transmitted in parallel. As a result, with MIMO new advanced imaging modes, such as simultaneous fully polarimetric acquisitions can be realized [11].

Nowadays DBF and MIMO are established techniques in communications [12]. However, a straight forward adaption of DBF and MIMO from the field of communication to SAR is not possible. The essential difference between both is the information, in which the user is interested in. While in communications, the transmitted signal is unknown and the channel characteristics should be suppressed, in radar the transmitted signal is known and the user is interested in the channel. DBF and MIMO are still in an early stage in SAR applications and bring new challenges with them. This thesis is motivated by making a significant contribution to algorithms, waveform types, requirements and limitations of new DBF-SAR and MIMO-SAR operation modes.

1.2. Outline and Contributions of this Work

This thesis is divided into eight chapters, which are organized as follows.

After this introduction, in **chapter 2** fundamentals of the basic SAR principle and a generalized signal model for MIMO-SAR is given. Based on that, the fundamental limitations of SAR are summarized, which show the system-inherent relation between azimuth resolution and swath width. An overview about the processing strategy of multi-channel SAR data and over various advanced DBF-SAR and MIMO-SAR imaging modes rounds off the chapter.

Chapter 3 is about waveform types for MIMO-SAR. At the beginning of the chapter, we attend to the problem formulation of orthogonal waveforms in MIMO-SAR. In this context, orthogonal means that the transmitted waveforms can be completely separated in the receiver. As will be shown, this results in a challenge, since in this case SAR offers little degrees of freedom. Then three different waveform types are introduced, which will fulfill the prior defined requirement of orthogonality, if they are combined with DBF on receive. Also, the radar ambi-

guity function is introduced as a valuable tool for evaluation of waveforms. The last section of the chapter gives a detailed comparison of the previously introduced waveforms by means of the ambiguity function and other performance parameters, like range resolution and signal energy.

For DBF on receive, the antenna has to fulfill certain requirements. These requirements, in terms of the antenna size, are derived in **chapter 4**. This is followed by a signal processing algorithm for a single transmit channel and multiple receivers. Major contribution of this chapter is not only, that the algorithm also covers the Earth's curvature and long signal durations, but also its extension to MIMO in the subsequent sections. Because DBF along elevation is a requirement for waveform separation, the algorithms for this task are derived and analyzed by simulations. This is done for the three waveform types of the last chapter individually.

During this work, it turned out that the DBF concept in combination with large swath widths and high resolutions (HRWS: High-Resolution Wide-Swath) is degraded in presence of topographic changes on Earth. This is due to a distortion between the expected time of arrival of the echo signal and the expected angle with respect to nadir, from which the echo arrives. Therefore in **chapter 5** an innovative algorithm is derived, which estimates the direction of arrival of the echo signal on the acquired raw-data with high accuracy and in real-time. The method is based on the so-called matrix pencil, which is a common approach in mathematics for solving linear equation systems. After some improvements to achieve a higher accuracy for the topography-adaptive-DBF, a series of different simulation tasks are performed, which serve as a proof of concept.

In **chapter 6** it comes to the ground-based MIMO-SAR demonstrator. This radar system is developed as part of this PhD work for verification of advanced DBF-SAR and MIMO-SAR imaging modes. Four transmit and eight receive channels, which can be operated simultaneously in the same frequency band at a center frequency of 9.6 GHz (X-band), allow a great flexibility. Especially the modular and fully coherent hardware design with a oscillator, shared by all components, is a significant advantage. After describing the system design with its antennas, the pre-processing and calibration steps are given, which are crucial for the following DBF, MIMO and SAR signal processing tasks. By using the correction steps, which are described in this section, the maximum signal quality is achieved.

Chapter 7 describes the experimental results of four outdoor measurements on a meadow with the ground-based MIMO-SAR demonstrator. The acquired measurement data in combination with the algorithms, which are presented and derived in this thesis, are used as a proof of concept. In the first section, the possibility of redeeming individual orthogonal waveforms in MIMO-SAR with a multi-channel reflector antenna is demonstrated. Experimental results of DBF on receive in the azimuth direction are given in the second section. A new acquisition mode for detecting multipath propagation effects in SAR-tomography is shown in the third section. Since simultaneous and fully polarimetric SAR measurements are of high significance in reducing the transmit duty cycle of the satellite, in the last section, fully polarimetric MIMO-SAR measurements with a fence as extended target are presented.

The remaining chapter of this thesis details the conclusions and a summary of all results, that are presented in this work.

2. Fundamentals and Principles of SAR and MIMO-SAR

This chapter serves as a crucial basis for the following chapters. Apart from the conventional SAR principle and its limitations, also the extension to multiple channels is derived.

At the beginning, the basic SAR principle for a single-channel system is derived briefly and the independence of the maximum achievable azimuth resolution from the distance between radar and target scene is shown.

In section 2.2 an analytical multi-channel SAR signal model can be found. It is kept as general as possible and applies to all following equations in this thesis.

A major problem in SAR is the trade-off that a large swath width and a high azimuth resolution can not be achieved simultaneously. This issue is analyzed in terms of the Pulse Repetition Frequency (*PRF*) and antenna dimensions.

All necessary steps for multi-channel SAR processing are given in section 2.4. First, digital beam-forming is used to combine the receive channels oriented in azimuth and elevation direction to an equivalent single channel for each transmitted waveform individually. Advantages, which result by using multiple channels are given at the appropriate points. This is followed by standard SAR processing of SAR raw data up to a final high-resolution image.

To be able to analyze different processing methods, a modular MIMO-SAR processing tool was developed. This tool handles simulated data, measurement data and even polarimetry.

An overview of new, highly innovative imaging modes to enhance the SAR capabilities and to overcome basic limitations in next generation SAR is shown in the last part of this chapter.

2.1. Conventional SAR Principle

In conventional SAR, a pulsed radar is mounted on a platform, which is moving with the constant velocity v_{sat} in along-track direction, whereas the antenna is

directed perpendicularly to the direction of movement[1], pointing towards the ground with the antenna tilt angle Θ_{tilt} vs. nadir. The projected antenna beam on the Earth moves with the velocity v_{E}, which can also be seen as the effective rate of transport of the antenna footprint over the Earth's surface (Earth rotation is neglected for ease). The relation between v_{sat} and v_{E} is given by [13]:

$$v_{\text{E}} = v_{\text{sat}} \cdot \frac{R_{\text{E}}}{R_{\text{E}} + h} \cdot \cos\left[\arcsin\left(\frac{r_0}{R_{\text{E}} + h} \cdot \sin\Theta_{\text{inc}}\right)\right]. \tag{2.1}$$

A sketch of this scenario can be found in Fig. 2.1. R_{E} denotes the Earth radius, h the orbit height over the Earth's surface, r_0 is the distance of closest approach and Θ_{inc} the incidence angle. Within the antenna footprint on the Earth's surface, an infinite number of distributed targets is illuminated. This is one great difference to standard surveillance radar, where only one or a small number of targets is observed. The received echoes of each transmitted pulse, repeated by the *PRF*, are stored in a two-dimensional data array for further processing. As will be described in more detail in section 2.4, the acquired raw data can be focused to a high-resolution SAR image, by applying compression filters in both directions. Further, detailed descriptions of the SAR principle and processing methods can be found in the standard literature [14–16].

Considering a fixed instance of time, targets which will be seen by the sensor yielding the same relative radial velocity between sensor and Earth, are lying on the surface of an imaginary cone. The axis of this cone is orientated along the moving direction, while the tip is placed at the radar. The intersection of the cone with the Earth's surface results in a deformed hyperbola. Accordingly all scatterers, which are lying on such a hyperbola, experience the same Doppler shift with reference to the sensor. These hyperbolas are also named iso-Doppler lines. Logically, targets at different hyperbolas, experience different Doppler shifts. Hence, the SAR principle is based on the possibility to separate targets from different hyperbolas by frequency filtering. In range direction, due to the signal propagation at the speed of light, targets lying at different distances from the radar can be separated with standard radar processing methods, such as range compression. The intersection of iso-Doppler and iso-range lines leads to a grid, on which the Radar

[1] A squint angle is neglected for ease.

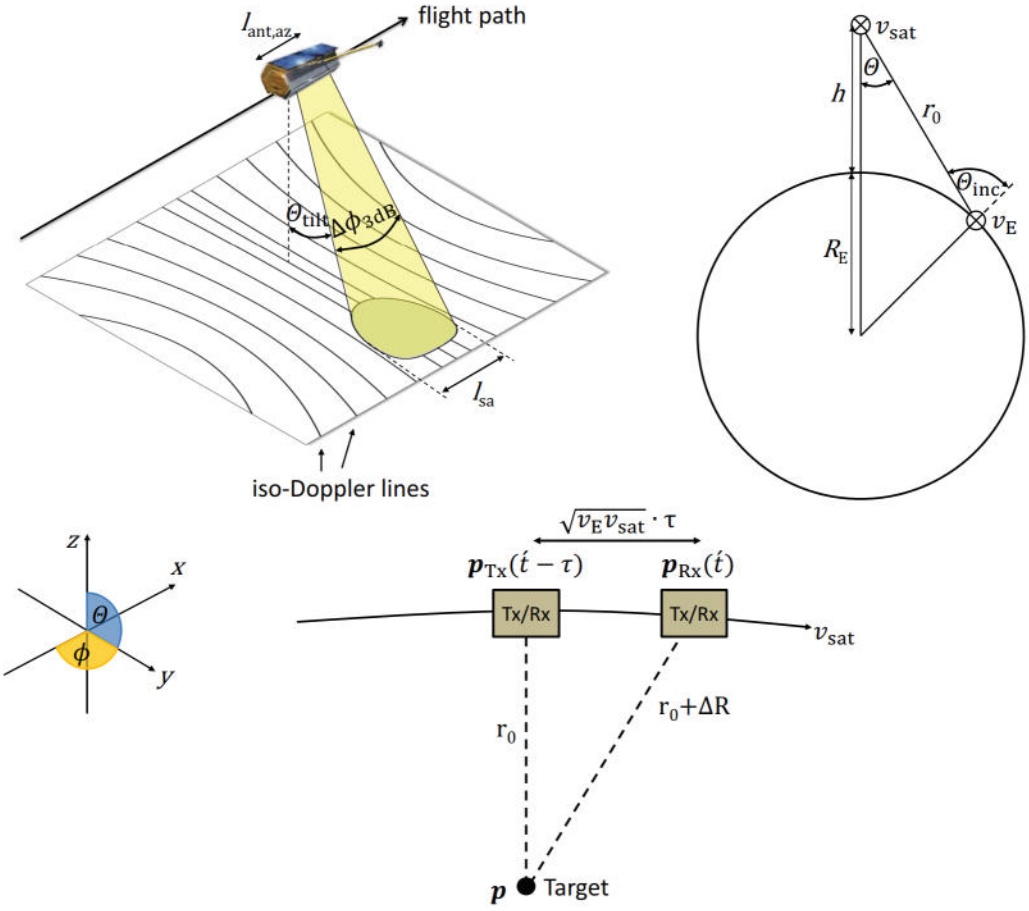


Figure 2.1. Illustration of the SAR principle.

Cross Section (RCS) can be computed for each node. This process is derived in detail next.

To understand the basic SAR principle, it is sufficient to assume a monostatic SAR sensor with transmit and receive antennas placed at time instance $\acute{t}$ at Cartesian coordinates $\boldsymbol{p}_{\mathrm{Tx}}(\acute{t}) = [x_{\mathrm{Tx}}(\acute{t}), y_{\mathrm{Tx}}(\acute{t}), z_{\mathrm{Tx}}(\acute{t})]$ and $\boldsymbol{p}_{\mathrm{Rx}}(\acute{t}) = \boldsymbol{p}_{\mathrm{Tx}}(\acute{t})$. $\acute{t}$ is quite often also referred to as slow-time, because usually the time variable for the signal propagation t (fast-time) and the time variable used along the moving direction of the sensor $\acute{t}$ (slow-time) are considered separately. This is due to the two-dimensional imaging geometry of SAR. Because of the different velocities, v_{E} and v_{sat}, and the sensor movement during the round-trip signal delay τ from the transmit antenna to the target and back to the receive antenna, it is more convenient to map the imaging geometry into an equivalent model. This is depicted in the lower part of Fig. 2.1. Apart from the distance of closest approach $r_0(\boldsymbol{p})$ to a point

$\boldsymbol{p}$ on the observed swath with coordinates $\boldsymbol{p} = [p_x, p_y, p_z]$, an additional length ΔR must be taken into account, which is in turn dependent on the effective sensor velocity $\sqrt{v_E \cdot v_{sat}}$. The time varying distance radar-to-target, can be expressed through Pythagoras theorem and Taylor series approximation as $r(\acute{t}, \boldsymbol{p})$ [13]:

$$\begin{aligned} r(\acute{t}, \boldsymbol{p}) =& \frac{\left\|\boldsymbol{p} - \boldsymbol{p}_{Tx}(\acute{t} - \tau)\right\| + \left\|\boldsymbol{p} - \boldsymbol{p}_{Rx}(\acute{t})\right\|}{2} = \sqrt{r_0^2(\boldsymbol{p}) + (\sqrt{v_E \cdot v_{sat}}\acute{t})^2} \\ \approx& r_0(\boldsymbol{p}) + v_E \cdot v_{sat} \cdot \acute{t}^2 \frac{1}{2r_0(\boldsymbol{p})}, \end{aligned} \tag{2.2}$$

with $\|.\|$ denoting the Euclidean norm. Using vector notation (bold symbols) helps for MIMO signal descriptions significantly.

Due to the time-variant range shift, the received signal experiences a modulation along azimuth. The resulting phase shift $\varphi(\acute{t})$ on the receive signal is given as

$$\varphi(\acute{t}, \boldsymbol{p}) = -\frac{4\pi}{\lambda_0} r(\acute{t}, \boldsymbol{p}) \qquad \text{for} \quad -\frac{T_{ob}}{2} \leq \acute{t} \leq \frac{T_{ob}}{2}, \tag{2.3}$$

where λ_0 is the carrier wavelength of the transmitted signal and T_{ob} is the observation time, during which a hypothetical point target is illuminated. The frequency shift f_{Dop} on each iso-Doppler line at time instance $\acute{t}$ can be calculated by differentiating the phase term with respect to time:

$$f_{Dop}(\acute{t}, \boldsymbol{p}) = \frac{1}{2\pi} \frac{\mathrm{d}\varphi(\acute{t}, \boldsymbol{p})}{\mathrm{d}\acute{t}} \approx -\frac{2}{\lambda_0} \cdot v_E \cdot v_{sat} \frac{\acute{t}}{r_0(\boldsymbol{p})}. \tag{2.4}$$

Thus, the azimuth response function $h_{az}(\acute{t}, t)$, which describes the signal modulation in along-track direction, is:

$$h_{az}(\acute{t}, t, \boldsymbol{p}) = \exp[\mathrm{j}\varphi(\acute{t}, \boldsymbol{p})] \cdot \delta(t - \tau(\acute{t})) = \exp\left[-\mathrm{j}\frac{4\pi}{\lambda_0} r(\acute{t}, \boldsymbol{p})\right] \cdot \delta(t - \tau(\acute{t})), \tag{2.5}$$

with $\mathrm{j} = \sqrt{-1}$ being the complex constant. The shifted Dirac delta distribution δ is used later in the signal model for convolution with the elevation response function.

With unlimited span of $|\acute{t}|$, the observation time T_{ob} and hence the Doppler-bandwidth increases. However, the azimuth response $h_{\mathrm{az}}(\acute{t}, t, \boldsymbol{p})$ is in addition weighted with the joint transmit-receive antenna pattern along azimuth and usually limited to the Half-Power Beam-Width (*HPBW*) $\Delta\phi_{3\mathrm{dB}}$. T_{ob} can then be expressed in terms of the maximum length of the synthetic aperture l_{sa} and the platform velocity or by using the approximation $l_{\mathrm{sa}} \approx r_0 \cdot \Delta\phi_{3\mathrm{dB}}$:

$$T_{\mathrm{ob}} = \frac{l_{\mathrm{sa}}}{v_{\mathrm{E}}} \approx \frac{r_0(\boldsymbol{p}) \cdot \Delta\phi_{3\mathrm{dB}}}{v_{\mathrm{E}}}. \tag{2.6}$$

An important fact is that each point is illuminated for a longer time than T_{ob} in reality, since the antenna also receives energy outside the *HPBW*. A larger Doppler bandwidth (and hence a higher resolution) can be achieved by using a larger observation time during processing.

An example of $h_{\mathrm{az}}(\acute{t}, t, \boldsymbol{p})$ with the parameters of TerraSAR-X ($v_{\mathrm{sat}} = 7.6 \cdot 10^6\ \frac{\mathrm{m}}{\mathrm{s}}$, $\lambda_0 = 3.1$ cm, $h = 514$ km, $l_{\mathrm{ant,az}} = 4.8$ m, $\Theta_{\mathrm{inc}} = 20°$) is depicted in Fig. 2.2.

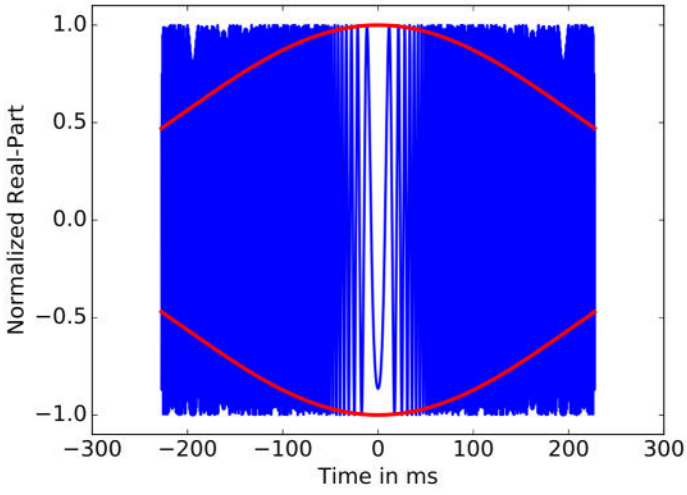


Figure 2.2. As an example, plot of the real-part of $h_{\mathrm{az}}(\acute{t}, t, \boldsymbol{p})$ with $v_{\mathrm{sat}} = 7.6 \cdot 10^6\ \frac{\mathrm{m}}{\mathrm{s}}$, $\lambda_0 = 3.1$ cm, $h = 514$ km, $l_{\mathrm{ant,az}} = 4.8$ m and $\Theta_{\mathrm{inc}} = 20°$. The curves in red color indicate the weighting by the azimuth antenna pattern over the observation time $T_{\mathrm{ob}} = 455$ ms.

Inserting Eq. (2.6) in Eq. (2.4) leads to an effective Doppler bandwidth of

$$\Delta f_{\mathrm{Dop}} = |f_{\mathrm{Dop}}(T_{\mathrm{ob}})| \approx \frac{2}{\lambda_0} v_{\mathrm{sat}} \cdot \Delta\phi_{3\mathrm{dB}}. \tag{2.7}$$

As an intermediate step for derivation of the azimuth resolution we get the Time-Bandwidth Product TB by multiplying Eq. (2.6) and Eq. (2.7):

$$TB = T_{\mathrm{ob}} \cdot \Delta f_{\mathrm{Dop}} \approx \frac{2r_0(\boldsymbol{p})}{\lambda_0} \cdot \frac{v_{\mathrm{sat}}}{v_{\mathrm{E}}} \Delta\phi_{3\mathrm{dB}}^2. \tag{2.8}$$

With the relation between effective antenna length in azimuth $l_{\mathrm{ant,az}}$ and $HPBW$ [17]:

$$\Delta\phi_{3\mathrm{dB}} = \frac{\lambda_0}{l_{\mathrm{ant,az}}}, \tag{2.9}$$

the optimum azimuth resolution δ_{sa} is given by the quotient of the antenna footprint on Earth and the time-bandwidth product (quotient of the real aperture and the compression gain in azimuth):

$$\delta_{\mathrm{sa}} = \frac{r_0(\boldsymbol{p}) \cdot \Delta\phi_{3\mathrm{dB}}}{TB} \approx \frac{\lambda_0 v_{\mathrm{E}}}{2 v_{\mathrm{sat}} \Delta\phi_{3\mathrm{dB}}} = \frac{v_{\mathrm{E}}}{v_{\mathrm{sat}}} \cdot \frac{l_{\mathrm{ant,az}}}{2}. \tag{2.10}$$

As one of the major advantages of SAR, the azimuth resolution is more or less independent from the distance between radar and target scene. The quotient of the platform velocity and the projected velocity even leads to an improved resolution for the spaceborne case. To achieve a higher azimuth resolution sometimes also a larger Doppler bandwidth is processed. In the following, a complete signal model according to this principle is derived.

2.2. Analytic MIMO-SAR Signal Model

In this section, a generalized MIMO-SAR signal model is introduced. Based on this model, special cases such as multistatic configurations can be derived. Since Ground Moving Target Indication (GMTI) is not within the scope of this work,

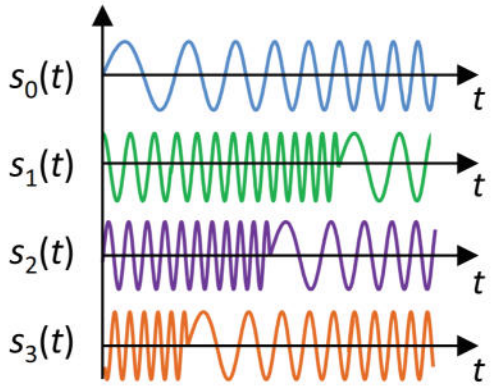


Figure 2.3. An example of a set of transmit waveforms in base-band with $N_{\mathrm{Tx}} = 4$.

the scene is assumed as to be time-invariant. Further conditions are the coherent operation of transmitter and receiver and the absence of inter-coupling effects. Other assumptions are directly named at the appropriate points. To keep it as simple and general as possible, we concentrate only on the basic parameters also used in the following chapters. The underlying model is inspired by other important signal models for radar, MIMO radar, SAR, DBF-SAR and MIMO-SAR and can be found in [9, 14, 18, 19].

2.2.1. Transmitter

An arbitrary set of waveforms in base-band $\boldsymbol{s}_{\mathrm{BB}}(t)$ has the form

$$\boldsymbol{s}_{\mathrm{BB}}(t) = [s_{\mathrm{BB},0}(t), s_{\mathrm{BB},1}(t), \ldots, s_{\mathrm{BB},k}(t), \ldots, s_{\mathrm{BB},N_{\mathrm{Tx}-1}}(t)]^{\mathrm{T}} \quad \text{for} \quad k \in \mathbb{N}_0^+ \text{ and } k < N_{\mathrm{Tx}}, \tag{2.11}$$

where N_{Tx} is the number of transmit channels and $^{\mathrm{T}}$ denotes the transpose of the vector. An illustrative diagram of the base-band waveform-concept with $N_{\mathrm{Tx}} = 4$ is shown in Fig. 2.3.

In general, the physical number of transmit antennas can be less than or equal to N_{Tx} (e.g. dual polarized antenna). These waveforms are up-converted to the RF (radio frequency) band with the angular carrier frequency $\omega_0 = 2\pi f_0$. The bandwidth B of each signal is assumed to be $B/2 < f_0$ to avoid negative frequency components. The set of transmitted pulses $\boldsymbol{s}(t)$ is then described by

$$\boldsymbol{s}(t) = \boldsymbol{W}_{\mathrm{Tx}}(t) \cdot \boldsymbol{s}_{\mathrm{BB}}(t) \cdot \exp\left[\mathrm{j}\omega_0 t\right] \tag{2.12}$$

and can be arranged, according to Eq. (2.11), as follows:

$$\begin{aligned} \boldsymbol{s}(t) = &\left[s_0(t), s_1(t), ..., s_k(t), ..., s_{N_{\mathrm{Tx}-1}}(t)\right]^{\mathrm{T}} \\ &\text{for} \quad k \in \mathbb{N}_0^+ \text{ and } k < N_{\mathrm{Tx}}. \end{aligned} \tag{2.13}$$

Within the base-band a variety of waveforms can be accommodated to define a tailored pulse containing these waveforms. They are then repeated by the *PRF*. The use of beam-forming weights $\boldsymbol{W}_{\mathrm{Tx}}(t)$ of the form

$$\boldsymbol{W}_{\mathrm{Tx}}(t) = \begin{bmatrix} w_{\mathrm{Tx},0,0}(t) & \cdots & w_{\mathrm{Tx},0,N_{\mathrm{Tx}}-1}(t) \\ \vdots & \ddots & \vdots \\ w_{\mathrm{Tx},N_{\mathrm{Tx}}-1,0}(t) & \cdots & w_{\mathrm{Tx},N_{\mathrm{Tx}}-1,N_{\mathrm{Tx}}-1}(t) \end{bmatrix} \tag{2.14}$$

allows to apply a time-variant DBF on transmit[2]. It may be noted that the elements of this matrix in general are complex. For better visualization, a basic block diagram showing the principle of DBF weighting can be found in Fig. 2.4.

2.2.2. Channel and Target

To describe the complete channel characteristics, it makes sense to divide them into propagation path and target. The propagation paths from the transmit antennas to the target and back to the receiving antennas are summarized with the associative property to a single channel impulse response for azimuth and elevation, respectively, while the targets placed at far-field are considered separately.

[2] In contrast to the described frequency-dispersive receive beam-forming algorithm in chapter 4, this beam-forming is independent of the signal's frequency for ease.

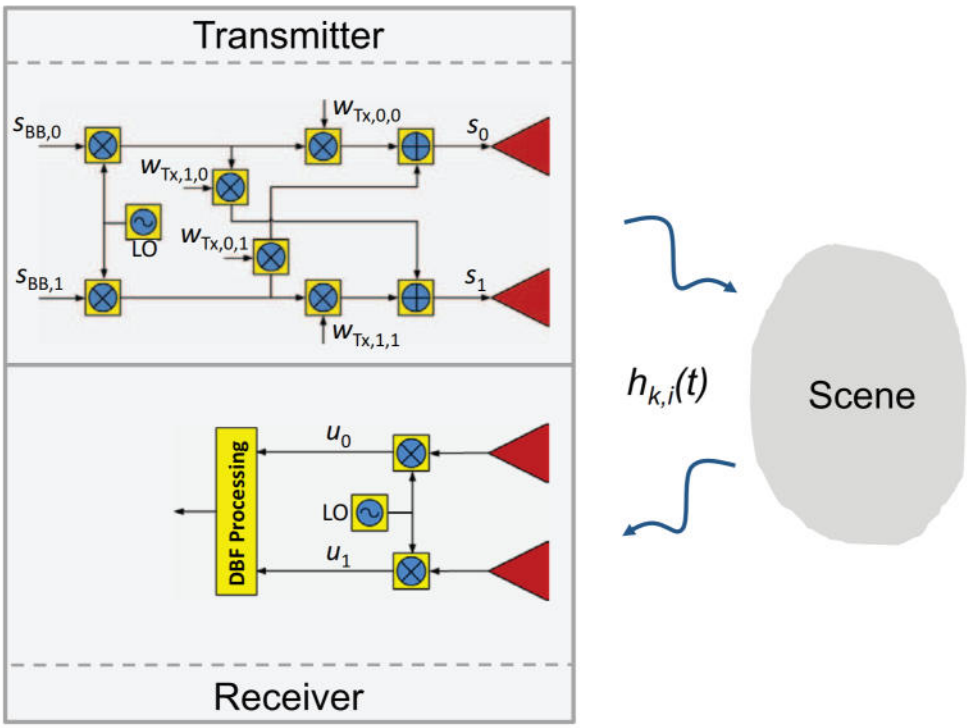


Figure 2.4. Basic block diagram for two typical transmit and receive channels.

Channel

Beginning with the channel, the echo of the transmit signal, which is reflected from a target placed in the far-field at position $\boldsymbol{p}$ is received at receive channel i after the delay $\tau_{k,i}$:

$$\tau_{k,i}(\acute{t},\boldsymbol{p}) = \frac{\left\|\boldsymbol{p}-\boldsymbol{p}_{\mathrm{Tx},k}(\acute{t}-\tau_{k,i}(\acute{t},\boldsymbol{p}))\right\|}{c} + \frac{\left\|\boldsymbol{p}-\boldsymbol{p}_{\mathrm{Rx},i}(\acute{t})\right\|}{c} = \frac{2r_{k,i}(\acute{t},\boldsymbol{p})}{c} \quad \text{for} \quad i \in \mathbb{N}_0^+,\ i < N_{\mathrm{Rx}}, \tag{2.15}$$

where i is the index of the receive channel, N_{Rx} the number of receive channels and $\boldsymbol{p}_{\mathrm{Tx},k}(\acute{t}) = [x_{\mathrm{Tx}}(\acute{t}), y_{\mathrm{Tx}}(\acute{t}), z_{\mathrm{Tx}}(\acute{t})]_k$ and $\boldsymbol{p}_{\mathrm{Rx},i}(\acute{t})$ the positions of the transmit and receive antenna phase centers. $c < c_0$ is a physical constant, which defines the propagation speed of the signal in the corresponding medium (c_0 is the speed of light in vacuum). Similar to the transmit channels, the number of receive antennas can be less than or equal to N_{Rx}. In accordance with Eq. (2.2), the equivalent range radar – target is

$$r_{k,i}(\acute{t},\boldsymbol{p}) = \sqrt{r_{0,k,i}^2(\boldsymbol{p}) + (\sqrt{v_\mathrm{E}\cdot v_\mathrm{sat}}\cdot\acute{t})^2} \approx r_{0,k,i}(\boldsymbol{p}) + v_\mathrm{E}\cdot v_\mathrm{sat}\cdot\acute{t}^2\frac{1}{2r_{0,k,i}(\boldsymbol{p})}. \tag{2.16}$$

Resulting from the two-dimensional imaging geometry and for later processing, it is necessary to split up the channel into two separate impulse response functions. For the channel impulse response along elevation we get:

$$h_{\mathrm{el},k,i}(\acute{t},t,\boldsymbol{p}) = s_k(t-\tau_{k,i}(\acute{t},\boldsymbol{p}))\cdot\delta(\acute{t}). \tag{2.17}$$

It may be recalled that $\delta(\acute{t})$, in the present case, corresponds to a unit point scatterer located at $\boldsymbol{p}$. Basically, it is the transmit signal, shifted by the round-trip delay. The Delta distribution at time-instance $\acute{t}$ becomes necessary for convolution with the channel impulse response along azimuth $h_{\mathrm{az},k,i}$, which can be written in accordance with Eq. (2.5) as

$$h_{\mathrm{az},k,i}(\acute{t},t,\boldsymbol{p}) = \exp\left[-\mathrm{j}\frac{4\pi}{\lambda_0}r_{k,i}(\acute{t},\boldsymbol{p})\right]\cdot\delta(t-\tau_{k,i}(\acute{t},\boldsymbol{p})). \tag{2.18}$$

In addition, the received signal is also effected by the antenna pattern of each individual transmit and receive antenna $C_{\mathrm{Tx},k}(\Theta(\boldsymbol{p}),\phi(\boldsymbol{p}))$ and $C_{\mathrm{Rx},i}(\Theta(\boldsymbol{p}),\phi(\boldsymbol{p}))$. The terms $\Theta(\boldsymbol{p})$ and $\phi(\boldsymbol{p})$ denote the elevation and azimuth angles between antenna and target measured with respect to nadir and boresight direction of the antenna. The exact dependency between the target position $\boldsymbol{p}$ and the elevation and azimuth angles Θ and ϕ is not yet important and given later in chapter 4. The channels of the MIMO radar with unequal behavior and attenuation over free-space and the atmosphere will be accounted for through the weighting factor $\overline{a}_{k,i}(\acute{t},t,\boldsymbol{p})$ in Eq. (2.19).

Target

A point scatterer placed at the Cartesian coordinates $\boldsymbol{p}$ can be modeled by the differential target scattering coefficient $\sigma_\kappa^0(\boldsymbol{p})$. Using the assumption $\left\|\boldsymbol{p}-\boldsymbol{p}_{\mathrm{Tx},k}\right\| >> \left\|\boldsymbol{p}_{\mathrm{Tx},k}-\boldsymbol{p}_{\mathrm{Rx},i}\right\| \;\forall\, i,k$, it is valid to assume that the angles for the impinging and reflected waves are equal. Further, the dependency on the polar-

ization state (horizontal or vertical) is given by the used channel, whereas the index κ indicates the scattering behavior in the corresponding polarization. For simplification, cross-coupling effects are neglected.

In fact, σ^0_κ, the complex scattering amplitude, relates the normalized ratio of impinging and reflected electromagnetic wave power at an infinitesimal small target and is thus not only dependent on Θ and ϕ (cf. Fig. 2.1), but also on the signal's frequency. The same applies for the antenna pattern. Signal distortions caused by that issue play an important role in broadband signals and can be corrected for by intensive processing methods [20].

The illuminated footprint on Earth is described by the intersection of the Earth surface and the antenna pattern with elevation and azimuth $HPBW$s $\Delta\Theta_{3\mathrm{dB}}$ and $\Delta\phi_{3\mathrm{dB}}$. All targets at positions $\boldsymbol{p}$ are within the footprint.

2.2.3. Receiver

For calculation of the received base-band signal, the channel impulse responses $h_{\mathrm{el},k,i}$ and $h_{\mathrm{az},k,i}$ are convolved through the convolution operator $*$. It results in a two-dimensional convolution, because both functions are dependent on each other through the Dirac distribution. In addition, weighting is applied by the antenna pattern, the scattering coefficient and the individual path attenuation. A final integration over all targets $\boldsymbol{p}$ leads to the received signal at receive channel i:

$$\begin{aligned} u_i(\acute{t},t) = \Bigg[\int_{\boldsymbol{p}} \sum_{k=0}^{N_{\mathrm{Tx}-1}} & \overline{a}_{k,i}(\acute{t},t,\boldsymbol{p}) \cdot C_{\mathrm{Tx},k}\left(\Theta(\boldsymbol{p}),\phi(\boldsymbol{p})\right) \cdot C_{\mathrm{Rx},i}\left(\Theta(\boldsymbol{p}),\phi(\boldsymbol{p})\right) \cdot \sigma_\kappa(\boldsymbol{p}) \\ & \cdot h_{\mathrm{el},k,i}(\acute{t},t,\boldsymbol{p}) * h_{\mathrm{az},k,i}(\acute{t},t,\boldsymbol{p})\, d\boldsymbol{p} + n(\acute{t},t) \Bigg] \cdot \exp\left(-\mathrm{j}\omega_0 t\right). \end{aligned} \tag{2.19}$$

$$\begin{aligned} \boldsymbol{u}(\acute{t},t) = \left[u_0(\acute{t},t), u_1(\acute{t},t), ..., u_i(\acute{t},t), ..., u_{N_{\mathrm{Rx}-1}}(\acute{t},t)\right]^{\mathrm{T}} \\ \text{for} \quad i \in \mathbb{N}_0^+ \text{ and } i < N_{\mathrm{Rx}}. \end{aligned} \tag{2.20}$$

This signal is further disturbed by Additive White Gaussian Noise (AWGN) $n(\acute{t},t)$. For brevity any dependence on the channel identity k,i is ignored. A final multiplication with the carrier frequency leads to a down-conversion to the base-band for sampling by Analog-to-Digital-Converters (ADC). The underlying sig-

nal model will be later used for waveform ambiguity analysis and serves as a basis for all further post processing steps summarized in Fig. 2.7.

2.3. Fundamental Limitations of SAR

Already during the first developments of SAR, the main limitations of this imaging technique were known. For that reason, R. O. Harger derived in year 1964 the SAR ambiguity function [21]. In contrast to the well-known radar ambiguity function from P. Woodward [22], this function is not based on the transmit signal only, but incorporates the SAR principle itself. Harger derived a complete SAR signal model and came to the conclusion that ambiguities may result if the sampling requirements do not fulfill the Kotelnikov sampling theorem[3] [24]. From this point, he derived the necessary design criteria for the physical antenna size, which plays a key role in the spatial sampling of the scene. Based on the so-called antenna constraint, a high resolution in azimuth and a large swath width can't be achieved at the same time. This conclusion results from the coupling of the antenna dimensions in azimuth and elevation via the *PRF*. This issue will be detailed shortly.

Many years later, in year 2000, A. Freeman has considered this dilemma from another point of view [25]. In his highly cited paper, he refined the constraint and focused only on the geometrical aspects of the antenna and scene. The conclusion of the paper showed that the requirements are not as strict as assumed before, whereas the discrepancy results from the spherical Earth model, which was now taken into account.

The conclusion of both views is the same: In a SAR with a single transmit and receive channel, the swath width can only be increased at the cost of azimuth resolution and vice versa. In the following, this dilemma is examined, since it is crucial to the contributions of this thesis.

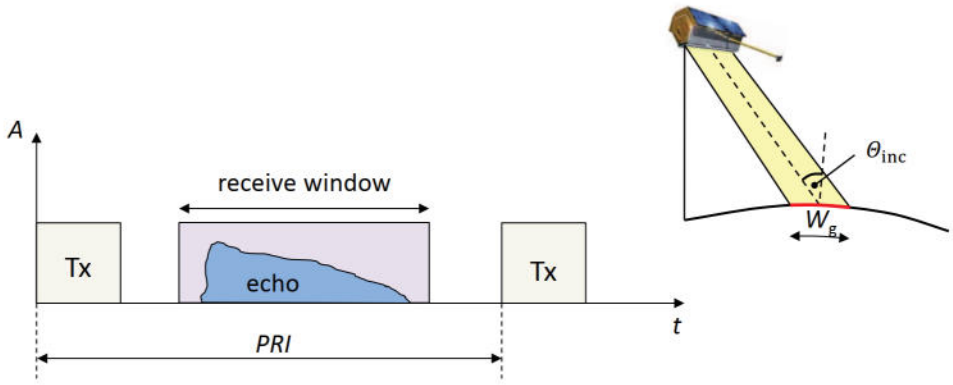
2.3.1. Range Ambiguities

The effect of range ambiguities is well known in the radar community [18]. By choosing a certain *PRF*, the maximum unambiguous range interval is then defined. This plays an important role. Reconsidering Eq. (2.12), the transmit signal

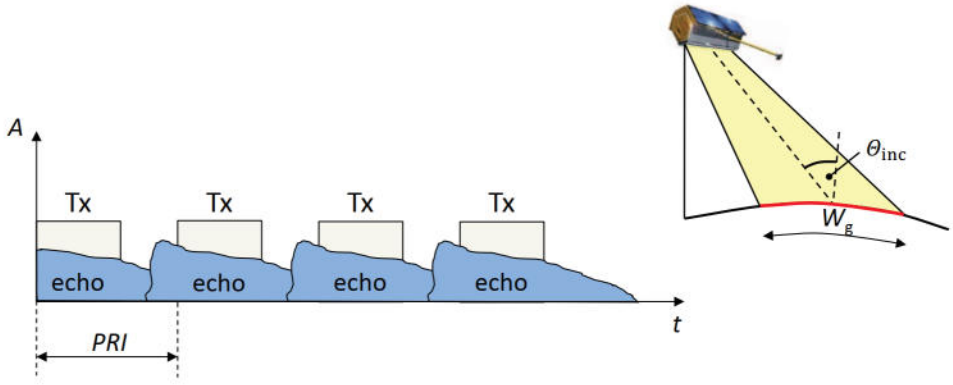
[3] Named after the discoverer V. A. Kotelnikov. This theorem was later reinvented by E. T. Whittaker, H. Nyquist and C. Shannon and can also be found under these names [23].

is repeated with the *PRF*. Between two adjacent transmitted pulses, a receive window is defined, during which the echo is recorded (cf. Fig. 2.5a). If the swath width W_g or the *PRF* is increased, the echoes of subsequently transmitted pulses will overlap. It is thus not possible to separate the echoes from different swath-ranges and thus ambiguities result. They are later visible in the final SAR image as repeated parts of the landscape. The maximum swath width W_g in dependence on the incidence angle Θ_{inc} can be shown to be:

$$W_g < \frac{c}{2 \cdot \sin(\Theta_{inc}) \cdot PRF}. \tag{2.21}$$



(a) Optimum choice of swath width and *PRF*.



(b) Non-optimum choice of swath width and *PRF*. The echo signals overlap and can not be separated anymore.

Figure 2.5. Dependence between swath-with and *PRF* in terms of range ambiguities.

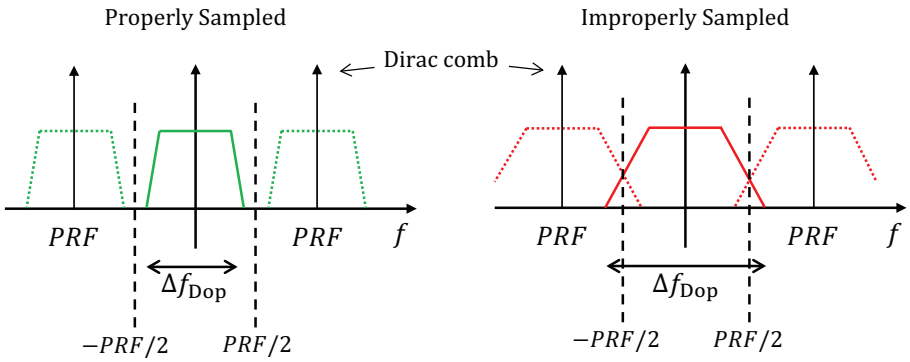


Figure 2.6. Back folding of Doppler spectra leading to azimuthal ambiguities.

From this equation it turns out, that if a large swath should be observed, then a low *PRF* is necessary. Unfortunately, this stands directly in conflict to the requirement of higher *PRF*s for avoiding azimuth ambiguities, as will be explained next.

2.3.2. Azimuth Ambiguities

In contrast to the problem formulation of range ambiguities, azimuth ambiguities are caused by an inadequate sampling. As previously derived in Eq. (2.10), a high azimuth resolution can only be obtained with a short antenna with a broad *HPBW*[4]. The resulting enlarged Doppler spectrum, which is seen by the receiver, will finally lead to an increased resolution (Eq. (2.8), (2.10)). This enlarged Doppler spectrum has to be sampled in accordance to the Kotelnikov sampling theorem. A visualization of the sampled Doppler spectra can be found in Fig. 2.6. The receive signal, which is sampled in azimuth direction at a rate of the *PRF*, can be considered as convolution with a Dirac comb, like in standard sampling theory [27]. This leads to a periodic signal repetition. If the *PRF* is chosen too small, or if the azimuth bandwidth is too high, then the aliasing effect occurs and the targets are folded back at wrong positions. The overlapping spectra can not be separated anymore leading to the ambiguous responses. It can be shown [13], that the maximum achievable azimuth resolution is restricted to:

[4]With phase spoiling techniques it is also possible to have a large antenna with a broad *HPBW* [26]. But for this an antenna array is necessary.

$$\delta_{\mathrm{sa}} = \frac{r_0 \cdot \Delta\phi_{3\mathrm{dB}}}{T_{\mathrm{ob}} \cdot \Delta f_{\mathrm{Dop}}} > \frac{r_0 \cdot \Delta\phi_{3\mathrm{dB}}}{T_{\mathrm{ob}} \cdot PRF}. \tag{2.22}$$

Thus, if a high azimuth resolution is demanded for, then a high *PRF* is necessary, which stands in contradiction to the requirement of range ambiguities. In the following, two possible methods are given, which decouple both requirements by DBF in azimuth or elevation.

2.4. Multi-Channel SAR Signal Processing

A first processing step in DBF-SAR is usually the combination of the receive channels to an equivalent single one. In dependence of the used DBF algorithm, different kinds of advantages can be achieved by using multiple channels. Examples are the reconstruction of sub-sampled data [10] or the spatial suppression of interferences and ambiguities [28]. In a special case, if azimuth DBF and elevation DBF consist of mathematical linear operations, the order of the used DBF algorithms can be exchanged. However, for a more robust range ambiguity suppression, which may involve advanced antenna nulling techniques, a combined beam-forming in both directions becomes necessary [29].

Referring to MIMO, the propagation path for each transmit channel is usually considered separately leading to an independent processing of the whole processing chain for each transmitted waveform. A selection of MIMO-SAR operation modes can be found at the end of this chapter.

Apart from DBF principles, in this section also a brief insight into standard SAR processing is given. All elementary steps, such as range and azimuth focusing are briefly depicted. An overview of the full processing chain can be found in Fig. 2.7. Also other alternative algorithms, such as Fast Factorized Back Projection [30] or Compressive Sensing [31] can be applied for focusing, but this is not within the scope of this work.

2.4.1. DBF in Elevation

Elevation DBF is the first step in the processing chain of Fig. 2.7. First thoughts were published in patents by Blythe in [32] and by Kare in [33]. Both propose analog beam-steering with a phased-array antenna to follow the echo, which ar-

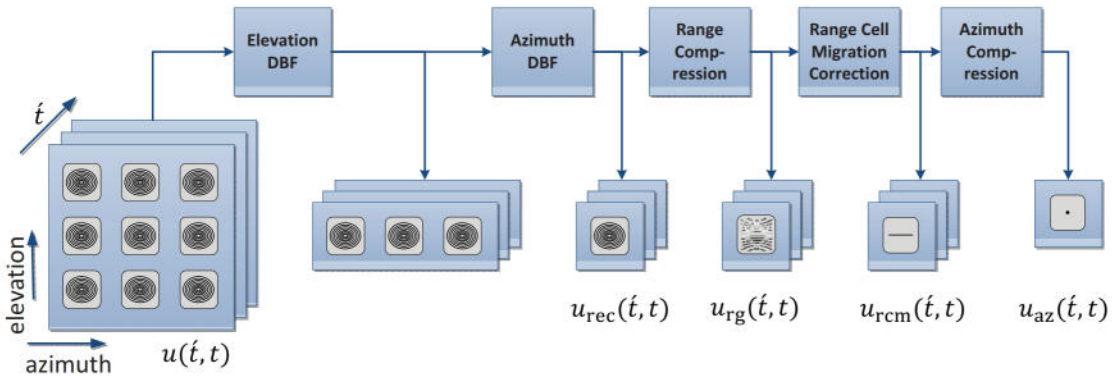


Figure 2.7. Classical SAR processing chain with multiple receive channels. The variables u_{rec}, u_{rg}, u_{rcm} and u_{az} represent the result of successive processor stages illustrated above. These stages will be detailed on the following pages.

rives from a small angular interval compared to the whole illuminated area. This technique was later named sweep SAR by A. Freeman in [34]. The same concept was extended by DBF in a patent by Suess et al. in 2002 [28]. This proposal is known under the name SCan On REceive (SCORE). SCORE receives high attention in the DBF-SAR community [9, 35, 36]. Numerous publications [37, 38] and purposeful proposals for spaceborne missions using this technique (NISAR [39], TanDEM-L [40]), were published in recent years. Using DBF on receive, not only the Signal-to-Noise Ratio (*SNR*) can be increased, but also the problem of range ambiguities can be abrogated.

In the proposed technique, on transmit a short antenna with a broad *HPBW* is used to illuminate the whole swath. Whereas on receive, a uniform linear antenna array (ULA) in elevation is used (cf. left upper image in Fig. 2.10). On receive, due to the side-looking geometry, each point on the ground is seen under a different look angle. For a known topography, the relation between Time of Arrival (ToA) and Angle of Arrival (AoA) can be derived and a directional beam, following the expected response on the ground, can be synthesized. In the receiver, all elements of the planar array antenna are activated forming a high gain narrow beam. Time-variant digital phase shifters steer the antenna beam to the wanted AoA. The advantages of SCORE are as follows:

- Increased *SNR* due to spatial filtering from directions without any echo.
- Known relation between AoA and ToA leads to the ability of suppressing range ambiguities.
- Separation of spatio-temporal transmit waveforms in MIMO-SAR becomes possible (see [41, 42]).

An extension of the SCORE technique is given in chapter 4.

2.4.2. DBF in Azimuth

An approach to overcome the minimum antenna constraint [25] is based on using multiple receive channels in azimuth, which are recorded independently and combined with a DBF algorithm.

Under the assumption that all receive apertures are closely separated in azimuth, they will share approximately the same footprint. According to Eq. (2.22), the resulting Doppler bandwidth has to be properly sampled by the *PRF*. This is illustrated for an example with three receive channels in Fig. 2.8. The effective phase centers, which are placed in the middle between the transmitter and each receive antenna are marked as crosses in the picture. It becomes directly visible, that the phase centers build a uniform constellation like a singe-channel SAR. Generalizing the classical Kotelnikov sampling theorem [27], it is possible to acquire the receive channels over azimuth with a lower sampling frequency than required and combine them later to a single channel.

While each receive channel is sampled with the same frequency (denoted as PRF_{sub}) as used for transmit, the relation to the resulting effective *PRF* is given by:

$$PRF_{\mathrm{sub}} = \frac{PRF}{N_{\mathrm{Rx}}}. \tag{2.23}$$

Obviously, if a single receive channel is considered, the repeating Doppler-spectra will partly overlap. The main idea behind the azimuth reconstruction method is that a separation becomes still possible due to different phasing between the spectra. Using the offset positions of the effective phase centers, each channel experiences an individual characteristic, which can be described with

an analytic mathematical model. The phase change due to marginal different path lengths from the target to the corresponding antennas can then be compensated with inverse filters. Finally, this results in a solution of a linear equation system. After summing up the obtained spectra, the equivalent single-channel response can be reconstructed. Because the effective sampling rate is increased to $PRF = N_{\mathrm{Rx}} \cdot PRF_{\mathrm{sub}}$, standard SAR processing steps can be applied next.

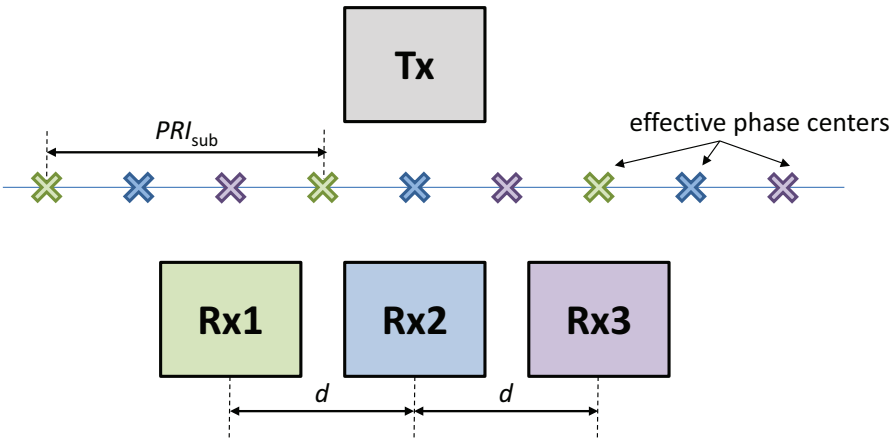


Figure 2.8. Effective antenna phase centers of three receive antennas in azimuth.

There are a couple of quite similar algorithms for channel reconstruction. They can be found in [10, 35, 37, 38, 43, 44]. All come to similar results with uniform sampling, while variations arise if the resulting PRF is not exactly an integer multiple of N_{Rx} times the chosen PRF and if different scene characteristics are assumed. A significant advantage of [38] is that this reconstruction method can also be applied for SAR with reflector antennas.

From now on, the combined raw data after DBF will be denoted as $u_{\mathrm{rec}}(\acute{t}, t)$.

2.4.3. Range Compression

The reconstructed single-channel raw-data signal is first focused in range direction for each acquired echo window separately. The range compression filter is a linear filter defined as the complex conjugate of the time reversed transmitted waveform $s_{\mathrm{BB},k}(t)$ and is applied as follows:

$$\begin{aligned} u_{\mathrm{rg},k}(\acute{t},t) =& u_{\mathrm{rec}}(\acute{t},t) * s^{*}_{\mathrm{BB},k}(-t) = \int_{-\infty}^{\infty} u_{\mathrm{rec}}(\acute{t},\tau)\cdot s^{*}_{\mathrm{BB},k}(\tau - t)d\tau \\ =& \mathcal{F}_{f}^{-1}\left\{\mathcal{F}_{t}\{u_{\mathrm{rec}}(\acute{t},t)\}\cdot\mathcal{F}_{t}\{s^{*}_{\mathrm{BB},k}(-t)\}\right\}. \end{aligned} \tag{2.24}$$

* denotes the complex conjugate of the respective signal and $\mathcal{F}$ and $\mathcal{F}^{-1}$ the Fourier and inverse Fourier transforms, respectively. The superscript indices, t, $\acute{t}$, f and $\acute{f}$, respectively refer the variables over which the integration of the function occurs. Note, that $\acute{t}$ and $\acute{f}$ are the Fourier-pair variables in slow-time, whilst t and f are the Fourier pair variables in fast-time. Range compression can be done either in time domain by convolution or with a multiplication in frequency domain. However, the range compression is often applied in frequency domain with the Fast Fourier Transform (FFT) algorithm for faster computation.

Eq. (2.24) shows strong similarities to the matched filter [12]. In contrast to the classical matched filter, where the aim is to optimize the *SNR* of the ingoing signal of the filter, in radar, the exact filter function is unknown due to channel distortions.

In addition to that, in SAR applications there is no realized compression gain wrt. *SNR* optimization, like in communication or standard direct aperture radar. If the signal at the filter input is band limited to the transmit signal's frequency, the filter output indicates the energy distribution over the swath along range. Finally, the *SNR* will remain the same before and after matched filtering [13].

2.4.4. Range Cell Migration Correction

Referring to Eq. (2.16), the slant-range to a hypothetical target varies during the observation time T_{ob}. Due to that, after range-compression, the resulting trajectory for each target looks like a curvature in the two-dimensional data domain (cf. Fig. 2.7). This effect is named range cell migration [14, 15, 45] and can be corrected with a linear filter.

However, the migration becomes just noticeable in a high-resolution SAR and must be corrected if the migration of the resulting curvature is more than half of a range resolution cell: $\delta_{\mathrm{rg}} < r_{0,k,i}\lambda_0^2/(16\delta_{\mathrm{sa}}^2)$ [14], while δ_{rg} denotes the range resolution. A typical example of a X-band SAR with a wavelength of 3.0 cm, an

azimuth resolution of 4.0 m and $r_{0,k,i} = 700$ km, needs for a range cell migration correction if the range resolution is finer than 2.8 m.

The described effect can be corrected for by multiplication of the range compressed data with a linear filter function in azimuth frequency domain. The time-shift, which must be corrected is given as:

$$\Delta t(\acute{f}, t) = -\frac{c^2}{4} \cdot t \cdot \left(\frac{\acute{f}}{f_0 \cdot c} \right)^2, \tag{2.25}$$

while $\acute{f}$ corresponds to the frequency along azimuth [45].

According to [15], Δt can be compensated for after range-variant interpolation in the range-Doppler domain signal. However it is important to note, that this is just an approximation and can not be applied for high-resolution systems – especially for squinted antenna beams. Hence, it is suggested to use alternative approaches, such as chirp scaling [46]. Since advanced SAR processing methods are not scope of this thesis, this linear filter approach is sufficient for basic understanding of SAR imaging. The range compressed signal after range cell migration correction is further denoted as $u_{\mathrm{rcm},k}(\acute{t}, t)$.

2.4.5. Azimuth Compression

Azimuth compression is closely related to the range compression, whereby the linear compression filter is applied on each azimuth line of $u_{\mathrm{rcm},k}(\acute{t}, t)$ separately. Like Eq. (2.24), azimuth compression can also be applied in time- or frequency domain with a reference azimuth response function $\widehat{h}_{\mathrm{az}}(\acute{t})$. This reference is adapted from Eq. (2.5), while there is no dependency on the fast-time variable t anymore. The reference time t, which is taken to obtain $\widehat{h}_{\mathrm{az}}$ is dependent on the reference, which was used for range cell migration correction. Finally, the focused data signal reads as:

$$u_{\mathrm{az}}(\acute{t}, t) = u_{\mathrm{rcm},k}(\acute{t}, t) * \widehat{h}^*_{\mathrm{az}}(-\acute{t}) = \mathcal{F}^{-1}_{\acute{f}} \left\{ \mathcal{F}_{\acute{t}}\{u_{\mathrm{rcm},k}(\acute{t}, t)\} \cdot \mathcal{F}_{\acute{t}}\{\widehat{h}^*_{\mathrm{az}}(-\acute{t})\} \right\}. \tag{2.26}$$

After this step, the phase shift due to the sensor movement is compensated and the data are completely focused. A typical SAR image results by plotting the gained data array as a gray scale image.

In case of a band limited signal, limited to the Doppler bandwidth, also no compression gain in the sense of *SNR* is realized. The *SNR* will be the same for the acquired raw data and the final SAR image [13].

2.4.6. MIMO-SAR Processing Tool

In order to verify different processing methods, a modular simulation tool was developed with the program IDL (Interactive Data Language). A program flow diagram can be found in Fig. 2.9. As starting point, the user can select between several sensor parameters, processing parameters and algorithms. It is also possible to select between simulated and measured data. Either MIMO-SAR raw data must be prior simulated, or measurement data, obtained with the MIMO-SAR demonstrator described in chapter 7, can be directly opened. This enables improved comparison between theory and praxis. The rest of the program runs independently with the chosen parameters. After opening the simulated or recorded raw data, the calibration is applied. Different algorithms can be found in [47–49]. In case of DBF on receive only, the strand on the right-hand side of the diagram is computed in the same order as previously described in this section. For MIMO-SAR, the program follows the strand on the left-hand side. The corresponding algorithm is explained in more detail in chapter 4. Apart from a SAR image as final product, every wanted information about computed temporary signals can be extracted.

2.5. Advanced DBF and MIMO Modes

Up to now, the MIMO-SAR signal model was derived and the main limitations of standard SAR were revealed. The focus of this section is to give an overview over different application scenarios of MIMO in imaging radar.

2.5.1. Fully Polarimetric SAR Imaging by Simultaneous Measurement of the Scattering Matrix

A further advantage of MIMO-SAR are fully polarimetric SAR measurements (sometimes also referred to as quadpol). With the use of polarimetry, the classification of man-made and natural scatterers by obtaining orientation, dielectric properties and shape of the scatterer, becomes possible. Striking examples for these are the estimation of soil moisture and the classification of biomass [40].

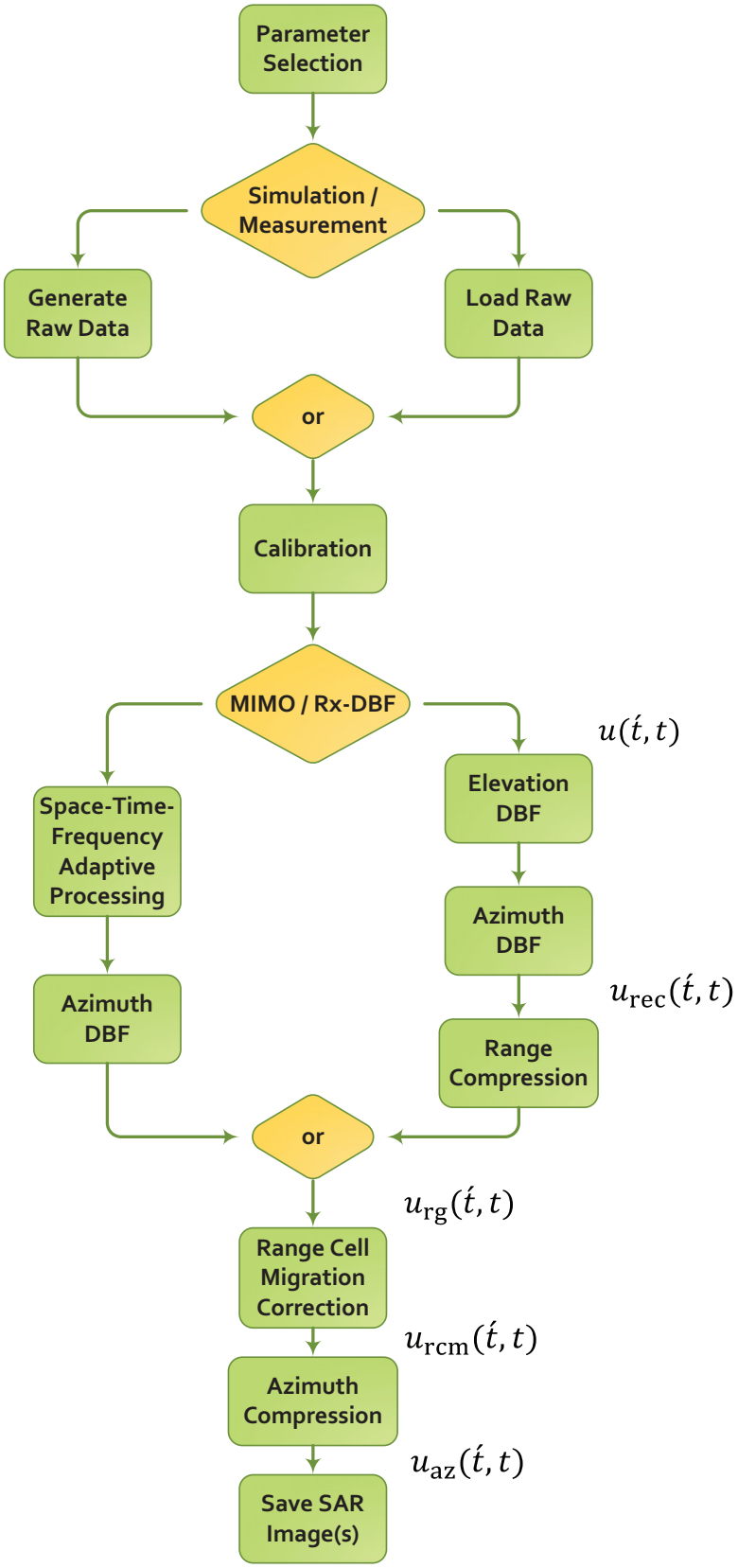


Figure 2.9. Flow diagram of the MIMO-SAR simulator and processor.

However, to obtain all four parameters of the scattering matrix (HH, HV, VH, VV), four independent measurements have to be taken. In the current state, the sensor transmits horizontal and vertical polarization in an interleaved mode. Both polarizations are received and recorded simultaneously. Thus, to keep the sampling rate the same, the *PRF* has to be increased by a factor of two, which decreases the swath width by the same factor. Consequently, the simultaneous acquisition of the whole scattering matrix would be a tremendous advantage. With the MIMO method proposed in [11], both polarizations can be transmitted at the same time, whereas the whole scattering matrix will be obtained later in the receiver with an innovative beam-forming algorithm. As a result, the swath width can be kept constant for s-matrix (quadpol) measurements. A sketch indicating the novel idea behind this mode is shown in Fig. 2.10 (top right-hand corner). Measurement examples will be given in section 7.4.

2.5.2. Interferometric Modes

The TanDEM-X mission uses already interferometry either in cross-track or along-track direction [50]. Cross-track (sometimes also referred to as across-track interferometry) interferometry is used to generate digital elevation models for obtaining topographic maps. Along-track interferometry is used for GMTI to extract the velocities of moving objects in the scene. For these modes an additional receive antenna is necessary, which is shifted in along-track or across-track, respectively, in order to create a baseline necessary for interferometric measurements.

However, in cross-track and along-track interferometry also contradicting requirements exist. For this reason the TanDEM-X mission suffers when acquiring over several areas multiple times with large gaps between the observations. The used time-multiplex mode has not the necessary flexibility and rapidly varying processes can not be taken into account.

The reason for the acquisition problem is based on the distance between the receive antennas i.e. the baseline. For a high phase-to-height sensitivity for obtaining digital elevation models and to track fast moving targets, a large baseline between the sensors is necessary. On the other side, to avoid height ambiguities or blind velocities a small baseline is desired. Up to now, only one of these two cases can be considered if the acquisition has to be done at the same time. In case of a bi-static MIMO system, at least two transmitters and receivers exist (Fig. 2.10). This leads to an additional phase center which makes it possible to

have two baselines. A short one for suppression of ambiguities and a second one with twice the length for high accuracy. In addition, a direct phase synchronization of the radar systems becomes possible. Also tomographic SAR with multiple baselines for 3-D imaging will be much more easy to implement.

2.5.3. Forward- and Nadir-Looking SAR

As already successfully demonstrated with the SIREV system [51], or ARTINO [52], by using DBF, forward-looking or nadir-looking SAR imaging becomes possible. The axes of the antenna apertures are oriented, in both systems, perpendicular to the flight direction and look towards the ground. Using special DBF processing methods, the spatial resolution in across-track direction is increased, enabling in turn imaging of the observed scene. A major advantage of the ARTINO system is the use of multiple transmitters. As the effective number of available channels will be given by the product of the number of Tx and Rx channels, $N_{\mathrm{Tx}} \cdot N_{\mathrm{Rx}}$; an additional channel on either receive or transmit thus leads to an significantly increased number of usable channels.

2.5.4. Hybrid SAR Modes

Conflicting user requirements on SAR data acquisitions pose currently a challenge. While one user is interested in a high-resolution acquisition in a disaster region, another user might be interested in the observation of a larger swath with lower resolution at the same time. Obviously, this can not be satisfied simultaneously. Using hybrid SAR modes, a combination of several acquisition modes becomes possible. For example, a second transmit antenna can be used to transmit an orthogonal waveform with high bandwidth to a small footprint, which lies within a bigger footprint illuminated by the first antenna. This is illustrated in Fig. 2.10 in bottom left corner. The echoes are recorded with an antenna array and independent processing can be applied for both areas [53].

2.5.5. Multistatic SAR

Multistatic SAR can be seen as an extension of hybrid SAR. Considering the high attention SAR continues to receive over the previous years, currently more than 30 satellite SAR systems exist and several more launches are planned. The sensors should not interfere with each other thus preventing the necessity of transmit-

ting orthogonal waveforms by each sensor. However, this is not possible, because MIMO-SAR needs for phase-synchronized radar hardware, a real multistatic SAR constellation with an unique relationship between each transmitter and receiver per definition would be necessary. An exemple of illumination with a small number of geostationary satellites with several low earth orbit (LEO) satellites operating as receivers is proposed in [54], as shown in Fig. 2.10, bottom right-hand corner.

2.5.6. MIMO-SAR Tomography

In standard SAR, the range and azimuth signals are mapped into a two-dimensional image, while information about the target height is not available. To extract also height information about the target scene, in repeat-pass and single-pass SAR tomography, multiple receive antennas oriented along elevation are used to estimate the AoA along that direction and for generating three-dimensional maps [55, 56].

As detailed in references [57, 58], in presence of multipath scattering, the true target position can not be determined correctly via SAR tomography using a single-pass system with one transmitter and multiple receivers. The reason can be given with an example illustrated in Fig. 2.11. From dihedral scattering it is known, that the effective phase center position is located at the intersection point of the two perpendicular surfaces. This point is marked with a red 'x' in the figure and it corresponds to the determined position via repeat-pass SAR tomography under the influence of multipath scattering mechanisms. In single-pass tomography, the receive beamformer always focuses to the position of the last scatterer and hence, the ground and the equivalent scattering position of the canopy are seen as individual targets. Obviously, both results are incorrect, as multipath echoes are present.

To overcome the described measurement error, in [57] it is suggested to use additionally multiple receive antennas, along with multiple transmit antennas, transmitting orthogonal waveforms. In case of redundant antenna phase centers, it is possible to form individual Tx-Rx antenna beam combinations in the post processing. After separation of the orthogonal waveforms, $N_{\mathrm{Tx}} \cdot N_{\mathrm{Rx}}$ raw data sets are available, where N_{Tx} and N_{Rx} are the numbers of transmit and receive antennas. Using a linear DBF algorithm, individual phase weights for each Tx-Rx channel combination can be applied to form independent transmit and receive

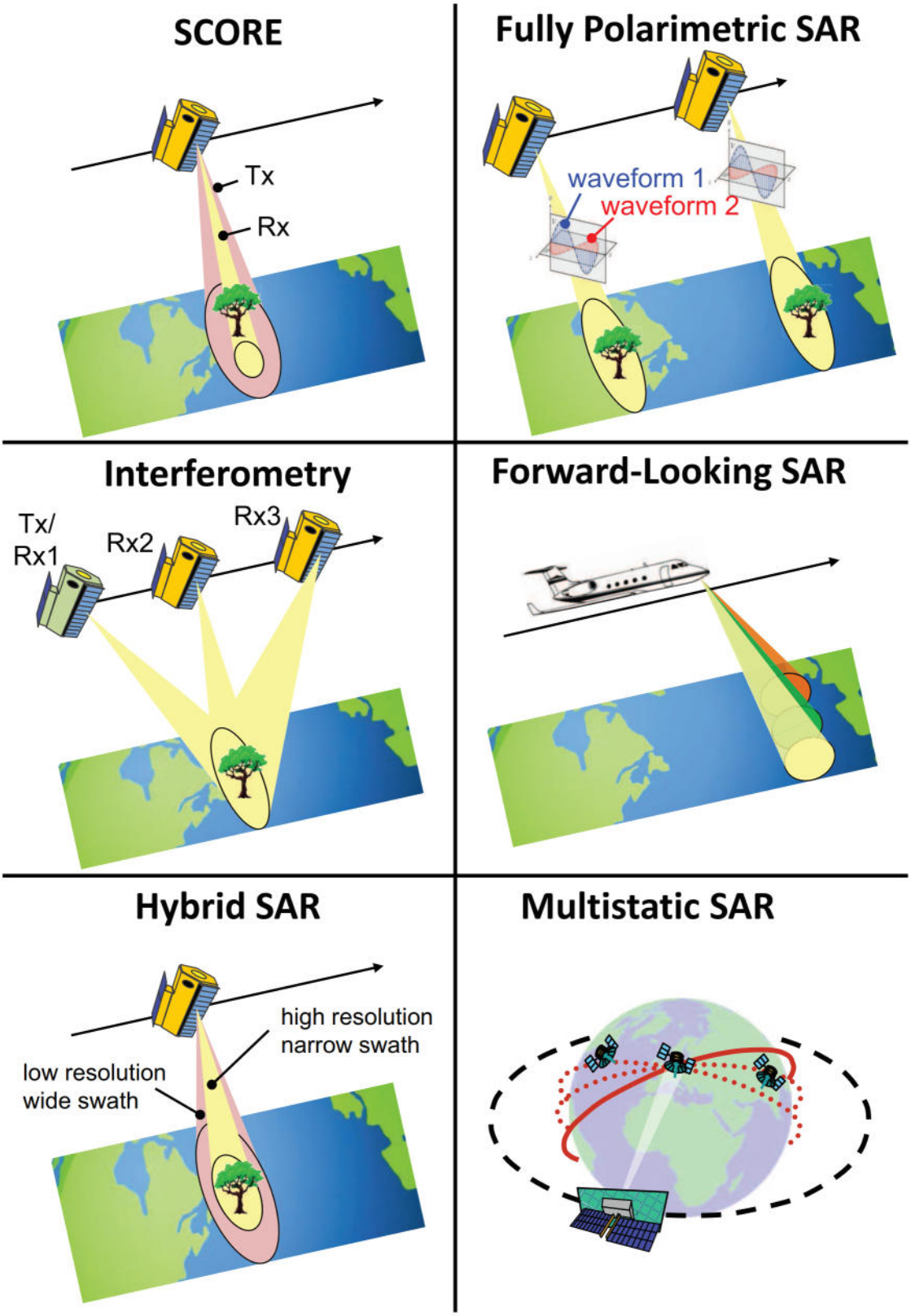


Figure 2.10. Advanced DBF-SAR and MIMO-SAR modes.

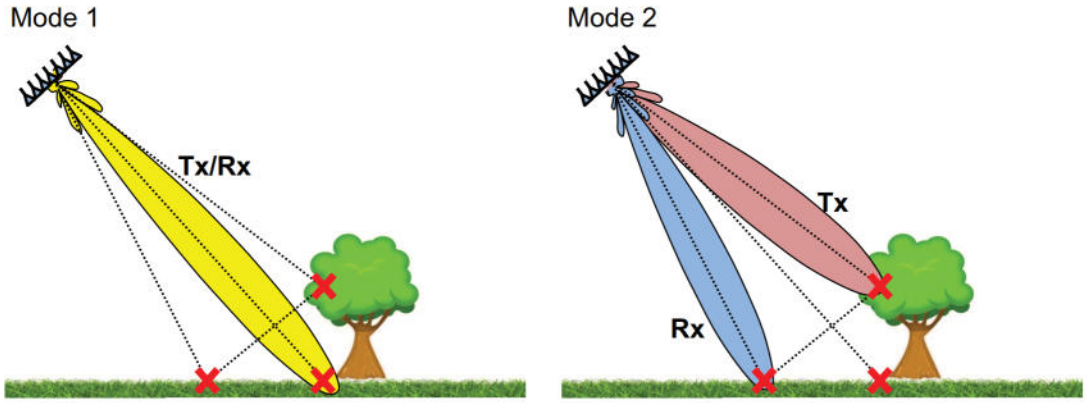


Figure 2.11. Principle of multipath detection with transmit and receive beams pointing in different directions. The cross at the edge of the tree trunk and the ground indicates the equivalent phase center of the reflection.

antenna beams by final signal summation. This can be followed by standard SAR processing, such as range and azimuth compression.

If it is assumed, that the transmit and the receive beams point at the same time in different directions, as indicated in Fig. 2.11, only dihedral (indirect) scattered signals can be detected, while direct scattering mechanisms are suppressed. If both beams point to the same direction, it is the opposite and dihedral scatterers are suppressed, while direct scattering becomes visible. If the output of both steering methods is compared, it is possible to locate multipath propagation effects and to correct them.

2.5.7. MIMO Circular SAR for Holographic SAR Tomography with High Altitude Pseudo-Satellites

A highly innovative concept, named MIMO Circular SAR, has been proposed in [59, 60]. In fact, this concept is a combination of several individual imaging modes.

In contrast to classical SAR modes, where the trajectory is straight, in Circular SAR (CSAR) the flown trajectory is circular [61]. As illustrated in Fig. 2.12, the same spot in the center is always illuminated by the antenna. This special acquisition type provides the potential of multi-angular measurements over 360°, which provides, in turn, 3-D reconstruction with a single pass, sub-wavelength

resolution in the x-y-plane (independent from the system bandwidth), shadow reduction, and a better understanding of the coherent 3-D radar backscattering.

Although it is possible to accomplish 3-D imaging with a single circular flight, the resulting reflectivity is distorted by undesired artifacts resulting from sidelobes in cone-shaped 3-D structures and rings or arcs in the 2-D domain. They are caused by the low resolution in the direction of height (z-axis) [61]. However, these sidelobes can be reduced by forming an additional synthetic aperture in elevation with multiple circular flights [62]. This mode, called holographic SAR tomography (HoloSAR), allows the formation of full 3-D reconstructions with suppressed sidelobes. Unfortunately, one of the limitations of HoloSAR is the covered area that is mainly determined by certain system parameters, such as the smallest *HPBW* between the range and azimuth directions, the *PRF*, as well as the range ambiguities.

To overcome this issue, in a first step, it is proposed to combine the HoloSAR imaging mode with DBF on receive in elevation and azimuth direction (cf. sections 2.4.1 and 2.4.2). The size of the spotlighted region is not confined anymore by the aforementioned system- and operation-parameters, and can be significantly increased. In a second step, multiple transmitters are used as proposed in section 2.5.1 to enable fully polarimetric imaging. This combination allows to study the target scattering behavior over 360° in all four polarization states.

In addition, HAPS (High Altitude Pseudo-Satellites) at altitudes between 17 km and 50 km (stratosphere) can be used [63]. Main advantages of HAPS are arbitrary flight tracks (e.g. fixed rotating circles), possible low-cost realization, and the reduction of additional atmospheric attenuation through the high stratosphere. The ability of flying circles enables to use them for CSAR and HoloSAR. With regard to the proposal in [60], and the illustration in Fig. 2.13, a Geostationary illuminator can be used as a transmitter, while the HAPS operate as receivers in a *swarm* constellation.

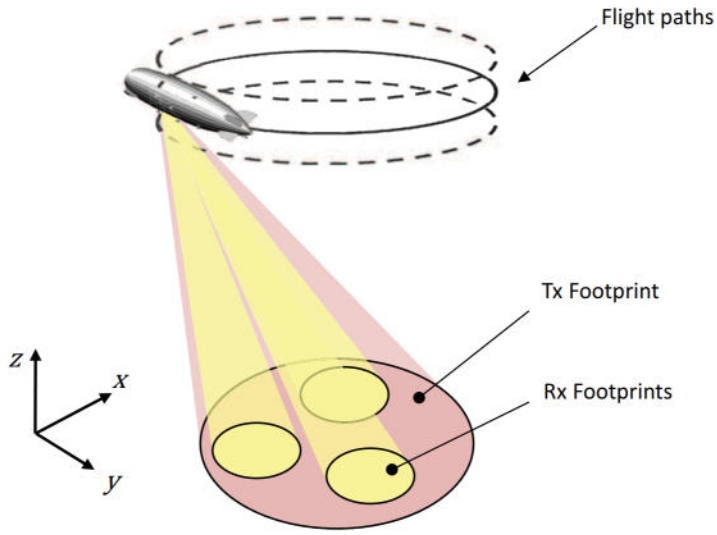


Figure 2.12. Basic MIMO CSAR geometry with transmit antenna beam in red color and multiple receive antenna beams in elevation and azimuth directions in yellow color.

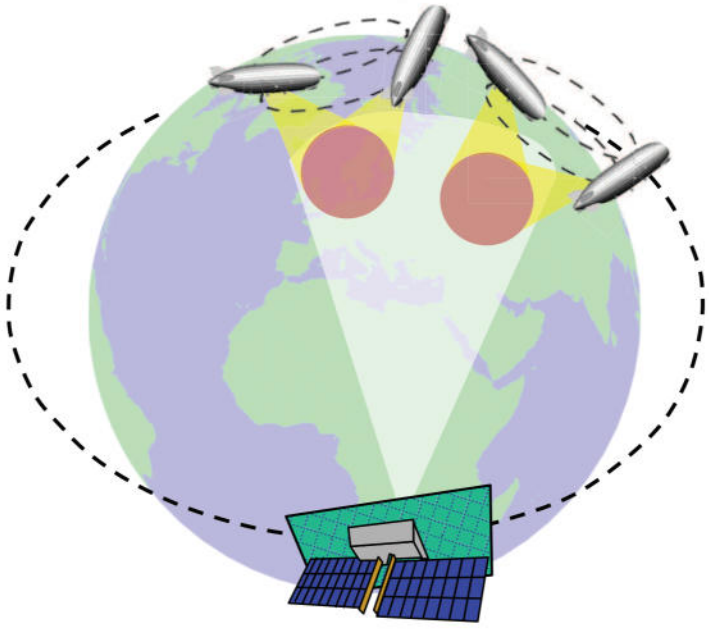


Figure 2.13. MIMO CSAR with a geostationary satellite as transmitter and multiple HAPS as receiver platforms.

3. Orthogonal MIMO-SAR Waveforms

In a MIMO-SAR system, the transmitted waveform signals overlap, thus generating a multiplicity of channels within the transmit mode, while the echo signals at the receive channels are acquired individually and concurrently. To be able to split up all possible channel combinations in the post processing, different approaches can be considered. Basically, MIMO systems need *orthogonal* waveforms or channels, in order to allow the transmitted waveforms to be completely separable in the receiver. Nowadays, in the field of communications the MIMO systems, methodologies and processing strategies are well in place. For radar applications these features have to be however, appropriately adopted. Due to this, we begin with a short overview about MIMO in the area of communication.

Because of the increasing amount of data, in communication it was necessary to boost the research on advanced techniques to differentiate the superimposed signals without disturbing other channels. In various communication applications, such as radio, television, telecommunication, or satellite navigation, multiplex techniques are used to distinguish between the transmitters. These techniques exploit channel capacities by using information about space (Angle of Arrival - AoA), polarization, frequency, time or correlation [12]. More precisely, we distinguish between Space Division Multiplex (SDM), Polarization Multiplex (PM), Frequency Division Multiplex (FDM), Time Division Multiplex (TDM) and Code Division Multiplex (CDM)[1]. In manifold applications, Orthogonal Frequency Division Multiplexing (OFDM) seems to be one of the most favored multiplex techniques. Striking examples are Digital Audio Broadcasting (DAB), Digital Video Broadcasting (DVB), Asymmetric Digital Subscriber Line (ADSL) and 3GPP Long Term Evolution (LTE) [65, 66].

With reference to MIMO-radars, the information about the channel is of interest and the transmitted signals are known, whereas in communication the users are usually interested in the information content of the transmitted sig-

[1] In more advanced methods, also combinations of those are used. For example in recent generations of professional navigation receivers [64], the combination of SDM and CDM is used for an improved mitigation of jammers.

nal. Because the aim is different, it is necessary to adapt the techniques from communications to radars. As will be explained in the first section of this chapter, the used waveforms for MIMO-radar and MIMO-SAR have certain requirements to fulfill, which makes it more difficult to separate the individual signals and channels. The suggested concept in this thesis uses a combination of FDM, TDM and SDM and will be further named *Space-Time-Frequency Adaptive Processing* (STFAP). Waveforms, which fit into this concept and the reason are also illustrated in more detail in this chapter.

In the field of MIMO-radar, OFDM is also one of the preferred solutions [67,68]. Extensive research, especially in the field of automotive radar, is currently done on this topic. RadCom, for example, is the combination of radar and communication [69]. This concept enables to exchange information between vehicles, while simultaneously making radar measurements (range and Doppler). This research topic served as a basis for J.-H. Kim, to research on waveform analysis for MIMO-SAR [70]. The waveform scheme, introduced by him was named OFDM chirp waveforms, which is one of the few that are further examined in this chapter.

In 2006, multidimensional waveform encoding with multiple chirp signals in a sawtooth-like frequency modulation, also known as Multiple Sub-Pulse (MSP) mode, was suggested as a technique to separate the transmitted pulses in the SAR receiver with DBF on receive [36]. Later, the suggested sub-pulse technique was generalized to so called Short-Term Shift-Orthogonal (STSO) waveforms [71]. This method is described later with aid of the MSP mode itself and Segmentally-Shifted Chirp (SSC) waveforms.

Apart from those, three further waveform types exist, which were proposed for MIMO-SAR. They are the *up- and down-chirp* modulations [72], the *chirp diverse waveforms* [73] and a further OFDM-based waveform [74]. Unfortunately, all these types provide just partial orthogonality and can only be used for small observation areas with a degraded *SNR*. Hence, they play a minor role for High-Resolution Wide-Swath (HRWS) MIMO-SAR. The first two methods are briefly depicted at the end of section 3.2.

Special emphasis is given in this chapter to the waveform comparison. Especially the Ambiguity Function (AF) is an important tool for waveform analysis in radar. This function allows to compare the waveforms in terms of orthogonality and is described in detail later. For an objective analysis, a catalog consisting of

several parameters, such as resolution, Integrated Sidelobe Ratio (*ISLR*), transmit energy, Doppler tolerance and practical implementation is compiled.

This chapter is divided into four sections. It starts with the orthogonality condition to show the necessity for a complete separation of the individual transmit signals without any mutual interferences. After describing the need for perfect orthogonality between the transmitted signals, the aforementioned waveform schemes are described. A detailed comparison between these is given in the last two sections under consideration of several performance parameters.

3.1. Orthogonality Condition

In contrast to MIMO-radars, a MIMO-SAR can not afford cross-correlation interferences. In other words, the waveforms should be perfectly orthogonal. Unfortunately for arbitrary shifts in time no orthogonal waveforms within the same frequency band exist. This leads to the difficulty examined in this section.

In non-imaging MIMO-radar applications, perfect separation of the waveforms is not necessary, because they are usually used to detect a few point-like targets. With the use of signal codes, e.g. Barker codes, complementary sequences or Frank codes, after pulse compression a part of the energy is smeared over the scene, but this energy does not vanish. In most of radar applications to detect dedicated targets with a sufficiently low false alarm rate, these codes are perfectly adequate [18]. This is because the interferences are very low compared to the optimal impulse response and in dependence of the used code, the interfering energy can be shifted to positions where no targets are present. For SAR, orthogonality has to be achieved with prior known waveforms for every shift in time. This is because the unwanted, correlating energy from the other waveforms will sum up for each single point target of the observed swath after coherent combination. By using existing orthogonal codes, the interfering energy smears also to positions where other targets are also present, and thus they can not be resolved for. In addition, usually the swath width is much larger than the pulse extent and hence already small interferences lead to degradations of the *SNR* of the final product. The echoes of the different transmit signals will completely overlap in the channel and it becomes impossible to separate them later in the receiver. Thus, the desired orthogonality condition to achieve is full orthogonality for arbitrary shifts τ between the signal $s_k(t)$ and any other orthogonal signal $s_i(t)$ [71]:

$$\int s_k(t) \cdot s_i^*(t-\tau)\,\mathrm{d}t = 0 \qquad \forall \qquad \tau \in \mathbb{R}, k,\, i \in \mathbb{N}_0^+ \text{ and } k \neq i. \tag{3.1}$$

From the given cross-correlation in time- and frequency domain, it becomes obvious that no signal parts may coincide. In any case, this condition can simply not be achieved with waveforms occupying the same frequency band. This is justified by the fact that every modulation or multiplex technique leads to correlating parts between the signals if they share the same frequency band.

In an alternative and equivalent explanation it is assumed, that a linear frequency modulated signal, which is commonly used in SAR, is transmitted. Main characteristic of this signal is that at each instance of time, only one frequency component is occupied. An illustration can be found in Fig. 3.1. The observed area, consisting of an infinite number of scatterers, reflects the SAR echo continuously back within the defined echo window. As a result, on receive the time-frequency plane within this window is completely filled, i.e. at each time instance the complete bandwidth is received.

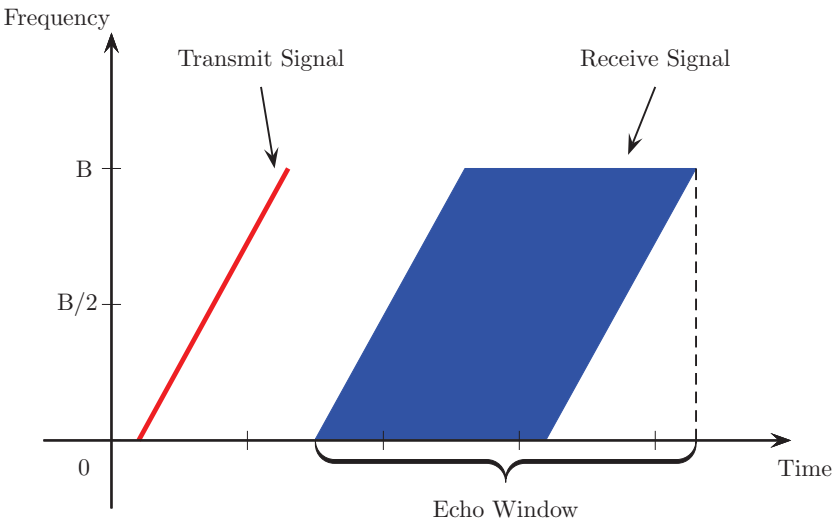


Figure 3.1. Illustration of the orthogonality problem in MIMO-SAR in the time-frequency plane with a linear frequency modulated transmit signal.

To avoid an overlap and thus ambiguities of the transmitted signals, an additional spatial filtering has been proposed in [41] and [71]. The basic idea behind

this approach can be expressed by introducing, as a first step, a restricted orthogonality:

$$\int s_k(t) \cdot s_i^*(t-\tau)\,\mathrm{d}t = 0 \qquad \forall \quad \tau \in \left]-\frac{\tau_\mathrm{p}}{N_\mathrm{Tx}} + \epsilon, \frac{\tau_\mathrm{p}}{N_\mathrm{Tx}} - \epsilon\right[, \tag{3.2}$$

such that the signals $s_k(t)$ and $s_i(t)$ have only orthogonal properties for a subset of time shifts, where the time interval is limited by the N_Tx-th fraction of the pulse duration τ_p. The additional margin described by ϵ ensures orthogonality for finite impulse responses at the edges of the interval. This allows a perfect separation of the echoes of neighboring objects for an overall signal delay $\tau < \tau_\mathrm{p}/N_\mathrm{Tx} - \epsilon$. Each waveform obtains finally the same maximum unambiguous range interval.

According to [75], the maximum swath width in dependency on the antenna steering angle results to be:

$$W_\mathrm{g} \leq \frac{\left(\frac{\tau_\mathrm{p}}{N_\mathrm{Tx}} - \epsilon\right) \cdot \frac{c}{2}}{\sin(\Theta_\mathrm{inc})}. \tag{3.3}$$

With the relation between incidence angle and steering angle Θ:

$$\sin(\Theta_\mathrm{inc}) = \frac{R_\mathrm{E} + h}{R_\mathrm{E}} \cdot \sin(\Theta), \tag{3.4}$$

a typical SAR with $h = 700$ km, $\tau_\mathrm{p} = 120\,\mu$s, $N_\mathrm{Tx} = 2$ and $\epsilon = 0$, the maximum tolerable swath width is plotted in Fig. 3.2.

If the condition of Eq. (3.2) is neglected, the maximum signal delay increases and the time-frequency plane of Fig. 3.1 is completely filled with the echoes, so that the quasi orthogonal transmit signals will finally also correlate in the receiver. In this case, they are no longer orthogonal. As will be shown later in section 3.4.3, the *SNR* drops stepwise at the edges of the interval.

From an initial point of view, in comparison to required swath widths of more than 300 km [40], the swath width in Fig. 3.2 is obviously too narrow. A main advantage of the suggested concept is, however, that the interfering energy of the other waveforms is moved to known positions outside the given time interval. By making use of the side-looking geometry in SAR, there is a unique relation be-

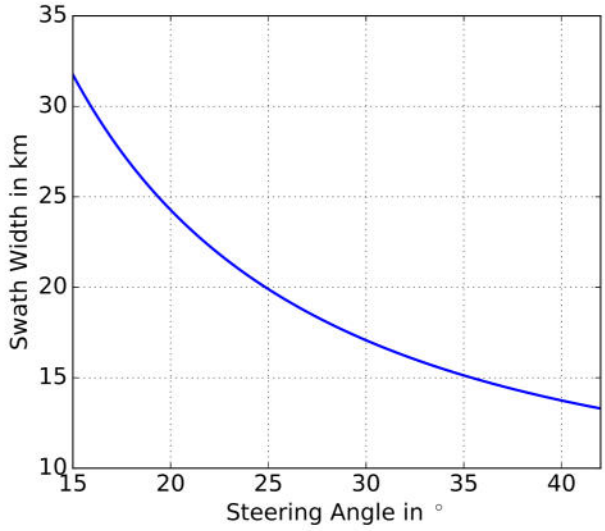


Figure 3.2. Maximum swath width for the condition of Eq. (3.2) with $h = 700$ km, $\tau_p = 120\,\mu$s, $N_{Tx} = 2$ and $\epsilon = 0$.

tween frequency, time and angle of arrival if a linear frequency modulated signal is used. This is graphically depicted with the information cube in Fig. 3.3 for a fraction of the echo signal. In principle, this figure is an extension of Fig. 3.1 to the AoA. The resulting curved, blue surface is infinitely thin[2], while the rest of the cube is filled with noise. The basic idea behind Eq. (3.2) is to find waveforms of certain structure, which do not intersect in the information cube. In a projection of these surfaces to the time-frequency plane, which is done in SAR without elevation DBF, the surfaces will overlap and look like in Fig. 3.1. Thus, filtering in three dimensions along that surfaces with a sufficient margin ϵ, enables to separate the waveforms completely without any disturbances. Due to the side-looking geometry of a SAR sensor, with the known geometric relation between AoA, frequency and time of arrival, a time-variant spatial filtering with an extension of the SCORE technique [28] can remove that unwanted energy of the other waveforms. Orthogonality for a wide-swath SAR system can then be fully satisfied. An explicit algorithm, fulfilling Eq. (3.1) is proposed in chapter 4. It should be noted, that this idea is also closely related to the topic of knowledge-based processing in radar [76].

[2]In the special case of layover, where signals are simultaneously backscattered from multiple directions (e.g. on mountains), this surface has an extension along the AoA axis.

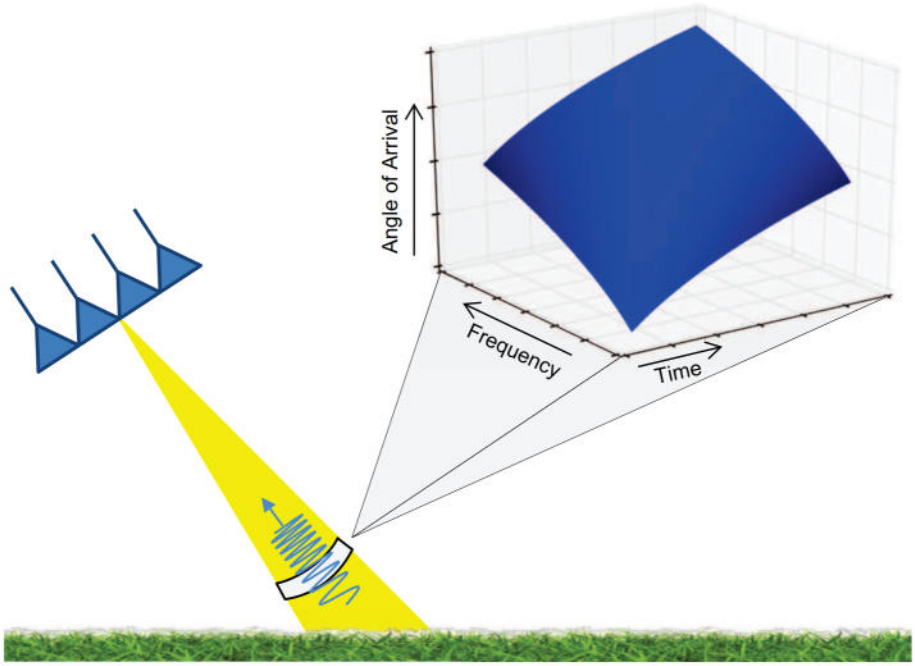


Figure 3.3. Representation of the receive signal due to a down-chirp, in incidence angle, time and frequency.

In the following sections, possible waveform types are presented, which can be used to ensure Eq. (3.1) in combination with DBF.

3.2. MIMO-SAR Waveforms

This section concentrates on three waveform types with a common structure. For completeness, in the last subsection further MIMO-SAR waveforms are also given. These waveforms have been proposed in literature, but do not fulfill the required orthogonality condition.

3.2.1. Standard Chirp Waveform

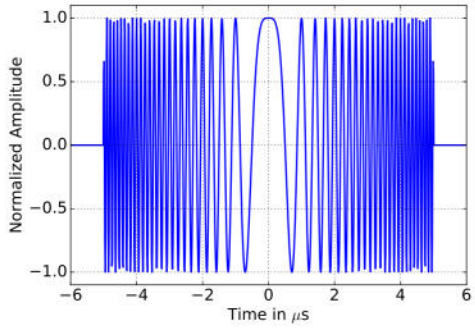
In most radar applications, a linear frequency modulated pulse is used, since it offers an optimum compromise between the requirements stated in sections 3.3 and 3.4 (high range resolution, hardly any auto-correlation degradations, unique range-Doppler coupling). This waveform is also called chirp waveform, given in base-band and in time domain by the equation:

$$s_{\mathrm{BB,chirp}}(t) = \exp\left(\mathrm{j}\pi K_{\mathrm{r}} t^2\right) \cdot \mathrm{rect}\left[\frac{t}{\tau_{\mathrm{p}}}\right], \tag{3.5}$$

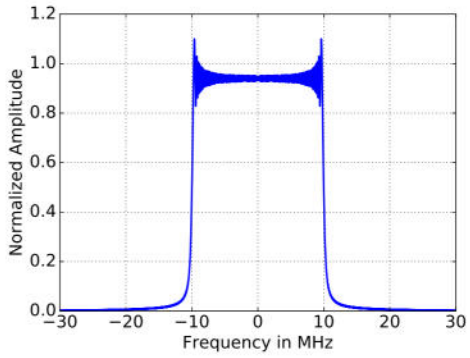
where the rect-function represents the pulse envelope and K_{r} is the modulation rate defined as

$$K_{\mathrm{r}} = \pm\frac{B}{\tau_{\mathrm{p}}}. \tag{3.6}$$

The $\pm$ indicates the trend of the slope (frequency vs. time). An increasing frequency ramp with a positive K_{r} is denoted as up-chirp, whereas a decreasing frequency ramp is denoted as down-chirp. Both signals may serve as a basis for the following chirp variations with identical properties. An important fact is that at each instance of time, just one frequency component is given. A plot of a typical up-chirp with $B = 20$ MHz and $\tau_{\mathrm{p}} = 10$ μs in time-domain is given in Fig. 3.4a and the corresponding time-frequency relation can be found in Fig. 3.1.



(a) Up-chirp in base-band and time-domain.



(b) Up-chirp in base-band and frequency-domain.

Figure 3.4. Standard chirp signal in time- and frequency domain with $\tau_{\mathrm{p}} = 10$ μs and $B = 20$ MHz.

An important fact is that the Fourier transform of the chirp-signal-envelope is not rectangular due to jump discontinuities at the edges of the spectrum. These result from Fourier series expansion and are known under the name Gibbs phenomenon [77]. In signal processing this topic is also highly discussed under the umbrella of ringing artifacts [78]. In radar, after range compression, they result

in higher sidelobes of each impulse response. In a single-channel system these artifacts can be easily compensated by windowing (e.g. Hanning, Hamming, Kaiser, ... [15]) during the pulse compression process. For multichannel radars a more detailed analysis is necessary, which can be found in section 3.4. The Fourier transform of a chirp signal can be expressed as

$$S_{\mathrm{BB,chirp}}(f) = \mathcal{F}\left\{s_{\mathrm{BB,chirp}}(t)\right\} = \frac{1}{\sqrt{2\pi}} \int s_{\mathrm{BB,chirp}}(t) \cdot \exp\left(-\mathrm{j}2\pi f t\right) \mathrm{d}t. \tag{3.7}$$

Eq. (3.7) is plotted in Fig. 3.4b with $B = 20$ MHz and $\tau_\mathrm{p} = 10$ μs. The jump discontinuities are about 10 % of the signal amplitude, which is a common value for every rectangular function.

All the following suggested waveform types bear this chirp-like structure.

3.2.2. OFDM-Chirp Waveforms

OFDM, in general, is a multi-carrier modulation technique. The individual transmit signals are having the same frequency spectrum, while the orthogonality is achieved with periodically interleaved sub-carriers [79, 80]. The OFDM chirp signals were introduced in [70] by J.-H. Kim. In his following publications this multiplex technique was further investigated [9, 81, 82]. Originally just defined for two transmit channels, it is straight forward to extend the scheme to more channels, as will be shown next.

For MIMO-SAR, the OFDM technique is applied on a standard chirp signal, while the overall signal duration is τ_p. In contrast to OFDM in communication, where the whole spectrum is occupied at each instance of time, in the present context the individual sub-carriers are swept in time due to the chirp-like waveform characteristic. A further difference to classical OFDM is the constant signal envelope with rectangular shape in time domain because of the pulse-like character. While a standard chirp occupies the complete frequency spectrum within B, the OFDM chirps share it with interleaved behavior. Due to the limitation of the overall bandwidth B and to retain the information content, N_Tx repetitions of the waveform in time-domain are necessary (this can also be seen in the periodicity of the discrete Fourier transform). An example for two transmit signals is illustrated in Fig. 3.5. The left-hand side shows the scheme of the orthogonal sub-carriers for $N_\mathrm{Tx} = 2$. Each sub-carrier is represented by a sinc-function, where the

maximum of one carrier is located at a null of the neighboring sub-carrier. The corresponding time-frequency representation is given on the right-hand side of the figure. It becomes apparent, that not only the signal itself is repeated, but there is also a frequency offset of Δf. This so called sub-carrier distance leads to the wanted spectral shift of the second waveform to achieve the interleaved carrier structure.

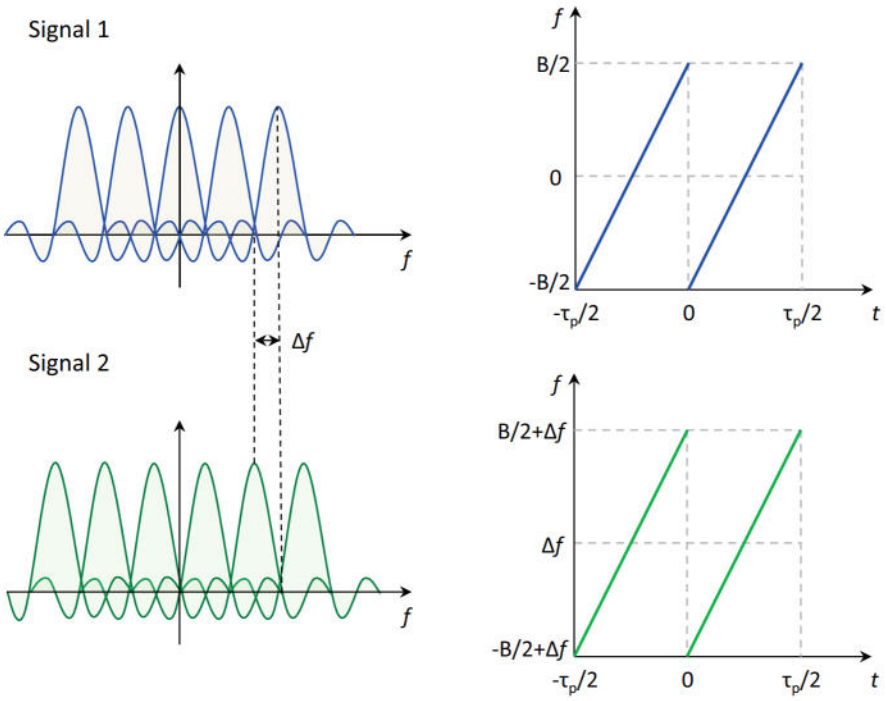


Figure 3.5. Scheme of the OFDM chirp waveforms for $N_{\mathrm{Tx}} = 2$; left-hand side: signal spectrum; right-hand side: time-frequency relation.

With reference to Eq. (3.5) an extension of the original definition of the OFDM chirp waveforms from [70] to an arbitrary number of N_{Tx} leads to:

$$\begin{aligned} s_{\mathrm{BB},k}(t) = & A \cdot \left(\sum_{m=0}^{N_{\mathrm{Tx}}-1} \exp\left(\mathrm{j}\pi K_{\mathrm{r}} N_{\mathrm{Tx}} \left(t + \frac{\tau_{\mathrm{p}}}{2} - \frac{\tau_{\mathrm{p}}(1+2m)}{2N_{\mathrm{Tx}}} \right)^2 \right) \right. \\ & \left. \cdot \operatorname{rect}\left[\frac{N_{\mathrm{Tx}}(2t+\tau_{\mathrm{p}}) - \tau_{\mathrm{p}}(1+2m)}{2\tau_{\mathrm{p}}} \right] \right) \cdot \exp\left(\mathrm{j}2\pi\Delta f k t\right). \end{aligned} \tag{3.8}$$

A is the amplitude, which is the same for every transmit waveform and m denotes the index of the repeated sub-chirp. The last exponential function in Eq. (3.8) leads to the sub-carrier offset of the k-th transmit signal. All remaining terms are equal to the standard chirp with the exception of a shift along the time axis for signal repetition. The sub-carrier distance Δf is set dependent on the chosen number of sub-carriers N_c and the pulse duration τ_p:

$$\Delta f = \frac{1}{N_\mathrm{c}\tau_\mathrm{p}}. \tag{3.9}$$

N_c is the product of sampling frequency f_S, which has to fulfill the Kotelnikov theorem and the signal duration[3]:

$$N_\mathrm{c} = f_\mathrm{S} \cdot \tau_\mathrm{p} = B \cdot \tau_\mathrm{p}. \tag{3.10}$$

A plot of a typical signal with $B = 10$ MHz, $\tau_\mathrm{p} = 10\,\mu$s, $N_\mathrm{Tx} = 2$ and $\Delta f = 1.0$ kHz can be found in Fig. 3.6. For better visualization, the signal was modulated on a carrier of $f_0 = B/2$. While the repetition of the chirps along the time axis can be directly seen, both waveforms look identical because $\Delta f << B$.

Finally, in time-domain the signals are completely orthogonal up to the limit given in Eq. (3.2). In frequency domain orthogonality is just satisfied for frequency shifts of less than Δf. This can be explained by means of the last exponential term in Eq. (3.8). Independent of the number of transmit waveforms, an additional frequency shift of Δf leads to $\exp(\mathrm{j}2\pi\Delta f k t) \cdot \exp(\mathrm{j}2\pi\Delta f t) = \exp(\mathrm{j}2\pi\Delta f (k+1)t)$, which equals the offset of the next Tx waveform. A detailed orthogonality analysis is given in the sections 3.3.2 and 3.4.4.

In OFDM, the DFT window length in the transmitter and the IDFT window length in the receiver must be the same to be able to separate the signals. Because the complete receive waveform has to be present within this window, in classical OFDM for wireless communication, a cyclic prefix to counteract the fading effect is appended to the signal. This converts the linear convolution between the channel and the transmitted signal into circular convolution thereby preserving orthogonality and eliminating inter-symbol interference [83]. At the receiver,

[3] Oversampling and a margin is neglected for ease of understanding.

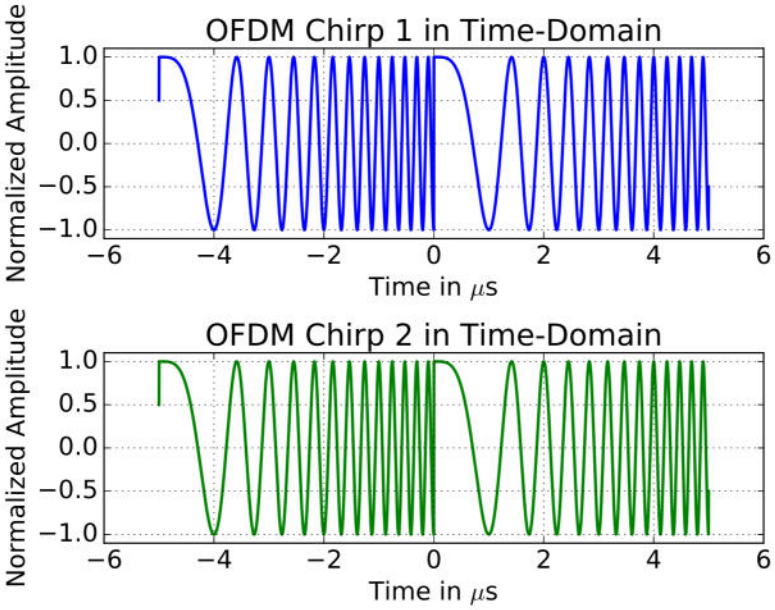


Figure 3.6. OFDM chirp in time domain with $N_{\mathrm{Tx}} = 2$, $\tau_{\mathrm{p}} = 10\,\mu\mathrm{s}$, $B = 10$ MHz, $\Delta f = 1.0$ kHz and $f_0 = B/2$.

the cyclic prefix is discarded and reverse transformation is performed in order to retrieve the data. Because in SAR and radar we are interested in the fading effect, instead of a *cyclic prefix*, on receive a *cyclic postfix* is applied on the received raw data. In the original document this approach was named circular-shift addition [9]. The upper limit of the cyclic postfix, which equals the limit of Eq. (3.2), needs for additional filtering with DBF. More details can be found in the introduction of the next chapter or in [82].

3.2.3. Multiple Sub-Pulse Mode

The Multiple Sub-Pulse (MSP) mode described in [36] is a mode, where multiple chirp-signals of same length, occupying the same frequency band are transmitted (compare Fig. 3.7). In the following two paragraphs, we differentiate between two types of sub-pulses. While in the first paragraph the common case with arbitrary delays between the sub-chirps is described, in the second paragraph we just give attention to a special case without any gaps. The latter type will later serve for further comparisons.

MSP with Arbitrary Gaps

Main changes of a sub-pulse in direct comparison to the normal chirp waveform of Eq. (3.5) are the value of the modulation rate, the reduction of the overall pulse duration to τ_{sub} and a shift on the time-axis to the individual sub-pulse center $t_{\text{c},k}$. The common chirp-like characteristic is still kept. An illustrative MSP signal with the same parameters as for the OFDM chirp signals ($B = 10$ MHz, $\tau_{\text{p}} = 10$ μs, $N_{\text{Tx}} = 2$, $f_0 = B/2$) and a gap of $\tau_{\text{s}} = 2$ μs is depicted in time-domain in Fig. 3.7. A more detailed definition of these parameters is derived within this section. The frequency ramps in Fig. 3.8 show the continuous and equal sweeping rate for every sub-pulse.

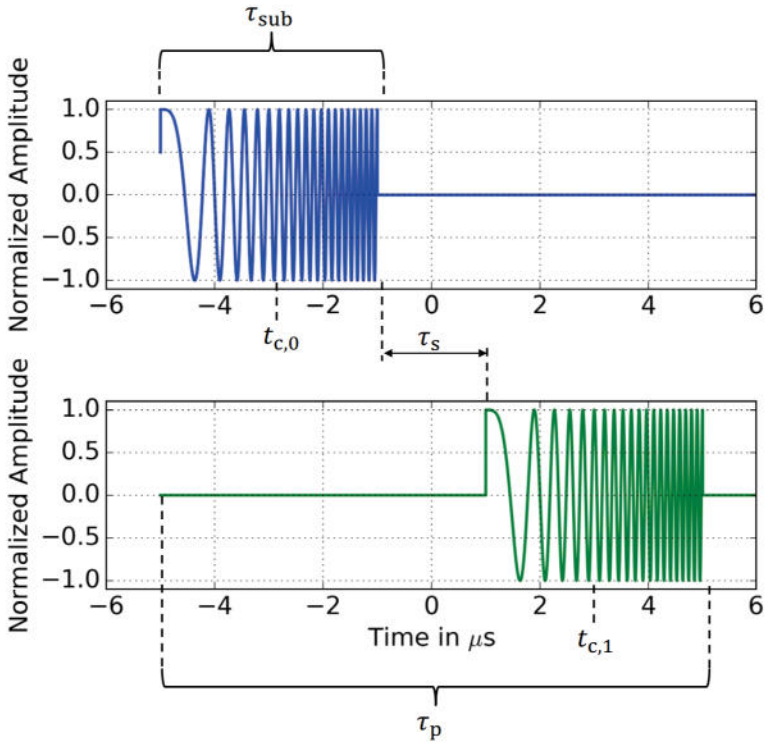
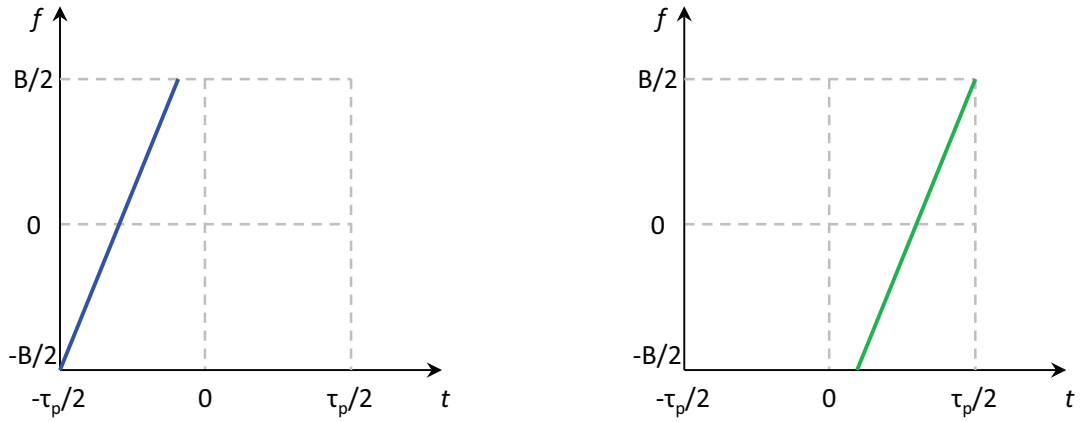


Figure 3.7. Illustration of the MSP waveforms with $B = 10$ MHz, $\tau_{\text{p}} = 10$ μs, $\tau_{\text{s}} = 2$ μs, $N_{\text{Tx}} = 2$, $f_0 = B/2$.

To have a common basis for later waveform comparison in this chapter, τ_{p} is set equal for the overall signal duration of all signals introduced in this chapter. As mentioned before, in the MSP mode the duration of each sub-pulse reduces to τ_{sub}, while positive or negative gaps of value τ_{s} are between them. The sub-pulse duration, which is the N_{Tx}-th fraction of τ_{p} minus the sum of all gaps is



(a) Signal s_0. **(b)** Signal s_1.

Figure 3.8. MSP waveform in the time-frequency plane.

$$\tau_{\text{sub}} = \frac{\tau_{\text{p}} - (N_{\text{Tx}} - 1)\tau_{\text{s}}}{N_{\text{Tx}}}. \tag{3.11}$$

Because all sub-pulses possess the full signal bandwidth, the chirp has to sweep within the shorter time-interval of τ_{sub} and the modulation rate of Eq. (3.6) must be redefined to:

$$K_{\text{r,sub}} = \pm\frac{B}{\tau_{\text{sub}}} = \pm\frac{B \cdot N_{\text{Tx}}}{\tau_{\text{p}} - (N_{\text{Tx}} - 1)\tau_{\text{s}}}. \tag{3.12}$$

For completeness, the shift of the sub-pulses along the time-axis and thus the center of the k-th sub-pulse can be expressed by

$$t_{\text{c},k} = -\frac{\tau_{\text{p}}}{2} + \frac{\tau_{\text{sub}}}{2} + k\tau_{\text{sub}} + k\tau_{\text{s}}. \tag{3.13}$$

The final description of the k-th sub-pulse reads as follows:

$$s_{\text{BB},k}(t) = A \cdot \exp\left(\text{j}\pi K_{\text{r,sub}}(t - t_{\text{c},k})^2\right) \cdot \text{rect}\left[\frac{t - t_{\text{c},k}}{\tau_{\text{sub}}}\right]. \tag{3.14}$$

Comparing this signal with Eq. (3.5) shows strong similarities. As will be shown in the next chapter, this is a significant advantage (dependent on the application), in view of the fact that normal chirp signals have proven themselves during the radar history.

Since a pulsed radar can not transmit and receive simultaneously and to keep the swath width constant (Eq. (2.21)), the transmit window should be kept as short as possible under consideration of the signal energy. By introducing additional positive gaps between the sub-pulses, less energy will be transmitted in that time-interval. As a result, only marginal values for $t_{c,k}$ can be accepted[4]. Negative values for τ_s improve the total power of a set of pulses, however the signal ambiguities have a smaller separation, which results in more strict antenna requirements for spatial filtering. Further analysis on these items can be found in the second half of this chapter.

MSP without Gaps

As special case of the MSP mode with arbitrary gaps, a simplification of Eq. (3.14) with $\tau_s = 0$ leads to the sub-pulse duration of

$$\tau_{sub} = \frac{\tau_p}{N_{Tx}}, \tag{3.15}$$

the modulation rate of

$$K_{r,sub} = \pm\frac{B}{\tau_{sub}} = \pm\frac{B \cdot N_{Tx}}{\tau_p}, \tag{3.16}$$

and the sub-pulse center of

$$t_{c,k} = -\frac{\tau_p}{2} + \frac{\tau_{sub}}{2} + k\tau_{sub} = -\frac{\tau_p}{2} + \frac{\tau_p(1+2k)}{2N_{Tx}}. \tag{3.17}$$

[4] To justify the expression *MIMO* for large positive gaps between the sub-pulses, for a wide-swath SAR the high time-spread of the channel leads to overlapping wavefronts of adjacent transmitted sub-pulses seen by the receiver. Hence, the radar receives at the same time different transmitted sub-pulses.

With the help of the last three equations, Eq. (3.14) results in a closed expression for each sub-chirp:

$$s_{\mathrm{BB},k}(t) = A \cdot \exp\left(\pm \mathrm{j}\pi \frac{B\,N_{\mathrm{Tx}}}{\tau_{\mathrm{p}}} \left(t + \frac{\tau_{\mathrm{p}}}{2} - \frac{\tau_{\mathrm{p}}(1+2k)}{2N_{\mathrm{Tx}}} \right)^2 \right) \cdot \mathrm{rect}\left[\frac{N_{\mathrm{Tx}}(2t+\tau_{\mathrm{p}}) - \tau_{\mathrm{p}}(1+2k)}{2\tau_{\mathrm{p}}} \right]. \tag{3.18}$$

This equation of a pulse train without any gaps between two adjacent transmitted sub-pulses can be used for a more convenient signal consideration and implementation than Eq. (3.14).

This sub-pulse waveform is only orthogonal for a subset of signal shifts in time and frequency. According to Eq. (3.14) and Eq. (3.18), the total pulse duration is τ_{p} and each sub-pulse is shorter or equal than $\tau_{\mathrm{p}}/N_{\mathrm{Tx}}$. Condition Eq. (3.2) is thus fulfilled for small swathes.

For greater time shifts the signals will correlate and cause interferences. Based on the suggestions made in [36], it is proposed to form N_{Tx} time-variant receive beams in elevation in order to filter spatially between each sub-pulse. Basically, each sub-pulse is traced by its own receive antenna beam to avoid the occurrence of signal ambiguities. The necessary algorithm is derived in chapter 4.

3.2.4. Segmentally-Shifted Chirp Waveforms

Another promising waveform for MIMO-SAR has been proposed in [71], later refined in [41] and firstly verified by an experiment in [84]. In the following we will name it Segmentally-Shifted Chirp (SSC) waveform. Basically, it consists of shifted chirp waveforms with equal modulation rate but different sub-pulse durations and bandwidths. Each two sub-pulses are combined to a single transmit signal of full bandwidth B and full pulse duration τ_{p}. To give an example in Fig. 3.9, the SSC signal is plotted in time-domain for $B = 10$ MHz, $\tau_{\mathrm{p}} = 10\ \mu$s, $N_{\mathrm{Tx}} = 2$ and $f_0 = B/2$. The upper plot shows the first waveform, which is made up of segments of the first waveform within τ_{p} that have been repositioned.

As previously mentioned, with absence of the first transmit signal, each waveform consists of two sub-pulses, while the full bandwidth and full pulse duration is used. To fulfill the orthogonality condition of Eq. (3.2), the sub-chirps

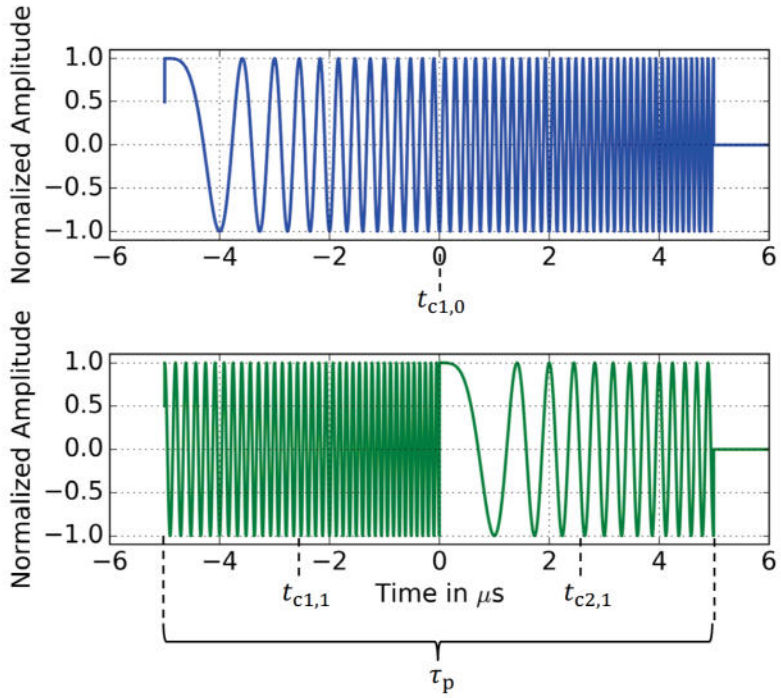


Figure 3.9. Illustration of the segmentally-shifted chirp waveform in time-domain for $B = 10$ MHz, $\tau_p = 10$ μs, $N_{Tx} = 2$ and $f_0 = B/2$. Upper plot: $s_0(t)$. Lower plot: $s_1(t)$.

are following a certain sequence, which becomes clearly noticeable in the time-frequency plots in Fig. 3.10a and Fig. 3.10b for two and in Fig. 3.10c for four activated transmit channels. While the modulation rate is the same for each waveform as defined in Eq. (3.6), we need two sub-pulse centers $t_{c1,k}$ and $t_{c2,k}$ for each splitted sub-pulse. They can be defined as

$$t_{c1,k} = \frac{k\tau_p}{2N_{Tx}} \tag{3.19}$$

and

$$t_{c2,k} = -\frac{(N_{Tx} - k)\tau_p}{2N_{Tx}}. \tag{3.20}$$

The duration of the sub-chirps are

$$\tau_{\mathrm{sub1},k} = \frac{(N_{\mathrm{Tx}} - k)\tau_{\mathrm{p}}}{N_{\mathrm{Tx}}} \tag{3.21}$$

and

$$\tau_{\mathrm{sub2},k} = \frac{k\tau_{\mathrm{p}}}{N_{\mathrm{Tx}}}. \tag{3.22}$$

It becomes directly understandable that $\tau_{\mathrm{sub1},k} + \tau_{\mathrm{sub2},k} = \tau_{\mathrm{p}}$. Using the last equations and adapting the formula for the standard chirp signal, the SSC waveforms can be written in a closed expression as

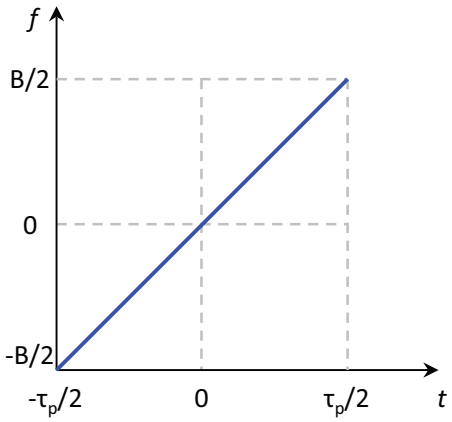
$$\begin{aligned} s_{\mathrm{BB},k}(t) =& A \cdot \exp\left(\mathrm{j}\pi K_{\mathrm{r}}\left(t + \frac{k\tau_{\mathrm{p}}}{N_{\mathrm{Tx}}}\right)^2\right) \cdot \exp\left(-\mathrm{j}\pi \frac{Bk}{N_{\mathrm{Tx}}}\left(t + \frac{k\tau_{\mathrm{p}}}{N_{\mathrm{Tx}}}\right)\right) \\ & \cdot \mathrm{rect}\left[\frac{N_{\mathrm{Tx}}t + k\tau_{\mathrm{p}}}{(N_{\mathrm{Tx}} - k)\tau_{\mathrm{p}}}\right] \\ & + A \cdot \exp\left(\mathrm{j}\pi K_{\mathrm{r}}\left(t - \frac{(N_{\mathrm{Tx}} - k)\tau_{\mathrm{p}}}{N_{\mathrm{Tx}}}\right)^2\right) \cdot \exp\left(\mathrm{j}\pi \frac{B(N_{\mathrm{Tx}} - k)}{N_{\mathrm{Tx}}}\left(t - \frac{(N_{\mathrm{Tx}} - k)\tau_{\mathrm{p}}}{N_{\mathrm{Tx}}}\right)\right) \\ & \cdot \mathrm{rect}\left[\frac{N_{\mathrm{Tx}}t - (N_{\mathrm{Tx}} - k)\tau_{\mathrm{p}}}{k\tau_{\mathrm{p}}}\right] \qquad \text{for} \quad k > 0. \end{aligned} \tag{3.23}$$

For $k = 0$ Eq. (3.5) has to be taken, since the first transmit waveform equals the standard chirp waveform, with full bandwidth and full pulse duration.

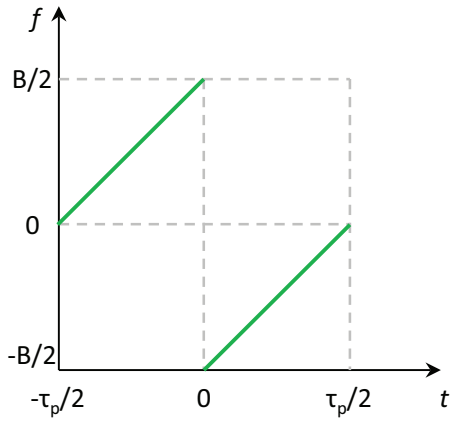
Since usually the swath width exceeds the pulse length, this type of waveform will also cause ambiguities. Therefore, after analyzing the waveforms in more detail, a solution to circumvent this limitation with the aid of digital beam-forming on receive is given.

3.2.5. Further Waveforms

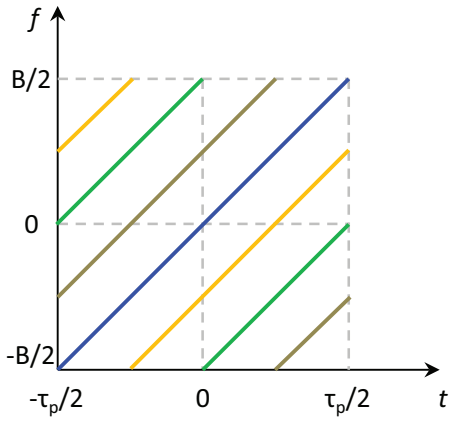
For completeness, in this section, two further signal types are introduced, which play a minor role for MIMO-SAR. The reason for that results from their structure,



(a) Signal $s_{\mathrm{BB},0}$ for two activated transmit channels.



(b) Signal $s_{\mathrm{BB},1}$ for two activated transmit channels.



(c) Signals $s_{\mathrm{BB},0} - s_{\mathrm{BB},3}$ for four activated transmit channels.

Figure 3.10. Segmentally-shifted chirp waveform in the time-frequency plane.

which does not allow a perfect separation between the waveforms for retaining HRWS observations.

Up- and Down-Chirp Modulation

In the past, it was extensively discussed to use alternating or even simultaneous up- and down-chirp signals as kind of orthogonal waveforms. This modulation concept was examined in more detail in [72]. Limited to a maximum number

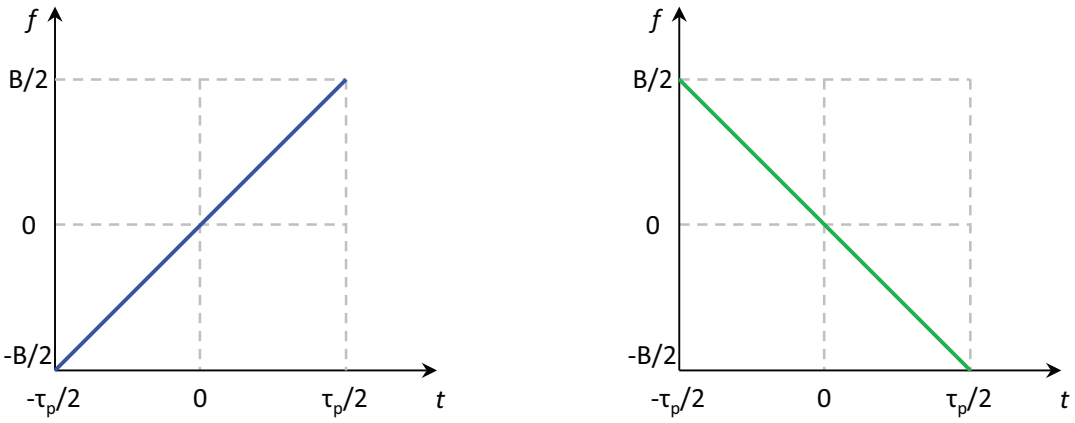
of only $N_{\mathrm{Tx}} = 2$ transmit channels, even for small observation areas this waveform type does not lead to the desired results. The reason for that becomes clear from the plot of the frequency ramps (Fig. 3.11). $s_0(t)$ and $s_1(t)$ already intersect in the time-frequency plane for a single point target – at a certain instance of time, which leads invariably to cross-correlation interferences. Every additional shift in time, which is caused by further point targets, results in more interferences. For a SAR with homogenous extended targets, the *SNR* will tend to zero, as proven in [41].

Both waveforms can be explicitly given as:

$$s_{\mathrm{BB},0}(t) = A \cdot \left(\mathrm{j}\pi \frac{B}{\tau_{\mathrm{p}}} t^2 \right) \cdot \mathrm{rect}\left[\frac{t}{\tau_{\mathrm{p}}} \right] \tag{3.24}$$

and

$$s_{\mathrm{BB},1}(t) = A \cdot \left(\mathrm{j}\pi (-\frac{B}{\tau_{\mathrm{p}}} t^2) \right) \cdot \mathrm{rect}\left[\frac{t}{\tau_{\mathrm{p}}} \right]. \tag{3.25}$$



(a) Signal s_0. **(b)** Signal s_1.

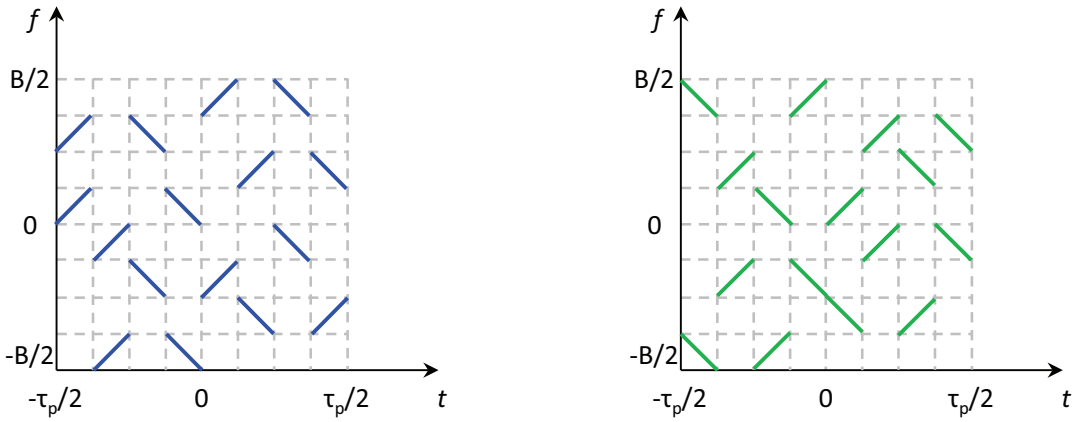
Figure 3.11. Illustration of the up-down chirp modulation.

Since this modulation concept does not generally work for HRWS-SAR, no further analysis is carried out.

Chirp Diverse Waveforms

The *chirp diverse waveforms* introduced by W. Q. Wang experience a steady improvement over the last years [73, 85, 86].

In this OFDM-based technique, multiple short sub-pulses are generated, which are modulated on individual sub-carriers. The number of carriers is lower than for classical OFDM signals, but usually higher than the number of transmit channels. Furthermore, the number of simultaneous active sub-carriers is independent of the number of sub-pulses and up- and down-chirp modulation can be used in parallel. As suggested in the original paper, a random matrix modulation concept helps to optimize the auto- and cross-correlation interferences between the waveforms. Thus, a set of many short sub-chirp signals shifted in the time-frequency plane is generated. An example with $N_{\mathrm{Tx}} = 2$ is shown in the time-frequency plane in Fig. 3.12.



(a) Signal s_0. **(b)** Signal s_1.

Figure 3.12. Illustration of the chirp diverse waveforms with $N_{\mathrm{Tx}} = 2$ in the time-frequency plane.

Simulation results with narrow swath widths are showing in [73] that this waveform type is promising for MIMO-SAR. But it was proven in [41], that this multiplex concept is not working for HRWS MIMO-SAR. As it becomes obvious from the time-frequency plots in Fig. 3.12, already small time shifts of s_0 and s_1 lead to an overlap of sub-chirps and thus in turn to cross-correlation interferences. However, a significant advantage of this waveform type is, that for de-correlation of the transmit signals, DBF on receive is not necessary. More detailed analysis

on this waveform type in comparison to the other waveforms of this chapter is carried out in the next section.

It should be noted that all of the aforementioned waveforms can be designed with this concept and can be seen as a special case.

3.3. Ambiguity Function

As previously described in the sections 2.3 and 3.1, ambiguities are mainly caused by the periodic signal repetition due to the *PRF* and by the signal itself. Other reasons may be the Doppler shift due to the moving platform or moving targets in the scene. To analyze the behavior of a radar waveform in terms of resolution, cross- and auto-correlation interferences and Doppler-tolerance, it has been found that the Ambiguity Function (AF) is an important tool for that purpose. Meanwhile there exist a couple of AFs, each focusing on other effects, while most of the functions are based on the first AF defined by Woodward in 1967 [22]. Apart from Woodward's AF, the most important AFs are the SAR Ambiguity Function defined by R. O. Harger in 1965 [21], the MIMO-Radar AF defined by G. San Antonio et.al. [87] and the Transmit Beamspace AF from Y. Li et.al. [88]. Because the SAR-AF is primarily not a function of the radar waveforms, it has dependencies on the antenna properties, *PRF* and azimuth resolution, as mentioned in section 2.3. A special case of the MIMO-Radar AF and the Transmit Beamspace AF will be handled in this section.

3.3.1. Description of the Ambiguity Function

At first, we focus on a single waveform with optimum properties for radar. The basic auto-correlation of a single waveform can then be graphically depicted by means of the Woodward's AF [22]. This function can be found in the *IEEE Standard Radar Definitions* [89] and plays an important role in the selection of radar signals and codes. The ambiguity function of the k-th waveform is defined as the squared magnitude of

$$\chi_k(\tau, f_v) = \int s_k(t) \cdot s_k^*(t-\tau) e^{\mathrm{j}2\pi f_v t} \, \mathrm{d}t, \tag{3.26}$$

where the parameter f_ν represents different Doppler shifts. It basically reflects the normalized matched filter.

For decades, linear frequency modulated signals with either increasing or decreasing frequency (up-chirp, down-chirp) were widely used in radar applications. They possess good properties in terms of range resolution and energy as shown next. The result of $|\chi_k|^2$ for a standard up-chirp with $B = 300$ MHz and a pulse duration of $\tau_p = 120$ μs is plotted in Fig. 3.13. The drop of the diagonal course from the maxima is a characteristic feature. The sharpness of the ridge along the two axes in Fig. 3.13 is related to the resolution of the radar. These features in turn, are dependent on the bandwidth of the signal and its duration (compare section 3.4.1). Because the area outside of the ridge is free of commonality between $s_k(t)$ and $s_k(t-\tau)$, no coupling between the two exists. This leads to the fact that in the aforementioned region there are no auto-correlation interferences.

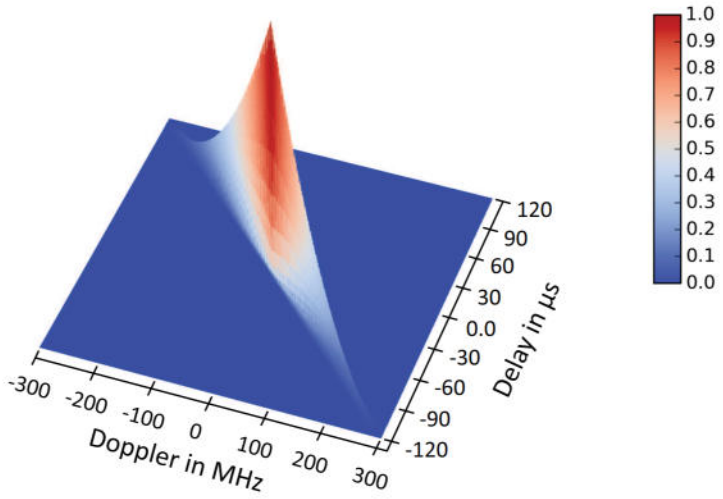


Figure 3.13. Ambiguity Function (Eq. (3.26)) of an up-chirp.

In recent years, a variety of MIMO-Radar Ambiguity Functions were derived. They focus on different properties of the radar and therefore are not directly comparable. In 2007 San Antonio et al. [87] developed a very good evaluation of these functions and introduced a generalized MIMO AF, which was later further analyzed by Chen [90]. San Antonio has shown, that the MIMO Ambiguity Function does not only depend on the signal itself, but also on the radar system, the used beam-forming algorithm, and the target. Basically, the MIMO AF shows that the

correlated signal energy can also be suppressed by a proper DBF. This equation involves all the parameters of the radar system, including the element spacing, antenna beam patterns, channel characteristics and the backscattering properties of the objects. Finally, the function presented in [87] depends on 16 independent parameters.

Because several factors have an impact, an analytical solution of this function is not readily possible. For this reason, Chen defined in [90] a more simplified form, which is also known as Cross Ambiguity Function. This AF focuses on the basic correlation between several transmit waveforms. For derivation Chen has introduced some constraints, which are valid for most MIMO-radar systems:

- No analog beam-forming – DBF is applied later during post-processing
- Targets are localized in the far field
- High time-bandwidth product: $TB > 100$
- Collocated antenna array – no bistatic/multistatic geometrical description
- Narrow-band assumption: $B/2 < f_0$.

The Cross AF reads as follows:

$$\chi'_k(\tau, f_v) = \int s_k(t) \cdot \left[s_k^*(t-\tau) + \sum_b s_b^*(t-\tau) \right] e^{\mathrm{j}2\pi f_v t} \, \mathrm{d}t \qquad \text{for} \quad b \in \mathbb{N}_0^+,\ b < N_{\mathrm{Tx}} \text{ and } b \neq k. \tag{3.27}$$

Since the correlation is a linear operation, it is reasonable to split Eq. (3.27) up into two parts, in the next step:

$$\begin{aligned} \chi'_k(\tau, f_v) &= \int s_k(t) \cdot s_k^*(t-\tau) e^{\mathrm{j}2\pi f_v t} \, \mathrm{d}t + \int s_k(t) \cdot \sum_b s_b^*(t-\tau) e^{\mathrm{j}2\pi f_v t} \, \mathrm{d}t \\ &= \chi_k(\tau, f_v) + \varsigma_k(\tau, f_v), \end{aligned} \tag{3.28}$$

with

$$\varsigma_k(\tau, f_\nu) = \int s_k(t) \cdot \sum_b s_b^*(t-\tau) e^{\mathrm{j}2\pi f_\nu t} \, \mathrm{d}t. \tag{3.29}$$

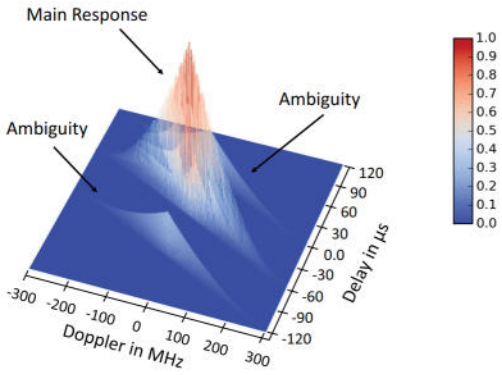
The first additive part of Eq. (3.28) is equal to the function defined by Woodward (Eq. (3.26)), while the second part (Eq. (3.29)) describes the unwanted interferences with the other transmitted waveforms. A signal suitable for MIMO-SAR should have a χ_k like that in Fig. 3.13 whereas $\varsigma_{k,b}$ should be zero for any shifts in time and frequency in the ideal case.

A major difference between the MIMO AF and the Transmit Beamspace AF (TB-AF [88]) is that the TB-AF is more generalized and also deals with coherent transmit signals, which are not a topic of this thesis and hence not mentioned in further analysis.

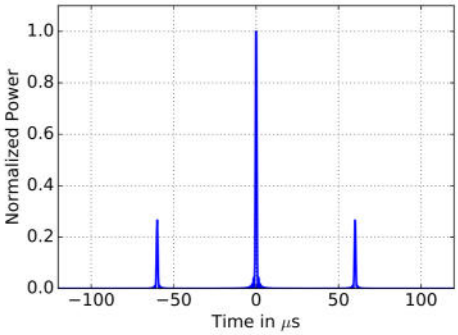
3.3.2. Ambiguity Function Analysis

Fig. 3.14a, Fig. 3.14c, Fig. 3.14e and Fig. 3.14g show the plots of the Cross Ambiguity Functions for the OFDM chirp signals (section 3.2.2), the MSP mode (section 3.2.3), the SSC waveforms (section 3.2.4) and for the Chirp Diverse waveforms (section 3.2.5) for $N_{\mathrm{Tx}} = 2$. Every set of waveforms has a total bandwidth of 300 MHz and a total pulse duration of 120 μs. It can be clearly seen that, apart from the Chirp Diverse waveform, the wanted main response (*main-lobe*) in the middle has exactly the same shape as for a standard up-chirp. The ambiguities, which result from the cross-correlation with the second transmit waveform, are concentrated on dedicated localized ridges for the three waveform types. Having a closer look at the axes, it turns out that these ridges are outside the limited interval of Eq. (3.2). As negative example, the AF of the Chirp Diverse waveform shows pronounced ambiguities, which are distributed within the limited interval of the time-frequency plane.

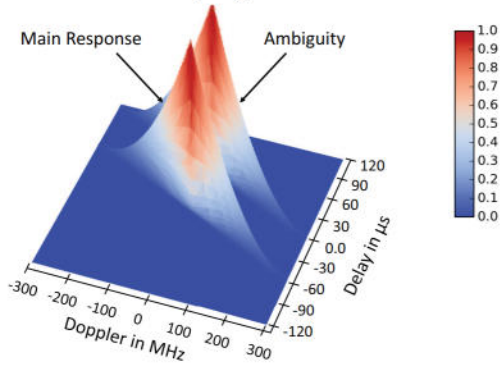
An eye-catching artifact in the OFDM AF plot is that the ridge in the middle is not completely filled, which results from the interleaving behavior of the sub-carriers. The repeating structure of each OFDM chirp causes also auto-correlation interferences, which are overlaid by the cross-correlation interferences. However, due to the sub-carrier spacing, the waveforms can be separated. Since on each ambiguous ridge just half of the full waveform correlates, just half of the signal energy is concentrated on such an ambiguity. Furthermore, each of the repeated



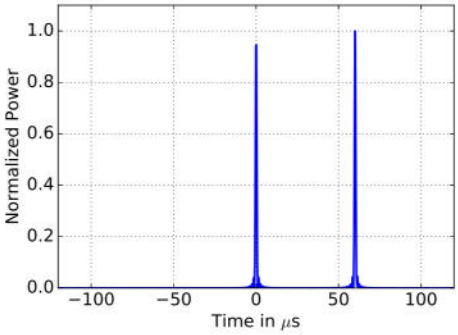
(a) Cross-Ambiguity Function of the OFDM chirp signal.



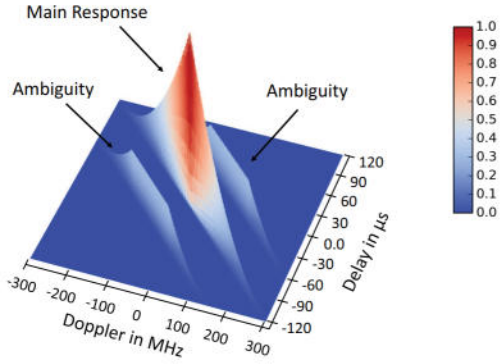
(b) $|\chi'(\tau,0)|^2$ with OFDM chirp signal.



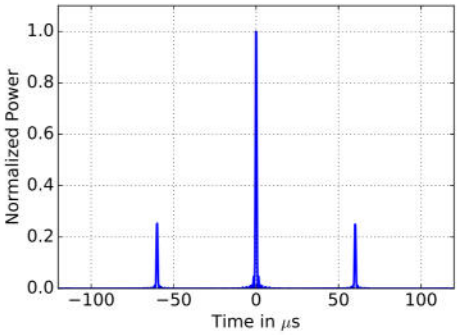
(c) Cross-Ambiguity Function of the MSP mode.



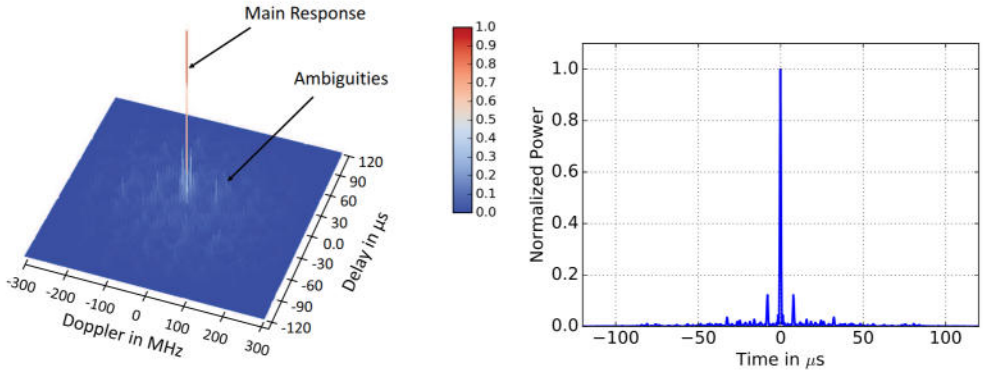
(d) $|\chi'(\tau,0)|^2$ with MSP mode.



(e) Cross-Ambiguity Function of the SSC waveform.



(f) $|\chi'(\tau,0)|^2$ with SSC waveform.



(g) Cross-Ambiguity Function of the Chirp Diverse waveform.

(h) $|\chi'(\tau, 0)|^2$ with Chirp Diverse waveform.

Figure 3.14. Cross-Ambiguity Functions with corresponding zero-Doppler cuts (Eq. (3.28)) of different waveforms.

sub-pulses implies the full signal bandwidth. The width of the ridge, and thus the resolution, is also the same.

Basically, the MSP mode is just a sequence of repeated chirp waveforms. From this fact it becomes obvious that the signal ambiguities have the same energy and the same resolution as the main impulse response. An exact repetition of the main ridge is the result.

With exception of the first waveform, in the SSC waveform mode all remaining waveforms consist of two shifted sub-pulses. This leads to two ambiguities for every further transmit signal. Each ambiguity shares half of the signal energy and half of the total bandwidth. This means that the signal ambiguities, which have to be suppressed have half the amplitude and also half the resolution of the auto-correlation. Due to the projection of the signal to the spherical Earth ground, the positions of the ambiguities are not symmetric, leading to a more complicated pattern synthesis for DBF suppression.

Because the Chirp Diverse waveform typically consists of several short sub-chirps with overlapping spectra, at specific time or frequency shifts certain sub-pulses correlate. This is even the case for a single transmit waveform. The energy of both waveforms is accordingly smeared in the AF plot. Already this fact makes this waveform type inapplicable for HRWS MIMO-SAR.

An important extraction from the three-dimensional AF plots are zero-Doppler cuts, expressing the impulse response for a point target in a static scene ($f_\nu = 0$ Hz). They can be found on the right hand side of Fig. 3.14 and serve as

aid for understanding the behavior of the waveforms. For better visualization, the number of transmit signals was set to $N_{\mathrm{Tx}} = 2$, while zero-Doppler cuts for $N_{\mathrm{Tx}} = 4$ can be found in Fig. 3.16.

A benefit of the OFDM, MSP and SSC waveforms is that they all pose same requirements for an additional filtering, because the separation between the signal ambiguities and the main response is equal. As mentioned before by San Antonio [87] and Krieger [36], the energy in the auto- and cross-correlation interferences can be suppressed via DBF. Using *a priori* knowledge about the scene geometry, antennas and waveforms, appropriate antenna patterns can be synthesized during post processing to enable HRWS MIMO-SAR without interferences caused by the very own waveforms of the radar. The detailed algorithm for suppression is given in chapter 4.

3.4. Waveform Performance Parameters

Requirements in terms of the signal are different for radar and for communication. In contrast to communication, where the focus is to exchange information between the users, in radar the signal is primarily used for detection and ranging, as already indicated by the acronym *radar*. As a result, a single high and sharp correlation peak is wanted if a target is detected[5]. However this is practically not possible. This drawback, which leads to broad or even to additional peaks and interferences, can often be accepted in radar but not in imaging radar, such as SAR. In SAR, further, strict restrictions for the signals arise. All important restrictions and their effects are itemized as follows.

3.4.1. Range Resolution

Per definition, resolution is the capability to detect two identical objects separated by a minimum distance δ_{rg} and to be able to resolve them from each other [89]. The range resolution is along the radial direction from the radar, while the azimuth and elevation angles are constant. To separate the backscattered signals from those two targets, it is at least mandatory to separate the two leading flanks of the pulses from each other; since usually the radar signals are

[5] This is also demanded in communication to avoid intersymbol interferences, but the final *SNR* can be usually significantly lower to extract the wanted information content from the noisy signal. Moreover, techniques to compensate e.g. fading effects or check sums to test the data for plausibility, or repeater for amplification can be used.

modulated (also referred to as intrapulse modulation). With reference to Fig. 2.1, the maximum obtainable ground range resolution of a SAR is defined as

$$\delta_{\mathrm{rg}} = w_{\mathrm{win}} \cdot \frac{c}{2B \cdot \sin \Theta_{\mathrm{inc}}}, \tag{3.30}$$

where w_{win} is the characteristic value for the used window function during the range compression process. Common values are $w_{\mathrm{win}} = 0.886$ for a rectangular window and $w_{\mathrm{win}} = 1.3$ for a Hanning window [15]. This maximum resolution can only be achieved, if the transmit signal envelope is completely rectangular, which is the case in all of the four suggested waveform types (OFDM, MSP, SSC and Chirp Diverse waveforms). In all other cases, any variances in the pulse shape lead to a decreased resolution. It is also worth noting that the problem of amplitude variation is also strongly related to the calibration of radar pulses, since the radar hardware leads to signal amplitude distortions.

The definition of range resolution leads to the demand for a high signal bandwidth. This bandwidth is usually limited by the maximum bandwidth of the hardware. In practice the values are usually lower than 15 % of the used carrier frequency.

Instead of using Eq. (3.30), it is also possible to determine the resolution from the 3dB-width of the impulse response, which equals the centered sinc-function in the zero-Doppler cuts of the AF. Both methods lead to the same result. Simulations for different N_{Tx} have shown, that each of the previously defined waveforms (OFDM-Chirp signals, MSP mode, SSC and Chirp Diverse waveforms) shares the full bandwidth and hence they have equal properties in terms of the resolution.

3.4.2. Integrated Sidelobe Ratio

In this subsection we are interested in impacts of the waveform type and the number of transmit waveforms on the Integrated Sidelobe Ratio (*ISLR*). Per definition, the *ISLR* is an indicator for the amount of energy in the sidelobes of the impulse response in relation to the amount of energy which is in the main-lobe of the impulse response. In Fig. 3.15 both amounts of energy are marked in green and blue color, respectively. For all suggested STSO waveform types, this value significantly depends on the chosen time segment, ΔT, of the output signal from

the matched filter. Following the definition of the *ISLR* [15], for a certain observation time ΔT we get:

$$ISLR(\Delta T) = \frac{\int_{-\Delta T/2}^{-T_{\mathrm{NBW}}/2} \chi'_k(\tau,0)\,\mathrm{d}\tau + \int_{T_{\mathrm{NBW}}/2}^{\Delta T/2} \chi'_k(\tau,0)\,\mathrm{d}\tau}{\int_{-T_{\mathrm{NBW}}/2}^{T_{\mathrm{NBW}}/2} \chi'_k(\tau,0)\,\mathrm{d}\tau} \qquad \forall \quad T_{\mathrm{NBW}} \leq \Delta T \leq \tau_{\mathrm{p}}, \tag{3.31}$$

where T_{NBW} is two times the 3dB-width of the impulse response.

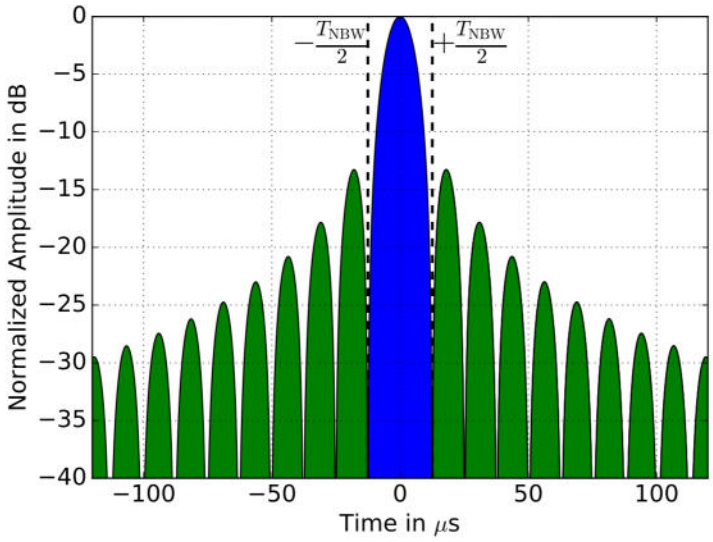


Figure 3.15. Impulse response function of an up-chirp. The green surface indicated the amount of energy within the sidelobes and the blue surface the energy within the main-lobe. The ratio between the two is defined as *ISLR*.

A typical value for the impulse response from a chirp signal is *ISLR* = -9.8 dB. Unfortunately the dynamic RCS of targets within a standard SAR scene exceeds usually this value and strong sidelobes may affect the rest of the image. Hence, it was suggested to use windowing to overcome the hard steps at the edges of the chirp spectrum. For example with Hanning windowing, the *ISLR* can be significantly reduced to about -21 dB at the costs of worsening the resolution by the factor w_{win} (compare Eq. (3.30)).

Basically, there are two inputs, which downgrade the *ISLR*. For large values of ΔT ($\Delta T > \tau_p/N_{Tx} - \epsilon$), the *ISLR* is not only an indicator for the amount of energy within the sidelobes, but also for the contribution of the signal inherent interferences, i.e. ambiguities, according to the repeating signal structure (see also zero-Doppler cuts, Fig. 3.14). For small values of ΔT waveform dependent degradations of the *ISLR* are a result of the Gibbs phenomenon. As previously explained with Fig. 3.4b in section 3.2, jump discontinuities arise in the chirp signal spectrum. In a single-channel radar, they can be suppressed by using window functions. Significantly in MIMO-SAR, windowing has to be applied after waveform separation and before range compression. Any discontinuity within the signal spectrum of a single signal can not be suppressed and leads finally to a lower *ISLR*.

For a more detailed and quantitative analysis, the *ISLR* was calculated for different values of ΔT, N_{Tx} and window types. To have a common basis, the following simulation parameters were used: $B = 300$ MHz, $\tau_p = 120\,\mu$s and for the plots, $N_{Tx} = 4$. The results can be found in Fig. 3.16 and Tab. 3.1. Already in all plots of Fig. 3.16 it becomes apparent that the *ISLR* rises stepwise after the observation time ΔT given in multiples of τ_p/N_{Tx}. As previously seen in the zero-Doppler cuts of the AF and in the signal orthogonality condition (Eq. (3.2)), for observation times outside the interval $\left]-\frac{\tau_p}{N_{Tx}} + \epsilon, \frac{\tau_p}{N_{Tx}} - \epsilon\right[$, we will get strong ambiguities, which lead to these steps. For sure, after the first step at τ_p/N_{Tx} the *ISLR* is higher than 0 dB, because not only the full energy of the second transmit waveform applies, but also the energy of the side-lobes of all remaining signals. More detailed information for every plot and value in the table is given for every waveform type individually.

OFDM Waveforms

The *ISLR* can also be seen as an extraction of the zero-Doppler cut, which is plotted on the right hand side of each *ISLR*-plot for better comparison. Since the OFDM chirps have larger auto-correlation interferences the closer they are at the main impulse response, the relative increase of the first steps of the *ISLR* is greater than the one for the last steps. We note in advance, in comparison to the other *ISLR* values for large observation times $\Delta T > (N_{Tx} - 1)\tau_p/N_{Tx}$, in OFDM this value is lower because of the interleaving structure of the sub-carriers. They do not fully correlate between the waveforms at the zero-Doppler cut. Having a

Table 3.1. Maximum *ISLR* for small observation intervals ($\Delta T < 0.1 \cdot \tau_p$) in dependence on N_{Tx}, window type and waveform.

Window	**Rectangular**			**Hanning**		
N_{Tx}	**2**	**4**	**8**	**2**	**4**	**8**
OFDM chirps	-9.7 dB	-9.7 dB	-9.7 dB	-21.1 dB	-20.9 dB	-20.0 dB
MSP chirps	-9.7 dB	-9.7 dB	-9.7 dB	-21.1 dB	-21.0 dB	-20.8 dB
SSC chirps	-9.5 dB ... -9.7 dB	-9.5 dB ... -9.7 dB	-9.5 dB ... -9.7 dB	-17.7 dB ... -21.2 dB	-17.7 dB ... -21.2 dB	-17.7 dB ... -21.2 dB
Chirp Diverse	-8.1 dB	-7.8 dB	–	-7.5 dB	-7.2 dB	–

closer look at the values for $\Delta T << \tau_p/N_{Tx}$, the curve rises slightly with increasing observation interval. This effect is a result of the sidelobes, which are stronger around the main peak of the impulse response.

Tab. 3.1 shows that the *ISLR* for $\Delta T < 0.1 \cdot \tau_p$ is more or less independent of the number of transmit signals. The small degradation for increasing N_{Tx} with Hanning windowing is an effect of the sub-carrier spacing Δf. Referring to the definition of the OFDM chirps, they consist of repeated sub-pulses and each sub-pulse occupies the full signal bandwidth. As a result, there are also no jump discontinuities within the signal spectrum excepting the outer edges as for a standard chirp. Due to the sub-carrier spacing Δf of every further transmit signal, the jump discontinuities become slightly broadened, which leads to a degradation of the *ISLR*. In dependence of how the window is set, the *ISLR* can also be kept constant over N_{Tx}, while lowering the range resolution.

In summary, the values are almost the same as for a standard chirp waveform.

MSP Waveforms

With reference to the AF-plot in Fig. 3.14, every additional transmit signal correlates completely after integer multiples of τ_p/N_{Tx}. After the first *ISLR* jump, where the second sub-pulse correlates, the *ISLR* rises after every step by the same value of 3 dB. For small values of ΔT ($<< \tau_p/N_{Tx}$) the *ISLR* shows the same behavior as for the OFDM chirps.

In the table, a significant advantage of the MSP mode can be seen. Since the waveforms are just a repetition of equal standard chirp signals, each sub-pulse

can be windowed as usual, since there is no intermodulation transition within a single transmitted sub-pulse waveform. The *ISLR* will have the same value as for a normal chirp. However with increasing number of N_{Tx}, the *ISLR* also degrades, which is visibly more significant with a Hanning window. With a larger number of transmit channels, there is more energy, which is not only concentrated at the peaks, but also within the side-lobes of the impulse response. Obviously, the higher amount of energy at these sidelobes has also an impact on the *ISLR* for small ΔT.

SSC Waveforms

In the *ISLR*-plot of the SSC waveforms, it becomes evident that the behavior is very similar to the OFDM signals with the exception that there are no interleaved sub-carriers leading to a higher *ISLR* for observation times $> (N_{\mathrm{Tx}}-1)\tau_{\mathrm{p}}/N_{\mathrm{Tx}}$. The *ISLR* at these positions is the same as for the MSP mode. Recalling the structure of the SSC waveforms, they have always one junction in the signal spectrum due to the sub-pulse transition (cf. Fig. 3.9), and thus a total number of three jump discontinuities. Dependent on the position, which is in turn dependent on the channel index k and the total number of transmit channels, they can be more or less suppressed by windowing. In a worst case scenario, the discontinuity is centered in the middle of the spectrum (e.g. $N_{\mathrm{Tx}} = 2$, $k = 1$), because there is always the maximum of the window function and no suppression occurs. To reduce the discontinuity at the center, it is suggested to smooth the transition between start and end of the second waveform. This can be explained by the fact, that this discontinuity is caused by a step function at the junction of the two sub-chirps in time-domain at the frequency $f = B/2$.

Having a closer look at the third row in Tab. 3.1, it is indicated that no specific values can be given, since the *ISLR* is dependent on k. The best achievable values are the same as for a standard chirp, because the SSC waveform with index $k = 0$ is equal to it. As previously mentioned, the minimum *ISLR* corresponds to the index $k = 1$.

Chirp Diverse Waveforms

The Chirp Diverse waveforms show auto- and cross-correlation interferences in the impulse response plot of Fig. 3.16h, which are not only concentrated at cer-

tain positions, but are also smeared along the whole time axis. This is due to the underlying structure of this waveform type with many short sub-chirps, which interfere. Notably, high peaks in the plot with a separation of $\tau_p/8$ are an artifact of the sub-chirps, which match at certain time shifts and thus fully correlate[6]. For short observation intervals ($\Delta T < \tau_p/N_{Tx}$) the *ISLR* rises rapidly due to the large amount of interfering energy over the whole extension of the impulse response. Stepwise jumps can be explained in terms of the peaks in the impulse response in Fig. 3.16h.

In general, this waveform type has a poor *ISLR* in comparison to the other three waveform types - even for short observation intervals. Because four transmit waveforms already fill the complete available structure of the used grid of the time-frequency plane (Fig. 3.16h) on transmit; an extension to $N_{Tx} = 8$ was not possible.

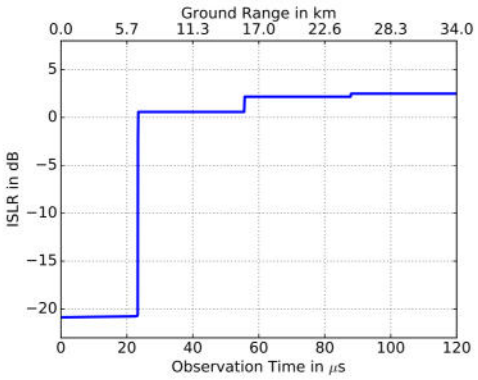
In summary, the *ISLR* characteristics are comparable between the OFDM and MSP chirps and can compete with those of a normal chirp signal. Especially the OFDM chirps show better results for a high number of transmit channels because of less cross-correlation interferences resulting from the sub-carrier spacing. The drawback in case of SSC chirps is that they may lead to pronounced sidelobes within the SAR picture, which overlay other targets with smaller RCS. The Chirp Diverse waveforms show the worst *ISLR* of all. At this point it is worth noting, that alternatively to the standard range compression, which is described in section 2.4.3, the ideal filter approach [91] can be used. This signal compression method achieves optimum results in terms of *ISLR* and *PSLR* for slightly distorted chirp-like signals at minor costs of resolution.

3.4.3. Transmit Energy

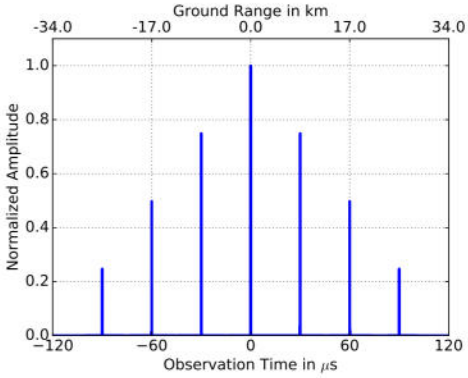
The maximum available energy is mainly limited by the resources of the satellite, by the duty cycle, and gain of the tube amplifier (power amplifier) used in the transmitter[7]. The energy of the signal $s_k(t)$ is defined as:

[6] The factor of 1/8 results from the number of individual sub-chirps in time domain of a whole transmit waveform.

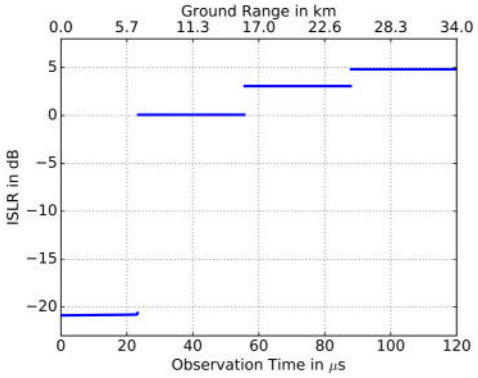
[7] Referring to section 2.3, the *PRF* is given by the geometry and azimuth resolution. Due the fact that the radar can not transmit and receive at the same time, the pulse duration determines also the maximum swath width.



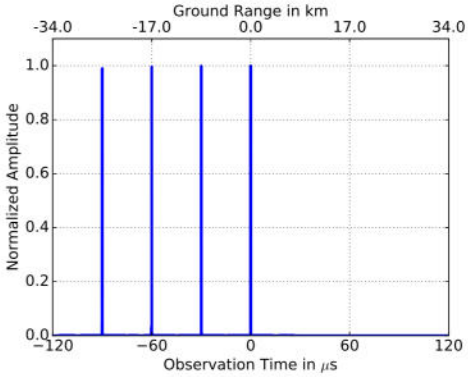
(a) *ISLR* of the OFDM waveform type.



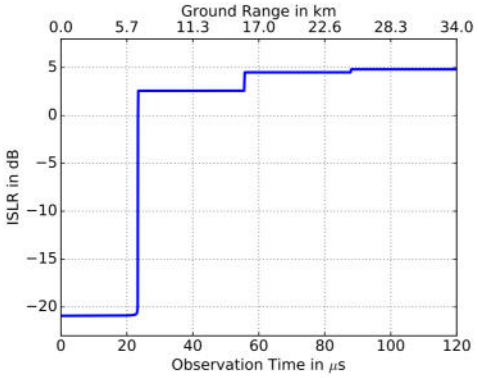
(b) Impulse response of the OFDM waveform type.



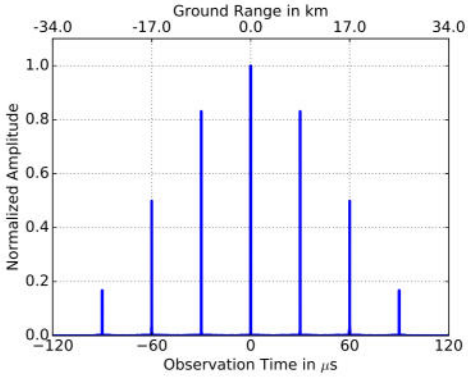
(c) *ISLR* of the MSP waveform type.



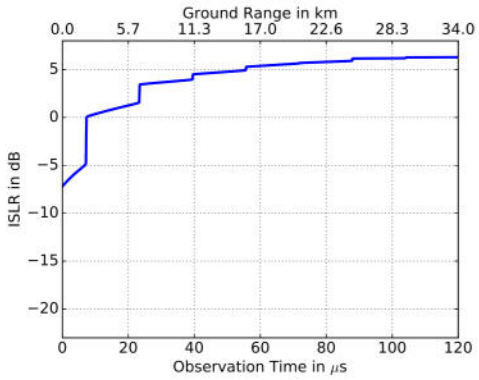
(d) Impulse response of the MSP waveform type.



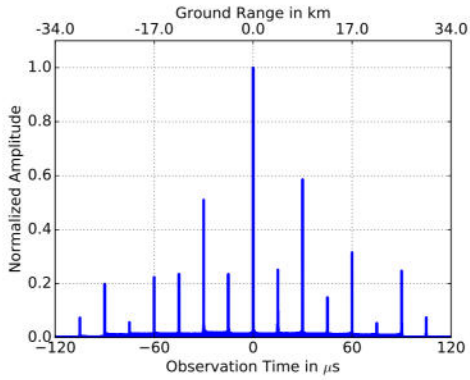
(e) *ISLR* of the SSC waveform type.



(f) Impulse response of the SSC waveform type.



(g) *ISLR* Chirp Diverse waveform.



(h) Impulse response Chirp Diverse waveform.

Figure 3.16. Integrated sidelobe ratios (Eq. (3.31)) with corresponding impulse responses of different waveforms with $B = 300$ MHz, $\tau_p = 120\ \mu$s, $N_{Tx} = 4$ and Hanning windowing. The upper abscissa axis of the impulse response plots is related to the geometrical positions of the interferences on the ground, while the following parameter were used: $\Theta \approx \Theta_{tilt} = 28.5°$ and $h = 700$ km.

$$E_k = \int_{-\infty}^{\infty} |s_k(t)|^2 \, \mathrm{d}t, \tag{3.32}$$

which is in turn the auto-correlation (zero lag) of the transmit signal function. Especially for the aforementioned signal types, the energy is independent of k, because in a set of waveforms $\boldsymbol{s}(t)$, each chirp shares the same (sub-)pulse duration. To have a common basis for later illustrative spaceborne case studies, we define that the overall transmit signal energy is the same for every waveform type. As a consequence, the signal peak-power must be adopted. Next, we give expressions for the signal energy of the waveform types individually.

OFDM Chirps, SSC Chirps and Chirp Diverse Waveforms

For rectangular pulses, the transmitted signal energy is simply the product of pulse duration and amplitude. In case of the OFDM, SSC and Chirp Diverse waveforms, the total signal energy is given by

$$E_{\mathrm{tot}} = A_{\mathrm{out}} \cdot \tau_{\mathrm{p}} \cdot N_{\mathrm{Tx}}. \tag{3.33}$$

A_{out} is the constant signal Root-Mean-Square (RMS) power flux at the output of the transmit amplifier in the last amplifier stage.

MSP Mode

By requiring that the total amount of transmit energy is equal for the OFDM, MSP and SSC waveforms, the expression for the MSP signals with arbitrary gaps between the sub-pulses can be written as

$$E_{\mathrm{tot}} = A_{\mathrm{out}} \cdot A_{\mathrm{amp}} \cdot \tau_{\mathrm{sub}} \cdot N_{\mathrm{Tx}}, \tag{3.34}$$

where A_{amp} is an additional amplification factor, defined as

$$A_{\mathrm{amp}} = \frac{\tau_{\mathrm{p}}}{\tau_{\mathrm{sub}}}, \tag{3.35}$$

which is a direct result of comparing Eq. (3.33) and Eq. (3.34). It turns out, that in the MSP mode we need an amplifier, which can handle a higher peak power, because $\tau_{\mathrm{sub}} < \tau_{\mathrm{p}}$. A possible advantage of using negative values for τ_{s} is that the chirp signals will overlap and more power can be transmitted within a shorter time interval.

3.4.4. Doppler Tolerance

In SAR and GMTI it is necessary to have a unique relation between time (slow-time) and Doppler frequency. Otherwise after range and azimuth compression, targets would appear additionally multiple times as ambiguities in the SAR image. However, this requirement is not fulfilled for the suggested STSO waveforms, as becomes evident in Fig. 3.14. For reasons of plausibility, it is at least mandatory to have a unique relation within the area of interest.

An approximation for the Doppler bandwidth of a SAR sensor is $\Delta f_{\mathrm{Dop}} \approx v_{\mathrm{E}}/\delta_{\mathrm{sa}}$ [14]. A low Earth orbit satellite, like TerraSAR-X has a ground velocity of around

7000 m/s. Under assumption of an azimuth resolution of 1.0 m, the Doppler bandwidth will be $\Delta f_{\mathrm{Dop}} \approx 7.0$ kHz. Moving targets (cars, ships, ...) generate obviously lower Doppler frequency shifts. This means that the waveforms must be orthogonal at least for Δf_{Dop} plus an additional margin. As we can see in the AF plots of the MSP and SSC signals (Fig. 3.14), their Doppler tolerance is $B/N_{\mathrm{Tx}} - 2\epsilon$. Since the signal bandwidths are typically some tens or hundred MHz, even for a large number of transmit signals they can be assumed as being completely orthogonal. The cross-correlation interferences of the Chirp Diverse waveforms are randomly distributed in the AF plot, which leads to the conclusion, that this waveform type is generally not suitable for HRWS MIMO-SAR applications.

In regard of Doppler shifts, a significant drawback of the OFDM signals is the interleaving behavior of the sub-carriers. Due to the small separation, which is given by Δf (Eq. (3.9)), just a small Doppler bandwidth and hence a low azimuth resolution can be tolerated. Since every sub-carrier is described by a sinc-function, in the ideal case, the first null of such a sinc-function should be at the maximum of the next sinc-function, as illustrated in Fig. 3.5. In SAR applications, due to the moving scene, the individual sub-carriers are shifted. This means they are not orthogonal anymore and lead to interferences between the signals. In order to analyze the amount of interference, the Inter-Carrier-to-Interference (ICI) ratio has been defined. It is the ratio between the power of an arbitrary reference sub-carrier and the total power of the interfering sub-carriers at this frequency. A plot of this ratio can be found in Fig. 3.17 with respect to the Doppler frequency normalized to the sub-carrier spacing ($\Delta f_{\mathrm{Dop}}/\Delta f$). For example, for a signal duration of $\tau_{\mathrm{p}} = 100$ μs, we get $\Delta f = 10$ kHz (see Eq. (3.9)). If the established value of a maximum Doppler tolerance of $1/10\Delta f$ is taken from literature, the maximum Doppler bandwidth, which can be accepted must be lower than 1 kHz in our example. It turns out that this value is significantly lower than the required limit of 7.0 kHz and the sub-carrier will strongly interfere. Since these interferences effect directly the *SNR* of the MIMO-SAR product (compare [41]), this value is definitely not acceptable. Generally, OFDM is used in communication, where information is exchanged and coding techniques for error control can be applied. In such applications, this interference ratio is mostly sufficient. However, to guarantee MIMO-SAR operation, an optimum interference suppression of at least 30 dB (ICI), the maximum Doppler tolerance is just $1/17\Delta f$ (this stands also in agreement with [82]). Finally, OFDM is just applicable in a limited way for

MIMO-SAR. At this point it is also worth noting, that an alternative solution for lowering the ICI has been suggested in [9], which can be used if no moving targets are in the observed area. The approach may also cope with moving targets if independent displaced phase centers in azimuth are used (cf. section 2.4.2), however this is not yet proven.

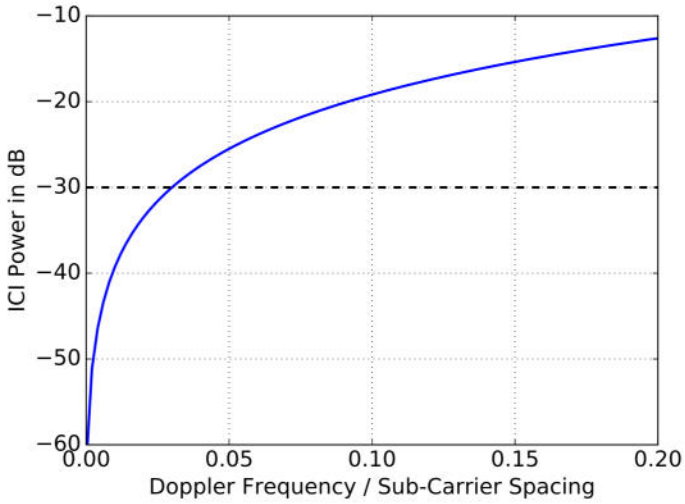


Figure 3.17. Inter-carrier-to-interference ratio with respect to the Doppler frequency normalized to the sub-carrier spacing ($\Delta f_{\mathrm{Dop}}/\Delta f$). The dotted line indicates the required ICI ratio.

3.4.5. Practical Implementation

Nowadays the generation of arbitrary waveforms with digital hardware is not an issue, however difficulties arise in post-processing. Due to a limited data rate from the satellite to the ground station, it is necessary to pre-process the received raw-data already on-board. While the MSP and SSC waveforms can be processed in real-time on-board of the satellite with the algorithm suggested in the next chapter, the OFDM chirp signals need an elaborate processing procedure for signal separation [9] (the approach is also summarized in section 4.6). Especially, the calculation of the DFT on-board of the satellite would be a significant drawback of the OFDM chirp waveforms. Therefore it is recommended to stream the data directly after the receive DBF process to the ground and to apply the DFT on ground. The proposed processing strategy for the Chirp Diverse waveforms by W. Q. Wang is a simple range compression with the respective transmit signal [73]

that does not require multiple receive channels. Accordingly the raw data can be completely processed on ground. It turns out, that this is a significant advantage of this waveform type, although it results in strong interferences.

3.4.6. Maximum Number of Transmit Signals

The maximum number of transmit signals is limited by the following aspects:

- The Doppler tolerance, which degrades linearly with the number of transmit signals.
- The available data rate, which can be streamed from the A/D converters to the memory and the maximum available memory itself. This occurs due to the limited data rate between satellite and ground station, a pre-processing for data reduction on-board of the satellite becomes mandatory. For that purpose, at least the transmit channels must be split up first, thereby leading to a N_{Tx}-times increased data rate.
- In dependence of the application and also the hardware implementation of the transmit channels (e.g. multiple transmit channels use a single hardware channel), the number of realized parallel hardware channels increases. Hence, not only the system complexity increases, but also the weight.
- A satellite has just a limited amount of available energy, which is delivered by solar panels. Since this energy must be shared by all transmit channels, N_{Tx} can not be increased arbitrarily while keeping the same average transmit power.
- Taking a constant pulse duration / duty cycle into account, with increasing number of transmit signals, the separation between the signal ambiguities decreases, which have to be suppressed by a certain DBF procedure. To synthesize a narrower antenna beam for suppression, a larger antenna is necessary, while for avoidance of grating lobes within the scene, also the number of receive channels must be increased.

In general, the overall system complexity and amount of data increases for every additional transmit channel. Depending on the available resources, the maximum number of N_{Tx} can be chosen.

3.4.7. Summary

The following table shows a summary of the aforementioned performance parameters for waveform analysis. At this stage, no statement about the *ISLR* can be made, because it is dependent on the signal processing and the number of waveforms. A choice for the best waveform type can also not be made, because this is dependent on the specific system specifications and requirements. However, it already seems evident that the Chirp Diverse waveforms and the OFDM signals can not compete with the MSP and SSC waveforms. As a consequence, they will play no role in the rest of the thesis.

Table 3.2. Overview of the waveform comparison.

Parameter/Waveform	**OFDM**	**MSP**	**SSC**	**Chirp Diverse**
Range Resolution	$w_{\text{win}}c/(2B)$	$w_{\text{win}}c/(2B)$	$w_{\text{win}}c/(2B)$	$w_{\text{win}}c/(2B)$
RMS Power Flux	A_{out}	$A_{\text{out}} \cdot \tau_{\text{p}}/\tau_{\text{sub}}$	A_{out}	A_{out}
Doppler Tolerance	$1/17\Delta f$	$B/N_{\text{Tx}} - 2\epsilon$	$B/N_{\text{Tx}} - 2\epsilon$	–
Practical Implementation	-	+	+	+

4. Elevation Beam-Forming and Waveform Separation

Especially for Moving Target Indication (MTI) in multichannel SAR systems, Space Time Adaptive Processing (STAP) plays an important role to extract information about moving targets within the observed scene [92]. Under the assumption, that the relation between Doppler spectrum and Angle of Arrival (AoA) of the receive signal is unique within a range cell, using STAP it is possible to determine the velocities and simultaneously the positions of moving objects.

In this thesis, we are not focusing on MTI, but the idea of exploiting additional information from the AoA is very useful. With the known geometrical relationship between the MIMO-SAR sensor and the observed area, a high-gain and narrow receive antenna beam can be synthesized via DBF, which tracks the pulse echo on the ground [28]. This spatial filter, also known as SCORE (cf. section 2.4.1), not only increases the *SNR* and suppresses range ambiguities, it can be also be designed to filter dedicated parts of the receive signal. With the Short-Term Shift-Orthogonal (STSO) signal types, which have been examined in the previous chapter, for the receive signal a unique relationship between the instantaneous signal frequency and the AoA in dependency on the time can be derived. If the receive signal is accordingly filtered in time, frequency and space (AoA), theoretically a perfect separation of the transmit waveforms can be ensured. The so introduced innovative concept and approach will be named Space Time Frequency Adaptive Processing (STFAP). Obviously, this frequency-variant and time-variant DBF algorithm needs high computational power. Hence, the content of this chapter is not only dedicated to the derivation of this frequency-variant and time-variant DBF algorithm, but also to its practical implementation on-board in real time.

This chapter is structured as follows. Since the waveform separation is applied on each echo window separately, in the first section, a simplified signal model based on the model from section 2.2 is introduced. In the second section, antenna requirements in terms of antenna size and number of elements for STSO

waveform separation are derived. Then the SCORE technique for a single transmit waveform is derived in detail, with special focus on the radar pulse extent due to the finite (i.e. non-vanishing) pulse duration [75]. Also, a concept for a hardware implementation of SCORE via a filter bank consisting of Finite Impulse Response (FIR) filters is presented. In the fourth and fifth section one of the major contributions of this chapter can be found: The STFAP algorithm for separation of the Multiple Sub-Pulse (MSP) and Segmentally-Shifted Chirp (SSC) waveforms. Since the processing scheme for the OFDM chirps is already detailed in [9], section 4.6 briefly summarizes this approach.

4.1. Adaption of the MIMO-SAR Signal Model for Waveform Separation Techniques

The separation process of the STSO waveforms is done for each set of transmitted pulses within one *PRI* separately. Because we focus only on the STFAP algorithm itself, we can simplify the common signal model from section 2.2. Based on this model, the so-called steering matrix is derived, which serves for the later calculation of the required DBF weights. The equation of the receive signal from Eq. (2.19) is repeated here:

$$\begin{aligned} u_i(\acute{t},t) = \Bigg[\int_{\boldsymbol{p}} \sum_{k=0}^{N_{\mathrm{Tx}-1}} & \overline{a}_{k,i}(\acute{t},t,\boldsymbol{p}) \cdot C_{\mathrm{Tx},k}\left(\Theta(\boldsymbol{p}),\phi(\boldsymbol{p})\right) \cdot C_{\mathrm{Rx},i}\left(\Theta(\boldsymbol{p}),\phi(\boldsymbol{p})\right) \cdot \sigma_{\kappa}^{0}(\boldsymbol{p}) \\ & \cdot h_{\mathrm{el},k,i}(\acute{t},t,\boldsymbol{p}) * h_{\mathrm{az},k,i}(\acute{t},t,\boldsymbol{p})\, d\boldsymbol{p} + n(\acute{t},t) \Bigg] \cdot \exp\left(-\mathrm{j}\omega_0 t\right). \end{aligned} \tag{4.1}$$

$\overline{a}_{k,i}$ is an amplitude factor accounting for free-space losses and channel imbalances, $C_{\mathrm{Tx},k}$ and $C_{\mathrm{Rx},i}$ are the transmit and receive antenna pattern respectively, σ_{κ}^{0} is the differential target scattering coefficient, $h_{\mathrm{el},k,i}$ and $h_{\mathrm{az},k,i}$ are the channel impulse responses in elevation and azimuth, and n is Additive White Gaussian Noise (AWGN).

To adapt the MIMO-SAR signal model for STFAP, the following assumptions are required:

- The DBF weights, which are calculated via the STFAP algorithm, are independent of the amplitude of the receive signal (non-adaptive DBF). Hence it is valid to neglect free-space losses and channel imbalances in further context $\Rightarrow \overline{a}_{k,i} = 1 \; \forall \, k, i$.
- The separation process of the proposed STSO waveforms from chapter 3 is done for each echo window individually. This allows to ignore the azimuth components of the signal model[1] $\Rightarrow \acute{t} = 0$. Accordingly, the channel impulse response along azimuth is constant over time and equal for all channels $\Rightarrow h_{\mathrm{az},k,i}(\acute{t}, t, \boldsymbol{p}) = 1 \; \forall \, k, i, \acute{t}, t$.
- Noise is assumed to be AWGN and, therefore, we use the same variable n for the noise after down-conversion to the base-band.

Under these aspects, the expression of the received raw data from Eq. (4.1) can be simplified to

$$\breve{u}_i(t) = \int_{\Theta} \sum_{k=0}^{N_{\mathrm{Tx}}-1} C_{\mathrm{Tx},k}(\Theta) \cdot C_{\mathrm{Rx},i}(\Theta) \cdot \widehat{\sigma}^0_{\kappa}(\Theta) \cdot s_k(t - \tau_{k,i}(\Theta)) \, \mathrm{d}\Theta + n(t). \tag{4.2}$$

The stress $\breve{}$ above u_i is used to indicate that the slow-time along azimuth is not used in this form. $\widehat{\sigma}^0_{\kappa}$ is an equivalent scattering amplitude, which is equal to the sum of all σ^0_{κ} over the angles ϕ and weighted by the joint Tx-Rx antenna pattern.

In DBF literature, it is common to use vector notation. Hereupon we follow this practice and express the time-delayed transmit signal $s_k(t - \tau_{k,i})$ as a product of the initial transmit signal $s_k(t)$ and a steering matrix (Eq. (4.8)) for the time shift. This steering matrix is related to the specific side-looking SAR geometry, where each point on the ground is seen under a different look angle (cf. Fig. 4.1). Any dependency of the Angle of Arrival (AoA) in azimuth direction is neglected[1].

[1] In fact, there is a dependency along azimuth, because there is a misalignment between the iso-range lines and the projected antenna pattern on ground. A solution for this problem, named *Cross Elevation Beam Range Ambiguity Suppression*, was proposed in [29]. This technique is based on adapting the elevation DBF weights with respect to dedicated sub-bands in azimuth and can be seen as an add-on to STFAP.

Therefore for a known topography, there is a fixed relation between Time of Arrival (ToA) and AoA. The AoA ϑ_k for each point can then be calculated as:

$$\widehat{\vartheta}_k(t) = \widehat{\Theta}_k(t) - \Theta_{\text{tilt}}, \tag{4.3}$$

with Θ_{tilt} being the antenna tilt angle versus nadir[2]. Because each transmit waveform can be shifted in time, the AoA changes too. Hence the AoA is defined for each transmit waveform with index k individually. Taking a spherical Earth model, the receive signal, which is received at the time instant t, corresponds to the angle [28]:

$$\Theta(t) = \arccos\left(\frac{4\cdot(R_{\text{E}}+h)^2 - 4\cdot R_{\text{E}}^2 + t^2\cdot c^2}{4\cdot(R_{\text{E}}+h)\cdot t\cdot c}\right), \tag{4.4}$$

while we note $\widehat{\Theta}_k(t) = \Theta(t-\tau_{k,i})$.

With reference to section 4.2.2, for DBF-SAR it is valid to assume a narrow antenna element spacing with respect to the signal's wavelength[3]. Hence the delay of the receive signal between two adjacent antenna elements can be expressed in form of a phase delay $\Delta\varphi_k$. With the known relation between instantaneous wavelength and frequency of the k-th transmit waveform: $\lambda_k(t) = c/f_k(t)$, for an Uniform Linear Array (ULA), $\Delta\varphi_k$ can be expressed by the separation d between two adjacent elements through

$$\begin{aligned}\Delta\varphi_k(t,\Theta) &= 2\pi f_k(t)\cdot(\tau_{k,0}(\Theta)-\tau_{k,1}(\Theta)) = \frac{2\pi}{\lambda_k(t)}(r_{k,0}(\Theta)-r_{k,1}(\Theta))\\ &= \frac{2\pi}{\lambda_k(t)}\cdot d\cdot\sin(\Theta_k(t)-\Theta_{\text{tilt}}) = \frac{2\pi}{\lambda_k(t)}\cdot d\cdot\sin\left(\widehat{\vartheta}_k(t)\right).\end{aligned} \tag{4.5}$$

This phase delay is used for the terms

$$z_k(t,\Theta) = \exp(\mathrm{j}\cdot\Delta\varphi_k(t,\Theta)), \tag{4.6}$$

[2]Considering the geometrical relationship between antenna array and target scene, the AoA is assumed to be the same for all elements: $\vartheta_{k,i} \approx \vartheta_k \;\forall\, i$.

[3]If the antenna element spacing is so large, that the condition $\left|\tau_{k,0}(\Theta)-\tau_{k,1}(\Theta)\right| \geq \lambda_0/c$ applies, true time-delay beam-forming [93] must be used.

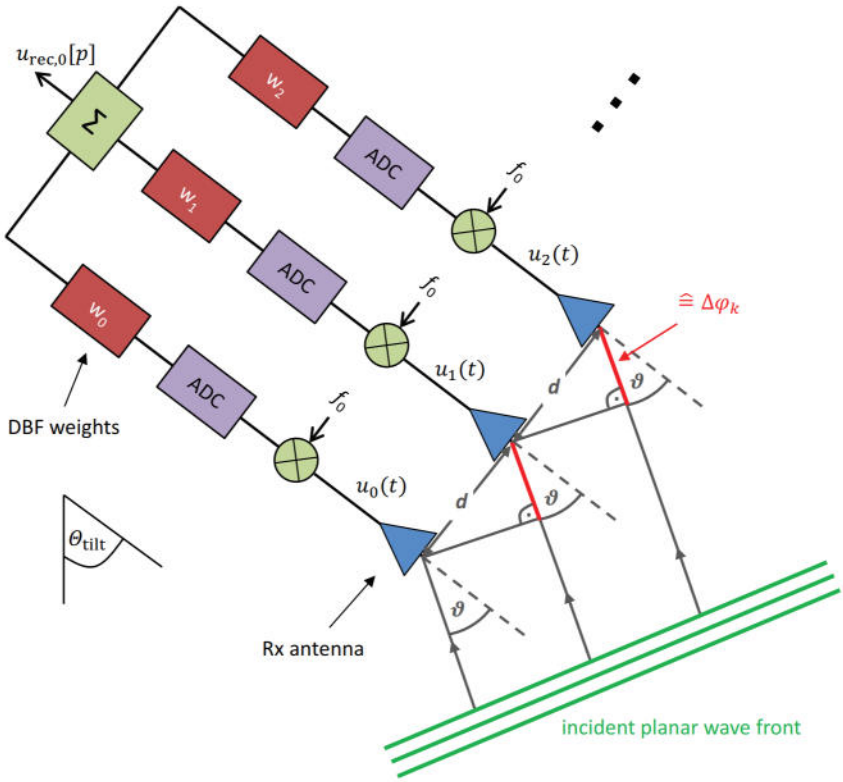


Figure 4.1. A planar wave incident at the antenna array with element separation d. In dependence on the AoA, between each two adjacent receive channels the same phase delay can be observed. After down-conversion and A-D conversion, the DBF weights are applied on each receive channel and the output signals are summed up.

which are used in turn for the DBF steering vectors:

$$\boldsymbol{a}_k(t,\Theta) = \left[z_k^0, z_k^1, ..., z_k^{N_{\mathrm{Rx}}-1}\right]^{\mathrm{T}}. \tag{4.7}$$

The transmit-channel dependent vectors are used for calculating the DBF weights in the next sections and can be summarized in a transposed Vandermonde matrix of shape:

$$\boldsymbol{A}(t,\Theta) = \left[\boldsymbol{a}_0, \boldsymbol{a}_1, ..., \boldsymbol{a}_{N_{\mathrm{Tx}}-1}\right]. \tag{4.8}$$

Finally, the receive signal from Eq. (4.2) is written in vector notation:

$$\breve{\boldsymbol{u}}(t) = \int_{\Theta} \widehat{\sigma}_{\kappa}^{0}(\Theta) \cdot \boldsymbol{C}_{\mathrm{Rx}}(\Theta) \odot \Big(\boldsymbol{A}(t,\Theta) \cdot [\boldsymbol{C}_{\mathrm{Tx}}(\Theta) \odot \boldsymbol{s}\left(t - \tau_{0,0}(\Theta)\right)] \Big) \mathrm{d}\Theta + \boldsymbol{n}(t), \quad (4.9)$$

where $\odot$ stands for the Hadamard product and the antenna pattern of the individual elements are arranged in vectors:

$$\boldsymbol{C}_{\mathrm{Tx}}(\Theta) = \begin{bmatrix} C_{\mathrm{Tx},0}(\Theta) \\ C_{\mathrm{Tx},1}(\Theta) \\ \vdots \\ C_{\mathrm{Tx},N_{\mathrm{Tx}}-1}(\Theta) \end{bmatrix} \quad (4.10)$$

and

$$\boldsymbol{C}_{\mathrm{Rx}}(\Theta) = \begin{bmatrix} C_{\mathrm{Rx},0}(\Theta) \\ C_{\mathrm{Rx},1}(\Theta) \\ \vdots \\ C_{\mathrm{Rx},N_{\mathrm{Rx}}-1}(\Theta) \end{bmatrix}. \quad (4.11)$$

DBF is based on the steering matrix $\boldsymbol{A}$. Due to its dependency on the three dimensions λ_k, Θ and t, these values are of high importance for the following STFAP concept. Before we attend to this complexity, in the next section, we define requirements on the receive antenna.

4.2. Antenna Design Requirements

As previously mentioned, each transmit antenna illuminates the whole swath uniformly within the *HPBW* and no beam-forming on transmit is applied. Because this is no special condition, standard SAR antenna design techniques can be used for the transmit case [14]. The same goes with the length of the receive antenna in azimuth direction, which is determined by the system's maximum achievable azimuth resolution (cf. section 2.1).

In state-of-the-art SAR applications, the antenna size in elevation is set to illuminate the whole swath in elevation direction uniformly (within the *HPBW*).

However, it is known, that due to the side-looking geometry, at certain instants of time, the echo signal is just received from a narrow angular interval. This valuable information is used for the SCan On REceive (SCORE) technique (section 2.4.1, [28]). In SCORE, a narrow receive beam, formed via DBF, tracks the echo which travels over the ground. Accordingly, it is valid to reduce the *HPBW* of the receive antenna significantly, thereby increasing the total antenna gain due to its increased aperture. However, there are boundary conditions, which have to be taken into account. In this section we will define the total antenna size in elevation and the number of elements to obtain optimum results for DBF-SAR and MIMO-SAR.

4.2.1. Optimum Size in Elevation

The aim of STFAP is to steer the maximum of the antenna main-lobe to the wanted signal and the nulls of the beam-pattern to ambiguities resulting from orthogonal waveforms. According to the last chapter, the STSO waveforms of repeating structure have a unique relationship between angle, time and frequency. Without restriction of generality, we can assume that transmit signal 1 is the wanted signal and transmit signal 2 is the unwanted ambiguity. If the antenna is steered such that the maximum pattern is directed to Θ_1 corresponding to the instantaneous frequency f_1 of transmit signal 1, then it is necessary to place a null at the same frequency of transmit signal 2 in order to provide sufficient suppression. This is visualized in Fig. 4.2 at a certain instant of time for the waveform types OFDM-Chirp waveforms, Multiple Sub-Pulses (MSP) and Segmentally-Shifted Chirp (SSC) waveforms (cf. sections 3.2.2 – 3.2.4). As can be seen, a novel approach lies in the fact that the antenna requirements are equal for all three waveforms, if the MSP signals are contiguously transmitted ($\tau_s = 0$).

To determine the necessary antenna null-to-null pattern-width (also known as Null Beam-Width: *NBW*) and hence the antenna size in elevation, we follow the approach by making use of the pulse extent. Because each transmitted pulse has a certain duration, hence on receive, at a certain instant of time the received signal is backscattered from an angular sector. As shown in Fig. 4.3, if the leading edge of the pulse passes a certain point at an arbitrary time instance t_0, then the lagging edge will pass the same point $t_0 + \tau_p$ seconds later. On receive, at any time delay τ, the echo at the phase center of each antenna element arrives

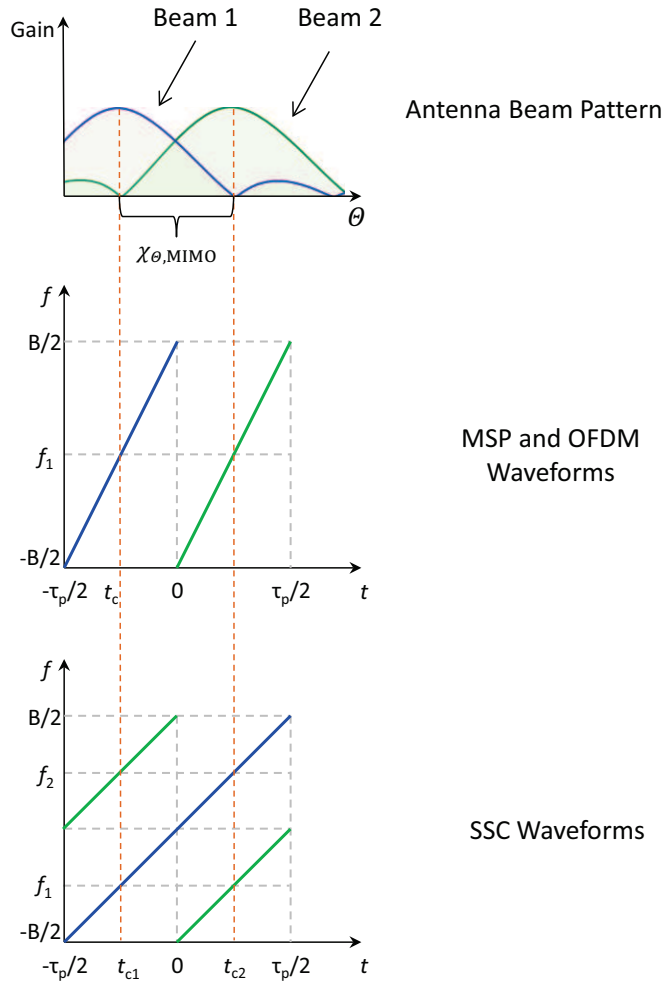


Figure 4.2. Suppression of the signal ambiguities of STSO waveforms with the antenna beam pattern shown for a certain instant of time.

simultaneously from all points located at distances between $2r_2/c$ and $2r_1/c$. This yields the slant range extent of

$$\chi_\rho = \frac{\tau_\mathrm{p} \cdot c}{2}. \tag{4.12}$$

This extent can be projected to the ground and according to [75], the angular pulse extent (cf. Fig. 4.3) for a spherical Earth in dependence of the steering angle and the pulse duration is

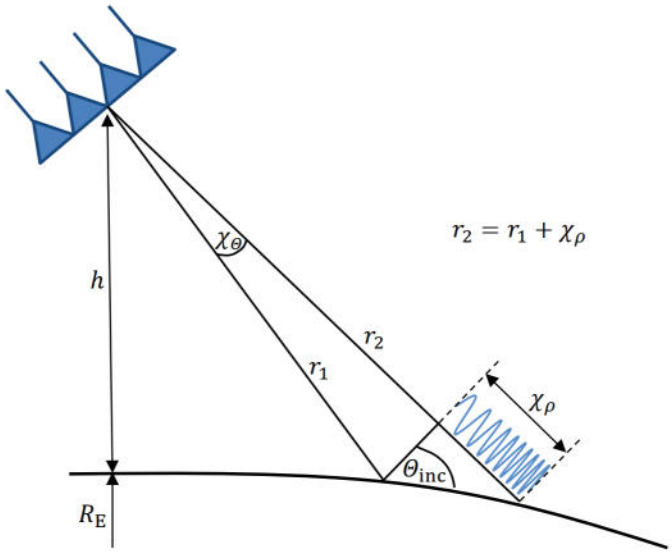


Figure 4.3. Illustration of the radar pulse extent. Due to the pulse duration τ_p at an arbitrary time instance, the echo is received from an angular section simultaneously.

$$\chi_\Theta(\Theta) = \frac{\chi_\rho}{(R_E + h) \cdot \left(\frac{(R_E+h)\cdot\cos(\Theta)}{\sqrt{R_E^2 - ((R_E+h)\cdot\sin(\Theta))^2}} - 1 \right) \cdot \sin(\Theta)}. \tag{4.13}$$

In Fig. 4.4 we can see the course of the angular pulse extension for the typical case of pulse durations $\tau_p = 80\ \mu s$, $100\ \mu s$, $120\ \mu s$, $140\ \mu s$, and $160\ \mu s$ and an orbit height of $h = 700$ km. As expected, χ_Θ reduces for higher steering angles.

As aforementioned, the *NBW* must be set to suppress the overlapping transmit waveforms. Since it is known, that in Eq. (4.13) the time between the leading and the lagging edge of the pulse is τ_p, substitution of the pulse duration by the time between equal frequencies of two waveforms (Fig. 4.2) gives the unambiguous angular sector. Therefore the slant range extent χ_ρ in Eq. (4.13) must be replaced by the unambiguous observed pulse interval χ_{MIMO}:

$$\chi_{\text{MIMO}}(\Theta) = \left(\frac{\tau_p}{N_{\text{Tx}}} - \epsilon \right) \cdot \frac{c}{2}. \tag{4.14}$$

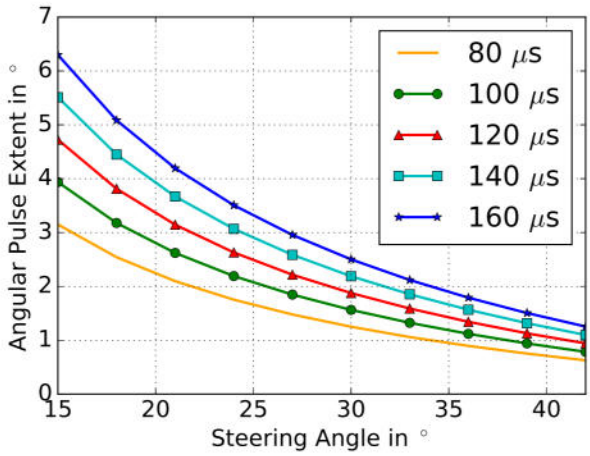


Figure 4.4. Angular pulse extent in dependence of the steering angle for the pulse durations $\tau_p = 80\ \mu s$, $100\ \mu s$, $120\ \mu s$, $140\ \mu s$ and $160\ \mu s$ and an orbit height of $h = 700$ km.

This equation results from the fact that the STSO waveforms of total duration τ_p show repeating characteristics after integer multiples of the delay τ_p/N_{Tx}. The term ϵ is an additional margin, which has been introduced in Eq. (3.2) and ensures orthogonality also at the edges of the waveforms. Therefore, for the angular extent of the unambiguous swath, we can write:

$$\chi_{\Theta,\mathrm{MIMO}} = \frac{\chi_{\mathrm{MIMO}}}{(R_E + h) \cdot \left(\frac{(R_E+h)\cdot\cos(\Theta)}{\sqrt{R_E^2 - ((R_E+h)\cdot\sin(\Theta))^2}} - 1 \right) \cdot \sin(\Theta)}. \tag{4.15}$$

$\chi_{\Theta,\mathrm{MIMO}}$ is also depicted in Fig. 4.2 as the width between the maximum of the antenna main lobe and the first null. Consequently, the null-to-null pattern-width must be

$$NBW = 2 \cdot \chi_{\Theta,\mathrm{MIMO}}. \tag{4.16}$$

While the receive antenna with N_{Rx} elements of equal spacing d has a total height of

$$l_{\text{ant,el}} = N_{\text{Rx}} \cdot d, \tag{4.17}$$

the null-to-null pattern-width without amplitude tapering will be [17][4]:

$$NBW = 2 \cdot \arcsin\left(\frac{\lambda}{N_{\text{Rx}} \cdot d}\right). \tag{4.18}$$

Insertion of Eq. (4.17) into Eq. (4.18), followed by setting equal Eq. (4.18) and Eq. (4.16), and rearranging the terms, leads to:

$$l_{\text{ant,el}} = \frac{\lambda_0}{\sin(\chi_{\Theta,\text{MIMO}})}. \tag{4.19}$$

The required antenna size in elevation is obviously dependent on the steering angle Θ. However, as we will show in the next sections, with DBF it is possible to broaden the *NBW* and to increase the physical antenna size in elevation without any difficulties. However, what remains is the lower limit of the size and we define for the minimum antenna height[5]:

$$l_{\text{min}} \geq \frac{\lambda_0}{\min\{\sin(\chi_{\Theta,\text{MIMO}})\}}. \tag{4.20}$$

Fig. 4.5 shows a plot of l_{min} for $N_{\text{Tx}} = 2$, $\epsilon = 0$ and $h = 700$ km as function of the pulse duration and the steering angles $\Theta = 15°, 25°, 35°, 42°$. It can be observed, that for longer pulse durations, the minimum antenna size in elevation becomes shorter. Since reasonable antenna heights can only be achieved for long pulse durations, we have to keep in mind that from a practical point of view, a duty cycle (ratio between pulse duration and pulse repeat interval) of more than 20 % will be impractical.

[4]This equation just holds for isotropic radiating antenna elements, which are fed in-phase (antenna beam is steered to the bore-site). Since for DBF usually antennas of small aperture and wide *HPBW* are used and since the beam broadening effect is small for reasonable steering angles ($\vartheta = \pm 14°$), both deviations can be neglected.

[5]In [41] an approximation for l_{min} is given. A cross check to Eq. (4.20) led to the same results.

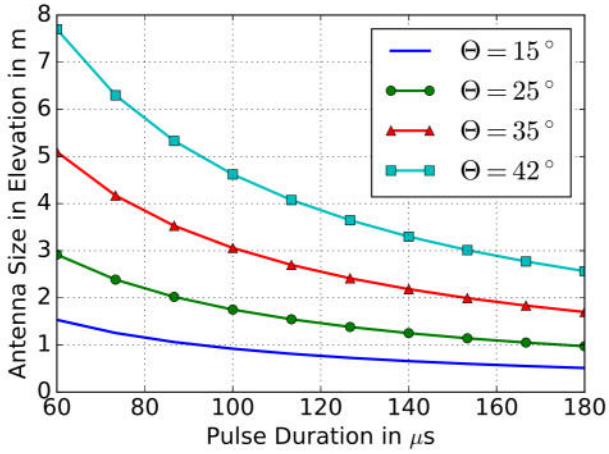


Figure 4.5. Minimum antenna size in elevation to separate the STSO waveforms as function of the pulse duration and steering angles $\Theta = 15°, 25°, 35°, 42°$; $\lambda = 3.16$ cm, $N_{\mathrm{Tx}} = 2$, $\epsilon = 0$ and $h = 700$ km.

4.2.2. Minimum Number of Antenna Elements

To determine a value for the minimum number of receive antenna elements, we have to consider the issue of element spacing for an antenna array of fixed length. Using the assumption of footnote 4 on page 113, according to [18], for element spacings $d > \lambda/2$ ambiguities, or so-called grating lobes, occur with an angular separation of

$$\Theta_{\mathrm{ambig}} = \arcsin\left(\frac{\lambda}{d} - 1\right) = \arcsin\left(\frac{N_{\mathrm{Rx}} \cdot \lambda}{l_{\mathrm{ant,el}}} - 1\right). \tag{4.21}$$

It is important to note that the grating lobes need not necessarily lie outside the illuminated swath. With an approximate knowledge of ToA and AoA, during signal processing implausible echo positions can be easily excluded. However, to enable more degrees of freedom in case of possible advanced operation modes, it is recommended to set Θ_{ambig} equal to the angular section of the whole swath.

Solving Eq. (4.21) for N_{Rx}, the minimum number of receive antenna elements is given by

$$N_{\mathrm{Rx,min}} \geq \left\lceil \frac{l_{\mathrm{ant,el}} \cdot [\sin(\Theta_{\mathrm{ambig}}) + 1]}{\lambda} \right\rceil, \tag{4.22}$$

while $\lceil\ \rceil$ denotes the ceiling function.

A typical antenna length of $l_{\mathrm{ant,el}} = 4.0$ m, a signal wavelength of $\lambda = 3.16$ cm and a swath of extension from 15° to 42° ($\Theta_{\mathrm{ambig}} = 27°$) gives

$$N_{\mathrm{Rx,min}} \geq \left\lceil \frac{4.0\ \mathrm{m} \cdot [\sin(42° - 15°) + 1]}{3.16\ \mathrm{cm}} \right\rceil = 184.$$

With respect to the amount of acquired data, which has to be recorded and processed, from the current point of view this fairly large number is not very practical. If the number of digital channels must be reduced and the grating lobes must lie outside the swath, we propose a combination of analog and digital beam-steering [94].

According to Eq. (4.20) and Eq. (4.22) the design parameters of the antenna have to be chosen carefully. It is also worth noting that in case of the MSP mode and OFDM chirps only $N_{\mathrm{Tx}} - 1$ signals have to be suppressed, since there is only a single ambiguity for every transmit waveform (Fig. 4.2). This may lead to a better suppression in contrast to the SSC waveforms. On the other hand, the ambiguous energy of the other waveform in the MSP and OFDM modes has the same amount as the wanted signal before suppression (compare section 3.4.3). If a null of the antenna is not met perfectly, the contribution will be more significant than for the SSC waveforms. A more detailed analysis is given in the forthcoming sections on filtering techniques.

4.3. Digital Beam-Forming on Receive - Single Transmit Waveform

In this section, we attend to the special case of receive DBF for a single transmit channel in full details. This section does not only serve as a crucial basis for the advanced STFAP technique in the following two sections, but also covers an improved version of the SCORE technique [28] for long pulse durations and real-time implementation in hardware.

4.3.1. Time-Variant Beam-Forming

In principle, SCORE is the time-variant version of the Minimum Variance Distortionless Response (MVDR) beam-forming algorithm [95], which is also known

as Capon's method [96]. MVDR belongs to the classes of non-parametric, data dependent, adaptive and optimum beam-formers, which minimize the noise content of their input signal, while keeping the amplitude of the wanted signal constant.

If a high-gain and narrow antenna beam should be steered to the off-nadir angle $\widehat{\Theta}_0$, the phase delays $\Delta\varphi_0(t, \widehat{\Theta}_0)$ must be compensated at each receive channel (cf. Fig. 4.1). This is followed by a coherent summation of the equalized signals. To calculate the required time-variant beam-forming weights $\boldsymbol{w}_{\mathrm{Rx},0}(t, \widehat{\Theta}_0)$ in order to track the echo of the first (and in this special case the only) transmitted waveform, the optimization problem stated as follows has to be solved:

$$\begin{aligned} &\text{minimize } \boldsymbol{w}^{\mathrm{H}}_{\mathrm{Rx},0}(t, \widehat{\Theta}_0) \cdot \boldsymbol{R} \cdot \boldsymbol{w}_{\mathrm{Rx},0}(t, \widehat{\Theta}_0) \\ &\text{subject to } \boldsymbol{w}^{\mathrm{T}}_{\mathrm{Rx},0}(t, \widehat{\Theta}_0) \cdot \boldsymbol{a}_0(t, \widehat{\Theta}_0) = N_{\mathrm{Rx}}, \end{aligned} \tag{4.23}$$

while $\boldsymbol{R}$ is the noise covariance matrix:

$$\boldsymbol{R} = E\left\{\boldsymbol{n}^{\mathrm{T}} \cdot \boldsymbol{n}^{*}\right\}, \tag{4.24}$$

with E denoting the expectation value. Under the assumption of a stationary process, $\boldsymbol{n}$ is the column vector of size N_{Rx} containing the RMS noise voltages over time. It is worth noting, that in most cases the vector containing the $\boldsymbol{n}$ is unknown. However, from dedicated noise measurements of the radar system an approximate noise signal can be obtained. Using the information, that AWGN is temporally and spectrally uncorrelated, the noise covariance matrix can be rewritten as

$$\boldsymbol{R} = v^2 \cdot \boldsymbol{I}_{N_{\mathrm{Rx}}}, \tag{4.25}$$

while v^2 is the noise power and $\boldsymbol{I}_{N_{\mathrm{Rx}}}$ is the identity matrix of size $N_{\mathrm{Rx}} \times N_{\mathrm{Rx}}$.

The first row in Eq. (4.23) demands for minimizing unwanted noise contributions to increase the overall *SNR* and the second row demands for a weighting vector, which compensates the phase delays $\Delta\varphi_0(t, \widehat{\Theta}_0)$ between the receive chan-

nels. The derivation of the optimum beam-forming weights can be found in detail in [95] and in [28] and leads to the expression

$$\begin{aligned} \boldsymbol{w}_{\mathrm{Rx},0}^{\mathrm{T}}(t,\widehat{\Theta}_0) &= N_{\mathrm{Rx}} \cdot [\boldsymbol{a}_0^{\mathrm{H}}(t,\widehat{\Theta}_0) \cdot \boldsymbol{R}^{-1} \cdot \boldsymbol{a}_0(t,\widehat{\Theta}_0)]^{-1} \cdot \boldsymbol{a}_0^{\mathrm{H}}(t,\widehat{\Theta}_0) \cdot \boldsymbol{R}^{-1} \\ &= N_{\mathrm{Rx}} \cdot [\boldsymbol{a}_0^{\mathrm{H}}(t,\widehat{\Theta}_0) \cdot \boldsymbol{a}_0(t,\widehat{\Theta}_0)]^{-1} \cdot \boldsymbol{a}_0^{\mathrm{H}}(t,\widehat{\Theta}_0) = \boldsymbol{a}_0^{\mathrm{H}}(t,\widehat{\Theta}_0). \end{aligned} \tag{4.26}$$

The reconstructed receive signal $u_{\mathrm{rec},0}(t,\widehat{\Theta}_0)$ is the multiplication of the receive signal $\check{\boldsymbol{u}}(t)$ (cf. Eq. (4.9)) with the complex conjugate of the steering vector $\boldsymbol{a}_0(t,\widehat{\Theta}_0)$:

$$\begin{aligned} u_{\mathrm{rec},0}(t,\widehat{\Theta}_0) &= \check{\boldsymbol{u}}(t) \cdot \boldsymbol{w}_{\mathrm{Rx},0}(t,\widehat{\Theta}_0) \\ &= \Bigg[\int_{\Theta} \widehat{\sigma_\kappa}(\Theta) \cdot C_{\mathrm{Tx},0}(\Theta) \cdot \boldsymbol{C}_{\mathrm{Rx}}(\Theta) \\ &\quad \odot \left[\boldsymbol{a}_0(t,\Theta) \cdot s_0\left(t - \tau_{0,0}(\Theta)\right)\right] \mathrm{d}\Theta + \boldsymbol{n}(t) \Bigg]^{\mathrm{T}} \cdot \boldsymbol{a}_0^{*}(t,\widehat{\Theta}_0). \end{aligned} \tag{4.27}$$

It is known from the last section, that at a certain point of time, due to the angular pulse extent, the echo signal is received within the angular interval $[\widehat{\Theta}_0 - \chi_\Theta/2, \widehat{\Theta}_0 + \chi_\Theta/2]$. However, the antenna is steered to the angular center at $\widehat{\Theta}_0$ of the echo signal. Thus we expect either a loss of signal energy or an ineffective use of the antenna, if the antenna *HPBW* does not fit to the pulse extent. In order to analyze the distortions on the receive signal due to DBF, we assume equal and uniform transmit receive antenna pattern. For simplicity, we also assume a homogenous scattering coefficient and therefore it is possible to make use of a common weighting factor C. Then, with help of the equation for the angular pulse extent (cf. Eq. (4.13)), the integral limits of $u_{\mathrm{rec},0}(t,\widehat{\Theta}_0)$ can be set. Using Eq. (4.8) for a single transmit channel, the reconstructed signal can be written as:

$$
\begin{aligned}
u'_{\mathrm{rec},0}(t,\widehat{\Theta}_0) &= C\cdot \int_{\widehat{\Theta}_0-\chi_\Theta/2}^{\widehat{\Theta}_0+\chi_\Theta/2} \boldsymbol{a}_0^{\mathrm{T}}(t,\widehat{\Theta}_0+\Theta)\cdot \boldsymbol{a}_0^{*}(t,\widehat{\Theta}_0)\cdot s_0(t-\tau_{0,0}(\Theta)\,\mathrm{d}\Theta \\
&\quad + \boldsymbol{n}^{\mathrm{T}}(t)\cdot \boldsymbol{a}_0^{*}(t,\widehat{\Theta}_0) \\
&= C\cdot \int_{\widehat{\Theta}_0-\chi_\Theta/2}^{\widehat{\Theta}_0+\chi_\Theta/2} \sum_{i=0}^{N_{\mathrm{Rx}}-1} \exp\left[\mathrm{j}\frac{2\pi}{\lambda}\cdot i\cdot d\cdot[\sin(\widehat{\Theta}_0+\Theta)-\sin(\widehat{\Theta}_0)]\right] \\
&\quad \cdot s_0(t-\tau_{0,0}(\Theta)\,\mathrm{d}\Theta + \boldsymbol{n}^{\mathrm{T}}(t)\cdot \boldsymbol{a}_0^{*}(t,\widehat{\Theta}_0) \\
&= C\cdot N_{\mathrm{Rx}}\cdot \int_{\widehat{\Theta}_0-\chi_\Theta/2}^{\widehat{\Theta}_0+\chi_\Theta/2} \mathrm{sinc}\left\{\frac{\pi\cdot d\cdot N_{\mathrm{Rx}}}{\lambda}\cdot\left[\sin(\widehat{\Theta}_0+\Theta)-\sin(\widehat{\Theta}_0)\right]\right\} \\
&\quad \cdot s_0(t-\tau_{0,0}(\Theta))\,\mathrm{d}\Theta + \boldsymbol{n}^{\mathrm{T}}(t)\cdot \boldsymbol{a}_0^{*}(t,\widehat{\Theta}_0).
\end{aligned}
\tag{4.28}
$$

A first conclusion is the amplification factor of N_{Rx} with reference to a single receive channel if $\chi_\Theta \to 0$. For greater χ_Θ and with increasing distance from the center of the main-beam, the signal amplitude gets attenuated by the sinc-function. This degradation is of high interest and we define from this term the Pulse Extension Loss (*PEL*) [75]. For that we make use of the approximation $\sin(\widehat{\Theta}_0+\Theta)-\sin(\widehat{\Theta}_0)\approx\cos(\widehat{\Theta}_0\cdot\Theta)$ and change the integration variable to $\Theta'=\Theta-\widehat{\Theta}_0$. The *PEL* reads as

$$
\begin{aligned}
PEL(\widehat{\Theta}_0) &= \frac{1}{\chi_\Theta}\int_{\widehat{\Theta}_0-\chi_\Theta/2}^{\widehat{\Theta}_0+\chi_\Theta/2} \boldsymbol{a}_0(t,\widehat{\Theta}_0+\Theta)\cdot \boldsymbol{a}_0^{\mathrm{H}}(t,\widehat{\Theta}_0)\,\mathrm{d}\Theta \\
&\approx \frac{1}{\chi_\Theta}\int_{-\chi_\Theta/2}^{+\chi_\Theta/2} \mathrm{sinc}^2\left\{\frac{\pi\cdot d\cdot N_{\mathrm{Rx}}}{\lambda}\cdot\cos(\Theta\cdot\Theta')\right\}\mathrm{d}\Theta',
\end{aligned}
\tag{4.29}
$$

while we write $PEL^{\mathrm{dB}} = -10\log\{PEL\}$ because this value is defined as a loss. In principle, the *PEL* is the ratio of the integrated array factor of the DBF antenna pattern within the interval $[\widehat{\Theta}_0-\chi_\Theta/2,\ \widehat{\Theta}_0+\chi_\Theta/2]$ and the angular pulse extent. As can be seen in the left-hand side of Fig. 4.6, if $HPBW < \chi_\Theta$, then a signif-

icant loss occurs. In this case the higher antenna gain is compensated by the *PEL*. If $HPBW > \chi_\Theta$ (right-hand side of Fig. 4.6), obviously there will hardly be any loss, but more noise will be collected. During system design a compromise between acceptable loss and *SNR* has to be found. Exactly this behavior can also be observed in the plot of Fig. 4.7, which shows the *PEL* with respect to the ratio $HPBW/\chi_\Theta$. For a typical spaceborne SAR with two different antenna sizen in elevation ($l_{\text{ant,el}} = 1.3$ m and $l_{\text{ant,el}} = 2.5$ m) and the parameters $h = 700$ km, $f_0 = 9.6$ GHz and $\tau_\text{p} = 120$ μs, the *PEL* is plotted against ground range in Fig. 4.8. It is known, that with increasing ground range, the angular pulse extent decreases at nominally constant antenna *HPBW*. Thus, the *PEL* also decreases. Since the pulse is of finite duration, there will be always a loss.

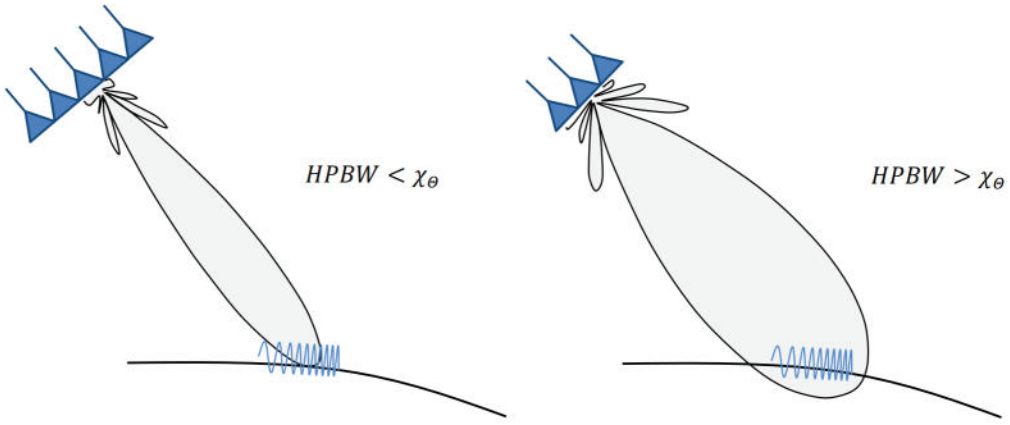


Figure 4.6. Tracking the echo via a narrow antenna beam. Left-hand side: Due to $HPBW < \chi_\Theta$ a loss occurs. Right-hand side: Due to $HPBW > \chi_\Theta$ the antenna is not effectively used.

Commonly used Approximations

To reduce the *PEL*, two solutions can be given. One solution is to shorten the antenna height by costs of the gain, while covering the whole pulse on the ground $\Rightarrow HPBW > \chi_\Theta$. Another solution is to synthetically broaden the antenna beam via frequency-variant DBF, which makes use of the frequency characteristic of the transmit signal. Under the assumption that an up-chirp or down-chirp is used, each AoA of the extended pulse on ground corresponds to a certain unique frequency component. The underlying idea, to use a broad frequency-variant antenna beam, has already been suggested in [28] and further investigated in

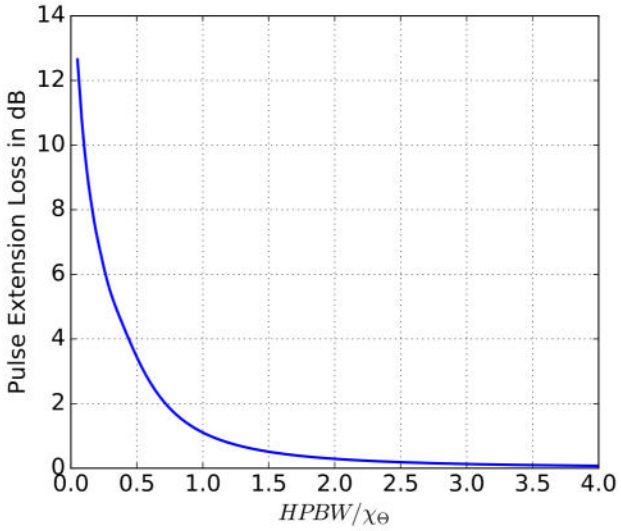


Figure 4.7. Pulse extension loss for the varying ratio $HPBW/\ \chi_\Theta$.

[97–99]. Unfortunately all of these authors made a simplification in their model, which is not valid for HRWS-SAR. It was proposed to point the time-variant antenna beam to the center of the extended pulse on the ground. Because the center corresponds only to the instantaneous center frequency f_0, all other frequencies, which are received at the same time, correspond to different AoAs. Basically, this equals the substitution of λ in the steering vectors of Eq. (4.8) by the center wavelength λ_0. The resulting phase error term was compensated for by a linear function, which gives the relationship between AoA and time. According to Eq. (4.4) the true relationship between ToA and AoA for the chirp center with respect to the ToA at the mid of the swath t_{mid} is

$$\Theta(t - t_{\text{mid}}) = \arccos\left(\frac{4 \cdot (R_{\text{E}} + h)^2 - 4 \cdot R_{\text{E}}^2 + (t - t_{\text{mid}})^2 \cdot c^2}{4 \cdot (R_{\text{E}} + h) \cdot (t - t_{\text{mid}}) \cdot c}\right). \tag{4.30}$$

This result contrast with the linear approximation:

$$\Theta(t - t_{\text{mid}}) \approx \left.\frac{\mathrm{d}\Theta(t)}{\mathrm{d}t}\right|_{t=t_{\text{mid}}} (t - t_{\text{mid}}), \tag{4.31}$$

used elsewhere. This is justified by the required simplicity, if SCORE should be realized by hardware components. The plot in Fig. 4.9 shows the variation of the

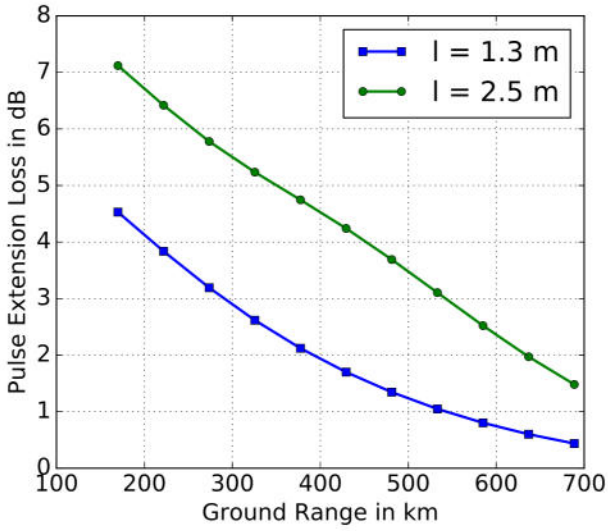


Figure 4.8. Pulse extension loss vs. ground range for the antenna aperture heights $l_{\text{ant,el}} = 1.3$ m and $l_{\text{ant,el}} = 2.5$ m and the parameters $h = 700$ km, $f_0 = 9.6$ GHz and $\tau_p = 120$ μs.

AoA in dependency on the ToA for both equations. It turns out that for narrow swath widths up to approx. $W_g = 80$ km (deviation less than 0.1°), this approximation is perfectly adequate. However for HRWS-SAR, the deviation of up to 6.9° from the true value at the near edge of the swath leads to unacceptable errors and proves the necessity for including the Earth's curvature. Unfortunately, it is not possible to simplify Eq. (4.30) without loosing required accuracy. The alternative solution, which uses the true relationships between signal and geometry will be presented in the subsequent subsection.

Apart from this error, a further important fact was neglected up to now. Under the umbrella of true time-delay DBF not only the dimensions of the antenna array itself are considered if $\Delta\varphi_{0,i} > 2\pi$ (cf. Eq. (4.5) and Fig. 4.1), but also the array factor of the antenna itself. This factor is frequency dependent and for huge signal bandwidths of $B >> c/(l_{\text{ant,el}} \cdot \sin\Theta)$ this error must be taken into account for DBF [93]. For the typical values $l_{\text{ant,el}} = 4.0$ m and $\Theta \in [-15°, 15°]$, the signal bandwidth must be much less than 290 MHz, which is impractical for HRWS-SAR and shows the significance of a true time-delay DBF.

In the next subsection we propose an innovative concept for a practical implementation of SCORE. It copes with the frequency dependency of the array factor

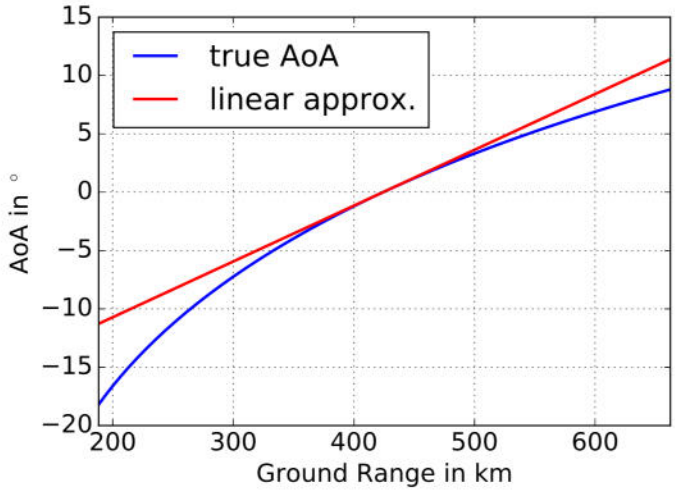


Figure 4.9. AoA in dependency on the ToA. Linear approximation and true curve. $\Theta_{\text{tilt}} = 33.2°$, $\Theta = 15°...42°$.

and also includes frequency-variant antenna beams with a correct relation between ToA and AoA.

4.3.2. Frequency- and Time-Variant Beam-Forming

It has been proven in the last subsection, that the proposed approaches with linear varying weights [28, 98] do not have the required accuracy for a HRWS SAR system. Therefore in this subsection we propose a solution to enable a cost-efficient and accurate implementation of SCORE on-board. A similar concept has already been proposed in [38] and [100]. This STFAP concept is graphically depicted on hand of a block diagram in Fig. 4.10. The received echo signal at each receive antenna is down-converted and digitized with ADCs. After band-pass division into several sub-bands of equal width, the time-variant DBF weights are applied on each sub-band. A final summation over all sub-band signals and receive channels leads to an equivalent single-channel raw-data set, which is streamed to the ground for further processing steps (cf. section 2.4). The basic idea behind this approach is to *divide* the information cube from Fig. 3.3 into small sub-cubes of equal size and to apply discrete weights on each sub-cube separately. This way, the receive signal, which is represented by the blue curved surface, can be completely restored without any loss. Moreover, the sub-cubes, which contain no signal but noise, can be suppressed. In the next pages, the necessary equations for this approach will be derived.

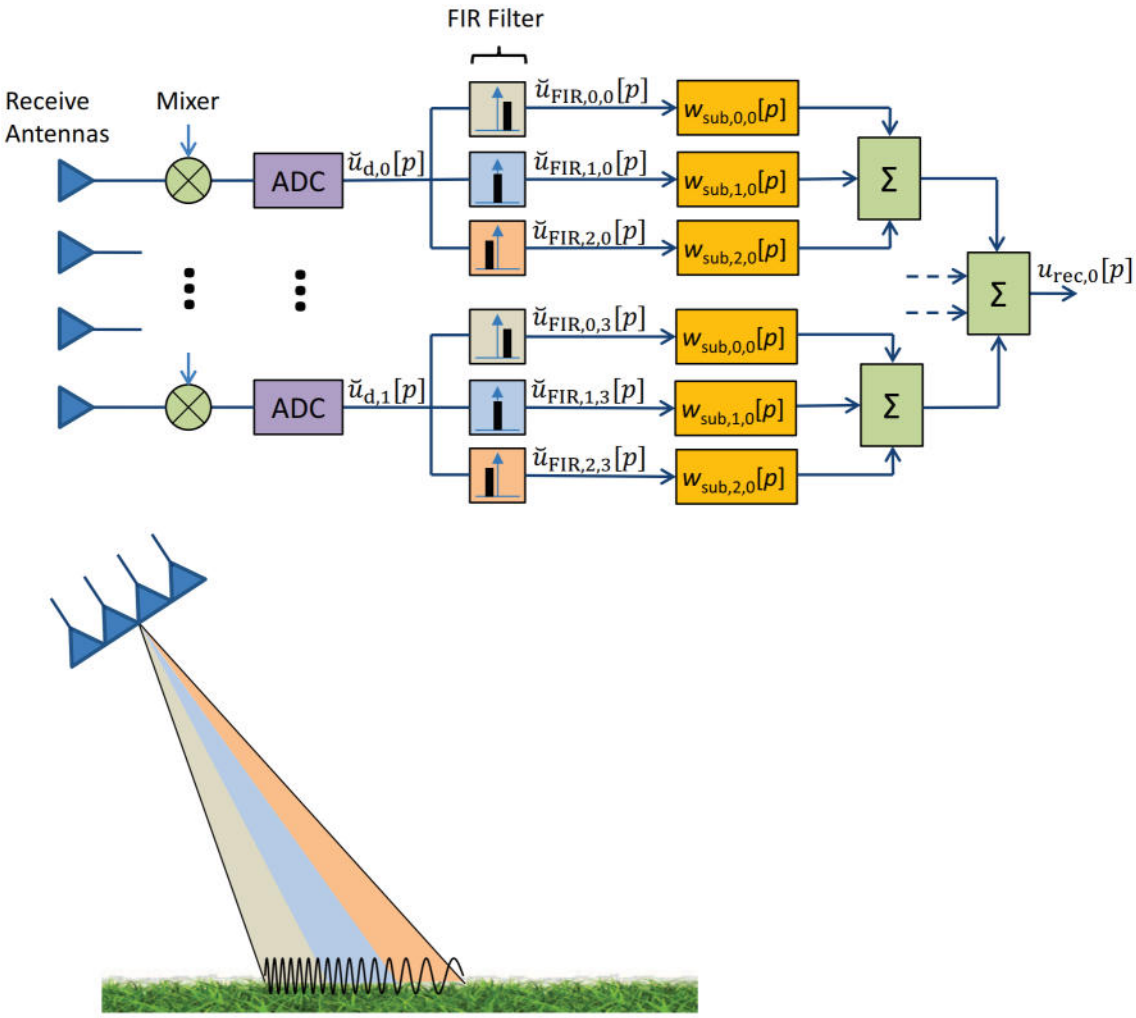


Figure 4.10. Upper part: Block diagram of the SCORE filtering process with two receive channels and three band-pass filters per channel. Lower part: Frequency-variant antenna beam following the reflections of an up-chirp.

The ADCs convert the signal $\breve{\boldsymbol{u}}(t)$ (cf. Eq. (4.9)) to its time-discrete form by sampling with the sampling frequency f_S:

$$\breve{\boldsymbol{u}}_d[p] = \sum_{\Theta_d} \widehat{\sigma}_\kappa^0[\Theta_d] \cdot \boldsymbol{C}_{Rx}[\Theta_d] \odot \Big(\boldsymbol{a}_k[p, \Theta_d] \cdot [C_{Tx}[\Theta_d] \odot s_0[p - p_0(\Theta_d)]] \Big) \Theta_d + \boldsymbol{n}[p], \tag{4.32}$$

while the discrete time-vector is

$$\boldsymbol{t}_{\mathrm{d}} = \left[t_0, t_1, ..., t_p, ..., t_{P-1}\right] \quad \text{with} \quad t_p = p/f_{\mathrm{S}} \quad \text{for} \quad P \in \mathbb{N}_0^+. \tag{4.33}$$

Accordingly, the AoAs are also transformed to their discrete form Θ_{d} and the initial time delay $\tau_{0,0}$ is written as p_0:

$$p_0 = \lfloor \tau_{0,0} \cdot f_{\mathrm{S}} \rceil, \tag{4.34}$$

with $\lfloor \, \rceil$ being the nearest integer function.

Finite Impulse Response Filter Weight Coefficients

The filter bank, which consists of band-pass filters, is implemented by Finite Impulse Response (FIR) filters [101]. The reason for this choice lies in the three basic advantages of FIR filters in comparison to others, such as Infinite Impulse Response (IIR) filters:

- FIR filters have a linear phase response. Hence, the important phase information of the raw-data signal is not distorted.
- They are easy to implement in hardware via Field Programmable Gate Arrays (FPGAs) or Application-Specific Integrated Circuits (ASICs).
- Because the output signal is obtained from the input signal by a finite number of multiplications and additions, they are stable.

As shown in Fig. 4.10, $\breve{\boldsymbol{u}}_{\mathrm{d}}[p]$ is split up and filtered by N_{FIR} dedicated FIR filters of equal bandwidth B_{FIR} with contiguous pass-bands. While the required filter bandwidth is obtained by the ratio of signal bandwidth and N_{FIR},

$$B_{\mathrm{FIR}} = \frac{B}{N_{\mathrm{FIR}}}, \tag{4.35}$$

the number of filters is dependent on the angular pulse extension. The aim of this bandpass division is to form a broad frequency-variant antenna beam, which has the same width as the total angular pulse extent, while each component beam is

narrow. Therefore, the ratio of χ_Θ from Eq. (4.13) and the *HPBW* of the antenna array gives the minimum number of FIR filters:

$$N_{\mathrm{FIR}} \geq \left\lceil \frac{\max\{\chi_\Theta\}}{HPBW} \right\rceil. \tag{4.36}$$

In order to preserve the complete information content of $\breve{\boldsymbol{u}}_{\mathrm{d}}$, the filter transfer function $H_{\mathrm{FIR},l}$ of the l-th filter is designed to have a rectangular shape in frequency-domain:

$$H_{\mathrm{FIR},l}[q] = \mathrm{rect}\left[\frac{2\pi q - \Omega_l}{B_{\mathrm{FIR}}}\right] \quad \text{for} \quad l \in \mathbb{N}_0^+ \text{ and } l < N_{\mathrm{FIR}}, \tag{4.37}$$

while the discrete frequency vector is

$$\boldsymbol{f}_{\mathrm{d}} = \left[f_0, f_1, ..., f_q, ..., f_{Q-1}\right] \quad \text{with} \quad f_q = q \cdot f_{\mathrm{S}} - f_{\mathrm{S}}/2 \quad \text{for} \quad Q \in \mathbb{N}_0^+. \tag{4.38}$$

The angular center frequency of each band Ω_l is chosen to avoid overlapping pass-bands and gaps between the individual bands:

$$\Omega_l = (B_{\mathrm{FIR}} \cdot (2l+1) - B) \cdot \pi. \tag{4.39}$$

From the theory of Fourier series it is known, that a rect-function in frequency domain results in a sinc-function after inverse discrete Fourier transform:

$$h_{\mathrm{FIR},l}[p] = \mathrm{DFT}^{-1}\left\{H_{\mathrm{FIR},l}[q]\right\} = \frac{B_{\mathrm{FIR}}}{2\pi \cdot f_{\mathrm{S}}} \cdot \mathrm{sinc}\left(\frac{p \cdot B_{\mathrm{FIR}}}{f_{\mathrm{S}}}\right) \cdot \exp\left(\mathrm{j}\,\frac{p \cdot \Omega_l}{f_{\mathrm{S}}}\right). \tag{4.40}$$

This filter impulse response function must be of infinite duration in order to get the desired pass-band of rectangular shape in frequency domain. However, FIR filters are of finite duration and the sinc-shaped filter response can therefore be only approximated. In addition, to save computational costs, the order of the

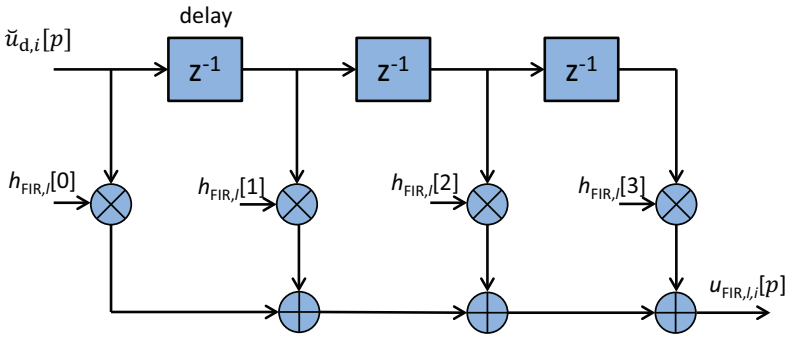


Figure 4.11. Block diagram of a FIR filter with 4 taps.

filter M_{FIR} is just of order of a few tens[6]. But as we will see later at the end of this subsection, this is in most cases absolutely sufficient.

The filtered signal is obtained after the discrete convolution of the input signal $\breve{\boldsymbol{u}}_{\mathrm{d}}$ with the filter impulse response $h_{\mathrm{FIR},l}$:

$$\breve{u}_{\mathrm{FIR},l,i}[p] = \sum_{m=0}^{M_{\mathrm{FIR}}} h_{\mathrm{FIR},l}[m] \cdot \breve{u}_{\mathrm{d},i}[p-m]. \tag{4.41}$$

Fig. 4.11 shows a block diagram, which depicts the process of discrete convolution within a FIR filter with the filter coefficients $h_{\mathrm{FIR},l}$.

Calculation of the Weights for the Minimum Variance Distortionless Response Beam-Forming Algorithm

While the DBF weights from the MVDR beam-former (cf. Eq. (4.26)) are calculated to sweep continuously over time and frequency, for a practical implementation of SCORE these weights are quantized. To avoid errors caused by the frequency dependence of the array factor (compare end of section 4.3.1), the sets of DBF weights are calculated with respect to the center of each individual frequency band. With the relationship between angular center frequency of the l-th pass-band and its wavelength

$$\widehat{\lambda}_l = 2\pi \frac{c}{\Omega_l}, \tag{4.42}$$

[6]The number of taps is equal to the filter length and one less than the filter order.

it is possible to transform the steering vector of Eq. (4.7) to its band-discrete version:

$$\widehat{\boldsymbol{a}}_{0,l}[p] = \left[\exp\left(\mathrm{j}\frac{2\pi}{\widehat{\lambda}_l}\cdot 0\cdot d\cdot\sin\left(\vartheta_{\mathrm{d},0}[p-\tilde{p}_l]\right)\right), \exp\left(\mathrm{j}\frac{2\pi}{\widehat{\lambda}_l}\cdot 1\cdot d\cdot\sin\left(\vartheta_{\mathrm{d},0}[p-\tilde{p}_l]\right)\right), \ldots, \exp\left(\mathrm{j}\frac{2\pi}{\widehat{\lambda}_l}\cdot (N_{\mathrm{Rx}}-1)\cdot d\cdot\sin\left(\vartheta_{\mathrm{d},0}[p-\tilde{p}_l]\right)\right)\right]^{\mathrm{T}}, \tag{4.43}$$

with $\vartheta_{\mathrm{d},0}[p-\tilde{p}_l]$ being the discrete AoA, which corresponds to the center position of the respective band-pass filtered pulse.

From Eq. (4.13), we know that the angular pulse extent varies over the steering angle and thus also the center of each band-pass filtered pulse varies. Accordingly, the specific delay $\tilde{p}_l$ is required:

$$\tilde{p}_l = \left\lfloor \frac{\tau_{\mathrm{p}}}{N_{\mathrm{FIR}}}\cdot\left(l-\frac{1}{2}\right)\right\rfloor. \tag{4.44}$$

The DBF weights $\boldsymbol{w}_{\mathrm{sub},l,0}[p]$ for each sub-beam are finally obtained by substituting $\boldsymbol{a}_0$ in Eq. (4.26) by $\widehat{\boldsymbol{a}}_{0,l}$:

$$\widehat{\boldsymbol{w}}^{\mathrm{T}}_{\mathrm{sub},l,0} = N_{\mathrm{Rx}}\cdot[\widehat{\boldsymbol{a}}^{\mathrm{H}}_{0,l}\cdot\widehat{\boldsymbol{a}}_{0,l}]^{-1}\cdot\widehat{\boldsymbol{a}}^{\mathrm{H}}_{0,l} = \widehat{\boldsymbol{a}}^{\mathrm{H}}_{0,l}. \tag{4.45}$$

It is an important fact, that for a non-changing topography these weights must not be computed for every echo window anew. Once they are calculated, they can be stored on-board in a look-up table to enable fast DBF in real-time. If the topography changes and the relation between Θ, t and f is not valid anymore, the topography-adaptive DBF concept, which is derived in the next chapter can be used.

A final summation over all filtered intermediate signals leads to the reconstructed raw data set

$$u_{\mathrm{rec},0}[p] = \sum_{l=0}^{N_{\mathrm{FIR}}-1} \sum_{i=0}^{N_{\mathrm{Rx}}-1} \breve{u}_{\mathrm{FIR},l,i}[p] \cdot \boldsymbol{w}_{\mathrm{sub},l,0}[i,p]. \tag{4.46}$$

This summation means actually a hardware simplification.

To proof that the signal $\breve{u}_{\mathrm{d},i}$ is completely reconstructed after FIR filtering, we run a simulation with an up-chirp waveform as input signal and the following filter parameters: $N_{\mathrm{FIR}} = 5$, $M_{\mathrm{FIR}} = 30$. The spectra of the output signals and their sum signal (blue curve) are plotted in Fig. 4.12. It can be seen, that the envelope of the sum signal is constant and the information content of the signal is completely preserved after the filter. A repetition of the simulation for Fig. 4.8 with an additional filter bank of the parameters $N_{\mathrm{FIR}} = [2,3,4,6,8]$, $M_{\mathrm{FIR}} = 100$ led to the result, which is plotted in Fig. 4.13. It can be clearly seen, that the *PEL* reduces with increasing number of filters, since the angular pulse extent is divided into narrow sub-bands. Already the use of two filters improves the *PEL* by up to 2.5 dB (cf. Fig. 4.8).

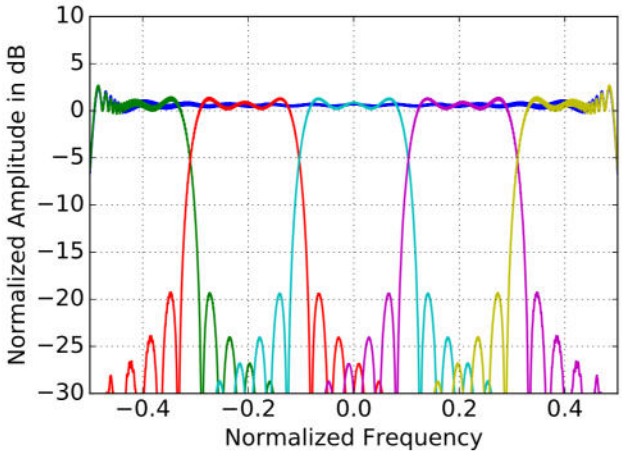


Figure 4.12. Resulting frequency spectrum after signal reconstruction with five FIR filters of order $M_{\mathrm{FIR}} = 30$; sum signal: blue curve in background.

4.4. Waveform Separation of Sub-Pulses

For separation of the sub-pulses (cf. section 3.2.3), we form N_{Tx} simultaneous antenna beams, while each beam tracks the echo of an individual sub-pulse. Sim-

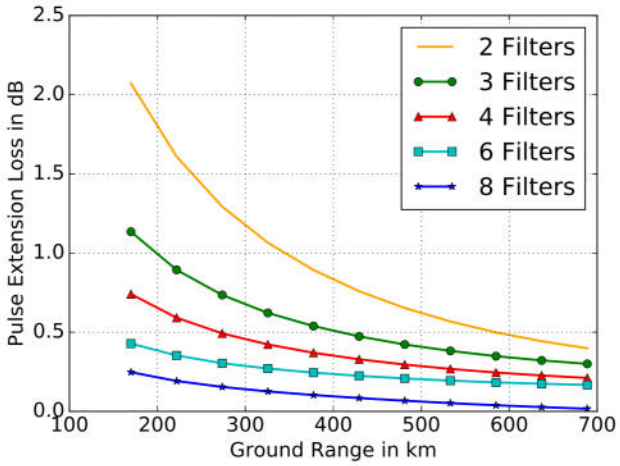


Figure 4.13. Pulse extension loss vs. ground range for the parameters $h = 700$ km, $f_0 = 9.6$ GHz, $l_{\text{ant,el}} = 1.3$ m, $\tau_p = 120$ μs, $N_{\text{FIR}} = [2, 3, 4, 6, 8]$, $M_{\text{FIR}} = 100$.

ilar to the information cube illustration of a single chirp waveform in Fig. 3.3, in Fig. 4.14 the information cube for the MSP waveforms with $N_{\text{Tx}} = 2$ is shown. As indicated by the annular shell of the receive signal in the lower part of the figure, a part of the waveform is plotted in the cube. A very important characteristic becomes directly visible: The blue and green curved surfaces are parallel and do not intersect. If the waveform separation is done in the time-frequency plane only, which is the common case in classical processing techniques, the planes overlap completely and can not be separated anymore. However with STFAP, signal processing of the received raw data is done along the time axis, frequency axis and angle of arrival axis in the information cube. Theoretically, if the antenna has suitable characteristics and if the geometrical model fits, this allows a perfect separation of the individual transmit signals.

In order to enable waveform separation on-board in real-time, it is necessary to avoid long-duration calculations, such as FFT and convolution. Further publications concentrate only on the separation of the MSP waveforms without any gaps between the sub-pulses [98, 102, 103]. Especially they do not consider the Earth's curvature, which has a strong impact for HRWS SAR (cf. Fig. 4.9). Also, the separation algorithm presented in [37] can not be practically implemented, because the whole multi-channel raw data has to be streamed to ground before DBF.

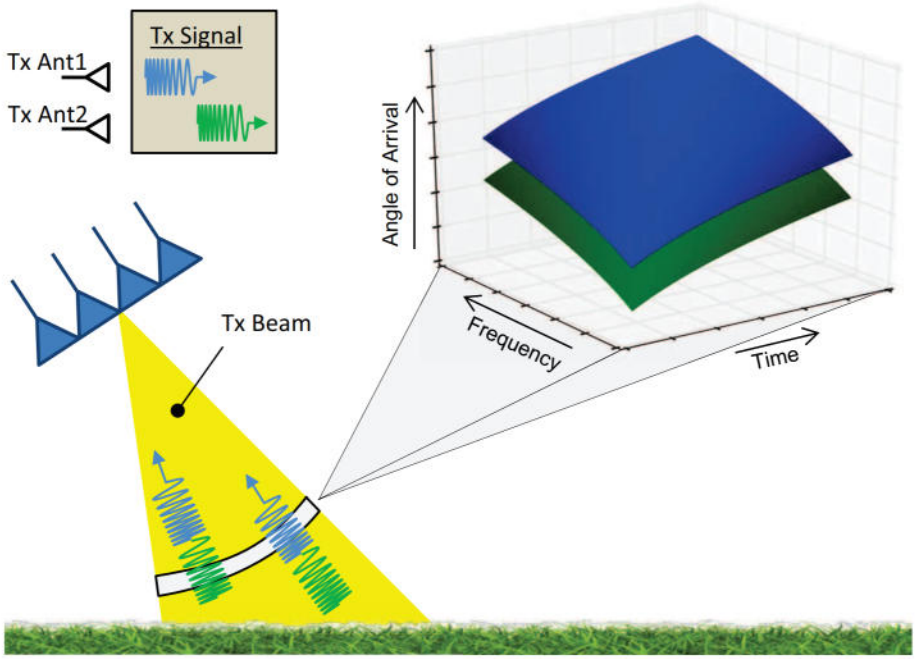


Figure 4.14. Representation of the receive signal from the MSP waveform in angle, time and frequency.

The major new contributions of the STFAP algorithm, which is introduced in this section are:

- Independence on the number of transmit waveforms
- Consideration of the spherical Earth model
- No prior range compression is needed to save computation time on-board

In the first subsection, we focus on the MVDR algorithm in its standard time-variant form. The second subsection is about the band-pass filter approach and the last subsection addresses a more advanced technique, which additionally places nulls of the antenna pattern within the ambiguous waveforms.

4.4.1. Time-Variant Beam-Forming for Waveform Separation

The basic principle for separation of sub-pulses is strongly related to the approach of section 4.3.1, where a narrow antenna beam tracks the echo on the ground. In the present case, N_{Tx} simultaneous antenna beams have to be formed, while each beam tracks an individual sub-pulse. With respect to Eq. (4.26), the beam-forming weights are calculated in the same way:

$$\boldsymbol{w}_{\mathrm{Rx},k}^{\mathrm{T}}(t,\widehat{\Theta}_k) = \boldsymbol{a}_k^{\mathrm{H}}(t,\widehat{\Theta}_k), \tag{4.47}$$

and define the time-variant steering directions for the sub-pulses.

Since the required AoA is dependent on the number of transmit signals and also on the type of STSO waveform, we have to give a dedicated expression for $\widehat{\Theta}_k$. In analogy to Eq. (4.4), for the MSP waveforms (with arbitrary gaps between the sub-pulses) the time-variant angle of the main lobe and also the nulls must be shifted with respect to the center of the waveform by $t_{\mathrm{c},k}$ (cf. Eq. (3.13)):

$$\widehat{\Theta}_k(t) = \arccos\left(\frac{4\cdot(R_{\mathrm{E}}+h)^2 - 4\cdot R_{\mathrm{E}}^2 + (t-t_{\mathrm{c},k})^2\cdot c^2}{4\cdot(R_{\mathrm{E}}+h)\cdot(t-t_{\mathrm{c},k})\cdot c}\right). \tag{4.48}$$

After weighting the receive signal $\check{\boldsymbol{u}}(t)$ (cf. Eq. (4.9)) with these weights, we can write for the reconstructed signal:

$$\begin{aligned} u_{\mathrm{rec},k}(t,\widehat{\Theta}_k) &= \check{\boldsymbol{u}}(t,\Theta)\cdot\boldsymbol{w}_{\mathrm{Rx},k}(t,\widehat{\Theta}_k) \\ &= \Bigg[\int_{\Theta} \widehat{\sigma}_\kappa^0(\Theta)\cdot\boldsymbol{C}_{\mathrm{Rx}}(\Theta)\odot\Big(\boldsymbol{A}(t,\Theta) \\ &\qquad \cdot\left[\boldsymbol{C}_{\mathrm{Tx}}(\Theta)\odot\boldsymbol{s}\left(t-\tau_{0,0}(\Theta)\right)\right]\Big)\,\mathrm{d}\Theta + \boldsymbol{n}(t)\Bigg]^{\mathrm{T}}\cdot\boldsymbol{a}_k^*(t,\widehat{\Theta}_k). \end{aligned} \tag{4.49}$$

To analyze this generalized expression, we set $N_{\mathrm{Tx}} = 2$. By making use of the angular pulse extent (cf. Eq. (4.28)), it is reasonable to split the integral to the extensions of the two sub-pulses. Therefore we can write for the receive signal:

$$\begin{aligned} \check{\boldsymbol{u}}(t,\widehat{\Theta}_0,\widehat{\Theta}_1) = &\int_{\widehat{\Theta}_0-\chi_\Theta/2}^{\widehat{\Theta}_0+\chi_\Theta/2} C_{\mathrm{Tx},0}(\Theta)\cdot\widehat{\sigma}_\kappa^0(\Theta)\cdot\boldsymbol{C}_{\mathrm{Rx}}(\Theta)\odot\boldsymbol{a}_0(t,\Theta)\cdot s_0\left(t-\tau_{0,0}(\Theta)\right)\,\mathrm{d}\Theta \\ &+\int_{\widehat{\Theta}_1-\chi_\Theta/2}^{\widehat{\Theta}_1+\chi_\Theta/2} C_{\mathrm{Tx},1}(\Theta)\cdot\widehat{\sigma}_\kappa^0(\Theta)\cdot\boldsymbol{C}_{\mathrm{Rx}}(\Theta)\odot\boldsymbol{a}_1(t,\Theta)\cdot s_1\left(t-\tau_{0,0}(\Theta)\right)\,\mathrm{d}\Theta \\ &+\boldsymbol{n}(t). \end{aligned}$$

(4.50)

Without any gap between both pulses ($\tau_s = 0$), it is valid to equate the upper and lower limits of the first and second integral, respectively to: $\widehat{\Theta}_1 - \chi_\Theta/2 = \widehat{\Theta}_0 + \chi_\Theta/2$.

With the first weighting vector of Eq. (4.47), we get, in analogy to Eq. (4.28), for the first signal[7,8]:

$$
\begin{aligned}
u_{\mathrm{rec},0}(t,\widehat{\Theta}_0,\widehat{\Theta}_1) = C \cdot & \int_{\widehat{\Theta}_0-\chi_\Theta/2}^{\widehat{\Theta}_0+\chi_\Theta/2} \boldsymbol{a}_0^{\mathrm{T}}(t,\widehat{\Theta}_0+\Theta)\cdot\boldsymbol{a}_0^{*}(t,\widehat{\Theta}_0)\cdot s_0(t-\tau_{0,0}(\widehat{\Theta}_0))\,\mathrm{d}\Theta \\
& + C \cdot \int_{\widehat{\Theta}_1-\chi_\Theta/2}^{\widehat{\Theta}_1+\chi_\Theta/2} \boldsymbol{a}_1^{\mathrm{T}}(t,\widehat{\Theta}_1+\Theta)\cdot\boldsymbol{a}_0^{*}(t,\widehat{\Theta}_0)\cdot s_1(t-\tau_{0,0}(\widehat{\Theta}_0))\,\mathrm{d}\Theta \\
& + \boldsymbol{n}^{\mathrm{T}}(t)\cdot\boldsymbol{a}_0^{*}(t,\widehat{\Theta}_0) \\
= C \cdot N_{\mathrm{Rx}} \cdot & \int_{\widehat{\Theta}_0-\chi_\Theta/2}^{\widehat{\Theta}_0+\chi_\Theta/2} \operatorname{sinc}\left\{\frac{\pi\cdot d\cdot N_{\mathrm{Rx}}}{\lambda}\cdot\left[\sin(\widehat{\Theta}_0+\Theta)-\sin(\widehat{\Theta}_0)\right]\right\} \\
& \cdot s_0(t-\tau_{0,0}(\widehat{\Theta}_0))\,\mathrm{d}\Theta \\
& + C\cdot N_{\mathrm{Rx}} \cdot \int_{\widehat{\Theta}_1-\chi_\Theta/2}^{\widehat{\Theta}_1+\chi_\Theta/2} \operatorname{sinc}\left\{\frac{\pi\cdot d\cdot N_{\mathrm{Rx}}}{\lambda}\cdot\left[\sin(\widehat{\Theta}_1+\Theta)-\sin(\widehat{\Theta}_1)\right]\right\} \\
& \cdot s_1(t-\tau_{0,0}(\widehat{\Theta}_0))\,\mathrm{d}\Theta + \boldsymbol{n}^{\mathrm{T}}(t)\cdot\boldsymbol{a}_0^{*}(t,\widehat{\Theta}_0).
\end{aligned}
\tag{4.51}
$$

The resulting antenna pattern, which is determined by the steering and weighting vectors, is crucial for the suppression of the other transmit waveform. Therefore, it is reasonable to define the Ambiguity Ratio AR for the sub-pulses as a function of the following pattern:

[7] The result for the second steering vector can be derived equivalently.

[8] Used intermediate step for calculation of the array factor: $\boldsymbol{a}_0^{\mathrm{T}}(t,\widehat{\Theta}_0+\Theta)\cdot\boldsymbol{a}_0^{*}(t,\widehat{\Theta}_0) = \sum_{i=0}^{N_{\mathrm{Rx}}-1}\exp\left\{i\cdot\mathrm{j}\cdot\frac{2\pi}{\lambda_0(t)}\cdot d\cdot\sin(\widehat{\Theta}_0(t)+\Theta(t))-\sin(\widehat{\Theta}_0(t))\right\} = \operatorname{sinc}\left\{\frac{\pi\cdot d\cdot N_{\mathrm{Rx}}}{\lambda}\cdot\left[\sin(\widehat{\Theta}_0+\Theta)-\sin(\widehat{\Theta}_0)\right]\right\}$.

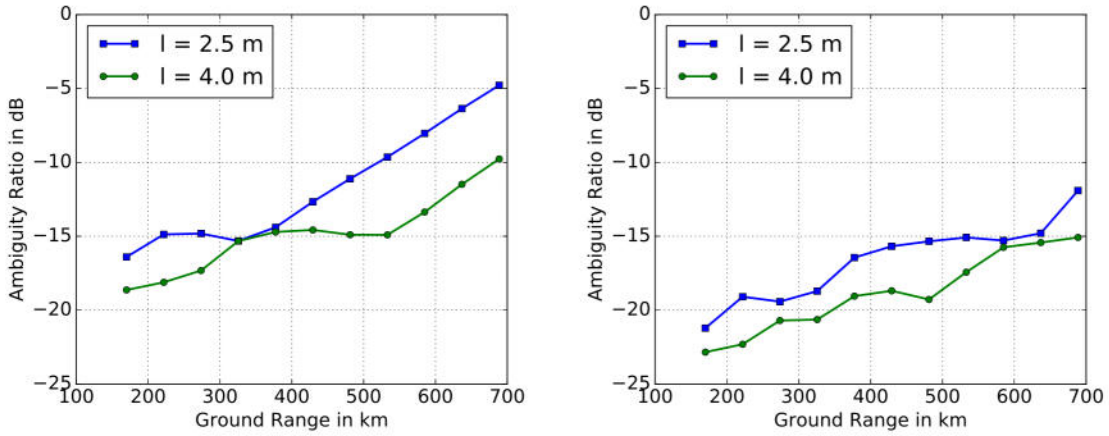
$$AR(\widehat{\Theta}_0, \widehat{\Theta}_1) = \frac{\left| \int_{\widehat{\Theta}_1 - \chi_\Theta/2}^{\widehat{\Theta}_1 + \chi_\Theta/2} \boldsymbol{a}_1^{\mathrm{T}}(t, \widehat{\Theta}_1 + \Theta) \cdot \boldsymbol{a}_0^{*}(t, \widehat{\Theta}_0)\, \mathrm{d}\Theta \right|^2}{\left| \int_{\widehat{\Theta}_0 - \chi_\Theta/2}^{\widehat{\Theta}_0 + \chi_\Theta/2} \boldsymbol{a}_0^{\mathrm{T}}(t, \widehat{\Theta}_0 + \Theta) \cdot \boldsymbol{a}_0^{*}(t, \widehat{\Theta}_0)\, \mathrm{d}\Theta \right|^2}. \tag{4.52}$$

From a comparison between Eq. (4.51) and Eq. (4.28), we note that there is an additional error term, which covers the interferences from the other waveform. In fact, this expression is strongly related to the (integrated) Range-Ambiguity-to-Signal-Ratio (*RASR*), while the *RASR* has been initially defined to analyze the range ambiguities if the condition in section 2.3.1 is not met. Ideally, the *AR* should be less than -25 dB to guarantee a sufficient orthogonality between the transmit channels.

The *AR* for the antenna sizes in elevation $l_{\mathrm{ant,el}} = 2.5$ m and $l_{\mathrm{ant,el}} = 4.0$ m is plotted in Fig. 4.15a, with the parameters $h = 700$ km, $f_0 = 9.6$ GHz, $\tau_\mathrm{p} = 120$ μs, $\tau_\mathrm{s} = 0$ s and $N_\mathrm{Tx} = 2$ have been used for the simulation. For a constant antenna size and a spherical Earth, the angular pulse extent drops with increasing ground range, while the *AR* rises. The antenna main-lobe with its constant *HPBW* cannot suppress the other waveform ideally for all steering angles and part of the unwanted energy is collected by the main-lobe and the side-lobes. This is illustrated in Fig. 4.16. The plot shows a simulated antenna pattern at a certain time instant, which is steered to antenna bore-site direction at $\Theta = 28.5°$. For the case of two MSP waveforms, the blue colored surface indicates the angular pulse extent of the first waveform, while the green colored surface indicates the angular pulse extent of the second waveform. It can be clearly seen, that there is a significant energy contribution of the second waveform.

Although a larger antenna leads to a better *AR*, the suppression of the ambiguous waveform is insufficient for each ground range position. Especially, the interfering energy from the main-lobe of the antenna pattern has a significant contribution. Since the gain at the side-lobes reduces with increasing distance from the main-lobe, a larger gap between both sub-pulses will obviously lead to a better suppression. For comparison, in Fig. 4.15b we show the *AR* with the same system parameters, however, with $\tau_\mathrm{p} = 150$ μs and $\tau_\mathrm{s} = 30$ μs. As can be observed, the *AR* is significantly better, unfortunately still not acceptable for most

applications. In the next two subsections, methods are presented, which lead to an improved suppression of the orthogonal waveform.



(a) $\tau_p = 120\ \mu s$, $\tau_s = 0$ s. **(b)** $\tau_p = 150\ \mu s$ and $\tau_s = 30\ \mu s$.

Figure 4.15. Plot of the AR versus ground range for the antenna sizes in elevation $l_{ant,el} = 2.5$ m and $l_{ant,el} = 4.0$ m and two sub-pulses with the parameters $h = 700$ km and $f_0 = 9.6$ GHz.

4.4.2. Time- and Frequency-Variant Beam-Forming for Waveform Separation

In this section, we present a novel approach for waveform separation using the band-pass FIR filter concept, which has also been proposed in section 4.3.2 of this thesis. With respect to Fig. 4.14, the processing is done grid-wise along the curved surfaces within the information cube. The block diagram for this processing step can be found in Fig. 4.17. Like in section 4.3.2, the receive signal of each receive antenna is divided with a bank of band-pass filters into narrow sub-bands. These signals are weighted with time-variant beam-forming weights in relation to the corresponding transmit waveform in a parallel processing structure. It is important to note that the DBF weights are not the same for the sub-pulses due to different AoA at a certain instant of time. After linear combination of the weighted sub-band signals of all receive channels, the equivalent single-channel raw-data set for each transmit channel is obtained. This data is finally sent to the ground-station for further SAR processing (cf. section 2.4).

The receive signal $\breve{\boldsymbol{u}}_d[p]$ is filtered with a total number of N_{FIR} FIR filters of equal bandwidth and contiguous pass-bands. To ensure, that the seen swath of

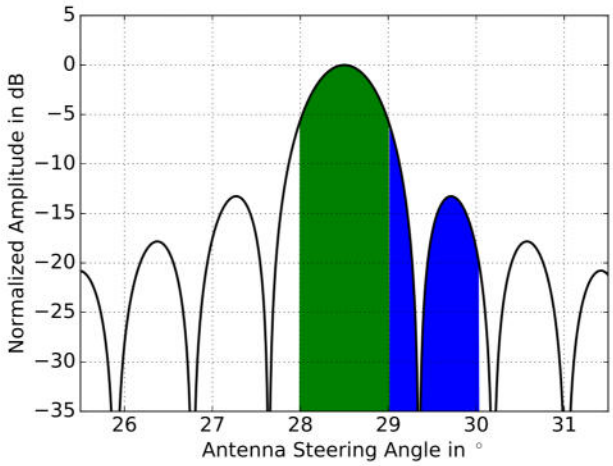


Figure 4.16. Simulated antenna pattern at a certain time instant, which is steered to antenna bore-site direction at $\Theta = 28.5°$. For the case of two MSP waveforms, the blue colored surface indicates the angular pulse extent of the first waveform, while the green colored surface indicates the angular pulse extent of the second waveform. For simulation, the following parameters were used: $h = 700$ km and $f_0 = 9.6$ GHz, $l_{\text{ant,el}} = 2.5$ m, $\tau_{\text{p}} = 120$ μs, $\tau_{\text{s}} = 0$ s.

extension χ_Θ is divided into sub-swathes of an extension, which is either less or equal to the extension of the unambiguous swath $\chi_{\Theta,\text{MIMO}}$, the number of filters must be

$$\check{N}_{\text{FIR}} \geq \left\lceil \frac{\max\{\chi_\Theta\}}{\chi_{\Theta,\text{MIMO}}} \right\rceil. \tag{4.53}$$

The stress $\check{}$ is used to indicate that multiple transmit channels are present and that the number of FIR filter is not the same as in Eq. (4.36). Following the same procedure as in section 4.3.2, the filter bandwidth is

$$\check{B}_{\text{FIR}} = \frac{B}{\check{N}_{\text{FIR}}} \tag{4.54}$$

and the filter impulse response function reads as

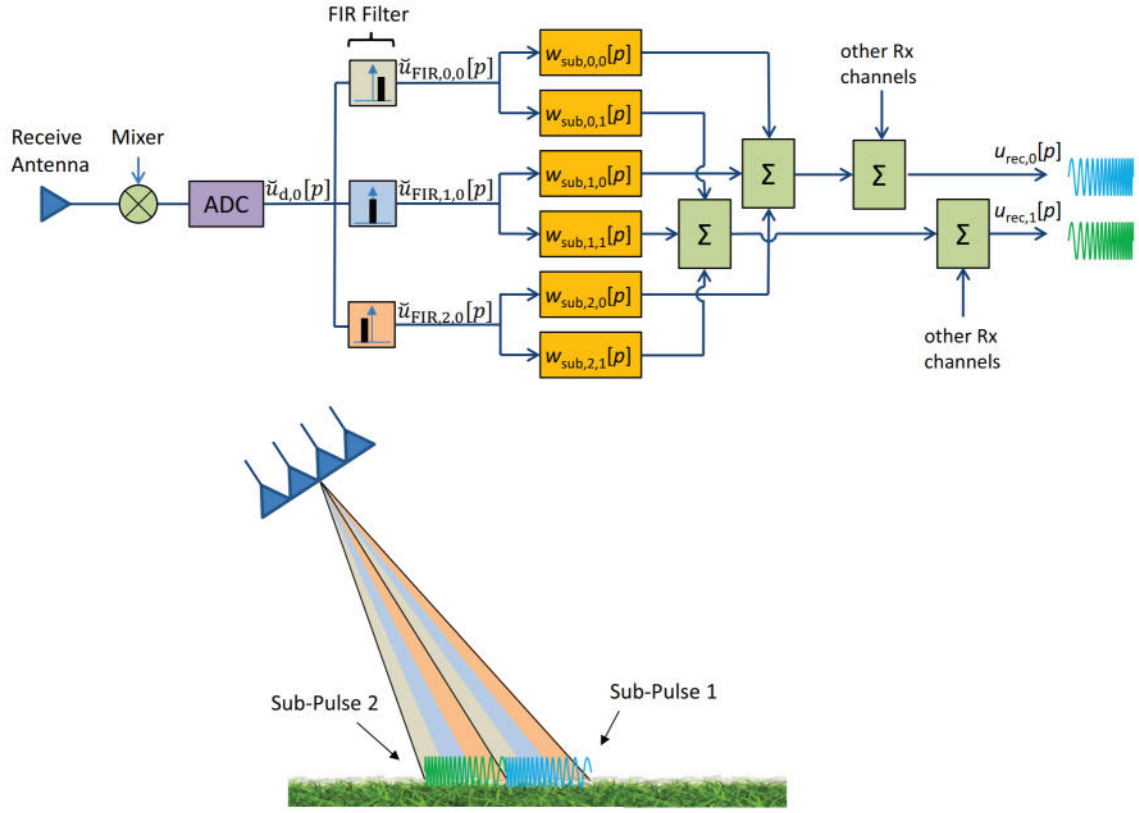


Figure 4.17. Block diagram of the STFAP filtering process for two transmit waveforms with three band-pass filters per channel (just a single receive channel is shown).

$$\check{h}_{\mathrm{FIR},l}[p] = \frac{\check{B}_{\mathrm{FIR}}}{2\pi \cdot f_{\mathrm{S}}} \cdot \mathrm{sinc}\left(\frac{p \cdot \check{B}_{\mathrm{FIR}}}{f_{\mathrm{S}}}\right) \cdot \exp\left(\mathrm{j}\,\frac{p \cdot \check{\Omega}_l}{f_{\mathrm{S}}}\right), \tag{4.55}$$

with the angular center frequencies

$$\check{\Omega}_l = (\check{B}_{\mathrm{FIR}} \cdot (2l+1) - B) \cdot \pi. \tag{4.56}$$

With respect to Eq. (4.41), the output signal of each filter is obtained through discrete convolution of the input signal $\check{\boldsymbol{u}}_{\mathrm{d}}$ with the filter impulse response $\check{h}_{\mathrm{FIR},l}$:

$$\check{u}_{\mathrm{FIR},l,i}[p] = \sum_{m=0}^{M_{\mathrm{FIR}}} \check{h}_{\mathrm{FIR},l}[m] \cdot \check{u}_{\mathrm{d},i}[p-m]. \tag{4.57}$$

For spatial filtering, the steering matrix of Eq. (4.8) can be transformed to its time- and band-discrete version,

$$\check{\boldsymbol{A}}[\check{\lambda}, \vartheta_{\mathrm{d}}, p] = \left[\boldsymbol{a}_0, \boldsymbol{a}_1, ..., \boldsymbol{a}_{N_{\mathrm{Tx}}-1}\right], \tag{4.58}$$

with the individual DBF steering vectors

$$\check{\boldsymbol{a}}_{k,l}[p] = \left[\exp\left(\mathrm{j}\frac{2\pi}{\check{\lambda}_l} \cdot 0 \cdot d \cdot \sin\left(\vartheta_{\mathrm{d},k}[p-\tilde{p}_l]\right)\right), \exp\left(\mathrm{j}\frac{2\pi}{\check{\lambda}_l} \cdot 1 \cdot d \cdot \sin\left(\vartheta_{\mathrm{d},k}[p-\tilde{p}_l]\right)\right), \right.$$
$$\left. ..., \exp\left(\mathrm{j}\frac{2\pi}{\check{\lambda}_l} \cdot (N_{\mathrm{Rx}}-1) \cdot d \cdot \sin\left(\vartheta_{\mathrm{d},k}[p-\tilde{p}_l]\right)\right)\right]^{\mathrm{T}} \tag{4.59}$$

and the angular center frequency of the l-th pass-band (Eq. (4.42))

$$\check{\lambda}_l = 2\pi \frac{c}{\check{\Omega}_l}. \tag{4.60}$$

$\vartheta_{\mathrm{d},k}$ denotes the time-discrete AoA with respect to Eq. (4.4).

According to Fig. 4.17, after band-pass filtering the time-variant DBF weights $\boldsymbol{w}_{\mathrm{sub},l,k}$ are applied for each transmit waveform separately in parallel. These weights are calculated by using the following equation, while $\boldsymbol{A}$ is substituted by $\check{\boldsymbol{A}}_l$:

$$\widehat{\boldsymbol{w}}^{\mathrm{T}}_{\mathrm{sub},l,k} = N_{\mathrm{Rx}} \cdot \boldsymbol{i}_k \cdot [\check{\boldsymbol{A}}_l^{\mathrm{H}} \cdot \check{\boldsymbol{A}}_l]^{-1} \cdot \check{\boldsymbol{A}}_l^{\mathrm{H}}. \tag{4.61}$$

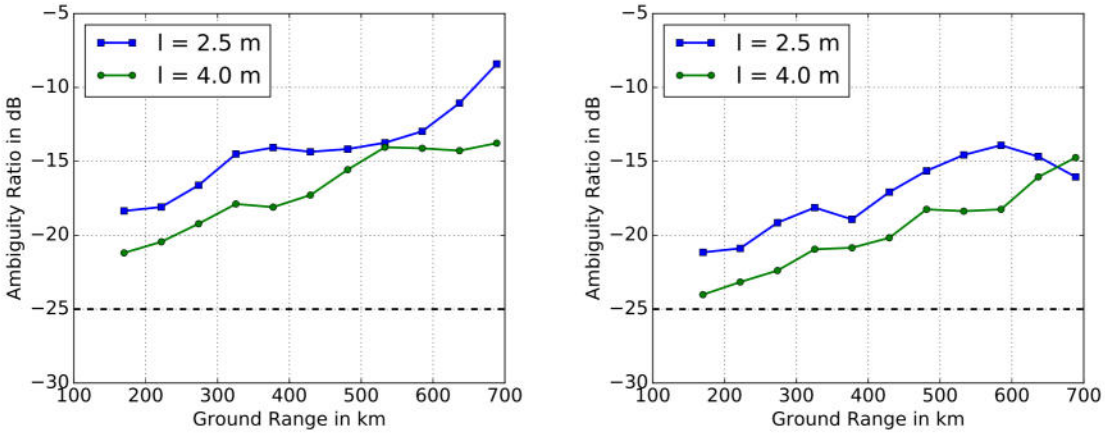
A final summation over the weighted signals for each transmit waveform separately gives the reconstructed raw-data:

$$u_{\mathrm{rec},k}[p] = \sum_{l=0}^{N_{\mathrm{FIR}}-1} \sum_{i=0}^{N_{\mathrm{Rx}}-1} \check{u}_{\mathrm{FIR},l,i}[p] \cdot \boldsymbol{w}_{\mathrm{sub},l,k}[i,p]. \tag{4.62}$$

In order to demonstrate the operational capability of STFAP with FIR filter, in Fig. 4.18a, we plot the *AR* for the parameters h = 700 km, f_0 = 9.6 GHz, τ_p = 120 μs, τ_s = 0s, N_Tx = 2, N_FIR = 6 and M_FIR = 100 for the typical antenna sizes in elevation $l_\mathrm{ant,el}$ = 2.5 m and $l_\mathrm{ant,el}$ = 4.0 m. The behavior of the *AR* leads to the conclusion, that after band-pass filtering, the same instantaneous frequency component of the orthogonal waveform as for the desired signal is insufficiently suppressed by the antenna pattern. One reason for this strong energy contribution is the relationship between antenna *HPBW* and angular pulse extent, which is only valid at a certain ground range in dependence of the antenna size in elevation. Another reason is the angular extent of this frequency filtered sub-pulse. The antenna null suppresses just a minor part of the second waveform and the level of the adjacent side-lobes is too high to guarantee an acceptable waveform separation.

Since there is no gap between both sub-pulses, a significant energy contribution comes from the part of the second waveform, which is within the first antenna side-lobe. This is illustrated in Fig. 4.19. The plot shows a simulated antenna pattern, which is steered to the first angular center of the angular pulse extent after band-pass filtering (left blue colored surface) at a certain time instant. For the case of two MSP waveforms, the colors correspond to the individual angular pulse extents after band-pass filtering with N_FIR = 6. Since N_Tx = 2, each color appears twice. It can be seen, that the blue colored ambiguity from the second transmit waveform is not ideally suppressed. This is due to the antenna size of $l_\mathrm{ant,el}$ = 2.5 m, which is too long for that special case. With the method described in the following subsection, the antenna null can be placed exactly at the center of that ambiguity to finally improve the *AR*. To counteract this issue, an additional gap between the sub-pulses can be introduced to move the orthogonal waveform further away from the main-lobe. Therefore, the simulation was repeated with the same parameters, however with a gap of τ_s = 30 μs between both sub-pulses. The result can be seen in Fig. 4.18b. Both curves agree with the predicted improvement of the *AR*. A more advanced solution is presented in the following

subsection. There we consider an improved waveform suppression technique, which is based on an adaptive placement of the antenna nulls.



(a) $\tau_p = 120\ \mu s$, $\tau_s = 0$ s. **(b)** $\tau_p = 150\ \mu s$ and $\tau_s = 30\ \mu s$.

Figure 4.18. Plot of the *AR* with FIR filtering versus ground range for the antenna sizes in elevation $l_{ant,el} = 2.5$ m and $l_{ant,el} = 4.0$ m and for two sub-pulses with the parameters $h = 700$ km, $f_0 = 9.6$ GHz, $N_{FIR} = 6$ and $M_{FIR} = 100$.

4.4.3. Time- and Frequency-Variant Beam-Forming with Null-Steering for Waveform Separation

An alternative to the MVDR beam-former, which was used in the last sections, is the Linear Constraint Minimum Variance (LCMV) beam-forming method [95]. While the MVDR algorithm just steers the antenna main lobe to the desired direction, the position of the nulls is neglected. Because the core challenge of STFAP is the suppression of the ambiguous waveforms by tailoring the antenna pattern, LCMV might lead to better results by placing the antenna nulls at the ambiguities. Aim of LCMV is to solve the following optimization problem:

$$\begin{aligned} &\text{minimize } \boldsymbol{w}_{Rx,k}^{H} \cdot \boldsymbol{R} \cdot \boldsymbol{w}_{Rx,k} \\ &\text{subject to } \boldsymbol{w}_{Rx,k}^{T} \cdot \boldsymbol{A} = N_{Rx} \cdot \boldsymbol{i}_k. \end{aligned} \tag{4.63}$$

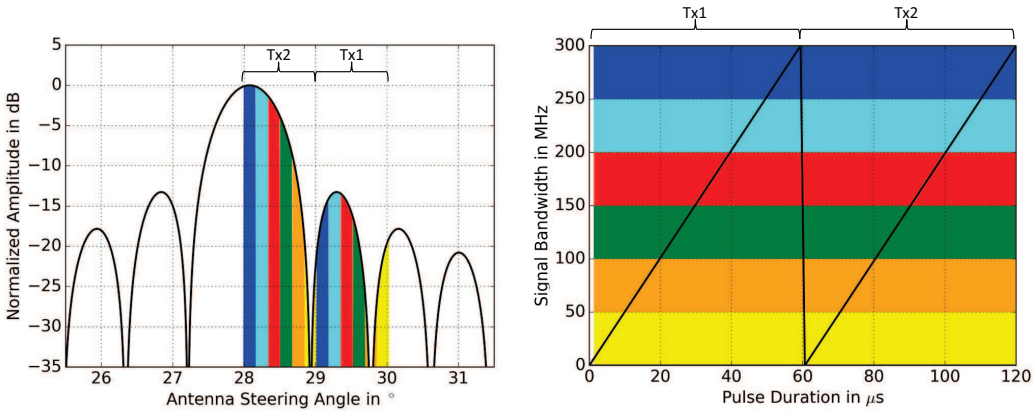


Figure 4.19. Simulated antenna pattern, which is steered to the first angular center of the angular pulse extent after band-pass filtering (left blue colored surface) at a certain time instant. For the case of two MSP waveforms, the colors correspond to the individual angular pulse extents after band-pass filtering with $N_{\mathrm{FIR}} = 6$. For simulation, the following parameters were used: $h = 700$ km and $f_0 = 9.6$ GHz, $l_{\mathrm{ant,el}} = 2.5$ m, $\tau_{\mathrm{p}} = 120$ μs, $\tau_{\mathrm{s}} = 0$ s, $B = 300$ MHz.

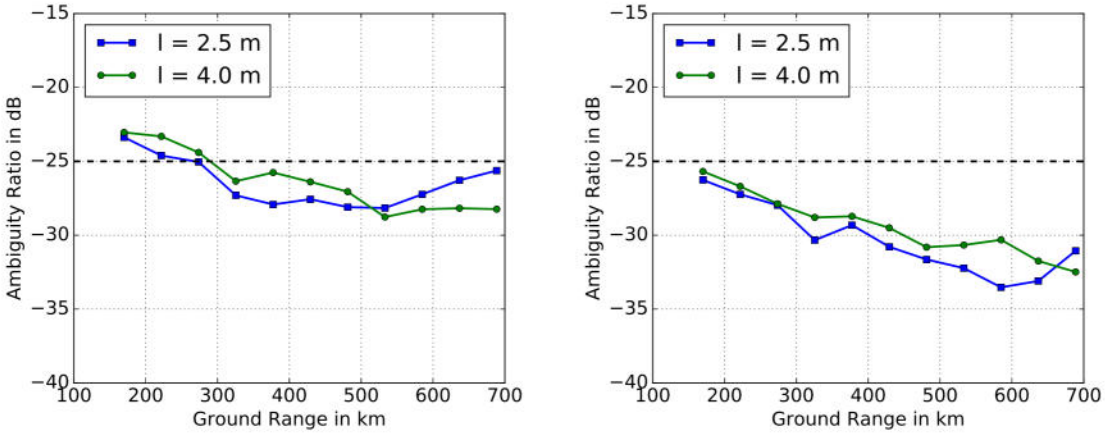
This means that for every k-th transmit waveform an individual set of beamforming weights is calculated, while $\boldsymbol{i}_k$ is the k-th column of the identity matrix $\boldsymbol{I}_{N_{\mathrm{Tx}}}$ of shape $N_{\mathrm{Tx}} \times N_{\mathrm{Tx}}$:

$$\boldsymbol{I}_{N_{\mathrm{Tx}}} = \begin{bmatrix} 1 & 0 & \cdots & 0 \\ 0 & 1 & \ddots & 0 \\ \vdots & \ddots & \ddots & 0 \\ 0 & \cdots & 0 & 1 \end{bmatrix} = \left[\boldsymbol{i}_0, \boldsymbol{i}_1, ..., \boldsymbol{i}_{N_{\mathrm{Tx}}-1}\right]. \tag{4.64}$$

$\boldsymbol{i}_k$ is also known as the constraint vector. The second row in Eq. (4.63) demands that the weights $\boldsymbol{w}_{\mathrm{Rx},k}$ have to be calculated in order to preserve the k-th waveform ($\boldsymbol{i}_k[k] = 1$), while the remaining nulls of $\boldsymbol{i}_k$ correspond to the signal ambiguities, whose directions are defined in $\boldsymbol{A}$. The derivation of the optimum beamforming weights for LCMV-DBF can be found in [95] and leads to the expression for the k-th waveform:

$$\begin{aligned} \boldsymbol{w}_{\mathrm{Rx},k}^{\mathrm{T}} &= N_{\mathrm{Rx}} \cdot \boldsymbol{i}_k \cdot [\boldsymbol{A}^{\mathrm{H}} \cdot \boldsymbol{R}^{-1} \cdot \boldsymbol{A}]^{-1} \cdot \boldsymbol{A}^{\mathrm{H}} \cdot \boldsymbol{R}^{-1} \\ &= N_{\mathrm{Rx}} \cdot \boldsymbol{i}_k \cdot [\boldsymbol{A}^{\mathrm{H}} \cdot \boldsymbol{A}]^{-1} \cdot \boldsymbol{A}^{\mathrm{H}}. \end{aligned} \tag{4.65}$$

For null-steering of the ambiguities, the weights, which have been defined in Eq. (4.47) and Eq. (4.61), are substituted by the weights of the LCMV beamformer. To investigate the improvement by this beam-forming technique, we repeat the simulations of the ambiguity ratio (Fig. 4.18a) with this set of weights. The result can be found in Fig. 4.20a. The plot shows a significant improvement in comparison to Fig. 4.15a and Fig. 4.18a. In any case, the LCMV algorithm performs well over the full swath, while an isolation between the two channels by more than 24 dB could be achieved. It can be also observed, that both antennas show a similar performance. Inserting a gap of $\tau_{\mathrm{s}} = 30$ μs leads to the simulation result of Fig. 4.20b. Both antennas enable a sufficient AR of more than 25 dB over the full swath. As a further improvement, via LCMV broad nulls can be formed, which improve the suppression of the other waveforms. Because the computational effort for calculation of the LCMV weights is not higher than for MVDR weights, we recommend to use LCMV beam-forming.



(a) $\tau_{\mathrm{p}} = 120$ μs, $\tau_{\mathrm{s}} = 0$ s.

(b) $\tau_{\mathrm{p}} = 150$ μs and $\tau_{\mathrm{s}} = 30$ μs.

Figure 4.20. Plot of the AR with FIR filtering and LCMV-DBF versus ground range for the antenna sizes in elevation $l_{\mathrm{ant,el}} = 2.5$ m and $l_{\mathrm{ant,el}} = 4.0$ m and for two sub-pulses with the parameters $h = 700$ km, $f_0 = 9.6$ GHz, $N_{\mathrm{FIR}} = 6$, and $M_{\mathrm{FIR}} = 100$.

4.5. Waveform Separation of Segmentally-Shifted Chirp Waveforms

In this section, it will be shown, that the basic approach to separate the SSC waveforms (introduced in section 3.2.4), is the same as for the MSP waveforms. The crucial difference between both waveform types can be seen in Fig. 4.2. At a certain instant of time and frequency, N_{Tx} AoA of the SSC waveforms have to be suppressed. This is one direction more than for the MSP mode. Because each SSC waveform consists of two sub-chirps (with exception of the waveform with index $k = 0$), also two AoAs to the centers $t_{\mathrm{c1},k}$ and $t_{\mathrm{c2},k}$ must be defined (cf. Eq. (3.19), Eq. (3.20)). However, at a certain instant of time and frequency, the echo arrives just from a single angle (unique relation visualized in Fig. 4.2, exception: $f_k = B/2$ with two valid AoAs) and we can write:

$$\widehat{\Theta}_k(t) = \begin{cases} \arccos\left(\frac{4\cdot(R_{\mathrm{E}}+h)^2-4\cdot R_{\mathrm{E}}^2+(t-t_{\mathrm{c1},k})^2\cdot c^2}{4\cdot(R_{\mathrm{E}}+h)\cdot(t-t_{\mathrm{c1},k})\cdot c}\right) \\ \text{if} \quad f_k \geq \frac{B(N_{\mathrm{Tx}}-k)}{N_{\mathrm{Tx}}} - \frac{B}{2} \quad \text{and} \quad k \neq 0 \\ \\ \arccos\left(\frac{4\cdot(R_{\mathrm{E}}+h)^2-4\cdot R_{\mathrm{E}}^2+(t-t_{\mathrm{c2},k})^2\cdot c^2}{4\cdot(R_{\mathrm{E}}+h)\cdot(t-t_{\mathrm{c2},k})\cdot c}\right) \\ \text{if} \quad f_k \leq \frac{Bk}{N_{\mathrm{Tx}}} - \frac{B}{2} \end{cases} . \tag{4.66}$$

The borders of $f_k \geq \frac{B(N_{\mathrm{Tx}}-k)}{N_{\mathrm{Tx}}} - \frac{B}{2}$ for the first and $f_k \leq \frac{Bk}{N_{\mathrm{Tx}}} - \frac{B}{2}$ for the second part of the SSC chirp can be obtained from the time-frequency plot in Fig. 3.10c. Since there is no linear dependency between ToA and AoA (cf. Fig. 4.9), the required angular separation between the nulls and the main-lobe is distorted for different ground-ranges. Hence it is important to adaptively steer the nulls independently of the steering direction of the main-lobe.

In Fig. 4.21 we can see the information cube for $N_{\mathrm{Tx}} = 2$. Like for the MSP mode, there is no intersection of the curved surfaces. This allows to filter the waveforms via STFAP.

In keeping with the results of the previous section, we strongly recommend to use FIR filtering and the advanced null-steering beam-former LCMV [95]. In section 4.2 it was proven, that the conditions for the antenna pattern are the same for the MSP and the SSC waveforms. Since the angular pulse extent is dependent on the total pulse duration, thus the required number of FIR filter is the same as

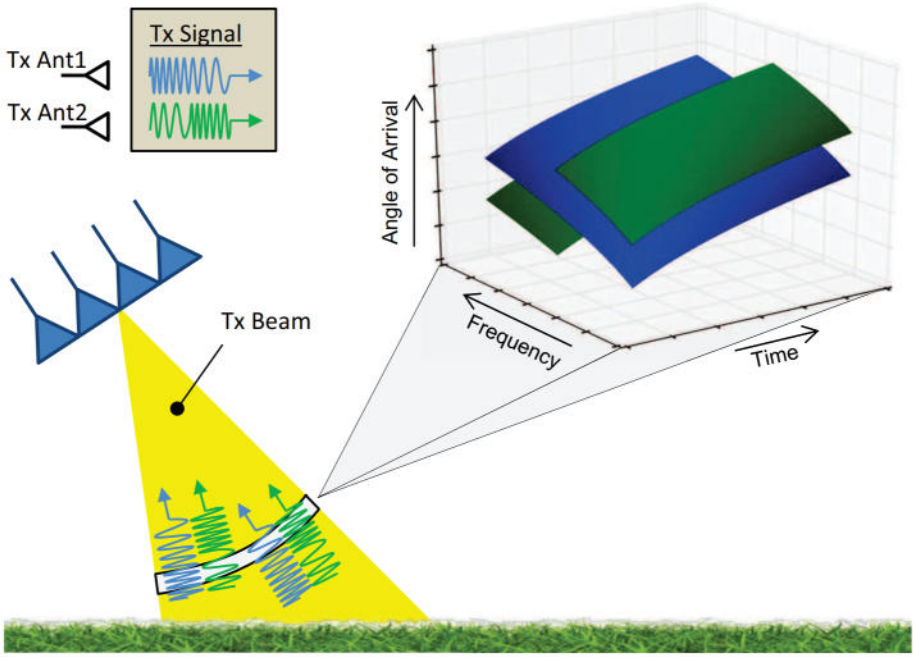


Figure 4.21. Representation of the receive signal from the SSC waveform in angle, time and frequency.

for the MSP mode. Accordingly, with exception of the AoA, it is possible to use the same definitions and equations.

A simulation result of the *AR* can be found in Fig. 4.22. Slight deviations in comparison to Fig. 4.20a can be observed. The reason lies in the fact, that the energy of the second waveform arrives from two angles. While in the MSP mode, the full energy is received from a single angle, in the given case just half the amount of energy is received from a single AoA. Taking the deformation of the antenna pattern due to ground projection into account, obviously both AoA-directions cannot be suppressed equally.

4.6. Waveform Separation of OFDM Chirp Waveforms

Last but not least, we describe the demodulation process of the OFDM chirp waveforms, which have been introduced in section 3.2.2. Because the whole approach has been already described in detail in [9, 82, 104], for completeness of this thesis, it is just briefly summarized here.

Since this waveform type is strongly related to classical OFDM, for the demodulation process, two important requirements must be fulfilled. First, the DFT

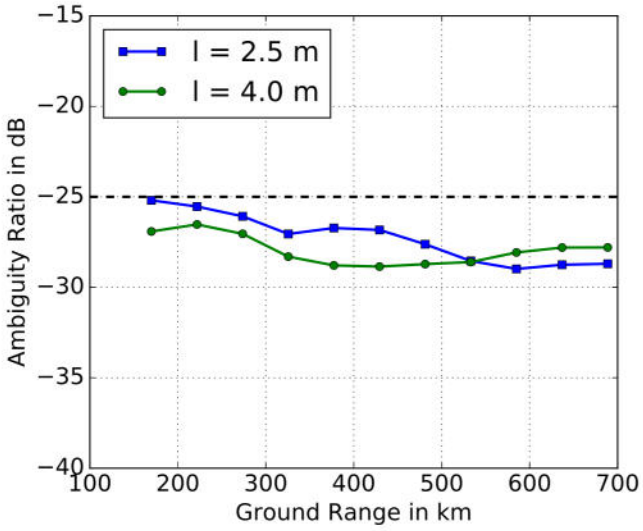


Figure 4.22. Plot of the *AR* with FIR filtering and LCMV-DBF versus ground range for two SSC waveforms with the parameters $h = 700$ km, $f_0 = 9.6$ GHz, $l_{\text{ant,el}} = [2.5\text{ m}, 4.0\text{ m}]$, $\tau_p = 120\ \mu$s, $N_{\text{FIR}} = 6$ and $M_{\text{FIR}} = 100$.

window length at the demodulator must be the same as that of the modulator DFT window. Second, the complete receive waveform has to be present within this window. Since it is known from section 3.1, that in SAR the delay spread contradicts this requirement, Kim proposed in [9] an innovative process to overcome this issue. As illustrated in the block diagram in Fig. 4.23, the next four paragraphs lead through this approach.

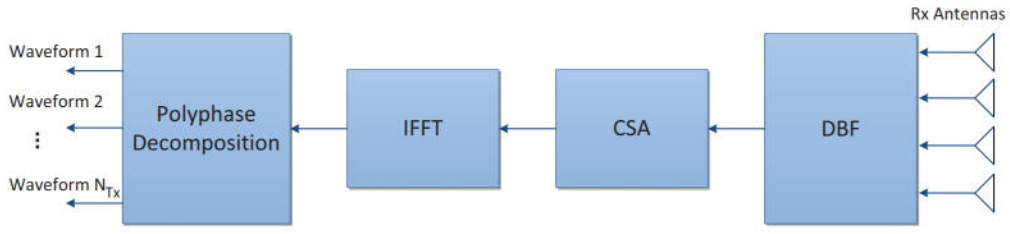


Figure 4.23. Block diagram of the demodulation process for the OFDM chirp waveforms.

Digital Beam-Forming on Receive

With DBF, the whole illuminated swath is divided into several sub-swathes of the maximum extension as defined in Eq. (3.3). This avoids signal ambiguities along range caused by the repeating structure of the OFDM chirps.

Circular Shift Addition (CSA)

For each sub-swath, a process called Circular-Shift Addition (CSA) is used. It is analogous to the cyclic prefix in conventional OFDM communication systems in order to eliminate inter symbol interferences caused by the time spreading of the channel (fading effect [83]). While in classical OFDM this cyclic prefix is added to the waveform on the transmit side, for the OFDM-chirp waveform separation, this must be done in the receiver.

In this process, the last samples of the received signal are added to the beginning of the signal as shown in Fig. 4.24 and only the first $N_c = f_S \cdot \tau_p$ samples are considered for demodulation. As in case of cyclic prefix, the CSA process also converts the linear convolution between the transmit signal and the channel impulse response into circular convolution in time domain or simply a product in frequency domain.

Inverse Discrete Fourier-Transform

The last two steps removed the fading effect, while preserving the information about the signal delay. In time-domain, the transmit waveforms still overlap, but the sub-carrier in frequency domain show the same interleaved characteristic as depicted in Fig. 3.5. Like in conventional OFDM demodulation, an inverse DFT transforms the time domain signal to frequency domain.

Polyphase Decomposition

Because it is known, that every N_{Tx}-th sub carrier belongs to the same waveform, with the polyphase decomposition the signal spectrum is split up to the corresponding transmit channels, respectively. Now, the transmit channels are separated and further SAR processing can be applied for every transmit channel separately.

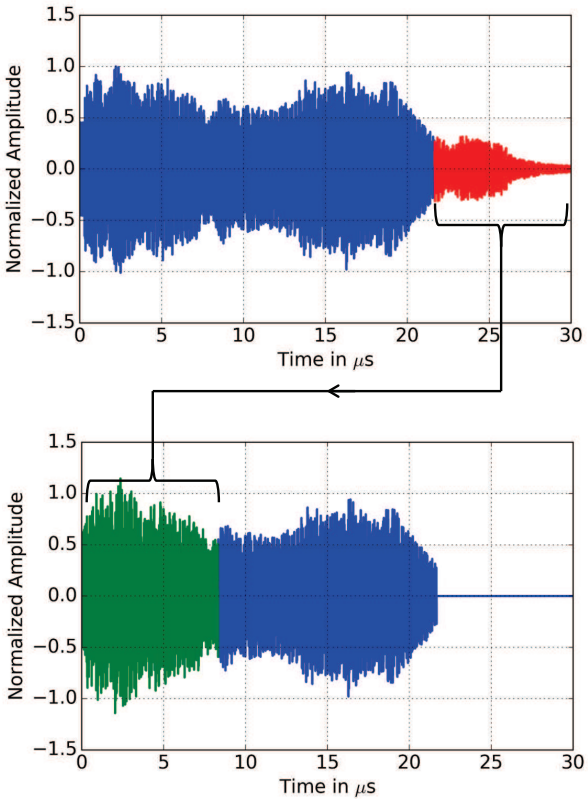


Figure 4.24. Illustration of the circular-shift addition on a typical receive signal.

5. Topography-Adaptive Elevation Beam-Forming on Receive

DBF-SAR and especially the suggested MIMO signal processing concept from the last chapter, require an antenna with narrow half-power beam-width. Under the assumption of a precisely known geometrical relation between the antenna array and the target scene, the used DBF steering vector is calculated. Unfortunately, in most cases this relation is not exactly known due to topographic changes, e.g. mountains. If this is neglected, the synthesized antenna beam will be steered to another direction than that of the signal. Depending on the antenna *HPBW* and the error in the Earth model, the resulting mis-pointing might lead to a significant loss of gain. Additionally, orthogonal waveforms can not be suppressed sufficiently in the MIMO mode.

To handle this issue, in [97] it was suggested to apply an additional algorithm prior to DBF, which estimates from the acquired raw-data the angle of the incident echo signal on the antenna array. This angle is also known as Angle of Arrival (AoA). Thereupon, the DBF steering vector can be adapted to form an antenna beam, which points to the correct direction.

In principle, the algorithm used for AoA estimation returns the maximum of the energy distribution on the antenna array over space. Because the relation between antenna beam pattern and radiated / impinging signal is usually described by means of spectral frequency components [17], it is valid to transfer that task to common spectral estimation algorithms [105]. These spectral estimators are used to obtain the distribution of the signal power over frequency for sampled signals in the time-domain. Due to the strong correspondence between the spatially dependent frequency and *temporal* signal frequency, many kinds of spectral estimators can be used for AoA estimation.

In the meantime, more than twenty different spectral estimation algorithms have been derived [105]. They can be categorized into two classes: non-parametric and parametric methods. Non-parametric estimators evaluate the Power Spectral Density (PSD) of the input signal by a direct and linear analysis of

the whole spectrum. Parametric estimators are also known as model-based estimators, as they are based on an assumed signal model. This model parametrizes the spectrum of known structures, and the used PSD estimator determines the value of the desired parameter. Since parametric estimators use additional information, they lead to more accurate results (if the signal model is correct). SAR is anyway based on a signal model and information about the signal structure and some properties about the geometric relations between SAR and Earth are known. Therefore, the preferred class of high-resolution parametric estimators can be applied. Established parametric algorithms are Spectral MUltiple SIgnal Classification (MUSIC) [106], Root MUSIC [107] and Estimation of Signal Parameters using Rotational Invariance Techniques (ESPRIT) [108]. These estimators are computationally very intensive, because they need to compute a correlation matrix from the received raw data. In addition, such estimators are derived for more common problems and hence are not very effective for SAR.

To fulfill the highest quality standards in DBF-SAR and MIMO-SAR, and to avoid the previously mentioned mis-pointing effect, it is necessary to derive an effective application orientated algorithm. It has been found, that the Matrix Pencil (MP) method, which was originally intended to solve a linear equation system, serves as a good starting point for that [109]. In the meantime, the MP also finds application in some basic angular estimation problems [110, 111] and even for back projection processing of inverse SAR [112]. This parametric approach does not need a calculation of a covariance matrix. With reference to the run-time, this is a significant advantage in contrast to other established methods, such as MUSIC or ESPRIT (a detailed comparison of the run-time between the estimators is given in section 5.4.1). Because the MP method is applied on-board, a concept for a possible practical implementation is given, which enables a precise and stable topography-adaptive elevation DBF in real-time.

The chapter is structured as follows. In the beginning, the detailed problem formulation and error analysis in the case of a mismatch between theoretical topographic model used for the DBF algorithm and reality, is given. After defining some requirements for the estimator, such as high resolution or stability, the MP in its basic form is introduced. Then further improvements on the MP and problem-based adaptions to DBF-SAR are derived. The second section ends with a concept for a practical implementation. To get an impression of the behavior,

capabilities, and performance of the suggested algorithm, the chapter concludes with simulation results.

5.1. Problem Formulation

Up to now, it has been assumed that the geometric relation between radar sensor and the Earth is known and the time-variant receive antenna beam is tracking the echoes according to the underlying geometric model. However, for an unknown topography, this relation is not established. Fig. 5.1 illustrates this distortion for a constant slant range distance r_0 at mountains of height Δh. For a more quantitative analysis, in the following we derive the antenna mis-pointing Θ_{mis} in terms of the vertical offset Δh. In the first step, by making use of the laws of sines and cosines, for certain antenna steering angles, the slant range r_0 can be calculated if no topography is present (cf. Fig. 2.1):

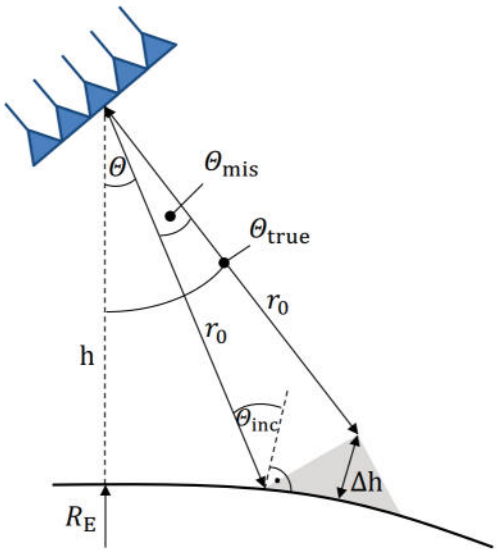


Figure 5.1. Illustration of the antenna mis-pointing due to topographic changes.

$$r_0 = \sqrt{(R_{\text{E}} + h)^2 + R_{\text{E}}^2 - 2(R_{\text{E}} + h)R_{\text{E}} \cdot \cos\left(\arcsin\left(\frac{R_{\text{E}} + h}{R_{\text{E}}} \cdot \sin\Theta\right)\right)}. \tag{5.1}$$

Keeping the slant range r_0 constant, by making use of the law of cosines again, the actual steering angle Θ_{true} at offset Δh can be calculated:

$$\Theta_{\text{true}} = \arccos\left(\frac{r_0^2 + (R_\text{E} + h)^2 - (R_\text{E} + \Delta h)^2}{2(R_\text{E} + h)r_0}\right). \tag{5.2}$$

The difference between the actual steering angle (Eq. (5.2)) and its reference Θ results in the antenna mis-pointing Θ_{mis}:

$$\Theta_{\text{mis}} = \Theta_{\text{true}} - \Theta. \tag{5.3}$$

Fig. 5.2 shows a plot of Eq. (5.3) with $h = 700$ km for the steering angles 15°, 20°, 30°, and 42°. As can be seen, the antenna mis-pointing increases linearly with increasing topographic height. At relatively flat areas with vertical terrain differences of less than 1.5 km, the echo may impinge at the receive antenna with an angular offset of around $0.2° - 0.4°$. Comparing this value with an antenna *HPBW* of 0.5° (cf. sections 4.2.2 and 4.3), in the worst case scenario, the antenna might point to a completely different direction. The suggested space-time-frequency adaptive processing concept will not work under these circumstances and random measurement values will be the result. Accordingly, for a MIMO-SAR with short-term shift-orthogonal waveforms, the nulls of the antenna pattern, for suppression the other waveforms, are also misplaced and the unwanted signal interferences can not be sufficiently suppressed (cf. section 4.6.1).

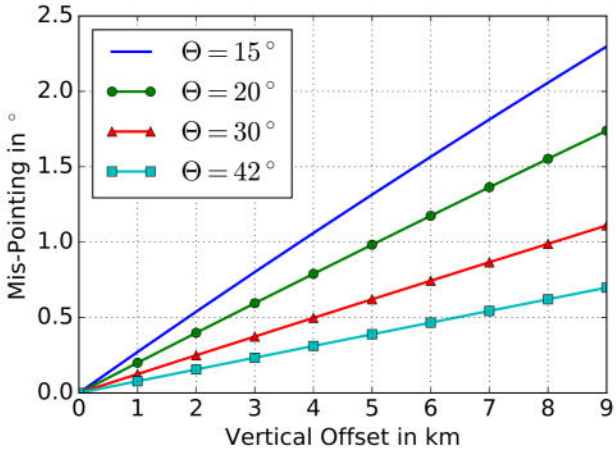


Figure 5.2. Antenna mis-pointing for various terrain heights and steering angles.

5.2. Matrix Pencil Method

In this section, we will derive the algorithm, which estimates the AoA profile along elevation for a certain recorded echo window (i.e. receive interval $1/PRF$). This procedure will be repeated either for each echo window or a group of windows to reduce the computational load. Additional improvements to address inherent SAR-effects on the signal and a concept for practical implementation in real-time on-board are also presented.

5.2.1. Adapted Signal Model for Direction of Arrival Estimation

Like other established AoA estimation methods, such as MUSIC [106], Root MUSIC [107] and ESPRIT [108], the Matrix Pencil (MP) is also based on a point target model with multiple dedicated targets. It is important to note, that any deviations due to extended pulses (cf. section 4.2.1), interfering signals (e.g. MIMO) or extended surface scatterers, result in errors during the calculations and affect the accuracy and stability of the algorithm. For ease of understanding, we start with the simplified point target signal model[1] and we analyze the estimation errors based on simulations at the end of this chapter.

Signal processing and hence also the AoA estimation is done at the digital stage of the receiver. With respect to the model of section 4.1, it is worthwhile to directly write the receive signal in its discretized form:

$$\overline{\boldsymbol{u}}[p] = \overline{\boldsymbol{A}}[p] \cdot \overline{\boldsymbol{\sigma}}^0 \cdot s_0[p - p_0] + \boldsymbol{n}[p], \tag{5.4}$$

while p is the index of the time sample according to Eq. (4.33) and $\overline{\boldsymbol{\sigma}}^0$ is the column vector of backscatter amplitudes (with the size: N_{Tar}). s_0 is a single transmit waveform, p_0 is the round-trip time-delay from the first transmit antenna to the target and back to the first receive antenna element, and $\boldsymbol{n}$ is Additive White Gaussian Noise (AWGN). $\overline{\boldsymbol{A}}$ is the steering matrix:

$$\overline{\boldsymbol{A}} = \left[\overline{\boldsymbol{a}}_0, \overline{\boldsymbol{a}}_1, ..., \overline{\boldsymbol{a}}_{N_{\mathrm{Tar}}-1}\right], \tag{5.5}$$

[1] Any influences by the antenna pattern are neglected for ease.

of the dimensions $N_{\mathrm{Rx}} \times N_{\mathrm{Tar}}$. N_{Tar} is the number of point targets and $\overline{\boldsymbol{a}}_m$ are the steering vectors:

$$\overline{\boldsymbol{a}}_m = \left[z_m^0, z_m^1, ..., z_m^{N_{\mathrm{Rx}}-1}\right]^{\mathrm{T}}. \tag{5.6}$$

The overline is used to distinguish from Eq. (4.8). In Eq. (4.8) the columns were used for the transmit channels, while in this chapter this dimension is used for the individual targets. Multiple transmitters are ignored, because the short-term shift-orthogonal waveforms from chapter 3 lead - due to their structure - to ambiguities. With the known signal structure, also the relative positions of the ambiguities to the main signal are known and can be excluded by plausibility arguments. z_m are the complex weights:

$$z_m[p] = \exp\left(\mathrm{j} \cdot \Delta\varphi_m[p]\right) = \exp\left(\mathrm{j} \cdot \frac{2\pi}{\lambda} \cdot d \cdot \sin(\vartheta_m[p])\right). \tag{5.7}$$

$\Delta\varphi_m$ is the phase shift of the receive signal between two adjacent receive channels and ϑ_m is the respective AoA. A graphical illustration can be found in Fig. 4.1. It is important to note, that the exponential terms lead to a phase shift of $\overline{\boldsymbol{u}}$ and do not distort the amplitude. If z_m is drawn in the complex plane, the values lie exactly on the unit circle. However, additional noise contributions cause distortions, which adversely affect these positions. In the next subsection, we concentrate on the undistorted case, and afterward we introduce advanced processing methods to improve the estimator's accuracy and stability in presence of noise and other interferences.

5.2.2. Angle of Arrival Estimation via the Matrix Pencil

A matrix pencil in mathematics is a linear equation system, which consists of matrices with complex elements [109]. The equations can be solved by finding the generalized eigenvalues of the MP. This standard task in mathematics was adapted to angular estimation problems in electrical engineering. The first derivations can be found in [110, 111].

To form the MP, at first the received raw-data signal at a certain instant of time p is arranged into a matrix of form

$$\boldsymbol{Y}[p] = \begin{bmatrix} \overline{u}_0[p] & \overline{u}_1[p] & \cdots & \overline{u}_L[p] \\ \overline{u}_1[p] & \overline{u}_2[p] & \cdots & \overline{u}_{L+1}[p] \\ \vdots & \vdots & \ddots & \vdots \\ \overline{u}_{N_{\mathrm{Rx}}-L-1}[p] & \overline{u}_{N_{\mathrm{Rx}}-L}[p] & \cdots & \overline{u}_{N_{\mathrm{Rx}}-1}[p] \end{bmatrix}. \tag{5.8}$$

A matrix with this symmetric arrangement is also called Hankel matrix. The pencil parameter L determines its shape and must satisfy the conditions

$$N_{\mathrm{Tar}} \leq L \leq N_{\mathrm{Rx}} - L \quad \text{if} \quad N_{\mathrm{Rx}} \quad \text{is even} \tag{5.9}$$

$$, N_{\mathrm{Tar}} \leq L \leq N_{\mathrm{Rx}} - L + 1 \quad \text{if} \quad N_{\mathrm{Rx}} \quad \text{is odd.} \tag{5.10}$$

In principle, L can be arbitrarily chosen within these intervals. As L determines later the amount of overlap between the two formed antenna sub-arrays, its value has obviously an effect on the accuracy of the estimated angle. In dependence of the noise level of the raw data, we recommend to choose L within the interval $[N_{\mathrm{Rx}}/3, N_{\mathrm{Rx}}/2[$ for either having a more efficient noise suppression or having an improved resolution. A more detailed analysis on this parameter is given in the simulation section at the end of the chapter.

At this point, already one important limitation of the MP method becomes noticeable. To estimate a total number of N_{Tar} angles, at least $2N_{\mathrm{Tar}}$ antenna elements are necessary for an even number of N_{Tar} and at least $2N_{\mathrm{Tar}} - 1$ antenna elements are necessary for an odd number of N_{Tar}. In addition, due to the matrix arrangements, at least four receive antennas are required. However, for a spaceborne DBF-SAR a large number of antenna elements is anyway required (compare section 4.2.2) and this limitation is not an issue for the definition of $\boldsymbol{Y}[p]$.

From Eq. (5.8) we can define two overlapping sub-matrices $\boldsymbol{Y}_0[p]$ and $\boldsymbol{Y}_1[p]$, which are shifted by a single element:

$$\boldsymbol{Y}_0[p] = \begin{bmatrix} \overline{u}_0[p] & \cdots & \overline{u}_{L-1}[p] \\ \overline{u}_1[p] & \cdots & \overline{u}_L[p] \\ \vdots & \ddots & \vdots \\ \overline{u}_{N_{\mathrm{Rx}}-L-1}[p] & \cdots & \overline{u}_{N_{\mathrm{Rx}}-2}[p] \end{bmatrix} \quad \text{and} \tag{5.11}$$

$$\boldsymbol{Y}_1[p] = \begin{bmatrix} \overline{u}_1[p] & \cdots & \overline{u}_L[p] \\ \overline{u}_2[p] & \cdots & \overline{u}_{L+1}[p] \\ \vdots & \ddots & \vdots \\ \overline{u}_{N_{\mathrm{Rx}}-L}[p] & \cdots & \overline{u}_{N_{\mathrm{Rx}}-1}[p] \end{bmatrix}. \tag{5.12}$$

These matrices correspond to the antenna sub-arrays, which are formed to estimate the linear spatial shift of the impinging signal between both sub-arrays. To find the AoAs, in an intermediate step, we are looking for the poles $z_m[p]$ of the receive signal, which can be directly obtained by calculation of the generalized eigenvalues $\boldsymbol{\Psi}$ (e.g. with the standard QR algorithm) of the equation system

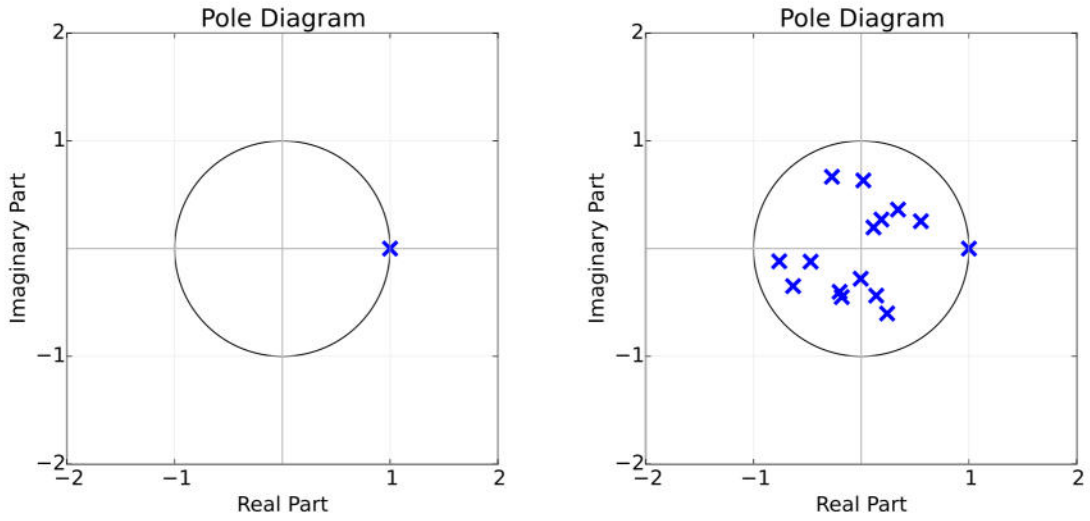
$$\boldsymbol{Y}_0^{\dagger}[p] \cdot \boldsymbol{Y}_1[p] = \left\{ \left[\boldsymbol{Y}_0^{*}[p] \cdot \boldsymbol{Y}_0[p] \right]^{-1} \cdot \boldsymbol{Y}_0^{*}[p] \right\} \cdot \boldsymbol{Y}_1[p] = \boldsymbol{\Psi} \cdot \boldsymbol{\Gamma}, \tag{5.13}$$

where $\boldsymbol{Y}_0^{\dagger}[p]$ denotes the Moore-Penrose pseudo inverse of $\boldsymbol{Y}_0[p]$ and $\boldsymbol{\Gamma}$ are the generalized eigenvectors. A more detailed derivation and decomposition of this equation can be found in appendix A.

With respect to Eq. (5.7), it is known that the eigenvalues $\boldsymbol{\Psi}$ must lie at the unit circle, because the only difference between the receive signals at the individual receive antennas is a phase shift. All other eigenvalues are not of interest. By tolerating a margin around the unit circle, which is dependent on the *SNR* of $\boldsymbol{Y}[p]$, an estimate of N_{Tar} can be obtained. To give an example, Fig. 5.3a shows a plot of the pole diagram containing the eigenvalues for $N_{\mathrm{Tar}} = 1$, $N_{\mathrm{Rx}} = 32$ and $L = 1$. The single estimated eigenvalue lies exactly at the unit circle and can be treated as a plausible value. In Fig. 5.3b we can find the pole diagram with the same simulation parameters as before, but with $L = 15$. Now, more values than necessary are estimated, while all false estimates are randomly distributed and not lying on the unit circle.

Finally, the demanded angles $\breve{\vartheta}_m[p]$ can be obtained from the imaginary parts of the found eigenvalues through solving Eq. (5.7) for $\breve{\vartheta}_m$:

$$\breve{\vartheta}_m = \arcsin\left(\frac{\mathrm{Im}\{\ln(z_m)\}}{\frac{2\pi}{\lambda} \cdot d} \right). \tag{5.14}$$



(a) $L = 1$. **(b)** $L = 15$.

Figure 5.3. Pole diagrams with the estimated eigenvalues $z_m[p]$ using the MP method for different pencil parameters, $N_{\text{Tar}} = 1$, $N_{\text{Rx}} = 32$.

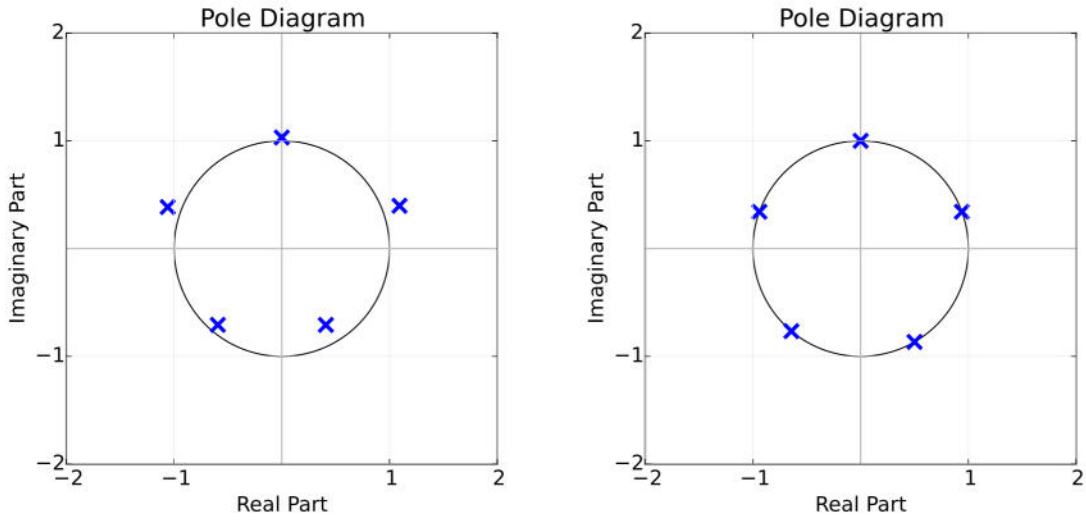
Because the generalized eigenvalues of Eq. (5.13) can not be determined accurately at higher noise levels of the raw data, the variance of the estimated angles will also increase. For an improved accuracy of noisy data and to adapt this preliminary method to the SAR case, some extensions are given in the next subsections.

5.2.3. Total Least Squares Matrix Pencil

The idea behind the Total Least Squares Matrix Pencil (TLS-MP) makes use of the knowledge that the poles of the generalized eigenvalues $z_m[p]$ must lie exactly on the unit circle [113]. Eigenvalues, which are perturbed by noise, lie close to the unit circle, because the pseudo-inverse of Eq. (5.13) can not be determined accurately. Via total least squares regression, these poles are *projected* to the unit circle (cf. Fig. 5.4) and more accurate results can be achieved.

The first computation step of the TLS-MP is the Singular Value Decomposition (SVD) of $\boldsymbol{Y}$ from Eq. (5.8):

$$\boldsymbol{Y} = \boldsymbol{\Lambda}_{\text{L}} \cdot \boldsymbol{\Sigma} \cdot \boldsymbol{\Lambda}_{\text{R}}^{\text{H}}, \tag{5.15}$$



(a) Generalized eigenvalues perturbed by noise.

(b) Generalized eigenvalues projected on the unit circle by TLS.

Figure 5.4. Principle of the Total Least Squares Matrix Pencil on hand of the pole diagram.

with $\boldsymbol{\Lambda}_{\mathrm{L}}$ and $\boldsymbol{\Lambda}_{\mathrm{R}}$ being the left and right singular vectors, respectively. Σ is a real-valued matrix containing the singular values along the main diagonal. From theory of matrix computations it is known, that $\boldsymbol{Y}$ has N_{Tar} non-zero singular values for the noiseless case ($\boldsymbol{n} = \boldsymbol{0}$). Otherwise, the raw-data matrix $\boldsymbol{Y}$ has more singular values, which are not equal to zero. These erroneous singular values and their corresponding singular vectors are not considered in the TLS-MP method. For this, the number of targets N_{Tar} must be known beforehand. Otherwise, it is recommended to make use of the threshold value μ. This value serves as decision-guidance between plausible and non-plausible singular values of $\boldsymbol{Y}$:

$$\mu \approx 10^{-N_{\mathrm{dig}} \cdot \mu_{\max}}, \tag{5.16}$$

with N_{dig} being the number of significant digits (e.g. $N_{\mathrm{dig}} = 3$) and $\mu_{\max}$ is the real part of the largest estimated singular value z_m:

$$\mu_{\max} = \Re\mathfrak{e}\left\{\max\{z_m\}\right\}. \tag{5.17}$$

N_{dig} is an empirical value chosen in dependence on the *SNR* of $\boldsymbol{Y}$. All eigenvalues greater than μ correspond to a target.

Since it is known, that all eigenvalues $z_m(t)$ with index $m > N_{\text{Tar}}$ are irrelevant, we can define a filtered version of the Hankel matrix as $\boldsymbol{Y}'$:

$$\boldsymbol{Y}' = \boldsymbol{\Lambda}'_{\text{L}} \cdot \Sigma' \cdot \boldsymbol{\Lambda}'^{\text{H}}_{\text{R}}. \tag{5.18}$$

$\boldsymbol{\Lambda}'_{\text{L}}$, Σ' and $\boldsymbol{\Lambda}'_{\text{R}}$ are the sub-matrices of $\boldsymbol{\Lambda}_{\text{L}}$, Σ and $\boldsymbol{\Lambda}_{\text{R}}$, respectively:

$$\begin{aligned} \boldsymbol{\Lambda}'_{\text{L}} &= \boldsymbol{\Lambda}_{\text{L},\{\},\{N_{\text{Tar}},N_{\text{Tar}}+1,\ldots\}}, \\ \Sigma' &= \Sigma_{\{N_{\text{Tar}},N_{\text{Tar}}+1,\ldots\},\{N_{\text{Tar}},N_{\text{Tar}}+1,\ldots\}}, \\ \boldsymbol{\Lambda}'_{\text{R}} &= \boldsymbol{\Lambda}_{\text{R},\{\},\{N_{\text{Tar}},N_{\text{Tar}}+1,\ldots\}}, \end{aligned} \tag{5.19}$$

while the indices ${}_{\{\},\{\}}$ are related to the common sub-matrix notation and denote the rows and columns, which are deleted of the respective matrix.

In analogy to Eq. (5.11) and Eq. (5.12), we form the two sub-matrices $\boldsymbol{Y}'_0$ and $\boldsymbol{Y}'_1$ from $\boldsymbol{Y}'$:

$$\begin{aligned} \boldsymbol{Y}'_0 &= \boldsymbol{\Lambda}'_{\text{L}} \cdot \Sigma' \cdot \boldsymbol{\Lambda}'^{\text{H}}_{\text{R},0} = \boldsymbol{\Lambda}'_{\text{L}} \cdot \Sigma' \cdot \boldsymbol{\Lambda}'^{\text{H}}_{\text{R},\{\},\{1\}}, \\ \boldsymbol{Y}'_1 &= \boldsymbol{\Lambda}'_{\text{L}} \cdot \Sigma' \cdot \boldsymbol{\Lambda}'^{\text{H}}_{\text{R},1} = \boldsymbol{\Lambda}'_{\text{L}} \cdot \Sigma' \cdot \boldsymbol{\Lambda}'^{\text{H}}_{\text{R},\{\},\{N_{\text{Tar}}-1\}}. \end{aligned} \tag{5.20}$$

In the final computation steps of the TLS-MP, we proceed in the same way as for the standard MP. After the calculation of the generalized eigenvalues of the term $\boldsymbol{Y}'^{\dagger}_0 \cdot \boldsymbol{Y}'_1$ (cf. Eq. (5.13)), the AoA $\check{\vartheta}_m[p]$ can be calculated via Eq. (5.14).

5.2.4. Forward-Backward Matrix Pencil

Forward-Backward (FB) averaging is an optimization method for spectral estimation, which was first suggested in [114]. While the FB approach is usually applied to improve the accuracy of MUSIC or ESPRIT, this kind of averaging can also be used for the MP [111]. The restriction of the FB-MP to symmetrical antenna arrays only is not an issue, because, for all the suggested SAR applications, we assume equispaced antenna arrays.

The principle of FB averaging can be summarized in the following way. The elements in Eq. (5.8) are counted with increasing number from the first antenna element onward, which can also be seen as to be the *forward* order. If this Hankel matrix is arranged in the reverse way (the *backward* order starts to count from the last antenna element), the values of the estimated AoAs will be approximately the same with exception of a negative sign and the noise influence. Since it is known, that the raw data is affected by noise and that more independent equations are less sensitive to noise, both ways, the forward and the backward approach are calculated and averaged. This can be done by direct averaging of the raw data of Eq. (5.8):

$$\widetilde{\boldsymbol{Y}} = \frac{1}{2}[\boldsymbol{Y} \cdot \boldsymbol{E} \cdot \boldsymbol{Y}^*] \cdot [\boldsymbol{Y} \cdot \boldsymbol{E} \cdot \boldsymbol{Y}^*]^{\mathrm{H}}, \tag{5.21}$$

with $\boldsymbol{E}$ being the exchange matrix:

$$\boldsymbol{E} = \begin{bmatrix} 0 & \cdots & 0 & 1 \\ \vdots & \iddots & 1 & 0 \\ 0 & \iddots & \iddots & \vdots \\ 1 & 0 & \cdots & 0 \end{bmatrix}. \tag{5.22}$$

If the FB-MP method should be used, then in Eq. (5.11) and Eq. (5.12) $\boldsymbol{Y}$ must be substituted by $\widetilde{\boldsymbol{Y}}$, (see footnote [2]).

From the laws of matrix multiplication it is known, that Eq. (5.21) can just be calculated, if $\boldsymbol{Y}$ has a quadratic form. This can be achieved by setting the pencil parameter to $L = (N_{\mathrm{Rx}} - 1)/2$ for an odd number of N_{Rx}. For an even number of N_{Rx}, the first or the last antenna element must be neglected.

From a numerical point of view, the variance of the estimated angles should be lower, because the FB-MP reduces the noise by averaging of independent equations. Unfortunately, the FB-MP does not always bring a benefit. In space-borne DBF-SAR, we expect to have much more antenna elements than AoAs ($N_{\mathrm{Tar}} << N_{\mathrm{Rx}}$) and thus the pencil parameter L can not be chosen ideally. The

[2] In a worst case scenario, the computation time for the full MP might be large due to the size of $\widetilde{\boldsymbol{Y}}$. If there is are several parallel-computational cores of the Central Processing Unit (CPU), the Island Algorithm will be significantly faster in a practical implementation [115].

output of the FB-MP is a total number of L AoAs, of those all can be considered as plausible values. In most cases, it is finally impossible to differentiate between a true and a *false* estimate. This effect has been also observed by Marshall in [116]. Thus, the FB-MP method is excluded in further considerations of this thesis.

5.2.5. Modification of the Matrix Pencil Method for Extended Angular Coverage

Up to now, in the last two subsections, we have proposed methods to improve the accuracy and stability of the basic MP in presence of noise. In this subsection we address to SAR inherent signal characteristics, since the point target model of Eq. (5.4) is an idealized point of view and neglects finite pulse durations in combination with extended scatterers.

From section 4.2.1 it is known, that the receive signal at each instant of time is the sum signal of all echoes within the angular pulse extent (cf. Eq. (4.13)). Accordingly, the true AoA spans an angular interval, while the MP needs a dedicated number for N_{Tar}. As a solution, prior known properties of the used chirp signal and an approximation of the geometrical structure of the scene can be used. Referring to [117], Hu decreased the variance of the MP estimator by using band-pass filters. The raw-data $\boldsymbol{Y}[p]$, which is used for the MP, is then less disturbed by noise, leading to a shift of the estimated poles closer to the unit circle. It was also proposed in section 4.3.2 to implement narrow-band band-pass filters in the receive channels, while the purpose was to reduce the effective pulse duration of the chirp signal – and hence also the angular pulse extent[3]. In contrast to [117], where pre-filtering was used to remove noise outside the spectrum of the signal, in the following case we additionally filter a part of the chirped pulse.

Apart from reducing the angular pulse extent and filtering noise, there is yet a further benefit of using frequency filters. Insofar the system complexity and the available amount of computational power for the calculation of the MP allows, we recommend to use a whole filter bank instead of a single filter. By following this approach, it is possible to estimate the AoA for each spectral part of the whole chirp (cf. Fig. 5.5). The individual values can be used for averaging to

[3] In a MIMO-SAR with short-term shift-orthogonal waveforms this approach also helps to suppress the other orthogonal transmitted waveforms, which are irrelevant for AoA estimation (cf. sections 4.4 and 4.5). Ambiguous AoA from the other waveforms can be easily excluded by using plausibility criteria, since their positions are approximately known with respect to the first signal.

lower the variance of the estimated angles. However, the angular segments do not have the same AoA and, therefore, they can not be directly averaged. Because the MP is applied at several instants of time and the segments of the divided-pulse shift over time, after certain delays they have equal positions. This means an additional buffer is required to correlate the angles of the extended pulse to different time instants. It should be noted, that this idea of averaging is strongly related to the moving window average approach in the next subsection.

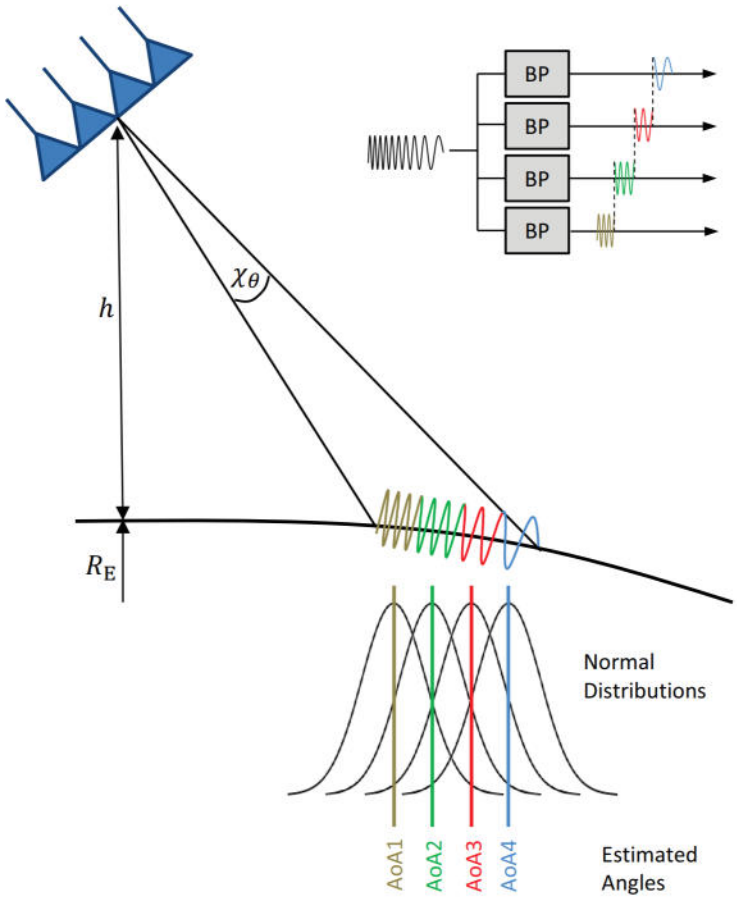


Figure 5.5. At a certain instant of time, the echo signal is received from an angular interval. After band-pass filtering, the chirp is synthetically narrowed and accordingly also the angular pulse extent. With respect to the maximum of each normal distribution after angle estimation, the AoA for each bin can be estimated.

To define the required filter bandwidth, it is necessary to have a look on the resolution limit of the MP and on the pulse extent first. Generally, the accuracy of an estimator is given by the PSD function, which is, in turn, dependent on the antenna dimensions and the *SNR* of the receive signal [105]. To identify two

point-like objects with individual AoAs, the sum of both PSD functions must give a unique result with two peaks. For closer angular separations, there is only one peak and just a single AoA can be estimated. In the following, we denote this angular limit as δ_{MP}. As we will see in later simulation results, in case of the MP, a plausible value is 1/10 of the antenna *HPBW* (for typical *SNR* values of 10...25 dB). This limit is equal to the maximum acceptable angular pulse extent (cf. Eq. (4.13)). Because χ_Θ varies over Θ, we take its maximum at the near edge of the swath and calculate the ratio $\max\{\chi_\Theta(\Theta)\}/\delta_{\mathrm{MP}}$, which gives the number of angular segments in which the pulse must be divided. The required filter bandwidth is the total signal bandwidth B divided by the number of segments:

$$B_{\mathrm{BP}} = \frac{B \cdot \delta_{\mathrm{MP}}}{\max\{\chi_\Theta(\Theta)\}}. \tag{5.23}$$

To give an example, for the values $\delta_{\mathrm{MP}} = 0.05°$, $B = 300$ MHz and $\max\{\chi_\Theta(\Theta)\} = 4.5°$, we get a reasonable filter bandwidth of $B_{\mathrm{BP}} \approx 3.3$ MHz. It turns out, that the filter bandwidth is substantially narrower than the chirp bandwidth. Since it is known that narrow band-pass filter at high frequencies are difficult to design, we recommend to filter the raw-data signal after down-conversion of the receive signal. Finally, the whole receive signal is split into 300 MHz / 3.3 MHz ≈ 91 individual segments.

5.2.6. Moving Window Average

In [118] is was proposed to use several independent snapshots in time for averaging. Under the assumption of single-tone signals only, the Hankel matrix of Eq. (5.8) can be appended side by side to form a huge matrix. With the minimum norm solution of this equation system, a more accurate result can be achieved. This idea was named multiple-snapshot Matrix Pencil. With reference to chapter 2, in radar and SAR, we are using frequency modulated signals and thus the signal characteristics will change between different snapshots in time. If the concept from [118] were to be applied for chirp signals, the averaged phase of the raw data signal would tend to zero and no plausible AoA could be estimated. However, in view of the very low *SNR* of the receive signals in a spaceborne SAR, because of the relatively large free-space attenuation, it is highly recommended to make use of an additional averaging method. Under the assumption of a fully

coherent radar system, it is suggested to compute the whole MP for each snapshot individually and to apply afterward on the obtained angles a moving window average to achieve a higher accuracy.

If this approach is followed, it must be considered, that due to the side-looking geometry in SAR, the AoA shifts continuously along range over time (cf. Eq. (4.30)) and an averaging over time will also lead to erroneous results. At this point we can take benefit of the limited accuracy of the estimator. By defining a window of size lower than the accuracy limit of the MP, it is possible to average over the samples within such a window without estimation of erroneous angles. With respect to the Time of Arrival (ToA) of the receive signal, this window shifts continuously over the swath. In the following, we will derive an expression for determination of the maximum number of snapshots N_{sn}, which can be used for this averaging method.

At first we have to first define the maximum size of a resolved range cell. For that, Eq. (4.13) can be equivalently utilized by using the analogies *angular pulse extent* $\leftrightarrow$ *accuracy of the estimator* and *minimum slant range extent* $\leftrightarrow$ *maximum size of a range cell*. After rearrangement to the slant range extent χ_ρ, we get:

$$\chi_\rho = \delta_{\mathrm{MP}} \cdot (R_{\mathrm{E}} + h) \cdot \left(\frac{(R_{\mathrm{E}} + h) \cdot \cos(\Theta)}{\sqrt{R_{\mathrm{E}}^2 - ((R_{\mathrm{E}} + h) \cdot \sin(\Theta))^2}} - 1 \right) \cdot \sin(\Theta). \tag{5.24}$$

A plot of this equation with the parameters of a typical spaceborne DBF-SAR sensor, which are listed in Tab. 5.1, can be found in Fig. 5.6. In Fig. 5.6, the graph of the slant range extent χ_ρ increases with increasing antenna steering angle. The minimum slant range extent is $\chi_\rho = 190.4$ m at $\Theta = 15°$. Since this extent is equal to the maximum size of the range cell, we can calculate the number of acquired samples within this cell:

$$N_{\mathrm{el}} = \left\lfloor \chi_\rho \cdot 2 \cdot f_{\mathrm{S}}/c \right\rfloor, \tag{5.25}$$

while $\lfloor\ \rfloor$ denotes the floor function. The factor of 2 is required because the slant range extent is related to the two-way propagation of the radar signal and just half of its true duration. With reference to Fig. 5.6, this number can be even increased for larger steering angles. But if a band-pass filtered signal is used

Table 5.1. Assumed typical parameters of a spaceborne SAR for AoA estimation.

Description	Parameter	Value
spatial resolution azimuth, range	$\delta_{\text{sa}} = \delta_{\text{rg}}$	0.5 m
antenna tilt angle w.r.t. nadir	Θ_{tilt}	28.5°
off-nadir steering angle of antenna	Θ	15° ... 42°
signal wavelength (center)	λ	3.16 cm
signal bandwidth	B	300 MHz
pulse duration	τ_{p}	120 μs
sampling frequency	f_{S}	$1.2 \cdot B = 360$ MHz
duration of recorded echo-window	τ_{echo}	1.8 ms
no. of samples fast-time	N_{sn}	650000
no. of receive antenna elements in elevation	$N_{\text{Rx,el}}$	43
no. of receive antenna elements in azimuth	$N_{\text{Rx,az}}$	3
antenna element separation	d	3λ
orbit height	h	700 km

(cf. previous subsection), the sampling frequency will be significantly reduced to $f_{\text{S}} = 1.2 \cdot B_{\text{BP}}$. Therefore, we recommend not only to average along elevation, but also along azimuth.

Following the requirement for azimuth sampling via the *PRF* (cf. Eq. (2.22)) and assuming, that the observed scene does not change rapidly within an azimuth cell of extension l_{cell}, it is reasonable to additionally average over a total number of

$$N_{\text{az}} = \lfloor l_{\text{cell}} / \delta_{\text{sa}} \rfloor \tag{5.26}$$

samples along azimuth.

To determine the total number of snapshots, which can be used for the moving window average MP, the snapshots along elevation and azimuth must be multiplied. Taking multiple receive channels along azimuth into account, the maximum number of snapshots, which can be used for a single AoA is given by

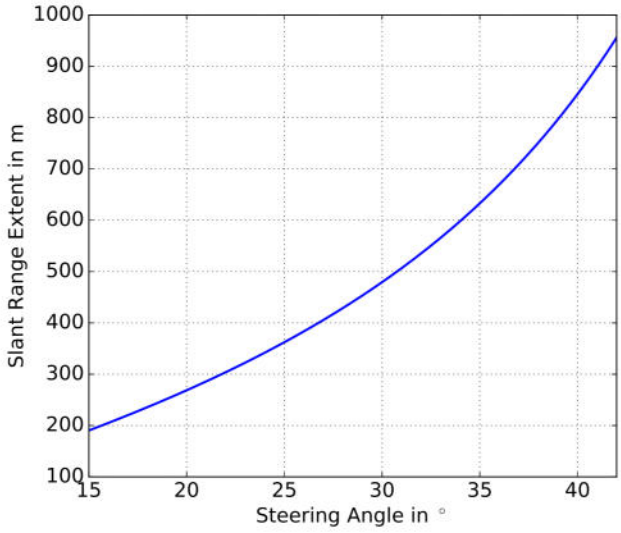


Figure 5.6. Slant range extent for an angular extent of $\chi_\Theta = 0.05°$ in dependence of the steering angle Θ at an orbit height over the Earth's surface of 700 km.

$$N_{\text{sn}} = N_{\text{el}} \cdot N_{\text{az}} \cdot N_{\text{Rx,az}}. \tag{5.27}$$

Using the values of Tab. 5.1 and $l_{\text{cell}} = 10.0$ m, we get:

$$\begin{aligned} N_{\text{el}} &= \left\lfloor 190.4\ \text{m} \cdot 2 \cdot 3.6\ \text{MHz} / 3 \cdot 10^8 \text{m/s} \right\rfloor = 4\ \text{samples}, \\ N_{\text{az}} &= \lfloor 10.0\ \text{m} / 0.5\ \text{m} \rfloor = 20\ \text{samples}, \\ N_{\text{sn}} &= 4 \cdot 20 \cdot 3 = 240\ \text{samples}, \end{aligned} \tag{5.28}$$

where we have used the more plausible sampling frequency of $1.2 \cdot B_{\text{BP}} = 3.6$ MHz for the band-pass MP. If the available computational resources allow averaging over so many values, this MP add-on will decrease the variance of the estimated angle significantly. Simulation results for the accuracy for different numbers of snapshots are given in the subsequent section 5.3.2.

It is important to note, that the moving window average can also be used in combination with the TLS-MP and the FB-MP.

5.2.7. Practical Implementation

In this subsection, we concentrate on the advanced TLS-MP with band-pass filtering and moving window average, since it is supposed to be the optimum choice for topography-adaptive DBF on receive in SAR.

Fig. 5.7 shows the simplified block diagram of the MP processor. Starting with the receive antennas, the received signals are down-converted to the IF band, digitized with Analog-to-Digital Converters (ADC) and calibrated to compensate hardware errors and their effects. As it was suggested in the last subsection, in each receive channel, band-pass filters select a narrow frequency band within the chirp bandwidth to reduce the effective pulse duration. To preserve the energy of the whole pulse, a bank of filters is used. A re-sampling with a lower sampling frequency, which is tailored to the bandwidth after filtering, lowers the overall computational complexity. In the following block, the TLS-MP algorithm is calculated. Not mentioned yet is the plausibility check, which is placed directly behind the TLS-MP. Since the MP is an estimator and its robustness is completely dependent on the acquired raw data, false estimates can not be excluded. From plausibility considerations, an angular interval can be defined, from which the echo will be expected. If the estimated angle lies within this interval, it passes the check, while otherwise a theoretical value is used[4]. The estimated AoAs are stored in a short-term buffer for a few samples, which were acquired within an angular resolution cell (compare moving window average MP in section 5.2.6). After the first averaging, the output is routed to a further averaging block, which computes the mean-values over the azimuth channels, because all aforementioned steps are parallelized along the azimuth dimension of the antenna array. Following the system chain further, the next buffer is used for the estimated angles along the azimuth slow-time. An implementation of this buffer as ring buffer is recommended, because only the last computed values are of interest. A final averaging of the estimated AoA over several Pulse Repetition Intervals (*PRI*) leads to highly accurate values, which can be used to adapt the beam-forming weights with respect to the estimated angle along elevation.

If multiple angles are estimated at the same time (cf. Fig. 5.1), separate buffers for the other AoA are required. The rest of the DBF and image processing must then be designed flexibly enough, to be adaptive to the appropriate scene.

[4]Alternatively, in substitution of the theoretical value also a mean value of the fore and aft estimated angle along range or a previously estimated angle can be used.

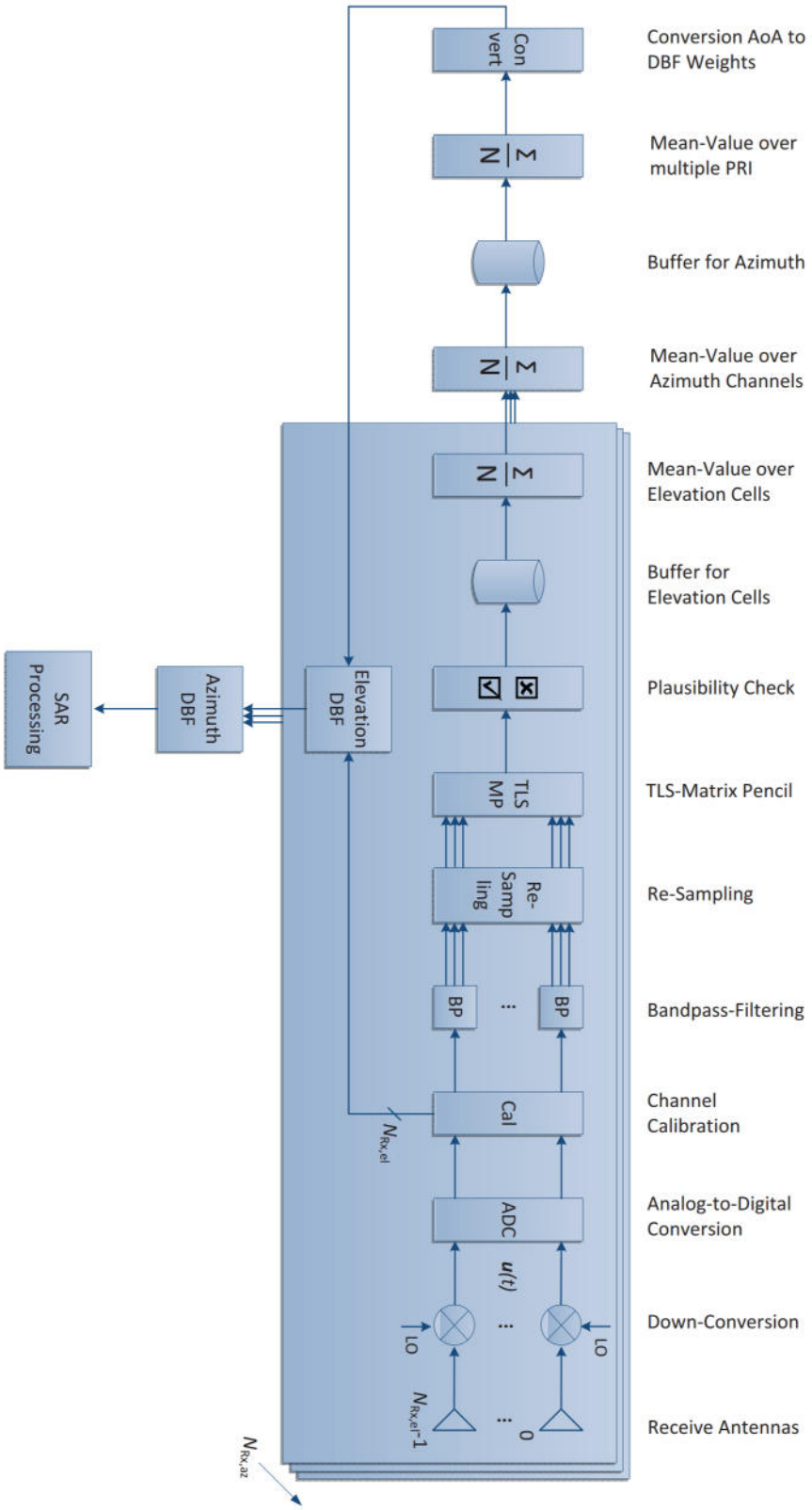


Figure 5.7. Practical implementation of the Matrix Pencil Method in a DBF-SAR system.

5.3. Performance Analysis

To get an insight into the behavior and accuracy of the MP, a series of simulations have been performed. For comparison with AoA estimators, which are established in the field of DBF, the algorithms Spectral MUSIC, Root MUSIC and LS-ESPRIT have been implemented [105]. An overview of the algorithms can be found in appendix B. The first subsection deals with the computational complexity of the algorithms. In the second subsection, basic simulation tasks with a single point target were performed. The remaining part of this section focuses on the MP itself with scenarios containing multiple point targets and targets with spatial extension. Before running the simulations, already some results can be noted. According to [105], it is expected that the accuracy of the estimators can be improved by changing the used parameters in the following way:

- Increasing the *SNR* of the received echo signal
- Increasing the physical length l of the antenna (at keeping the number of antenna elements fixed)
- Increasing the number of antenna elements N_{Rx} (at keeping the aperture length constant)
- Decreasing the angular distance of the AoA from the antenna's broadside direction: $\min\{|\Theta - \Theta_{\mathrm{tilt}}|\}$
- Increasing the number of independent snapshots N_{sn} (i.e. increasing the sample size for averaging)

This prediction is the result of derivations by the Cramer-Rao Lower Bound (CRLB). This bound gives the accuracy of an arbitrary estimator in terms of its input parameters. Quantitative results can be found in the corresponding subsections in the following.

To have a common basis for all simulations, a spaceborne DBF-SAR with the system parameters listed in Table 5.1 serves as reference for all simulations. Estimators, which require band-pass filters, use a filter bandwidth of $B_{\mathrm{BP}} = 2.5$ MHz. Regarding the practical realization, the output signal of each filter has also been re-sampled to the lower sampling frequency of $f_{\mathrm{S}} = 1.2 \cdot B_{\mathrm{BP}} = 3.0$ MHz.

5.3.1. Evaluation of the Computational Complexity

Usually, the computational complexity of an algorithm is expressed using the big O notation $\mathcal{O}$ [119]. It describes the asymptotic behavior of the algorithm's run-time if the arguments (e.g. Tab. 5.1) tend to a certain value. This has the significant advantage, that the comparison is fair and independent of the implementation (programming style and language), operating system, and computer. Unfortunately, a straightforward comparison between the estimation algorithms of this chapter is still difficult, since the covariance matrix for Spectral MUSIC, Root MUSIC and LS-ESPRIT is computed for the whole acquired echo window with N_{sn} samples. Thus, the swath is divided into smaller sub-swath cells, while each cell consists of a total number of $N_{\mathrm{sn,sub}} = N_{\mathrm{sn}} / N_{\mathrm{subsw}}$ samples. Then the algorithms are repeatedly applied to finally cover the full swath.

The computational complexities of the proposed estimators are (for more detailed derivations see appendix B):

Complexity MP:

$$N_{\mathrm{sn}} \cdot \mathcal{O}\Big(|3L^2 \cdot N_{\mathrm{Rx}} - 2L^3| + (N_{\mathrm{Rx}} - L)^3\Big), \tag{5.29}$$

Complexity TLS-MP:

$$N_{\mathrm{sn}} \cdot \mathcal{O}\Big(L^3 + |3(N_{\mathrm{Rx}} - L) \cdot (N_{\mathrm{Tar}} - 1) \cdot (2 + L)| + |3L^2 \cdot N_{\mathrm{Rx}} - 2L^3| + |(N_{\mathrm{Rx}} - L)^3|\Big), \tag{5.30}$$

Complexity Spectral MUSIC:

$$N_{\mathrm{subsw}} \cdot \mathcal{O}\Big(N_{\mathrm{sn,sub}}^3 + N_{\mathrm{sn,sub}}^3 N_{\mathrm{Rx}}(N_{\mathrm{Rx}} - N_{\mathrm{Tar}}) + N_{\mathrm{sn,sub}} N_{\mathrm{Rx}}^2\Big), \tag{5.31}$$

Complexity Root MUSIC:

$$N_{\mathrm{subsw}} \cdot \mathcal{O}\Big(4N_{\mathrm{sn,sub}}^3 + N_{\mathrm{sn,sub}}^2(N_{\mathrm{Rx}} - N_{\mathrm{Tar}}) + N_{\mathrm{sn,sub}} N_{\mathrm{Rx}}^2 + N_{\mathrm{Tar}} \cdot \log\{N_{\mathrm{Tar}}\} + 1\Big), \tag{5.32}$$

Table 5.2. Run-time of the proposed estimators for the assumed system of Tab. 5.1. $L = 3$, $N_{\mathrm{Tar}} = 3$ and $N_{\mathrm{subsw}} = 1000$.

Algorithm	$N_{\mathrm{Rx}} = 31$ $B = 100$ MHz	$N_{\mathrm{Rx}} = 31$ $B = 300$ MHz	$N_{\mathrm{Rx}} = 43$ $B = 100$ MHz	$N_{\mathrm{Rx}} = 43$ $B = 300$ MHz
Spectral MUSIC	$\mathcal{O}(925 \cdot 10^{10})$	$\mathcal{O}(239 \cdot 10^{12})$	$\mathcal{O}(473 \cdot 10^{12})$	$\mathcal{O}(473 \cdot 10^{12})$
Root MUSIC	$\mathcal{O}(442 \cdot 10^{8})$	$\mathcal{O}(111 \cdot 10^{10})$	$\mathcal{O}(112 \cdot 10^{10})$	$\mathcal{O}(112 \cdot 10^{10})$
LS-ESPRIT	$\mathcal{O}(109 \cdot 10^{8})$	$\mathcal{O}(275 \cdot 10^{9})$	$\mathcal{O}(276 \cdot 10^{9})$	$\mathcal{O}(276 \cdot 10^{9})$
MP	$\mathcal{O}(500 \cdot 10^{7})$	$\mathcal{O}(148 \cdot 10^{8})$	$\mathcal{O}(143 \cdot 10^{8})$	$\mathcal{O}(423 \cdot 10^{8})$
TLS-MP	$\mathcal{O}(519 \cdot 10^{7})$	$\mathcal{O}(153 \cdot 10^{8})$	$\mathcal{O}(146 \cdot 10^{8})$	$\mathcal{O}(431 \cdot 10^{8})$

Complexity LS-ESPRIT:

$$N_{\mathrm{subsw}} \cdot \mathcal{O}(N_{\mathrm{sn,sub}}^3 + N_{\mathrm{sn,sub}} N_{\mathrm{Rx}}^2 + N_{\mathrm{Tar}}^3). \tag{5.33}$$

Using the radar system parameters listed in Tab. 5.1, $L = 3$, $N_{\mathrm{Tar}} = 3$ and $N_{\mathrm{subsw}} = 1000$, the run-times for the individual algorithms are listed in Tab. 5.2. The dependence on the signal bandwidth B, which is related to the sampling frequency by $f_{\mathrm{S}} = 1.2 \cdot B$, leads to a change of the number of acquired samples per echo window: $N_{\mathrm{snap}} = 220 \cdot 10^3$ for $B = 100$ MHz and $N_{\mathrm{snap}} = 650 \cdot 10^3$ for $B = 300$ MHz.

It becomes directly apparent, that the run-time of Spectral MUSIC is always the highest and about 10^3 – 10^4-times higher than for the MP. Also Root MUSIC and LS-ESPRIT need a fairly large number of iterations. Especially changes of the signal bandwidth have a greater impact than for the MP-based algorithms. This can be justified by the expensive computation of a correlation matrix of size $N_{\mathrm{sn,sub}} \times N_{\mathrm{sn,sub}}$ in those methods. In the end, the TLS-MP is faster in comparison to the covariance methods.

It should be kept in mind, that the computational effort of all six algorithms can be further reduced by using the method, which was proposed in section 5.2.5. After band-pass filtering, the sampling frequency can be reduced and thus the run-time of the algorithms is also reduced significantly.

5.3.2. Basic Angular Estimation for a Single Point Target

In this subsection, we will consider basic angular estimation tasks with the help of a single point target:

1. Varying *SNR*:

   It is expected, that for higher *SNR* the AoA can be estimated more accurately. The simulation results, given in this paragraph, should prove this prediction and show the different behavior and accuracies of the proposed estimator algorithms. For the simulations, a point target was located at $\vartheta = +1.5°$ from antenna broadside direction ($\Theta = 30.0°$) and its specific target scattering coefficient was varied at a constant noise level to realize a *SNR*-range from 0.0 dB to 35.0 dB.

   Fig. 5.8 shows the Root-Mean-Square Error (RMSE) of the estimated angle $\check{\vartheta}$ with respect to the expectation value ϑ. The result was obtained after a Monte Carlo simulation with a total number of 100 independent trials. In general, it can be observed that the variance decreases with increasing *SNR*, which stands in direct agreement with the results of the CRLB. A general observation lies in the fact that all methods, for *SNR* values > 7 dB display a weak dependence of the RMSE against *SNR*. LS-ESPRIT has a quite high variance in comparison to the other methods. The observed trends of MP ($L = 2$) and TLS-MP ($L = 2$) are very similar, while Root MUSIC has a slightly higher variance for high *SNR* levels. Overall, all algorithms converge with increasing *SNR* to the true value.

   In section 5.2.6 it was suggested to apply a moving window average on the MP to lower the variance of $\check{\vartheta}$. According to this idea, the following simulations results show, in how far the variance of the TLS-MP can be lowered by averaging over a certain number of independent snapshots of the same scene. Basically, this approach is equivalent to improving the *SNR* of the echo signal. Accordingly it is expected that averaging will have the same effect like higher *SNR*.

2. Length of the Antenna Array:

   In this section, the dependence of the variance solely on different electrical antenna lengths l is analyzed. This analysis is carried out therefore, in the absence of noise and no additional averaging techniques are applied. To

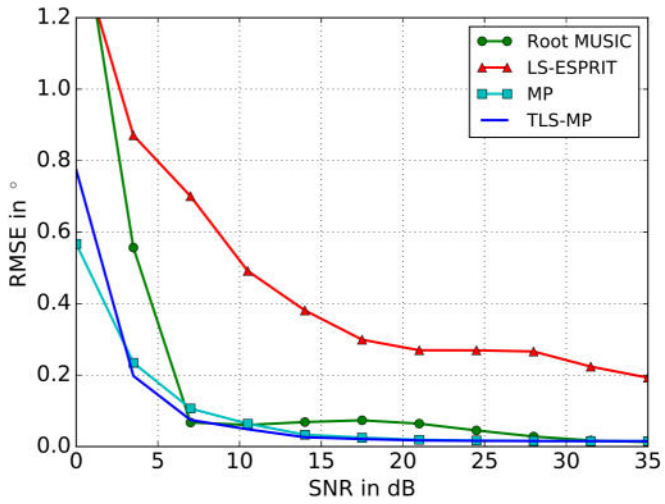


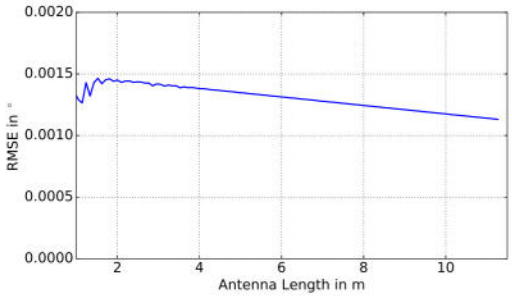
Figure 5.8. RMSE of the estimated angle with respect to the expectation value over varying *SNR*.

change the antenna size, it is either possible to vary the number of elements or to vary the element separation. Both cases are treated next.

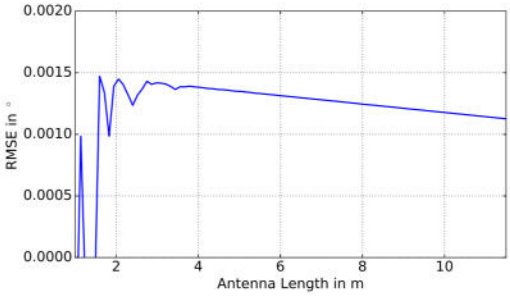
A direct comparison between Fig. 5.9a and Fig. 5.9 shows, that the results are equal regardless whether N_{Rx} or d is varied. After a minimum electrical antenna length of approximately 3.0 m, there is practically no influence on the variance. Because the *HPBW* of a smaller antenna would be greater than 1.3°, which is not suitable for the suggested DBF concepts, this limit can be accepted. The bias of less than 0.0015°, which decreases with increasing antenna length, agrees with the prediction from the CRLB and is negligible for SAR applications. In fact, the observed bias value is not an effect of the *SNR*, since there was no noise added in this simulation. In view of the observations noted in the next paragraph, an explanation lies in the angular position of the target at $\Theta = 30.0°$, which brings a systematic error with respect to the antenna steering angle (cf. next paragraph). If the target would be exactly at antenna broadside direction ($\Theta = 28.5°$), there would be no dependence on the antenna aperture size or number of elements.

3. Varying Steering Angle:

   The CRLB predicts, that the accuracy of the estimated angle decreases with increasing AoA from antenna broadside direction. In fact, the simulation



(a) Antenna length varied over a fixed element spacing of $d = 3\lambda$, $N_{\mathrm{Rx}} = 4 \ldots 120$.



(b) Antenna length varied over a fixed number of elements: $N_{\mathrm{Rx}} = 61$, $l_{\mathrm{ant,el}} = 0.1\ \mathrm{m} \ldots 10.2\ \mathrm{m}$.

Figure 5.9. RMSE of the estimated angle with respect to the expectation value over varying antenna length.

shows in Fig. 5.10, that the bias rises linearly up to 0.01° at the edges of the swath. Because this deviation leads to a significant contribution with respect to the maximum tolerable accuracy of $\delta_{\mathrm{MP}} = 0.05°$, this effect has to be corrected for. The corresponding correction values can be obtained from the simulation results in dependence on the known geometry of the used antenna.

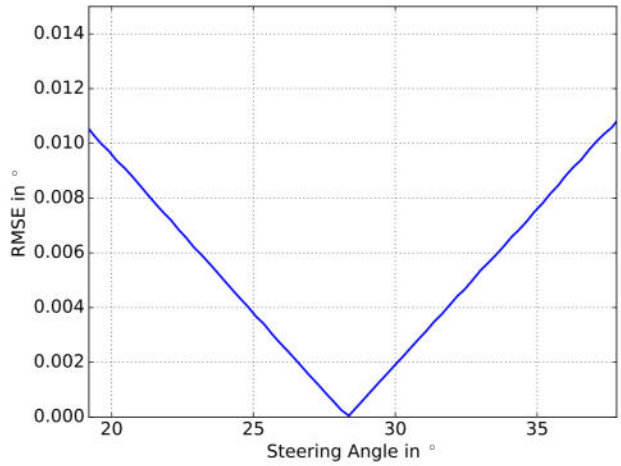


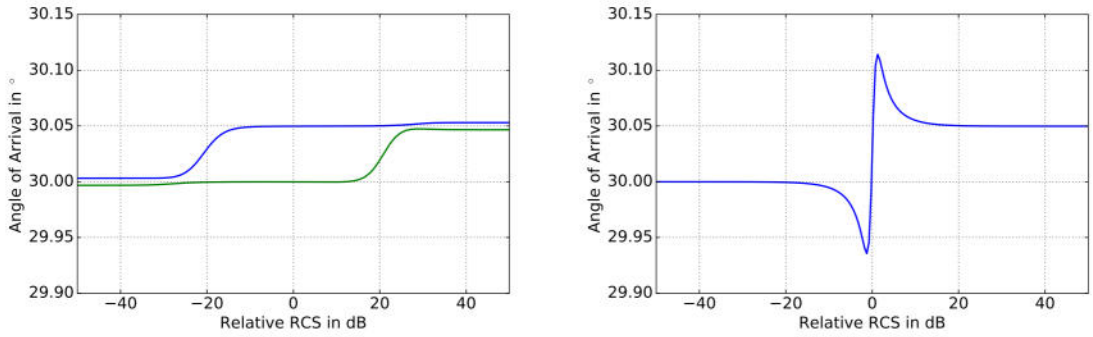
Figure 5.10. RMSE of the estimated angle with respect to the expectation value over varying steering angle.

5.3.3. Multiple Individual Targets

In the scenario considered here, two point targets at $\Theta_1 = 30.0°$ and $\Theta_2 = 30.05°$ have been simulated. While the first target has a constant RCS, the RCS of the second target was varied with respect to the first one in the range -50 dB ... 50 dB. Noise perturbation was neglected.

The plot in Fig. 5.11a shows the estimated AoAs with the two largest eigenvalues of Eq. (5.13), $L = N_{\text{Tar}} = 2$. One can see, that the targets with an angular separation of only 0.05° can be sufficiently resolved if the relative difference between the two RCS is less than ±20 dB. We note, for instance, within a RCS range of [20 dB, 50 dB], no information about the AoA can be given, since the low RCS of the second target is completely dominated by the first. Outside the bounds of [-30 dB, 30 dB], the second target response appears as noise and both estimated angles correspond to the strongest target. However, there is mutual interaction between the two targets and the expectation values could not be exactly reached with a negligible bias of +/-0.003°.

In another case, also two point targets have been simulated. But the TLS-MP was calculated on purpose with the wrong assumption $L = 2$, $N_{\text{Tar}} = 1$. The result in Fig. 5.11b shows a step at a relative RCS of 0.0 dB and that the angle of one of the two targets could be estimated without any bias.



(a) TLS-MP with $N_{\text{Tar}} = 2$.

(b) TLS-MP with $N_{\text{Tar}} = 1$.

Figure 5.11. Estimated angle for two simulated point targets at $\Theta_1 = 30.0°$ and $\Theta_2 = 30.05°$ with varying relative RCS.

5.3.4. Targets with Spatial Extension

Up to now, only basic angular estimation tasks with point targets have been considered. This is beneficial to get an impression, how the MP behaves in different cases. Since for spaceborne SAR scenarios with large homogenous scatterers, e.g. forests or crops are of importance, a final simulation is necessary, which proofs the suitability of the MP method for such areas of operation.

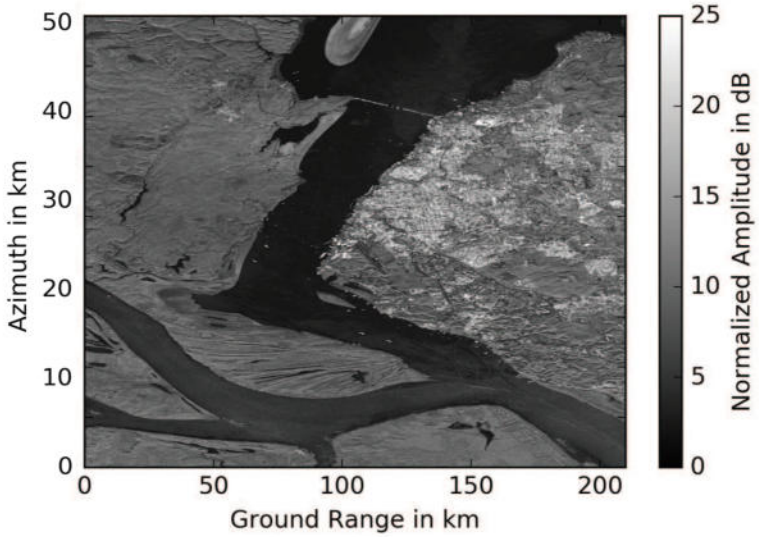
Apart from the simulation parameters listed in Tab. 5.1, a realistic scene has been simulated with 10 point-like targets per wavelength along slant-range and a dynamic (random) RCS variation of 25 dB. To extract the equivalent measured RCS profile along elevation, an original SAR image, acquired with TerraSAR-X has been taken, re-shaped to the maximum scanning angle along elevation ($\Theta = 18° \ldots 37°$) and a quasi azimuth extension of 50.0 km. The antenna footprint along azimuth direction is assumed to have the same width as the re-sampled picture of 50 km. Thus it is valid to sum up the samples along azimuth to get the equivalent range profile.

A plot of the original scene and with the simulated RCS course along the AoA is depicted in Fig. 5.12. Following the processing scheme, which was suggested in section 5.2.7, a few simulation parameters were adapted in accordance to the previous simulation results. In addition, $N_{\mathrm{Snap}} = 30$ independent snapshots along the range direction for every range resolution cell are taken. As recommended, the correction values from the simulation results in the sections 5.3.2.2 and 5.3.2.3 have been also considered.

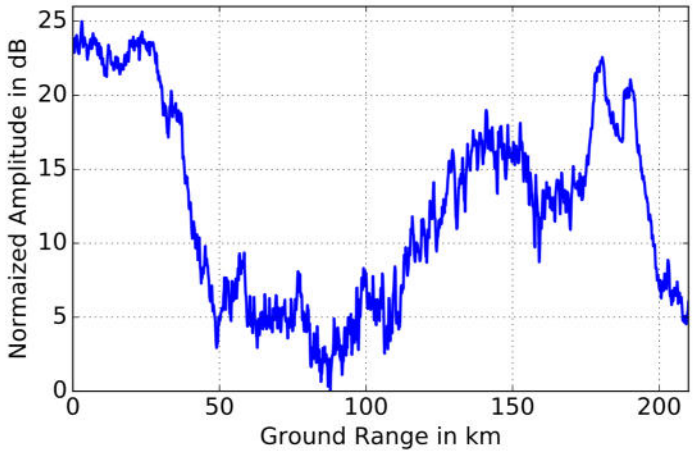
In Fig. 5.13 we can see the deviation of the estimated angle vs. the true AoA without correction of the steering error over Θ. The trend is very similar to that shown in Fig. 5.10 and no influence due to surface scattering mechanisms is visible. After correction of the steering error, there is still a deviation (cf. Fig. 5.14) of up to 0.007°. Since the curve increases non-randomly from antenna broadside direction, it seems to be the result of a systematic error based on the used correction values.

5.3.5. Concluding Remarks

The predictions made in [105] with the CRLB can be completely confirmed: The behavior of the MP in dependence of the electrical antenna length, number of independent snapshots, steering angle, and *SNR*, corresponds to the predictions.



(a) Original SAR scene of Manaus acquired with TerraSAR-X.



(b) Extended range profile.

Figure 5.12. Original SAR scene and extracted range profile.

A comparison of MUSIC, Root MUSIC and LS-ESPRIT shows, that the MP outperforms for the case of spaceborne DBF-SAR significantly. The MP can be even applied in scenarios, where the other algorithms completely fail to work (e.g. extended targets). This is because the other estimators have been derived for application in communications, where the problem formulation is completely different. While the advanced version of the MP with a combination of TLS, multiple snapshots and band-pass filtering is highly related to the DBF-SAR signal

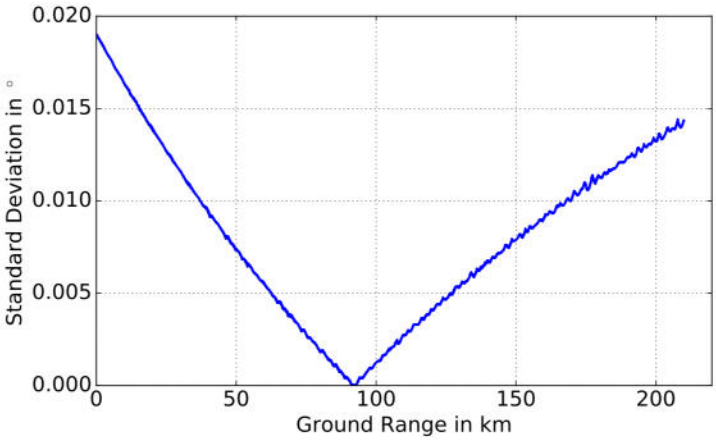


Figure 5.13. Standard deviation of the estimated angle from the expectation value along the swath.

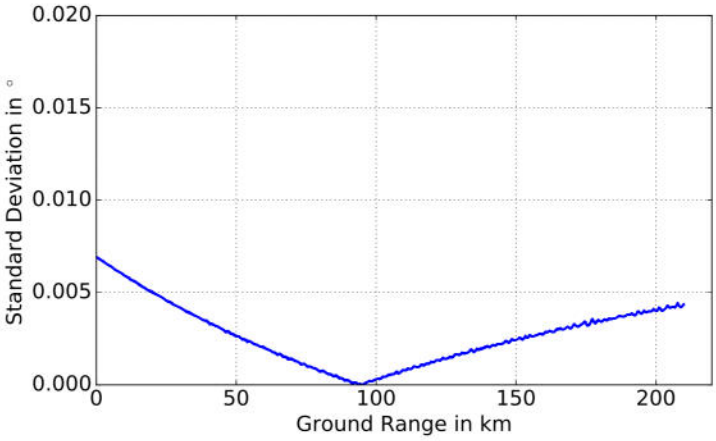


Figure 5.14. Standard deviation of the estimated angle from the expectation value along the swath with correction.

model, the FB-MP finds no application. However, one of the major advantages of the MP is the very fast computation without the need for a correlation matrix. This satisfies the implementation in real-time on-board of a satellite to enable topography-adaptive DBF.

6. Ground-Based MIMO-SAR Demonstrator

This chapter gives an overview of the MIMO-SAR demonstrator. The purpose of this radar system is to test and verify new techniques and concepts for future radar systems, such as DBF-radar, MIMO-radar, DBF-SAR and MIMO-SAR. Especially the modes described in the previous chapters of this thesis are of interest, for which outdoor DBF-SAR and MIMO-SAR measurements were performed with the demonstrator.

As a starting point, in the first section the X-band radar instrument with four transmit and eight receive channels is described. In this section, we address for the transmit chain, the receive chain, and the calibration part, separately. This is followed by the description of the full-coherent system design concept with synchronization capabilities between the modular radar hardware components. An analysis on the harmonic signal components caused by amplifier and microwave mixer is given in section 6.3. Afterward, the dual-polarized microstrip patch antennas, used for the measurements described in chapter 7, are briefly presented. The subsequent section gives an overview over the motorized SAR platform with a step-motor and its controller. Pre-processing and calibration steps to condition the acquired raw data for DBF, MIMO and SAR algorithms are described in the last two sections of this chapter.

6.1. Architecture of the Radar System

A photo of the modular, reconfigurable radar with multiple transmit and receive channels is shown in Fig. 6.1. The configuration described in this thesis, operates in X-band with four transmit and eight receive channels (basic system parameters and a generalized block diagram can be found in Tab. 6.1 and Fig. 6.2). The modular 19" form factor and the fully-coherent system design via a single shared 1.0 GHz LO (Local Oscillator) signal, allows great flexibility of system changes and extensions to more transmit and receive channels, or other frequency bands. At present, the radar can also be operated in P-band (up to 500 MHz) and Ka-Band (up to 40 GHz). An embedded PC controls the whole radar system via cus-

Table 6.1. System parameters of the MIMO-radar demonstrator.

Parameter	Value
max. bandwidth	300 MHz
RF center frequency	9.58 GHz
typical LO frequency	9.375 GHz
IF center frequency	205 MHz
max. output power	22.5 dBm
typical DAC and ADC sampling rate	1 GS/s per channel
DAC and ADC resolution	10 bit
no. of transmit channels	4
no. of receive channels	8
dynamic range (receiver)	≈43 dB

tom written software in the programming languages C/C++ and Python, while the data is transferred over the bus-systems namely Universal Serial Bus (USB), Ethernet, compact Peripheral Component Interconnect (cPCI), and PCI eXtensions for Instrumentation (PXIe) within the hardware complex. All 19" chassis are mounted in a single rack, which can be placed on the ground for radar measurements. Alternatively, the rack can be mounted on a motorized platform for SAR measurements.

The independent simultaneous data recording for each receive channel allows for true DBF. In addition to the applications mentioned in section 2.5, the obtained information can be used to suppress spatial ambiguities in the signal, to increase the total gain of the receiver, and to suppress spatial interferences. Basic system properties have been already presented in references [120] and [121].

For a more detailed overview of the system, we address the transmit chain, the receive chain, and the calibration crate separately.

6.1.1. Transmit Path

As mentioned already, the radar has four identically structured transmit channels. A detailed block diagram of a single transmit channel from the Arbitrary Waveform Generator (AWG) up to the antenna port is depicted in Fig. 6.3. The signal powers, amplifier gains (G), Conversion Losses (CL), and Insertion

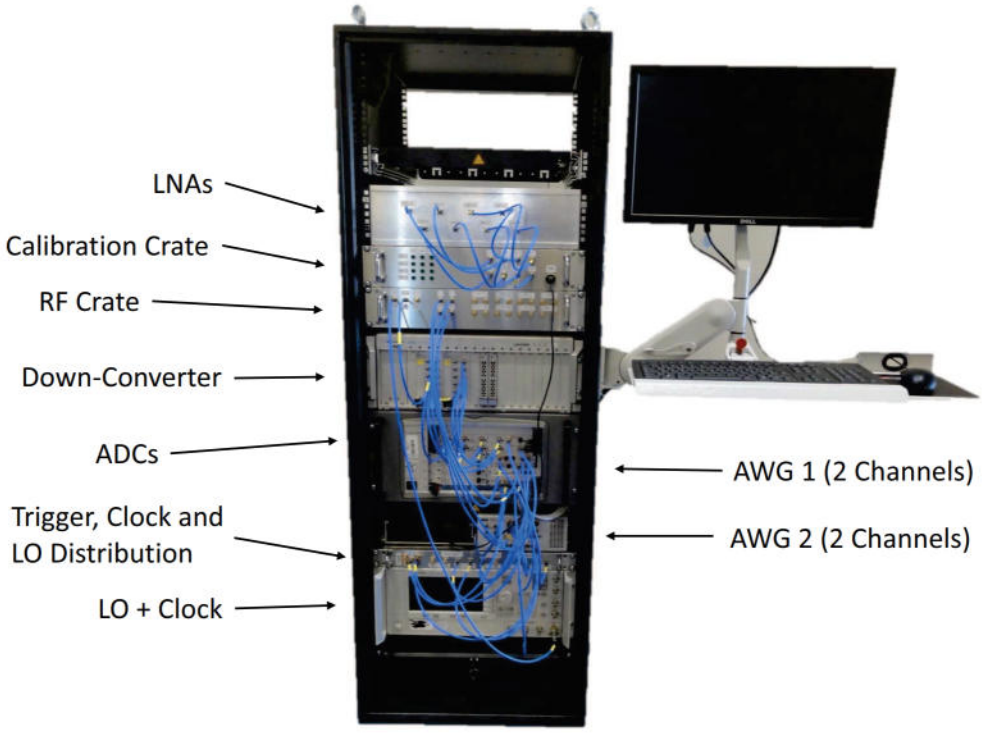


Figure 6.1. Photo of the ground-based MIMO-radar demonstrator.

Losses (*IL*) of each component are written at the corresponding positions in the block diagram.

A software tool (custom written and available in MATLAB, IDL, LabVIEW and Python) generates the desired set of transmit waveforms and saves each of them in a separate binary file with a quantization of 10 bit per sample. These files are uploaded to the internal memory of two AWGs with two channels each. One of them is operated as a master and one in a slave mode. To configure both AWGs for playback, further parameters, such as additional amplification and low-pass filters must be pre-defined in the graphical user interface of the control software. Once the master AWG is configured and the rising edge of an external trigger signal is detected, the waveforms of duration τ_p are played. For synchronization issues, both signal generators are operated with the same shared clock signal of 1.0 GHz (maximum signal bandwidth: 450 MHz).

The output signal of the AWGs is attenuated with an analog attenuator to operate the Intermediate Frequency (IF) Low-Noise Amplifier (LNA) within the Spurious-Free Dynamic Range (*SFDR*) [122]. Operation within the *SFDR* serves

to generate no additional intermodulation products, which may distort the transmit signal (cf. section 6.3). Obviously, the signal amplitude of the AWGs can also be adjusted to a lower level, to avoid the need for an additional attenuator. However, the AWG is a digital device and accordingly generates quantized values. If the available 10 bit dynamic range of D-to-A conversion is not utilized, then the generated waveform may suffer higher distortions. Thus, each waveform is generated by using the maximum number of bits.

An additional signal generator with flexible frequency settings up to the Ka-band (f_0 = 40.0 GHz) serves as LO for up-conversion of the IF signal to the X-band with microwave mixers. After up-conversion to the desired Radio Frequency (RF) band, which is centered at 9.58 GHz, the signal is attenuated and then bandpass-filtered. The filter serves for suppression of the LO and the lower sideband of the signal. This is a basic requirement, because otherwise they would later affect the received signal during the down-conversion process. Due to the elliptic filter design, most of the LO and lower sideband energy is reflected by the filter. Because this unwanted signal would be reflected back and forth between mixer and filter, an attenuator is inserted (test measurements for the signal quality showed significant improvements caused by the attenuator). A High-Power Amplifier (HPA) amplifies the remaining RF-signal up to a mean output power of 22.5 dBm. The electronically controlled microwave switch serves for different operation modes and is part of the calibration crate, explained in section 6.1.3. Ultra low-loss cables with a length of 10.0 m and a total insertion loss of 6.0 dB lead finally to the transmit antenna.

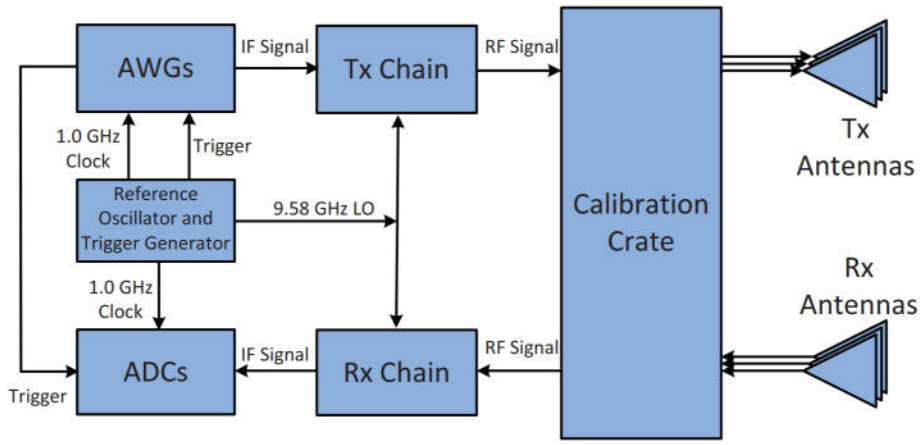


Figure 6.2. Simplified block diagram of the MIMO-radar system.

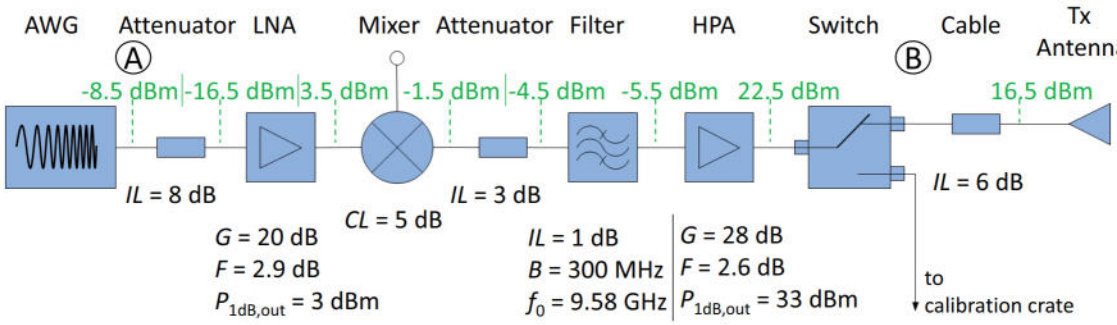


Figure 6.3. Block diagram of a single transmit channel.

For characterization of all four transmit channels, a Vector Network Analyzer (VNA) was used to measure the s-parameters over frequency [122] (between the points Ⓐ and Ⓑ in Fig. 6.3). Because it is known, that the parameter s_{21} is related to the system's transfer function, the course of this parameter over frequency is plotted in Fig. 6.4. The absolute power level of the vertical axis was obtained from the known transmit powers of the VNA and of the AWG. It becomes apparent, that due to manufacturing tolerances, there are strong differences of up to ≈ 2 dB between the channels, which must be compensated. More details about this calibration routine are given in section 6.6.

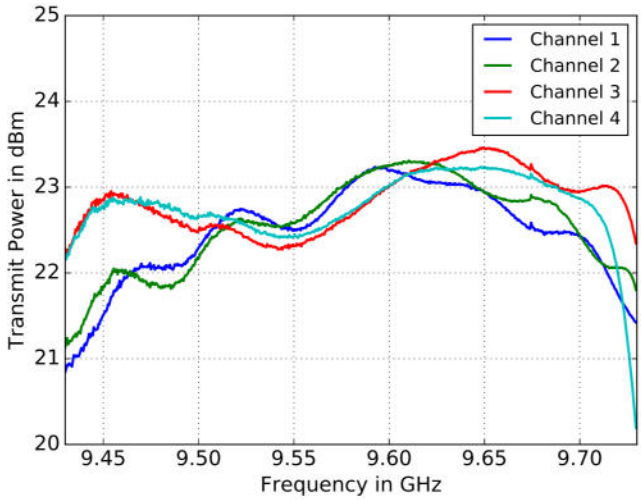


Figure 6.4. Transmit powers of the individual transmit channels without the cables to the antennas. The mean output powers are: Ch1: 22.5 dBm, Ch2: 22.5 dBm, Ch3: 22.8 dBm, Ch4: 22.8 dBm. Measured with the vector network analyzer ROHDE&SCHWARZ ZVA24.

6.1.2. Receive Path

As with the transmit channels, the MIMO-SAR has eight identically structured receive channels (cf. Fig. 6.5). Behind each receive antenna, a LNA is attached as close as possible to the antenna. This avoids an increase of the noise figure due to the long cables with an insertion loss of 6.0 dB, which lead from the antenna platform to the radar rack. The influence of the component's position, within a cascade, on the total noise figure F is given by the Friis cascade formula [122]. According to this formula, the closer a device is to the beginning of a chain, the greater is its influence on the noise figure. Since the noise figure of a passive device (e.g. a cable) is equal to the inverse of the insertion loss of the device, and as this noise figure is significantly larger than the noise figure of a LNA, the used LNAs are mounted as close as possible to the receive antennas. The total noise figure F_{cas} is given by

$$F_{\text{cas}} = F_1 + \frac{F_2 - 1}{G_1} + \frac{F_3 - 1}{G_1 \cdot G_2} + \ldots + \frac{F_{N_{\text{cas}}} - 1}{\prod_{m=1}^{N_{\text{cas}}-1} G_m}, \tag{6.1}$$

with N_{cas} being the number of components in the chain. Considering the LNA with $G_1 = 35.0$ dB, $F_1 = 0.9$ dB and the ultra low-loss cable with $F_2 = -IL = -6.0$ dB, the overall noise figure of the two components is $F_{\text{cas}} = 0.9\,\text{dB} + (6.0\,\text{dB} - 1)/35.0\,\text{dB} = 1.23\,\text{dB}$[1].

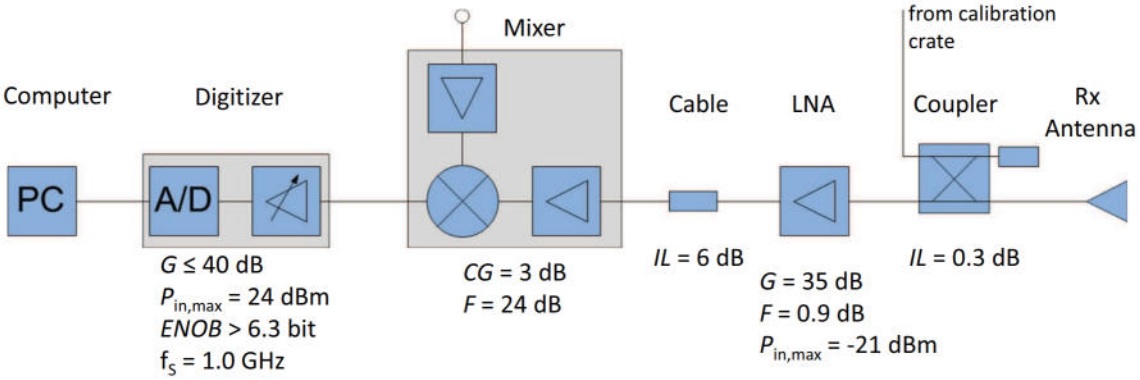


Figure 6.5. Block diagram of a single receive channel.

[1] For comparison, the noise figure with reversed positions would be $F_{\text{cas}} = 6.0\,\text{dB} + (0.9\,\text{dB} - 1)/(-6.0\,\text{dB}) = 4.9\,\text{dB}$, which would lead to a SNR loss of 3.7 dB.

The cables lead from the antenna platform to the radar rack with microwave couplers with a branch to calibration signals. Active sub-harmonic microwave mixers of conversion gain $CG = 3$ dB and a noise figure of $F = 24$ dB serve for down-conversion of the RF signal to the IF-band. A LO distribution network enables to share the same 9.58 GHz signal for each receive channel as also used for the up-conversion. Dependent on the antenna gains and the backscattering coefficient of the measurement scene, amplifier with adjustable gain amplify the IF signal to the desired signal level, in order to exploit the full-scale bit-range of the AD-converter of N_{bit}=10 bit. To avoid an unnecessarily degradation of the *SNR* level, this adjustment is absolutely important. In general, for a signal with equiprobable signal levels, the peak-signal-to-rms-quantization-noise ratio is given by [123]:

$$SNR = 4.8 + 20 \cdot \log_{10}\left\{2^{ENOB}\right\} = 4.8 + 6 \cdot ENOB \qquad \text{(in dB)} \quad \text{for} \quad ENOB \geq 3. \tag{6.2}$$

Due to noise and distortions, which are introduced by the non-ideal ADC, the 10 bit range reduces to the Effective Number Of Bits ($ENOB < N_{\text{bit}}$), which is according to the ADC datasheet: $ENOB > 6.3$ bit. From that follows a maximum achievable *SNR* of $4.8 + 6 \cdot 6.3 > 43$ dB. The remaining components of the receive chain do not have a significant impact on *this SNR*. The signal quality, however, still depends on the total noise of the analog receiver chain. To obtain a maximum degree of coherency, for sampling, the same 1.0 GHz clock signal is used as for signal generation with the AWGs. Further, the two 4-channel digitizer cards are synchronized via the AS-bus (Auto Synchronous).

Both digitizer are controlled by C/C++-software via a PCIe-bus connection. Primarily, the radar system operator can set several parameters in a graphical user interface, such as sampling frequency, acquisition time (length of receive window), (de)activate channels, bit quantization and number of receive windows to record (cf. Fig. 6.6).

A ring-buffer of length 256 kSamples (256 μs at $f_S = 1.0$ GHz) is implemented in each channel of the digitizer and receives the sampled raw-data continuously (cf. Fig. 6.7). Once a trigger signal occurs as an indicator for start-of-acquisition, data from that time marker on is transferred to the Random-Access Memory (RAM) of the computer with a size of 8 GB. The buffer size is based on the length of the

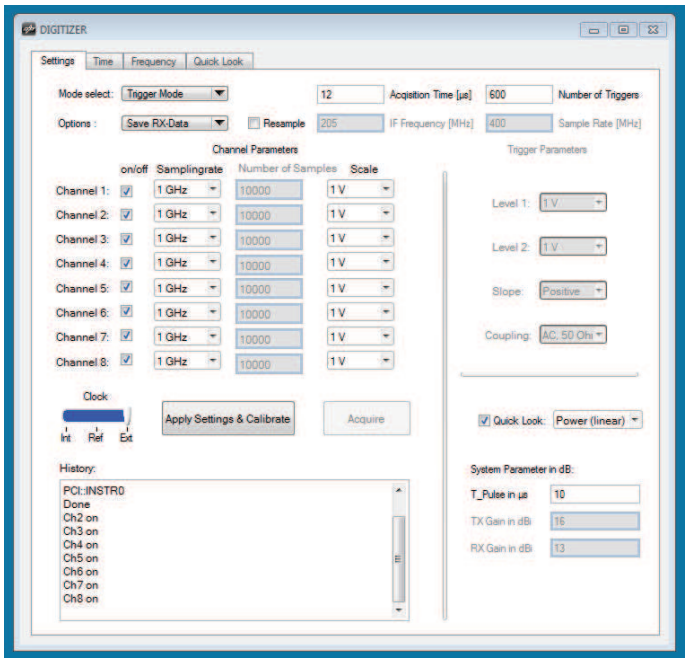


Figure 6.6. Screenshot of the graphical user interface to control the digitizer.

receive window and defined beforehand. Because a high *PRF* should be enabled, and since it is faster to write the data to the RAM instead to the Solid-State Drive (SSD) of the control PC, all acquired receive windows of all channels are written to the RAM during the measurement[2]. After the measurement of the entire SAR scene is finished, the recorded data is converted to a binary HDF-5 file format structure and transferred from the RAM to the SSD. To allow a first evaluation of the measurement, the raw data is visualized on the user interface for each receive channel in time- and frequency domain. The software tool even offers a *Quick Look* processing for an initial feedback about the target position along range and its RCS.

6.1.3. Calibration Crate

The generated waveforms and the signal echoes are distorted by the non-linear behavior of the radar components over frequency and time. Additionally, manufacturing tolerances of the cabling with approximately 37 m for a single closed loop from the AWG through the antennas to the ADCs lead to different phases

[2]In case of measurements with lower requirements on the *PRF*, but with a high number of receive windows, an individual operation mode was implemented, which allows to transfer the data to the SSD for each receive window individually.

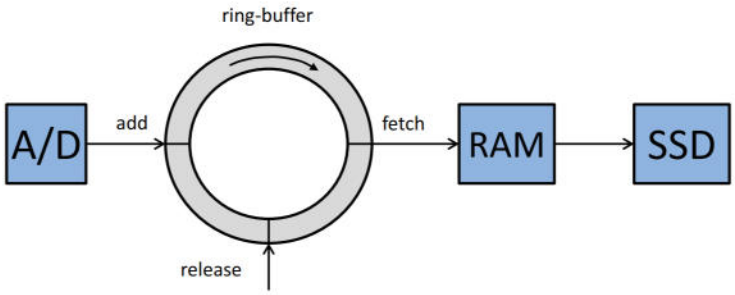


Figure 6.7. Block diagram of the ring-buffer implementation in the digitizer. The acquired data is streamed over the ring buffer to the RAM. Once the data stream is exhausted, the data is streamed to a SSD.

between the channels. In established systems, like TerraSAR-X [6] or the F-SAR [124], the transmit signal is led through a calibration loop to characterize the systems response [125]. The acquired information is later used for the reference function in range compression and calibration. For this issue, a calibration crate was constructed and placed between the HPA and the antenna in the transmit path, and between the antenna and the LNA in the receive path (compare block diagrams in Fig. 6.2 and Fig. 6.8). Two photos can be found in Fig. 6.9. It enables to short cut each possible combination between transmit and receive channels in front of the antennas (the antennas are characterized separately). The recorded system response is later used to correct for amplitude and phase differences between the channels.

Three different operation modes are offered to the radar system operator by the control software: transmit (green path), calibrate (brown path) and idle (red path). To switch between the modes, which can be adjusted for every transmit channel individually, microwave coax-switches are controlled via a digital relay board. This board receives a coded signal via USB and sets its corresponding outputs to the selected operation mode from the software. LEDs (Light Emitting Diodes) indicate the respective settings on the hardware rack.

In the transmit mode, the filtered and amplified signal is directly routed to the transmit antennas, while in the idle mode, the signal is routed to a dummy load to switch off the corresponding channel. In the calibration mode, the reference signal (the same signal, which is also used for the transmit mode) is routed through power dividers, power combiners and couplers to the receive channels. Each transmit waveform can then be fed into all eight receive channels to char-

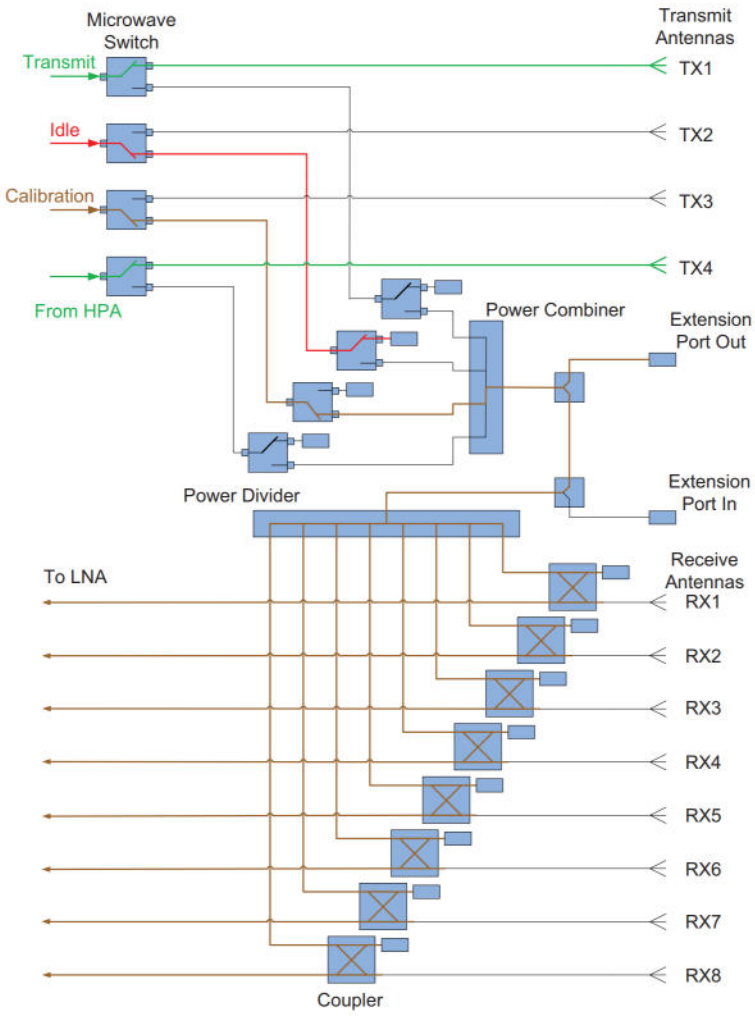


Figure 6.8. Block diagram of the calibration crate.

acterize each possible Tx-Rx combination with a replica signal. Additional input and output ports allow extensions to further transmit and receive channels. For later correction of the raw-data, the calibration signals are used as described in more detail in section 6.7.

Amplitude and phase imbalances of the paths through the calibration crate are characterized by a vector network analyzer. Since only passive devices are used in the calibration crate, it is assumed that the measured values are relatively time-invariant. Because they are the same for all measurements, these additional correction factors are included as constants within the signal calibration steps.

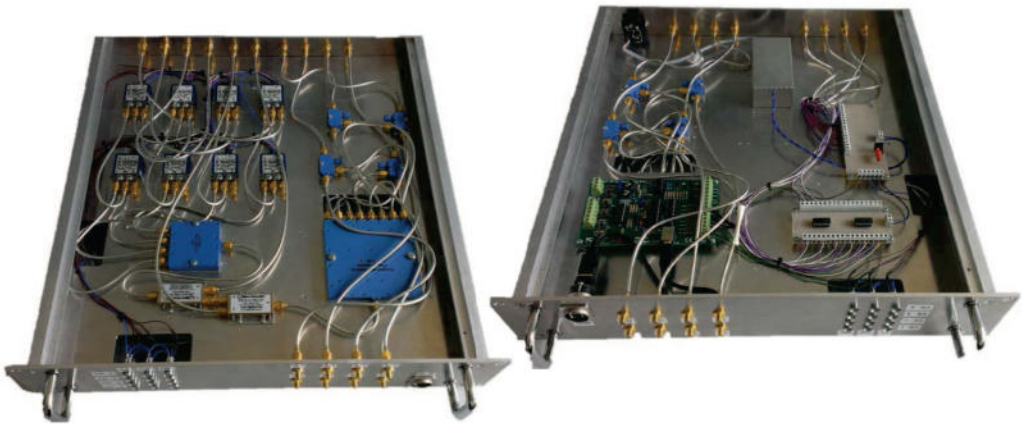


Figure 6.9. Photos of the calibration crate. Left-hand side: Upper layer with microwave components; Right-hand side: lower layer with power supply, digital electronics, and microwave couplers.

6.2. Hardware Synchronization and Coherent System Design

A SAR sensor is a fully coherent system, which utilizes phase information from the received echo signal [14]. In accordance with advanced single-channel imaging radars, such as the F-SAR [124] or TerraSAR-X [6], for the MIMO-SAR demonstrator a common LO- and clock-signal is distributed and shared by all components. Especially for MIMO and DBF modes, where multiple independent operating channels are combined, a fixed mathematical relationship between all shared signals within the radar is indispensable. In keeping with this requirement, an especial distribution crate for the clock, LO and trigger signals was developed. It is divided in two sections, one for the high frequency part (clock and LO) and one for the low frequency part (trigger).

Overall Clock Signal

Without exception, all signals within the MIMO radar system are derived from a single LO signal, generated by a stable Oven-controlled Crystal Oscillator (OXO) of 10 MHz. This signal is converted to 1.0 GHz and 9.58 GHz with frequency-multiplier and -divider, and microwave mixer (cf. Fig. 6.10). These two frequencies serve as basis for distribution to all crates. The 1.0 GHz clock signal is used for signal generation with the AWGs and for signal sampling with the AD-converters. For up- and down-conversion of the IF signal to the RF-band and vice versa, the 9.58 GHz signal is used.

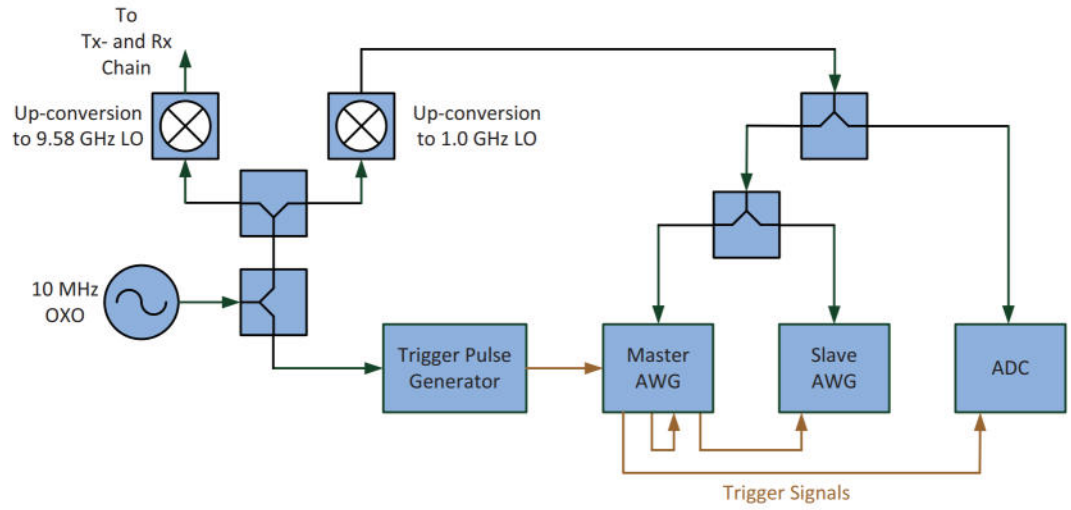


Figure 6.10. Concept of the LO and trigger distribution network.

From first impressions, the frequency of the distributed 1.0 GHz signal may seem to be an uncommon choice, since it is a standard to use a 10 MHz reference signal for synchronization of microwave devices (phase-stable method). A 10 MHz signal, which is used for inertial Phase-Locked Loops (PLL), introduces jitter, because of a limited reaction time. Several independent running PLLs would lower the degree of coherency and deteriorate the SAR performance [126]. An improved solution for the present case avoids the use of PLLs. In this phase-coherent method, a common clock signal of 1.0 GHz is directly used or it is converted to other frequencies with harmonic mixers, frequency multipliers and dividers. Inertial transient effects can thus be avoided. Each self-developed crate and each modular component of the MIMO-SAR demonstrator has the possibility to be fed with an external reference signal or to share its internal clock via a coupled output connector for system extensions.

In a test measurement, every 20.0 s a chirp signal of $\tau_p = 10\mu s$ is routed through the whole radar system, while the antennas were disconnected and now open feeds were bridged with interconnects. For evaluation, each acquired chirp signal is correlated with the very first one. After sinc-interpolation, the maxima indicate the system drift with reference to the first chirp. As can be seen in Fig. 6.11, the radar is very stable and drifts over the measurement time of 5 hours by maximum 4.0 ps (13.5° in X-band). Since usually the measurement times are shorter than 5 minutes and a new calibration signal can be acquired between two data takes, a possible system drift of 5 min/5 hours $\cdot$ 13.5° = 0.2° within this interval must

be tolerated. Empirical observations and the measurement results, which will be presented in the next chapter, show that effects caused by the drift can not be observed.

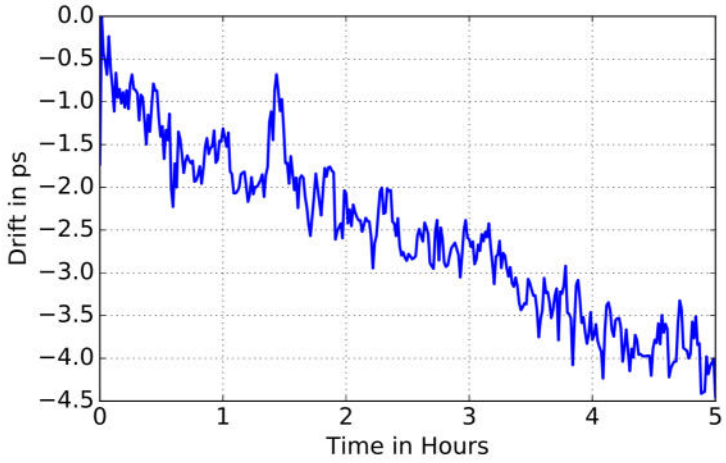


Figure 6.11. System drift over 5 hours.

Trigger Signals for Constant PRF

To guarantee a stable system operation, it is not only sufficient to share common LO and clock signals by the components. Since the system is pulsed with a constant *PRF*, it may happen that a trigger signal, used as indicator to open a transmit or receive window, occurs between two discrete digital samples. Rounding to the next sample will cause an unacceptable error, because the gap of $1/S_f = 1.0$ ns between two samples corresponds to a range shift of $c_0/S_f = 30$ cm, which equals, in turn, around 10 wavelengths in X-band. If this issue is not considered, a coherent processing of several acquired echoes would be impossible.

For that reason, a common trigger signal distribution network is constructed, which uses the same reference signal as the rest of the MIMO-SAR demonstrator. The block diagram is illustrated in Fig. 6.10. Beginning with the 10 MHz reference OXO, its output signal is split up and converted to the aforementioned 1 GHz LO, the 9.58 GHz for up- and down-conversion, and for the trigger generator. This generator is controlled via a dedicated computer and adjusts the desired *PRF*. The trigger signal is routed to the master AWG, which provides a trigger signal to itself and to the slave AWG (and to further slave AWGs if available). Back-coupling of the master AWG is necessary for self-synchronization and due

to internal delays of the AWG itself. If these synchronized trigger signals are indicated by the AWGs, both start to play the transmit waveforms simultaneously. Once the transmission window is opened, the master AWG sends a further trigger signal to the AD-converter, which directly set a marker on their ring-buffer to store the acquired signals from that point on for a pre-defined duration (width of the echo window). Due to very short delays during transition between transmit and receive for the ground-based MIMO-SAR measurements, the echo window is opened at the same time as the AWGs start to play the waveforms.

6.3. Nonlinear Signal Distortions

In most pulsed radar systems, solid-state transmit amplifiers are operated in saturation. Reasons for that are the constant signal envelope on the one hand (cf. section 3.4.1 – range resolution) and the exploitation of the maximum available system power on the other hand. A drawback in this situation is the occurrence of non-linearities within the chirp spectrum if a superheterodyne transmitter is used. These distortions are primarily caused by harmonics, which occur at integer multiples of the instantaneous frequency and by the intermodulation products [122]. With respect to the Ambiguity Function analysis and plots in section 3.3.2, any distortion in the transmit signal cause additional interferences. This may result in loss of signal orthogonality in MIMO-SAR. Because the orthogonality condition from Eq. (3.2) can not be met anymore, the *SNR* of the SAR product is finally limited by the level of the harmonics and intermodulation products. Hence, it is worth analyzing the signal distortions of the MIMO-SAR demonstrator in detail.

The variation of the non-linearities over the used signal spectrum becomes visible in the time-frequency plot, also described as spectrogram. Since a signal can either be viewed in time- or frequency domain, the Short-Time-Fourier-Transform (STFT) computes the signal spectrum block-wise, leading to a two-dimensional spectrogram. In general, the STFT of the waveform $s_k(t)$ is defined as

$$\wp_b(\omega) = \int_{-\infty}^{\infty} s_k(t) \cdot \exp(-\mathrm{j}\omega t) \cdot w_{\mathrm{win}}(t-b)\,\mathrm{d}t, \tag{6.3}$$

while the used window is centered around $t = b$.

In reference to Heissenberg's uncertainty principle, the precision of time and frequency measurements are inversely proportional to each other. The resulting limit is also called Gabor limit, named after D. Gabor, who made intensive information analysis on signals [127]. He found, that optimum results for a STFT can be achieved, if a Gaussian window is used. This is due to the fact, that the Gaussian function has the same shape in time- and frequency domain. The Gaussian window is defined as

$$w_{\text{win}}(t) := \frac{1}{\gamma\sqrt{2\pi}} \exp\left(-\frac{t^2}{2\gamma^2}\right) \qquad \text{if} \qquad \gamma > 0, \tag{6.4}$$

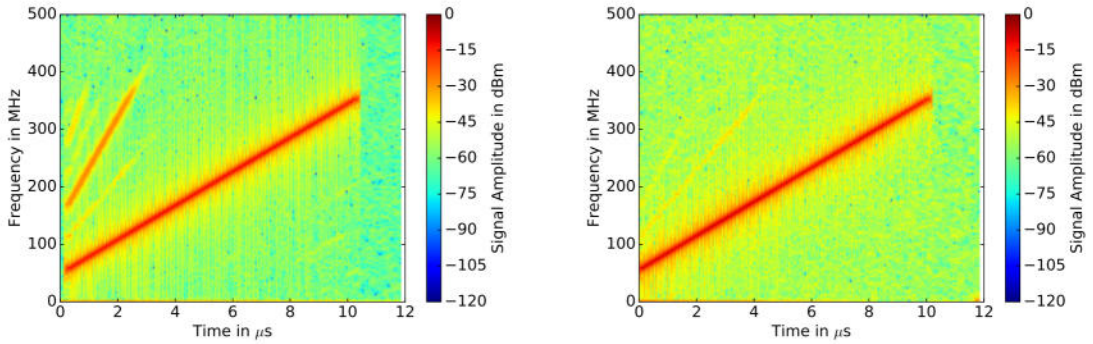
while the optimum choice of the parameter γ is dependent on the analyzed signal. If w_{win} is such a Gaussian window, the STFT is also named Gabor Transform. The final spectrogram is obtained by plotting $|\wp_b(\omega)|^2$.

In the early stage of the MIMO-SAR demonstrator development, high levels of harmonics could be observed in the transmit signal. For reference, in Fig. 6.12a we can see a spectrogram plot of a measured up-chirp signal with B = 300 MHz and $\tau_{\text{p}} = 10\,\mu$s, which was routed from transmit channel 1 through the calibration crate to receive channel 1. At a signal level of -11.0 dBm, the 3$^{\text{rd}}$ order harmonics were only 16 dB lower (weaker) than the ideal chirp. In a single-channel radar system, these distortions can be modeled and corrected during the calibration process (e.g. as done for TerraSAR-X [128]). For MIMO-SAR, this approach is not possible, because the harmonics are overlaid by the other orthogonal signals. In order to reduce or to suppress the nonlinearities, two suggestions can be made:

If the transmit waveform is directly generated in a higher frequency band in a way, that the following condition is fulfilled: $2 \cdot f_{\text{low}} > f_{\text{low}} + B$, then the harmonics are outside the spectrum of the chirp waveform and can be filtered via standard bandpass filters, while f_{low} is the lower frequency of the IF signal.

Another solution is not to operate the amplifier in saturation. According to [122], if an amplifier is operated within the Spurious Free Dynamic Range (*SFDR*), all intermodulation products are below the noise level N_0 and do not cause any distortions. The *SFDR* is defined as

$$SFDR = \left(\frac{OIP_3}{N_0}\right)^{2/3}, \tag{6.5}$$



(a) Before replacement of the amplifier with higher 3rd order intercept point.

(b) After replacement of the amplifier with higher 3rd order intercept point.

Figure 6.12. Spectrogram plots of calibration chirp signal in loop Tx1 – Rx1 with $B = 300$ MHz and $\tau_p = 10\ \mu$s.

while OIP_3 is the 3rd order intercept point at the output of the amplifier. However, the nonlinear frequency response of the amplifier leads to a nonlinear envelope of the chirp signal. According to section 3.4.1, this envelope can be seen as a window function and it causes a reduced range resolution. Using a pre-defined envelope function of the IF waveform in the waveform-generator, which compensates for the nonlinearities of the transmit chain inversely, an optimum waveform can be generated at the costs of transmit power. Alternatively, a compromise between acceptable level of harmonics and output power has to be found[3].

For the applications of the MIMO-SAR demonstrator, a loss of transmit power is not a key issue. Accordingly, the LNAs of all four transmit chains were replaced by amplifiers with a higher 3rd order intercept point and more gain. A spectrogram plot of the calibration chirp signal with the same parameters as the ones used for Fig. 6.12a is shown in Fig. 6.12b. The level of 3rd order harmonics is at least 32–36 dB below the signal level of -7.6 dBm, which is absolutely acceptable. This significant enhancement enables MIMO-SAR measurement results with improved orthogonality between the transmit signals. The used approach to *pre-distort* (pre-conditioning) the IF waveform, is explained in section 6.6.

[3]Microwave mixer also introduce inter-modulation products during up-conversion to the RF band. Hence, they should also not be operated in saturation.

Table 6.2. Patch antenna parameters.

Parameter	**Value**
technology	aperture coupled microstrip patch antenna
polarization	dual linear H + V
max. gain	13.8 dBi
center frequency	9.6 GHz
3dB bandwidth	900 MHz
HPBW elevation	60°
HPBW azimuth	16°
cross polarization suppression	> 20 dB

6.4. Antennas

Different types of antennas can be used for the MIMO-SAR demonstrator, e.g. horn, patch, log-periodic or reflector antennas. A flexible and adjustable mounting on an antenna platform was designed and built for enabling flexible adjustments of the antenna element spacing and tilt angles.

Apart from standard gain horn antennas, dual-polarized microstrip patch antennas (cf. photo in Fig. 6.13) are used for all obtained measurement results in chapter 7. These antennas are in-house developments and will be also used for the airborne DBF-SAR of the German Aerospace Centre (DLR). Basic antenna parameters are listed in Tab. 6.2.

Since the antennas are excluded from the calibration loop of the calibration crate, and because their radiation characteristics over azimuth and elevation have an influence on the measurement result, the antenna beam-patterns over their full bandwidth of 900 MHz were measured in an anechoic chamber. Plots of the measured elevation and azimuth cuts in the polarization states HH, VH, HV and VV can be found in Fig. 6.14. Like the other system characteristics, also this information is included in the calibration process of the signal processor.

Another antenna type, which was especially developed for the MIMO-SAR demonstrator, is an elliptical X-band DBF reflector antenna with eight feed elements in offset configuration. It is used to verify advanced operation modes for future spaceborne SAR missions, which will use a deployable DBF reflector

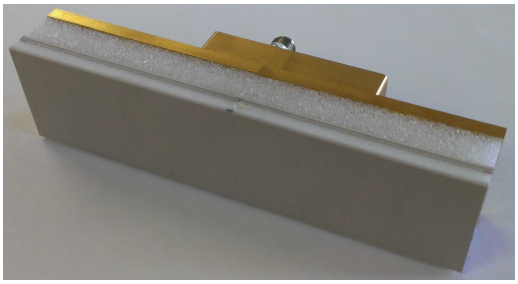


Figure 6.13. Photo of a single patch antenna.

antenna [40]. DBF-SAR and also MIMO-SAR measurement results obtained together with the radar demonstrator can be found in [129,130], and in section 7.1.

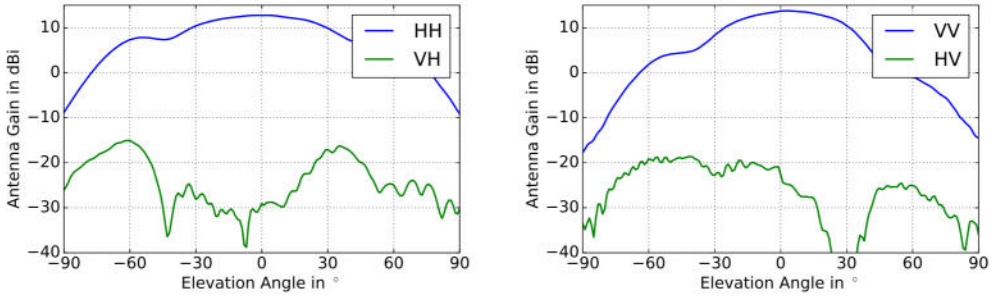
6.5. SAR Configuration

As can be seen in Fig. 6.1, the RF and calibration crates developed in-house and the modular components (e.g. AWG, ADC, ...) are mounted in a single rack. It can be placed on the ground for MIMO-radar measurements or it can be assembled on a motorized rail wagon to conduct MIMO-SAR measurements. The following two subsections give a more detailed description of the SAR platform itself and the used step motor.

6.5.1. SAR Platform

A photo of the SAR platform can be found in Fig. 6.15. It is composed of three units/sections. While the first section is meant for the radar system rack, the section in the middle serves as the antenna platform and the third section is used for the motor control unit with power supply. To flexibly mount the system racks together with their extensions and additional components, the frame of the platform is made of aluminum profiles with standardized notches.

Having a total length of 2.3 m, a width of 1.4 m and a weight of approx. 800 kg, the SAR platform rides along a railroad track of length 126 m in both directions. It is even possible to mount other kinds of wheels for usage on asphalted roads. The area around the rails is surrounded by a lawn and a sand container, which serve as background for the measurements. Before each measurement, the antennas are assembled on the antenna platform and its height is continuously variable with a motor driven lift from 0.8 m up to 7.5 m. An Uninterruptable Power Sup-



(a) Main cut in elevation, receive: horizontal polarized.

(b) Main cut in elevation, receive: vertical polarized.

(c) Main cut in azimuth, receive: horizontal polarized.

(d) Main cut in azimuth, receive: vertical polarized.

Figure 6.14. Receive mode antenna patterns of a microstrip patch antenna at 9.58 GHz.

ply (USV) in the motor control rack enables a full radar system operation during the measurements, without any extra external cabling for the power.

A further feature of the demonstrator is the special two-gear drive from the motor to the axis to have either a faster speed or a higher torque. In order to avoid damages or accidents and to protect the motor if the wagon drives against an obstacle, a security-coupling (clutch) is integrated. If the torque exceeds a certain limit, the security-coupling disconnects immediately the axis from the step motor and the SAR platform stops its movement.

6.5.2. Step-Motor

The SAR platform is electric driven with a 2-phase hybrid step-motor at a maximum output torque of 368 Nm. While four quarter steps are required for a full rotation of the rotor, a planetary gear (gear ratio of 1:200), which is directly attached to the motor, drives the two-gear drive. Dependent on the application

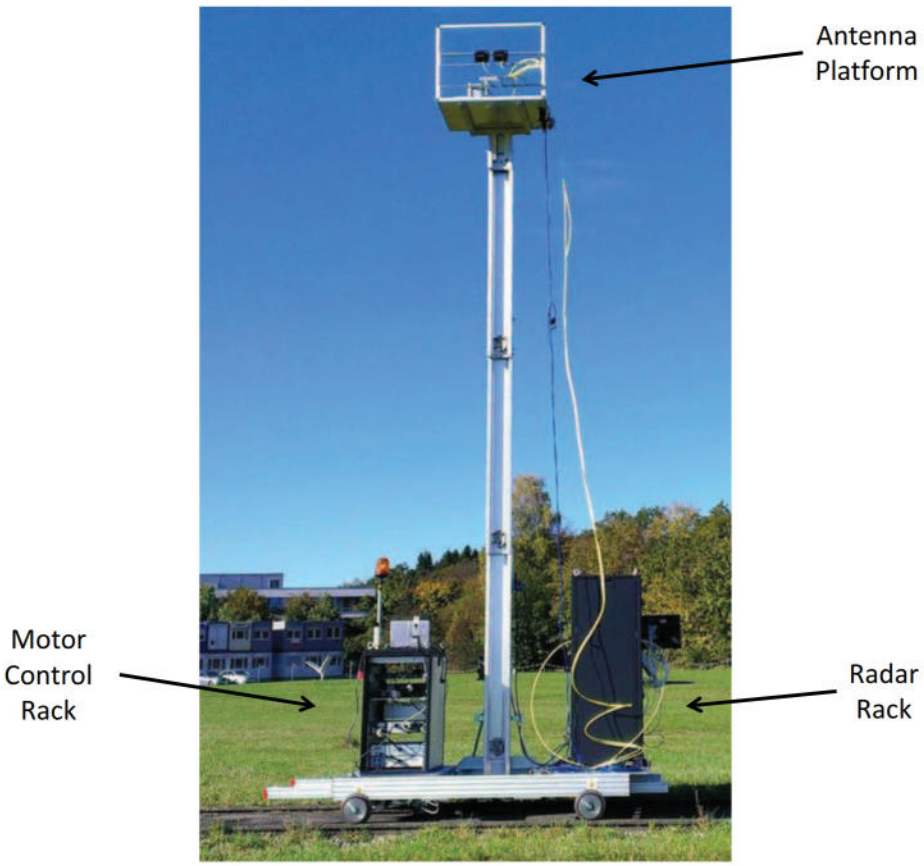


Figure 6.15. MIMO-SAR demonstrator during measurement.

(higher torque or higher velocity), the system operator can select between one of the two gears, which are realized by two toothed pulleys and a toothed belt. In dependence of the chosen gear and the circumference of the wheels, the driving distance per quarter step of the motor is 0.00196 mm or 0.00131 mm, respectively. Operation with a maximum motor control frequency of 40 000 steps/s leads to the maximum velocity of 0.98 m/s for the first gear and 0.65 m/s for the second gear. To prevent a too high moment of inertia during start and stop actions, flexibly adjustable acceleration and deceleration ramps are defined in the in-house developed control software.

The step motor itself is controlled via a modular *PhyMotion* step-motor control consisting of power stage, power supply module, indexer (multiplexer) for switching between several motors, communication interface between computer and controller, and finally the controller itself. Commands for start, stop, velocity, and acceleration and deceleration ramps are sent from the overall control

computer in binary format plus check-sums to the motor control unit via an Ethernet connection. In addition, with the custom written software, it is also possible to read out the motor position from an encoder and to ascertain to the absolute position of the SAR platform.

6.6. Signal Pre-Conditioning and Pre-Processing

The non-linear behavior of the radar hardware, particularly the amplifier gain dependence, over frequency leads to distortions of the signal amplitude, when the amplifiers are not operated in saturation (cf. section 6.3). As known from section 3.4.1, this causes a degradation of the maximum available range resolution and should be compensated. For the MIMO-SAR demonstrator this is done by measuring a reference signal through the calibration loop of the calibration crate and an enduing compensatory correction of the signal's envelope. Without going into much detail, the desired transmit waveforms are uploaded to the AWG, individually routed through the calibration crate and thus the response of all eight receive channels are recorded. The signal envelopes for all Tx-Rx channel combinations are determined, smoothed by Savitzky-Golay filters [131] and the mean value over the receive channels is calculated. The respective transmit waveforms are corrected by this determined envelope and used for the measurements.

In order to prepare the acquired raw data, which is saved in the HDF-5 file format, for calibration and processing, some pre-processing steps are necessary. Apart from the acquired raw-data, which is structured in a three-dimensional domain in fast-time, receive windows, and receive channels; the HDF-5 file contains the header with additional information, such as sampling frequency, length of the receive windows, and channel-dependent correction factors for calibration from the network analyzer measurements.

First of all, for DBF and SAR processing, the real sampled data of each receive channel $u_{\mathrm{re},i}[\acute{p}, p]$ must be converted to complex data by using the Hilbert transform [27]. The Hilbert transform is equivalent to a non-causal filter. Because a realization of such filters is practically not possible, they are often approximated by Finite Impulse Response (FIR) filters in discrete signal processing. While this approximation leads to distortions in the signals' amplitude, which are strong at the edges of the signal spectrum, the phase response is maintained over frequency [132]. The imaginary part of the complex valued receive signal $\check{u}_i$ is ob-

tained by FIR filtering of the acquired real part with the Hilbert transfer function h_{Hil}, and the real part of $\check{u}_i$ is equal to $u_{\mathrm{re},i}$ and shifted by the group delay of the FIR filter (cf. Fig. 6.16):

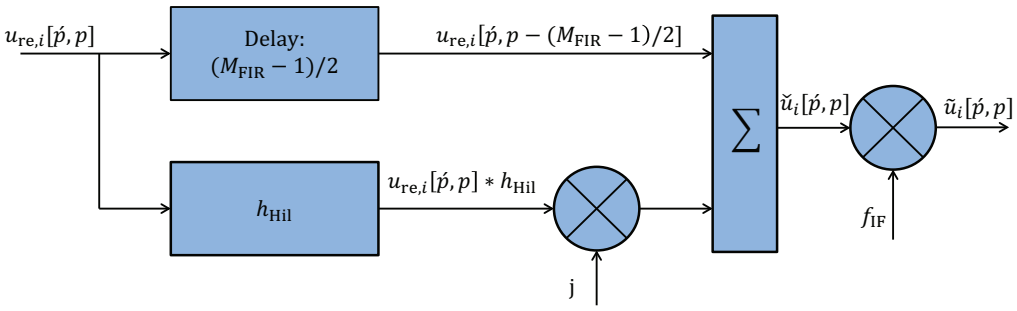


Figure 6.16. Practical implementation of the Hilbert transform by a FIR filter.

$$\check{u}_i[\acute{p},p] = u_{\mathrm{re},i}[\acute{p},p-(M_{\mathrm{FIR}}-1)/2] + \mathrm{j}\cdot\sum_{m=0}^{M_{\mathrm{FIR}}} h_{\mathrm{Hil}}[m]\cdot u_{\mathrm{re},i}[\acute{p},p-m] \qquad \forall \quad \acute{p}. \tag{6.6}$$

Where

$$h_{\mathrm{Hil}}[p] = \frac{f_{\mathrm{S}}}{\pi\cdot p}[1-\cos(\pi\cdot p)] \qquad \text{for} \quad p\neq 0$$
$$\text{and} \tag{6.7}$$
$$h_{\mathrm{Hil}}[p] = 0 \qquad \text{for} \quad p=0$$

and M_{FIR} being the order of the filter (no. of taps = filter order + 1). Because for the MIMO-SAR demonstrator, the processing time is not important, usually 100 taps are used. After down-conversion from the intermediate center frequency of the receive signal f_{IF} (usually set to f_{IF} = 205 MHz) to the base-band via

$$\tilde{u}_i[\acute{p},p] = \check{u}_i[\acute{p},p]\cdot\exp(-\mathrm{j}2\pi f_{\mathrm{IF}}p) \qquad \forall \quad \acute{p}, \tag{6.8}$$

supplementary windowing in frequency-domain along fast-time, e.g. by Hanning or Hamming windows, reduces the distortions, which are caused by the Hilbert transform:

$$u_{\mathrm{d},i}[\acute{p},p] = \mathrm{DFT}^{-1}\left\{\mathrm{DFT}\left\{\tilde{u}_i[\acute{p},p]\right\} \cdot w_{\mathrm{win}}[p]\right\} \qquad \forall \quad \acute{p}. \tag{6.9}$$

As required, $u_{\mathrm{d},i}[\acute{p},p]$ can also be re-sampled to a lower sampling frequency to reduce the overall amount of data and computational effort. The raw-data is then prepared for calibration and MIMO-SAR processing.

6.7. Signal Calibration

Apart from the signal pre-conditioning to increase the flatness of the transmitted waveform (cf. last subsection), on the received signal some further calibration routines are applied in the post-processing in the following order:

1. Time Alignment from Pulse-to-Pulse:

   The receive signal is sampled with a sampling interval of 1.0 ns, while the analogue trigger signal, which is used to define the beginning of the receive window, occurs somewhere between two discrete samples. If the starting point of the successive received window is displaced over the time span of 1.0 ns, then a significant loss of coherence will occur. This corresponds to a phase error in X-band in the order of approximately 10 wavelengths. A coherent SAR processing would be impossible this way. In order to circumvent this time shift, an additional trigger interpolator, which is integrated in the digitizer, gives accurate information about the position of the trigger signal between two samples for every receive window separately. These interpolated time-values t_{horpos} are used to shift the whole time-axis for each sampled receive window, enabling a coherent processing:

$$\begin{aligned} p_{\mathrm{horpos}} &= \left\lfloor t_{\mathrm{horpos}} \cdot f_{\mathrm{S}} \right\rceil, \\ \widehat{u}_{\mathrm{d},i}[\acute{p},p] &= u_{\mathrm{d},i}[\acute{p},p - p_{\mathrm{horpos}}]. \end{aligned} \tag{6.10}$$

2. Absolute Calibration:

   To compensate system-internal delays and attenuations, which are caused by components and cabling, the whole MIMO-radar system was characterized by a VNA. While it is assumed, that the measured s-parameters are constant over time, they are used to extract absolute target positions and receive powers by adjustment of the absolute signal levels.

3. Raw-Data Based Calibration:

   When required, additional raw-data calibration algorithms can be applied to achieve an improved amplitude and phase synchronization between the channels. Several methods, which are based on contrast metrics and adapted from image processing, or covariance methods, are already known [9, 47, 48]. Unfortunately, the usefulness of the chosen algorithm is completely dependent on the observed scene (homogenous, many strong structures, point target(s), ...) and they should be applied with carefulness. However, with these methods it is not only possible to correct the imbalances between the channels, but also to compensate high-order phase errors resulting from sensor movement, and to compensate the Doppler centroid.

4. Replica Signal:

   The recorded reference signal, which is routed through the calibration loop of the demonstrator, is distorted by the non-linear characteristics of the radar hardware. Because the transmitted and received signals in a true SAR measurement are affected by the same errors, we suggest to use this reference signal as substitute for $s_{\mathrm{BB},k}$ during the range compression process in Eq. (2.24). Obviously, this correction method allows to correct only constant and slow-time varying system drifts, such as the temperature behavior of the radar. Basically, there are two ways to apply the acquired reference signal for range compression.

   The filter function, which is used for range compression, is by convention defined as $h = s_k^*(-t)$. But an elimination of the pulse shape can only be justified if the filter function is $h = 1/s_k(-t)$, which is also known as *general pulse compression* [14]. While the phase term is compensated in both methods, the envelope is solely inversely corrected in the general pulse compression method. For a non-constant signal envelope, the impulse response is

broadened with the standard range compression method. This is due to the fact, that the distorted envelope can be considered as a window function (cf. Eq. (3.30)). Using the inverse compression method, the resolution will be kept. However, if noise is taken into account, then due to amplification of the signal by the inverse envelope, also the noise will be amplified, which in turn leads to a degraded *SNR*. Dependent on the radar system parameters and the requirements (*SNR* or resolution), the optimum solution for the range compression filter has to be found.

In this context it is also worth noting, that the measured antenna pattern (cf. section 6.4) are also corrected in the individual DBF algorithm. The exact implementation is finally dependent on the used radar operation mode.

7. Experimental Results of DBF and MIMO Measurements

In order to verify the advanced signal processing methods, which are described in this thesis, measurements were conducted with the MIMO-SAR demonstrator of chapter 6. Four important experimental setups and the results, which have been obtained by these measurements are presented in this chapter.

This chapter is structured as follows. The measurement described in the first section uses a reflector antenna with a digital feed consisting of eight elements for DBF on receive. Two Segmentally-Shifted Chirp (SSC) waveforms (cf. section 3.2.4) are transmitted via two horn antennas and their signal-inherent ambiguities are suppressed via spatial diversity realized with DBF in elevation.

The result of the second measurement is about multi-channel reconstruction in azimuth. In a real SAR acquisition on a lawn, a planar array of receive antennas with three independent apertures was used. The sub-sampled raw-data was reconstructed, in reference to section 2.4.2, with the algorithm presented in [10]. Finally, azimuth ambiguities caused by sub-sampling could be suppressed via DBF.

A highly innovative measurement result is presented in section 7.3. As an application example of MIMO-SAR, the separation of multipath propagation effects in SAR tomography is demonstrated.

The final measurement shows the use of polarimetry in MIMO-SAR. It is shown, that simultaneous fully polarimetric measurements in SAR are possible without any reduction of the swath width or of the resolution in comparison to the standard quad mode for polarization measurements.

7.1. Digital Beam-Forming on Receive with a Reflector Antenna for Suppression of Signal Ambiguities

To demonstrate that signal ambiguities caused by Short-Term Shift-Orthogonal (STSO) waveforms (cf. chapter 3) can be suppressed by DBF on receive, a mea-

surement was conducted with the MIMO-SAR demonstrator (cf. chapter 6). Additionally, as already indicated, instead of using the radar in its standard configuration with patch antennas, a reflector antenna with a digital feed array was used. Accordingly, this experiment not only verifies the applicability of MIMO-SAR, but also the use of DBF-SAR in combination with reflector antennas. In contrast to the long pulse durations reported in the work of Stewart in [133], in the present measurement, the pulse duration was reduced with respect to the swath width. This allows to investigate the full potential of the waveform-separation method with DBF instead of investigating the signal cross-correlation interferences only.

7.1.1. Description of the Experiment

For the demonstration and verification of the STSO waveforms with the MIMO-radar demonstrator, an outdoor measurement in the range direction was conducted. The radar was positioned on the roof of a building and the eight receive channels were connected to the feed elements of an elliptical DBF reflector antenna pointing to a lawn with point-like targets. For transmission, two direct radiating horn antennas were used. With respect to the repeating structure of STSO waveforms, signal ambiguities in range are expected if no advanced signal processing technique is used. By applying elevation DBF algorithms on the received raw data, these ambiguities can be theoretically suppressed (cf. chapter 4). Aim of the experiment is to prove, that a sufficient de-correlation can also be achieved in practice.

Radar Measurement Scenario and Signals

The MIMO-radar demonstrator with eight receive channels, operating in X-band at a center frequency of $f_0 = 9.58$ GHz, was placed on top of a building at a height of 11.5 m. Five trihedral corner reflectors with a RCS of 35.5 dBsm each, served as point-like targets at the ground-range positions 21.5 m, 28.0 m, 38.7 m, 48.3 m, and 62.0 m (slant-range positions: 25.0 m, 30.8 m, 40.7 m, 50.0 m, and 63.3 m). A photo of the setup is given in Fig. 7.1.

On transmit, two Segmentally-Shifted Chirp (SSC) waveforms (cf. section 3.2.4) were transmitted simultaneously with a pulse duration of $\tau_p = 0.4\,\mu$s and a signal bandwidth of $B = 300$ MHz. Due to the short pulse duration, the ambiguities are expected to be located at a slant-range of ±30.0 m (cf. Eq. (3.3)) from the real

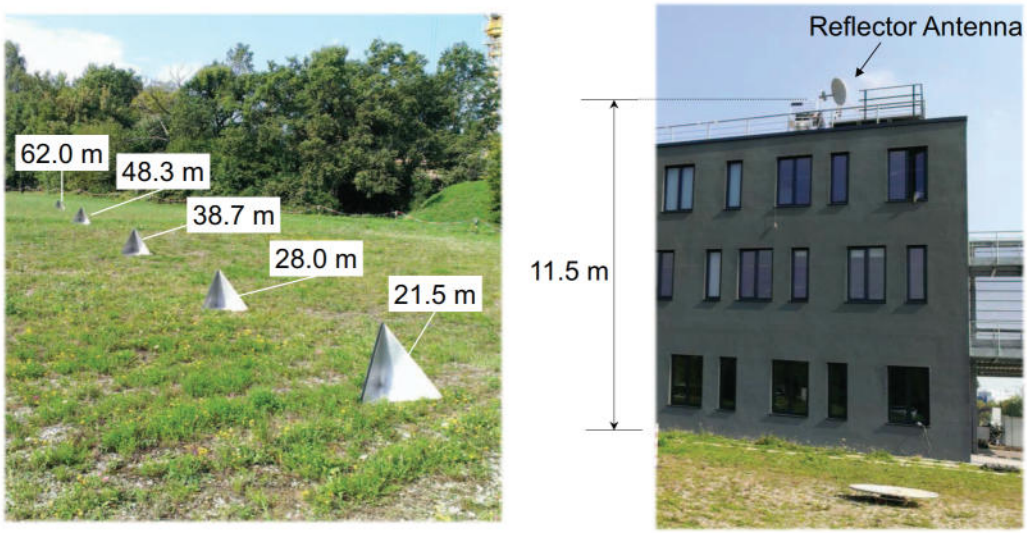


Figure 7.1. Photo of the measurement setup for the DBF experiment with a reflector antenna. Left-hand side: Five corner reflectors on a lawn as point-like targets. Right-hand side: Reflector antenna on the roof of the building.

impulse response of each target. Accordingly, they appear within the observed scene. Because the slant-range to the target area is less than the pulse extent, the radar transmits and receives simultaneously. To reduce coupling effects from the transmit antennas to the receive antennas, for the transmitter part separate standard gain horn antennas were used, which illuminate the swath directly. The used reflector antenna is described in the following section in more detail.

Reflector Antenna

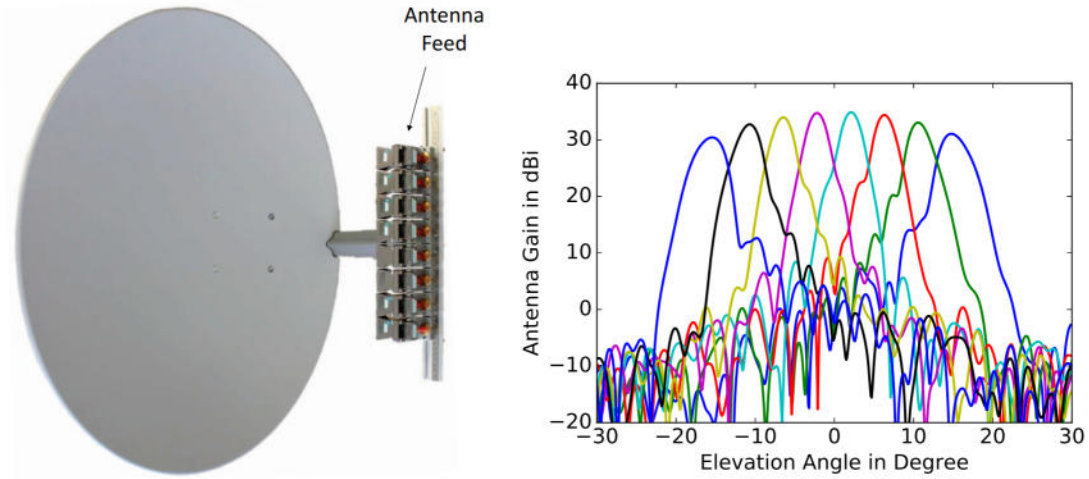
Deployable reflector antennas, with multiple channels, are receiving more and more attention for future spaceborne SAR missions, like Tandem-L [39, 40, 100]. In order to verify advanced DBF techniques in SAR, an elliptical reflector antenna with eight channels in elevation and offset configuration was developed. The most important antenna parameter are summarized in Tab. 7.1 and a photo can be found in Fig. 7.2. In contrast to planar array antennas, where every element illuminates approximately the same area directly, reflector antennas have narrow beams, which point to different directions. This becomes visible in the measured antenna pattern in Fig. 7.2. First measurement results obtained with this antenna in static scenes can be found in [42, 100, 129].

Table 7.1. Reflector antenna parameters.

Parameter	Value
shape	elliptical (1.0 m x 0.7 m)
polarization	V
max. gain	37 dBi
no. elements in elevation	8
element spacing	4.4 cm
center frequency	9.6 GHz
HPBW elevation	1.2°
HPBW azimuth	2.7°

7.1.2. Processing and Measurement Results

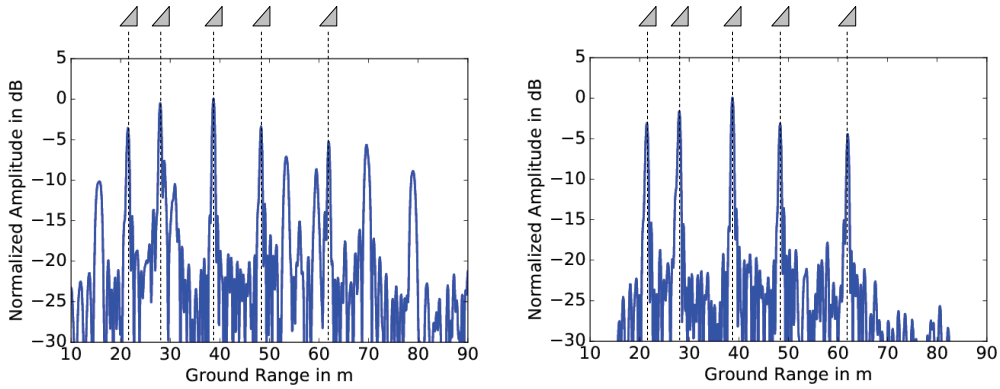
Fig. 7.3a shows the plot of the range compressed data with linear combination of all receive channels without DBF (unity weighting). A match with the theoretical prediction is clearly noticeable: The ambiguities are located at a slant-range distance of ±30 m away from the real impulse responses and have an amplitude which is about 6 dB lower (cf. zero-Doppler cuts of ambiguity function section 3.3.2). It must be noted, that in Fig. 7.3a the data is plotted against



(a) Photo of the reflector antenna with feed elements.

(b) Measured antenna pattern of the reflector antenna.

Figure 7.2. Photo and antenna pattern of the DBF reflector antenna with eight feed elements.



(a) Data without DBF processing. The measured range profile with the impulse responses of five targets is overlaid by signal ambiguities.

(b) Data with DBF processing. The signal ambiguities are suppressed and the responses of the five corner reflectors are clearly visible.

Figure 7.3. Range-compressed data of the experiment using Segmentally-Shifted Chirp (SSC) waveforms and a reflector antenna.

ground-range and the signal ambiguities are therefore not symmetrically around the impulse response.

In Fig. 7.3b the result with application of DBF can be seen. For signal processing, the approach described in section 4.5 was used. Due to the reflector antenna, which needs special computation of the beam-forming weighting vector, the Minimum Variance Distortionless Response (MVDR) algorithm [95] was applied by using the measured antenna beam-pattern. Five sharp peaks are visible in the plot and the ambiguities could be suppressed beyond the noise level. A high suppression of the ambiguities was possible because of the very narrow beam-pattern with a *HPBW* of 1.2° in elevation. This proves, that the SSC waveforms can be used for high-resolution MIMO-SAR imaging! At this point it is worth noting, that the same experiment was repeated with slightly varied parameters and with OFDM chirp waveforms (cf. section 3.2.2). Results and more detailed processing steps are presented in the master thesis of Madanahalli [104]. In summary, also the results of his thesis prove the applicability of MIMO-SAR with high resolution and large swath widths.

For a final confirmation of the waveforms and the DBF algorithm, a further experiment, emulating a real SAR measurement scenario with a fence as extended scatterer was conducted in section 7.4 of this thesis.



Figure 7.4. Photo of the measurement scene for the azimuth DBF experiment. Five trihedral corner reflectors on a lawn can be seen.

7.2. Demonstration of Digital Beam-Forming in Azimuth

7.2.1. Description of the Experiment

The concept of using multiple independent apertures in azimuth for DBF-SAR with a planar antenna is summarized in section 2.4.2. For the experiment, five trihedral corner reflectors were placed on a lawn. A photo of the scene is shown in Fig. 7.4. With the MIMO-SAR demonstrator (cf. chapter 6) a standard up-chirp waveform with a pulse duration of $\tau_p = 10\,\mu$s and a bandwidth of $B = 300$ MHz was transmitted. All relevant SAR-system parameters can be found in Tab. 6.1 and Tab. 7.2. On the receive side, three receive channels with an element separation in azimuth of 10 cm were sampled simultaneously with a *PRF* of 10 Hz (uniform sampling). The principle of the resulting effective phase centers corresponds exactly the sketch illustrated in Fig. 2.8.

7.2.2. Measurement Results

In Fig. 7.5a we can find the SAR image of the first receive channel, which was processed via standard SAR signal processing with range cell migration correction, using the *PRF* of 10 Hz. The five targets are clearly visible in shape of ellipses. For channel reconstruction with multiple receive channels, the same data set was

Table 7.2. Radar instrument settings and system parameters of the azimuth-DBF experiment.

Description	Parameter	Value
pulse repetition frequency	PRF	10 Hz
velocity	v	0.1 m/s
sensor height	h	6.5 m
number of receive channels	N_{Rx}	3
element separation	d	0.1 m

used. To verify the principle of channel reconstruction, as a first signal processing step, the raw data was digitally sub-sampled to $PRF_{\mathrm{sub}} = PRF/N_{\mathrm{Rx}} = 3.33$ Hz. Afterwards, the data was combined with the DBF algorithm of Krieger et al. in [10]. As can be seen in Fig. 7.5, both images – before and after reconstruction – look almost identical and no ambiguities can be observed. Fig. 7.6 shows the azimuth and range cuts of the impulse response of the corner reflector, which was located at 11.8 m in azimuth and 12.0 m in range. The expected resolutions of 0.65 m in range (cf. Eq. (3.30)) and 0.05 m in azimuth direction (cf. Eq. (2.22)), could be reached without any degradations after DBF. Deviations at the side-lobe level are due to residual phase errors after calibration.

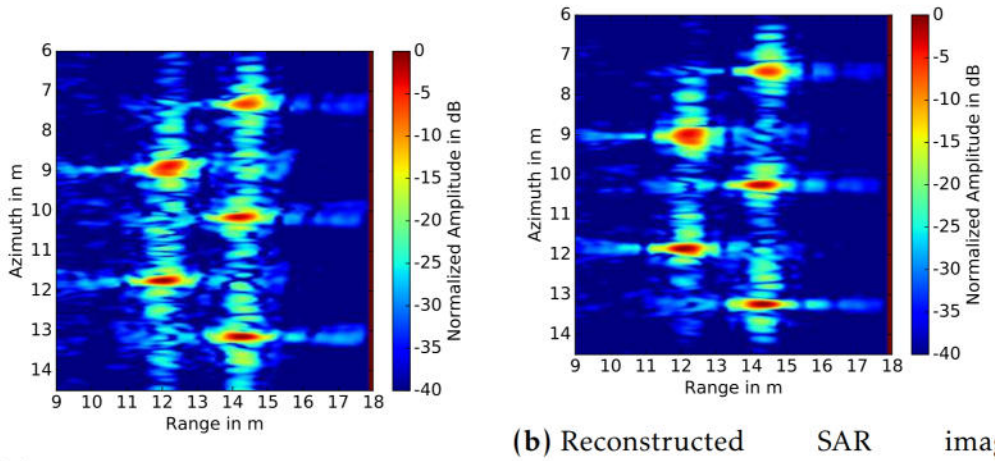
This result verifies, that the concept of DBF-SAR in azimuth direction is working and that the raw data can also be directly sub-sampled at the analog-to-digital converter.

7.3. Detection of Multipath Propagation Effects in SAR-Tomography

The experiment, which is described in this section, concentrates on MIMO-SAR tomography (more details can be found in section 2.5.6). The basic idea is to localize multipath propagation effects by making use of a combined transmit and receive DBF technique.

7.3.1. Description of the Experiment

In MIMO-SAR tomography the antenna beams are steered in elevation for each along-track position of a SAR data set separately. Accordingly, as a first proof

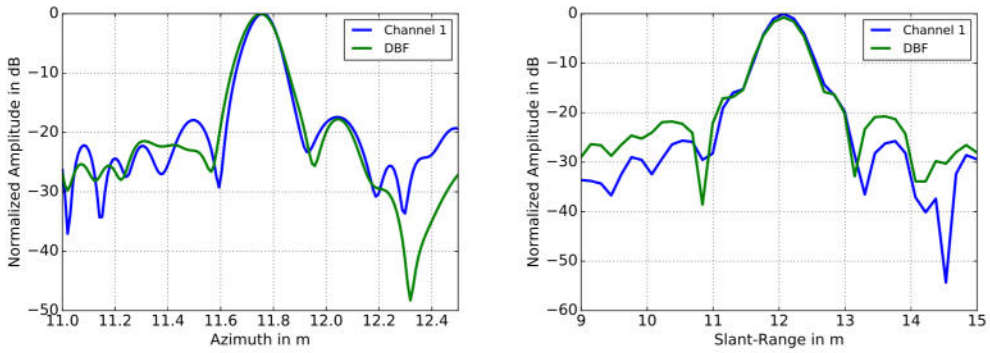


(a) SAR image of a single receive channel (PRF = 10 Hz).

(b) Reconstructed SAR image with three receive channels (PRF_{sub} = 3.33 Hz).

Figure 7.5. Processed SAR images of the azimuth DBF experiment. After channel reconstruction, both images look almost identical.

of the concept, it is sufficient to conduct the experiment in the range / elevation direction for a single echo window with a non-moving MIMO-radar. This has the advantage, that no additional errors may be added. Basic aim of the experiment is to identify two perpendicularly placed metal plates unambiguously as a dihedral scatterer. This can be achieved by steering the transmit and the receive antenna beams to different directions. A gap around the virtual phase center at the edge-junction of the metal plates should show, that there is no reflection if the antenna



(a) Range cut.

(b) Azimuth cut.

Figure 7.6. Cuts in range and azimuth through a single corner reflector. The impulse responses show strong similarities before and after DBF.

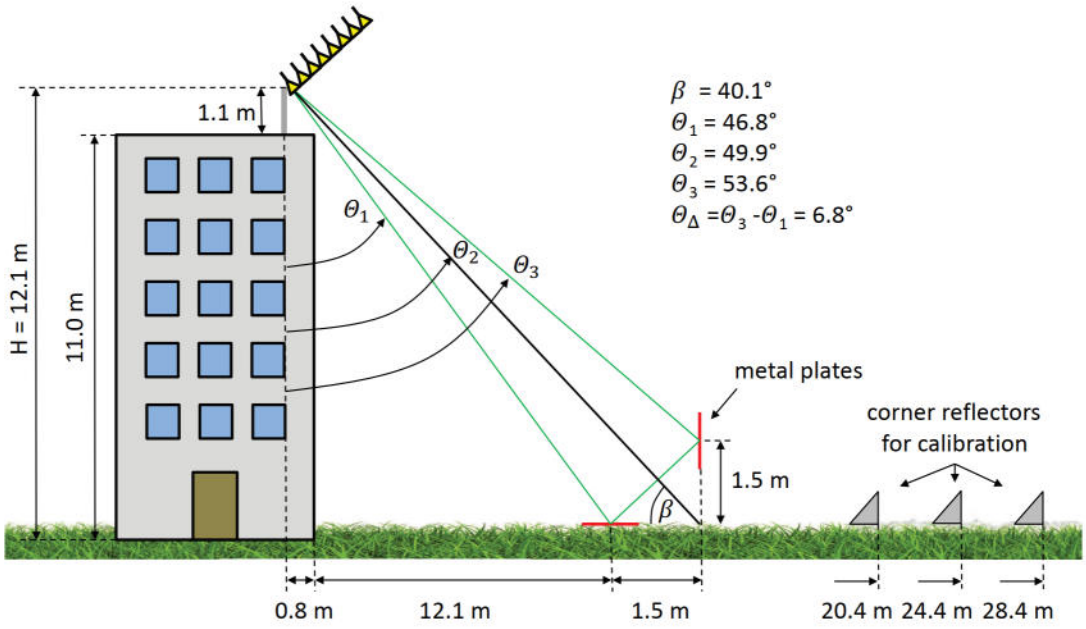


Figure 7.7. Sketch of the measurement setup used for the multipath propagation detection experiment.

beam is steered to that point. Details of the scene and the antenna array are given next.

Radar Measurement Scenario and Signals

The MIMO-radar demonstrator (cf. chapter 6) was placed on top of the roof of a building. A sketch and a photo of the measurement setup are shown in Fig. 7.7 and Fig. 7.8, respectively. Three trihedral corner reflectors at ground range distances of 20.4 m, 24.4 m, and 28.4 m served as reference point targets for a later signal calibration.

Two perpendicular metal plates of size 0.5 m x 1.0 m, placed at slant-range distances of approximately 18.8 m, are used as a double-bounce target. The incident wave on the horizontally placed plate is reflected forward to the vertical plate, which reflects the signal back to the radar and vice versa. The angle of the phase center at the virtual intersection point was $\Theta_2 = 49.9°$. According to the chosen geometry, it is assumed that the plates can not be resolved as dihedral scatterer after standard range compression or standard tomographic processing, e.g. single-pass SAR tomography. Further it is expected, that no reflections occur at the absorbing material, on which the vertical metal plate is placed.

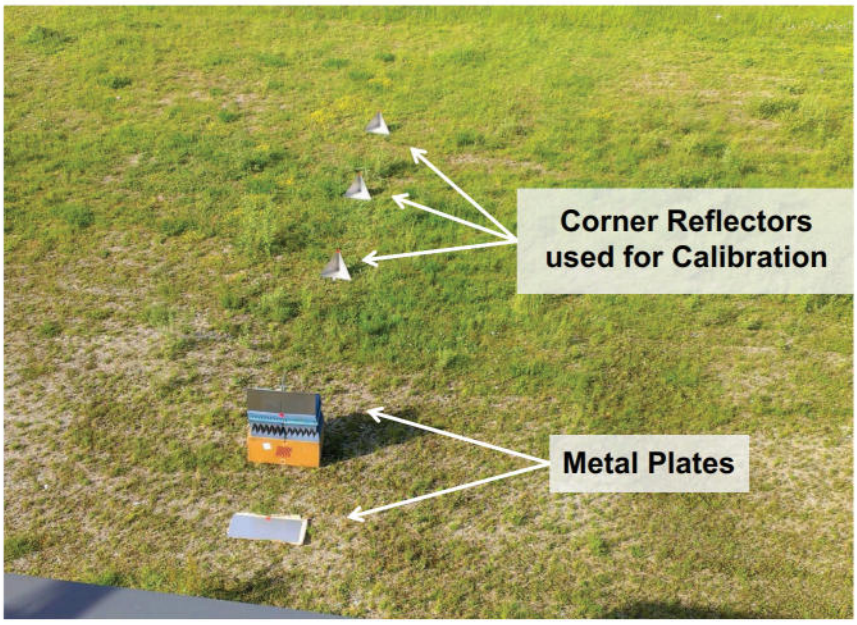


Figure 7.8. Photo of the measurement setup used for the multipath propagation detection experiment.

To avoid effects caused by not imperfectly orthogonal waveforms, and since the scene does not change over time, the transmit signals were transmitted in a time-multiplex mode, while all receive channels were recording simultaneously. Finally, by neglecting antenna coupling effects, orthogonal data sets for each channel combination are available. For the transmit waveforms up-chirp signals with a pulse duration of $\tau_p = 10\ \mu s$ and $B = 300$ MHz bandwidth were used.

Antenna Array

Two antenna carriers, mounted on a handrail at the roof edge of the building, were used to fix the transmit and receive antennas (cf. Fig. 7.9). A horizontal separation of 0.50 m was introduced between the transmit and receive antenna phase centers to avoid too high coupling effects. While the receive antennas were standard gain horn antennas with a gain of 10.0 dBi and *HPBW*s along elevation of $\Delta\Theta_{3dB,el} = 48.5°$ and along azimuth of $\Delta\Theta_{3dB,az} = 47.4°$, for transmission, patch antennas with a gain of 14.1 dBi each and *HPBW*s of $\Delta\Theta_{3dB,el} = 60°$, $\Delta\Theta_{3dB,az} = 16°$ have been used (cf. section 6.4).

The element spacing of the eight receive antennas was chosen to be $d_{Rx} = 0.15$ m, whereas the distance between the four transmit antennas was $d_{Tx} = 0.35$ m (cf. Fig. 7.9). This leads to minimum *HPBW*s in elevation of the

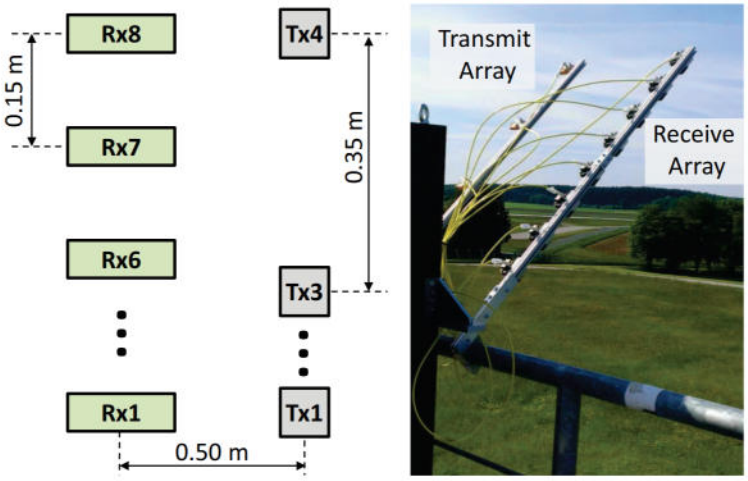
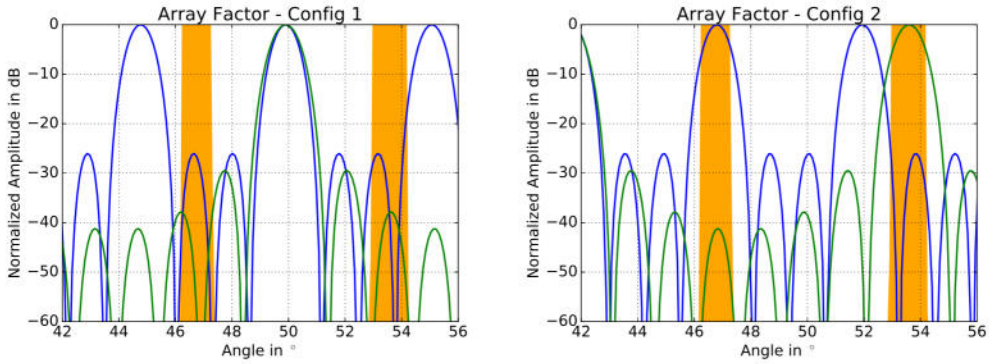


Figure 7.9. Sketch and photo of the antenna array used for the experiment.

synthesized antenna beams of $\Delta\Theta_{\mathrm{Rx,3dB}} = 1.1°$ for the receive and $\Delta\Theta_{\mathrm{Tx,3dB}} = 1.3°$ for the transmit array, respectively. Due to the large element spacings in comparison to the signal wavelength, grating lobes will appear along the elevation angle at $\Theta_{\mathrm{GL,Tx}} \approx \arcsin\left(c_0/(f_0 \cdot d_{\mathrm{Tx}})\right) = \pm 5.1°$ in the transmit case and at $\Theta_{\mathrm{GL,Rx}} \approx \arcsin\left(c_0/(f_0 \cdot d_{\mathrm{Rx}})\right) = \pm 12.0°$ in the receive case. In relation to the measurement scenario, the chosen geometry of the antenna arrays enable to form two different antenna beam configurations, which can be used to prove the proposed concept.

In the first beam-configuration, the transmit and the receive antennas are pointing to the same direction. An example is given in Fig. 7.10a, where the array factors of the transmit (blue color) and receive (green color) antenna beams are plotted with a steered position of $\Theta = 49.9°$. The orange shaded areas indicate the positions of the two metal plates in the scene. As can be seen, the combined Tx-Rx beam pattern can image at maximum one of the two plates. Accordingly, an imaging of both plates simultaneously would not be possible. In the second beam-configuration, the antenna arrays point to different directions with an offset of $\Theta_\Delta = 6.8°$ (cf. Fig. 7.10b). Using this value, at the same time, each metal plate is illuminated with an individual antenna beam. Hence, in this configuration, the plates should be visible. In both plots of Fig. 7.10 we can also see, that the first grating lobe of the transmit antenna is set within the area of interest (due to the limited number of available transmit channels). However, this should not lead to any disturbances, because a null of the antenna beam falls into the



(a) The antenna beams pointing to the same direction: $\Theta = 49.9°$ and $\Theta_\Delta = +0.0°$.

(b) The antenna beams pointing to different directions: $\Theta = 46.8°$ and $\Theta_\Delta = +6.8°$.

Figure 7.10. Array factor of the transmit (blue) and receive (green) antenna beams. The orange color indicates the positions of the two metal plates.

main-lobe of the receive antenna. Finally, the Tx and Rx antennas are sufficiently decoupled.

7.3.2. Calibration

Apart from the pre-processing and calibration steps, which are used to synchronize the channels of the radar hardware (cf. section 6.7), additional signal calibration was applied to increase the quality of the processed results. Especially due to the short ranges between radar and target and due to the large extent of the antenna array in comparison to the scene, a highly accurate synchronization between the channels becomes mandatory.

The first signal correction step is the compensation of the free-space attenuation according to the Friis equation. This leads to an amplification by the power of four along the range direction. Next, the data set of each channel combination is individually range compressed leading to $N_{\mathrm{Tx}} \cdot N_{\mathrm{Rx}} = 4 \cdot 8 = 32$ range profiles of the observed scene. An example of the corrected and range compressed signal for the first channel combination (Tx1 & Rx1) can be found in Fig. 7.11. While the three trihedral corner reflectors appear with the same normalized amplitude of 0.0 dB, the metal plates with a lower radar cross section generated an amplitude of -13.6 dB. The ground range positions agree with those mentioned in Fig. 7.7.

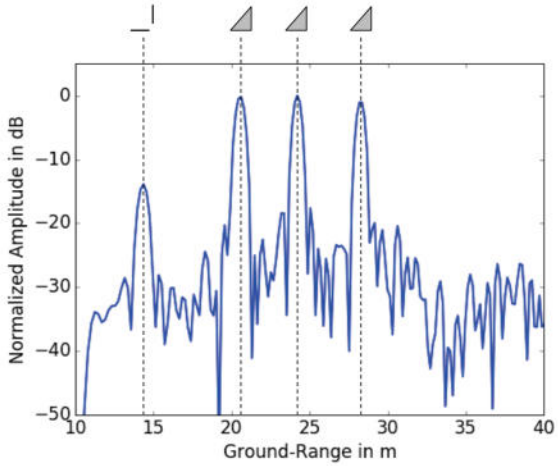


Figure 7.11. Range-compressed and calibrated data set of the first transmit and receive channel: $|u_{\mathrm{rg},1,1}(t)|^2$.

The range compressed signal is divided into three range sections, while each section contains the scattering response of a single corner reflector. Then, the phase course of each section is computed and compared to the simulation, while redundancy due to multiple transmit channels helped to decrease the synchronization errors by calculation of the mean values. This leads to the last applied calibration step, where the mean values of the estimated phases of the measurement data were adapted to the phases from the model of the computer simulation. The result is plotted in Fig. 7.12, while the antenna tilt angle was corrected by +0.4° to $\Theta_{\mathrm{tilt}} = 135.4°$ and on each receive channel an additional phase offset of +90° ($\hat{=} + 8.0$ mm in X-band) was introduced. The remaining phase error after correction was about ±45°, which leads in a worst-case scenario to an acceptable antenna mis-pointing of ±0.19°.

7.3.3. Processing and Measurement Results

Because of the large element spacing, each antenna has a different looking angle for each target, which complicates the DBF processing. While in standard receive-only DBF algorithms only the far-field condition holds, we have to generalize this concept for the near-field. This leads to a multistatic formulation of the radar geometry. With respect to Eq. (2.15), the signal delay from the transmit antenna to the ground and back to the receive antenna is $\tau_{k,i}(t)$. For near-field focusing, these time delays are calculated for each ground range position in de-

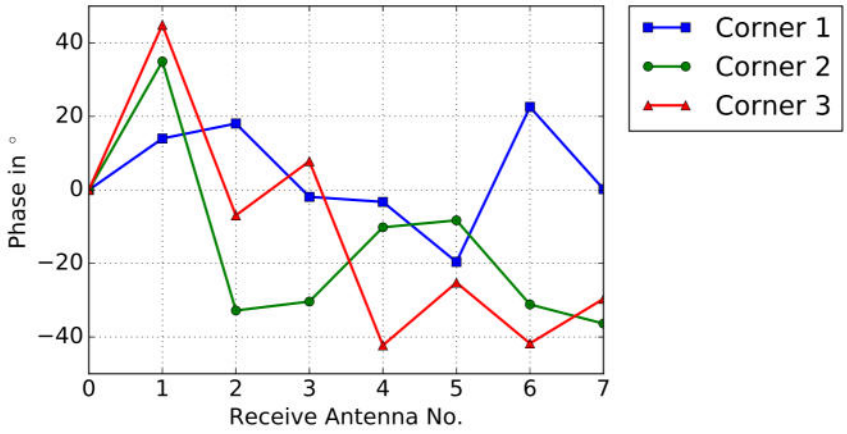


Figure 7.12. Remaining phase error of the three corner reflectors with respect to the simulation for the first transmit channel.

pendence of the fast-time t. Taking the antenna pair with indices $k = i = 0$ as reference, next we define a differential time delay with the property

$$\Delta\tau_{k,i}(t) = \tau_{k,i}(t) - \tau_{0,0}(t). \tag{7.1}$$

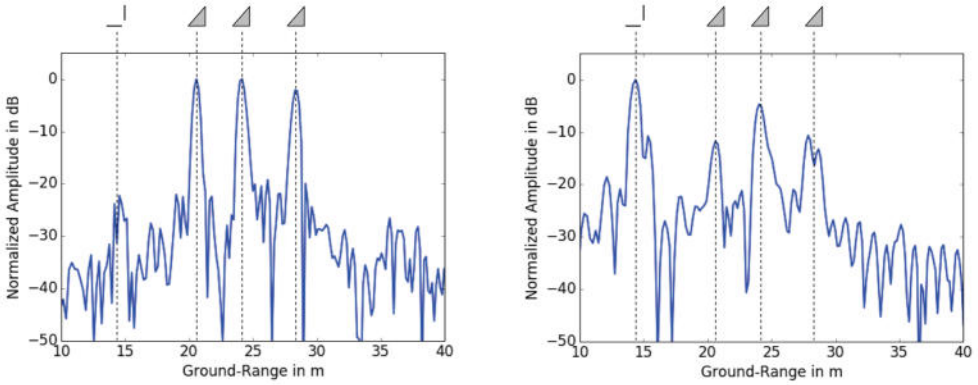
For beam-forming it is necessary to shift each range compressed data set $u_{\mathrm{rg},k,i}(t)$ by the delays $\Delta\tau_{k,i}(t)$:

$$u_{k,i}(t) = u_{\mathrm{rg},k,i}\left(t - \Delta\tau_{k,i}(t)\right). \tag{7.2}$$

Usually this is done in signal processing with the time-shifting property of the Fourier transform in frequency domain. A final summation of $u_{k,i}(t)$ over all transmit and receive channel pairs leads to the range compressed and spatially filtered range profile of the illuminated scene:

$$u_{\mathrm{DBF}}(t) = \sum_{k=0}^{N_{\mathrm{Tx}}-1} \sum_{i=0}^{N_{\mathrm{Rx}}-1} u_{k,i}(t). \tag{7.3}$$

In the following, we concentrate on the previously mentioned antenna beam configurations 1 and 2.



(a) Transmit and receive antenna beams pointing to the same direction: $\Theta_\Delta = 0°$.

(b) Transmit and receive antenna beams pointing to different directions with an offset of $\Theta_\Delta = 6.8°$.

Figure 7.13. Range compressed data after DBF: $|u_{\mathrm{DBF}}(t)|^2$.

In the first configuration, the transmit and the receive beams point to the same direction ($\Theta_\Delta = 0°$). The weighted and combined range compressed data are depicted in Fig. 7.13a. In comparison to the uncombined data from Fig. 7.11, the resulting DBF gain, which is measured at the corner reflectors is 14.4 dB (the diagrams are, however, normalized). The theoretical gain of $10 \cdot \log\{N_{\mathrm{Tx}} \cdot N_{\mathrm{Rx}}\} = 15.1$ dB could not be achieved due to remaining calibration errors (in particular the topography of the ground). As it becomes apparent, the metal plates appear suppressed with a maximum amplitude of just -22.3 dB. This stands strongly in agreement with the side-lobe level of the array factor (cf. Fig. 7.10a). In fact, in comparison to Fig. 7.11 the whole signal level changed after DBF and the suppression does not equal the normalized amplitude of Fig. 7.13a. However, this can be explained by the combined gain of the antenna, which focuses also on the lawn.

In the second antenna beam-configuration, the transmit antenna points to the ground with a constant angular offset of $\Theta_\Delta = +6.8°$ with reference to the receive antenna beam (cf. Fig. 7.10b). Basically, the angular offset is obtained by adjusting the equivalent range distance from the antenna to a hypothetical target on the ground by using trigonometric functions. The result is plotted in Fig. 7.13b. There, the corner reflectors are suppressed, while the metal plates appear clearly as a single target. With respect to the single channel case, the resulting DBF gain, which is measured at the maximum of the impulse response of the plates, is 11.8 dB.

A perfect suppression or focusing of the metal plates could not be achieved in both DBF modes, because of the geometrical extension of the metal plates along azimuth. In addition, the wide antenna beams in azimuth direction illuminate a significant part of the lawn with non-negligible scattering coefficient, which also influences the results of the experiment.

7.3.4. Conclusions of the Experiment

The concept of multipath propagation detection via MIMO techniques in single-pass SAR tomography leads to an additional degree of freedom, which allows to extract additional information about the scattering behavior of the targets. Measurement results of a real radar scene have shown, that the suggested concept is working. For the future, it is recommended to repeat this preliminary measurement with simultaneously transmitted, orthogonal waveforms and extended volume scatterers (e.g. trees, crops) in a real SAR mode. Since it is known, that the type of scattering mechanism has also an impact on the polarization state of the radar signal, a combination with fully polarimetric measurements would also be a desirable activity.

7.4. Fully Polarimetric SAR Imaging by Simultaneous Measurement of the Scattering Matrix

7.4.1. Fully Polarimetric SAR Imaging with Orthogonal Waveforms

One application example of advanced MIMO-SAR imaging are simultaneous full polarimetric measurements of the four s-matrix elements (cf. section 2.5.1). In contrast to state-of-the-art full polarimetric techniques in SAR, the advantage of MIMO is the simultaneous acquisition of all four components of the complex scattering matrix (HH, HV, VH, VV) without any reduction of the swath width. With the MIMO method, which was firstly proposed in [11], both polarizations can be transmitted at the same time with non-interfering (orthogonal) waveforms, whereas the whole scattering matrix will be obtained later in the receiver with the beam-forming algorithm of chapter 4. Up to now, simultaneous fully polarimetric SAR imaging has been verified by measurements with individual point targets [130]. However, from section 3.1 it is known, that extended homogenous targets are very sensitive to interferences from imperfectly orthogonal

waveforms. To show that the advanced processing and de-correlation technique presented in chapter 4 is able to handle this issue, an experiment with a fence as extended target was conducted.

7.4.2. Measurement Scenario and Signal Processing

The measurement was conducted on a lawn with the MIMO-SAR demonstrator (cf. chapter 6). On the ground, we placed a fence of size 4.0 m x 10.0 m and a grid size of 2.5 cm x 5.0 cm to have a distributed target. Photos are given in Figs. 7.14 and 7.15. Since two transmit channels are sufficient (one channel for H-polarization and one for V-polarization), only two sub-pulses in the MSP mode are transmitted per pulse repetition interval. To test the potential of STFAP, very short pulses of duration $\tau_p = 0.3\,\mu$s were used. This leads not only to an overlap of the echos for the observed area, but also to a low amount of transmitted energy. To circumvent this loss of energy and to get a higher *SNR*, the *PRF* was increased to 6.0 Hz at a platform velocity of 0.1 m/s. According to the suggested STFAP concept, two receive antenna beams are formed by DBF, while each sub-pulse is tracked by its own beam. However, the seen pulse length of $> \tau_p \cdot c_0/2 = 45.0$ m is greater than the antenna *HPBW* of 10.1° after DBF combination, and thus a pulse extension loss might result [75]. With the used STFAP technique, broad frequency-variant antenna beams are formed and the loss will not occur. Each receive channel was split into ten bandpass-divided sub-channels, while each sub-channel shared one tenth of the full signal bandwidth (cf. Fig. 4.17). This is done for the horizontal and vertical receive channels individually to get four independent data sets, which correspond to the HH, HV, VH and VV polarization states of the scattering matrix. This is followed by standard SAR processing steps, i.e. as range compression, range-cell migration correction, and azimuth compression. For reference, the measurement was repeated with the conventional fully polarimetric mode with separate measurements for each transmitted polarization state.

7.4.3. Measurement Results

To achieve a high accuracy of the measurement results, first of all, a separate measurement with a single corner reflector in the scene was conducted. Based on the acquired raw-data, the algorithm presented in [47] was applied. The comparison

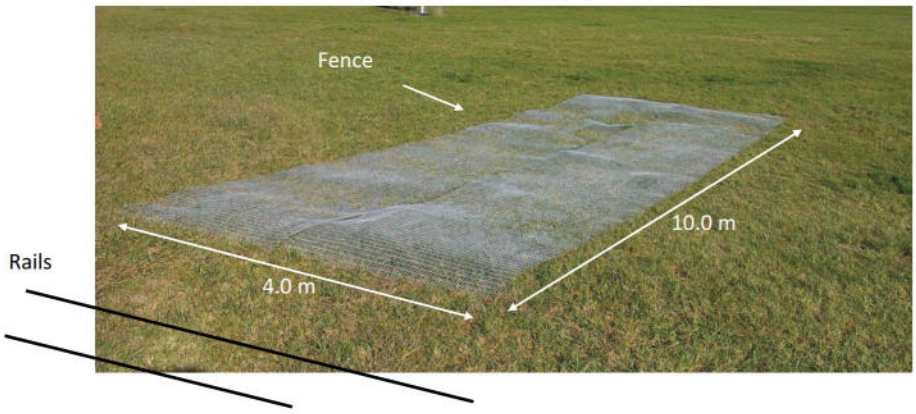


Figure 7.14. Photo of the measurement scene: A fence on the lawn as surface target.

between the uncalibrated and the calibrated impulse response of the target can be found in Fig. 7.16. After DBF on receive (SCORE) processing, approximately 3 dB *SNR* could be gained, while the resolution remains unchanged. The estimated correction values for amplitude and phase were used for the measurement with the surface target.

As an intermediate result for the measurement with the fence, in Fig. 7.17, the acquired raw-data signal for the first receive channel after FIR filtering in frequency domain is plotted. A total number of 10 FIR filters with 100 taps each has been used to cover the full signal bandwidth. The remaining signal processing steps are as described in section 4.4.3.



Figure 7.15. Photo of the measurement scene: MIMO-SAR demonstrator with a fence as surface target.

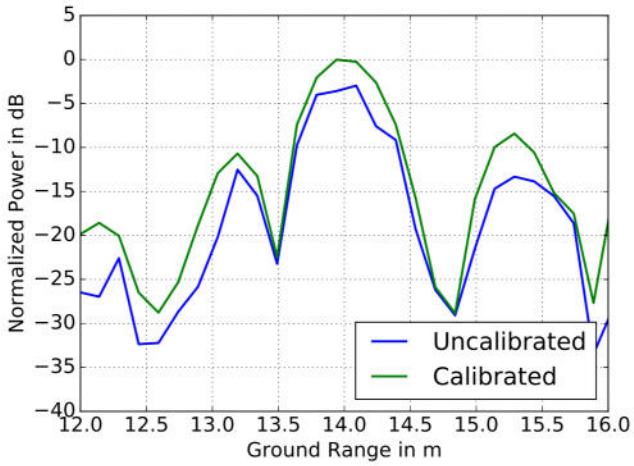


Figure 7.16. Comparison of calibrated and uncalibrated impulse responses of a corner reflector after DBF on receive.

In Figs. 7.18a, 7.18c, and 7.18e the processed MIMO-SAR images, containing the co- and cross-polarized data sets, can be found. Very *eye-catching* is the strong backscattering of the fence in the co-polar measurements (HH, VV). This is because the scattering mechanism at the wires of the fence does not rotate the electromagnetic field vector like in the case of dihedral scattering. From a theoretical point of view, the cross-polar measurement results (HV, VH) should be equal and possible differences are an artifact from calibration, the sensitivity of DBF, and filtering. Thus, only the mean value between the two SAR images is plotted.

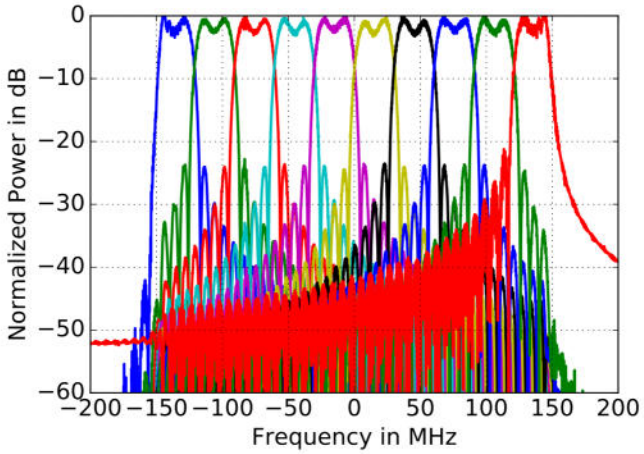
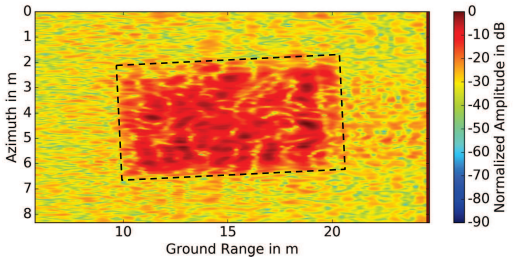


Figure 7.17. Acquired raw-data signal of the first receive channel after band-pass filtering with a bank of 10 FIR filters with 100 taps.

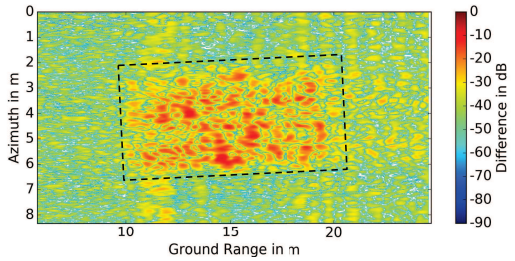
The plots of amplitude difference between the measurement results due to the present method and the ones obtained with the classical fully polarized mode with individual measurements, are depicted in Figs. 7.18b, 7.18d, and 7.18f. While the mean difference in the co-polarization states is -29.4 dB in HH (std. dev.: 0.0049), and -28.7 dB in VV (std. dev.: 0.0054), the mean difference in cross-polarization is significantly higher: -21.4 dB in (|HV| + |VH|)/2 (std. dev.: 0.0234). Since the mean measured radar cross section differs between the co- and cross-polarized data sets by approximately 6 dB, this deviation is absolutely acceptable. From these results it can be concluded, that the suggested concept of STFAP is also working for extended targets and polarization.

7.4.4. Conclusions of the Experiment

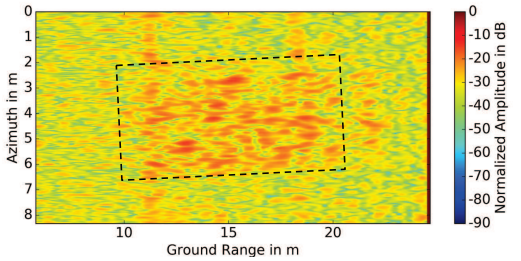
The concept of STFAP in combination with fully polarimetric measurements was firstly verified in [130] for point-like targets. However, SAR is a sensor for observation of large areas with homogenous RCS and a proof of concept with point-like targets is not enough. Due to the fact found under this experiment, the acquisition mode of simultaneous fully polarimetric acquisition was successfully verified with an extended target. Since it is expected that future spaceborne SAR missions will operate with DBF and MIMO modes, this achievement can be seen as a first milestone for the development of such systems. In the future, further investigations for differences in degree of coherence and cross-correlation interferences between the waveforms are planned. Especially a comparison and performance analysis of the multiple sub-pulse mode with alternative waveform types would be a significant step forward.



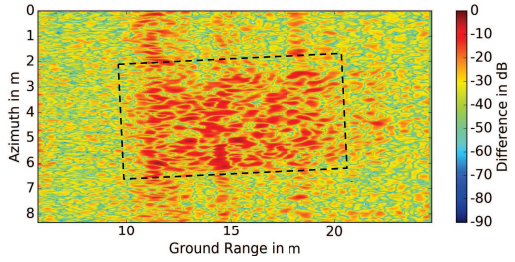
(a) Focused SAR image in polarization state HH.



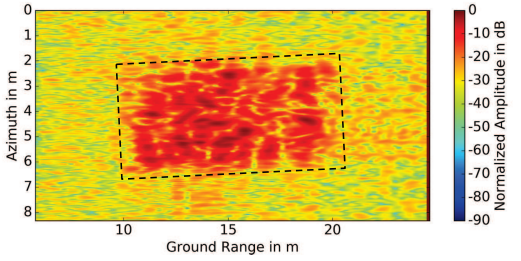
(b) Difference in polarization state HH (mean: -29.4 dB, std. dev.: 0.0049).



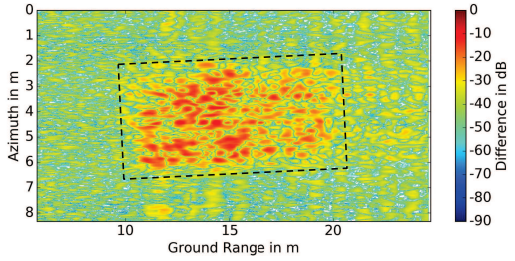
(c) Focused SAR image in polarization state $(|HV|+|VH|)/2$.



(d) Difference in polarization state $(|HV|+|VH|)/2$ (mean: -21.4 dB, std. dev.: 0.0234).



(e) Focused SAR image in polarization state VV.



(f) Difference in polarization state VV (mean: -28.7 dB, std. dev.: 0.0054).

Figure 7.18. Left-hand side: Focused SAR images of the simultaneous fully polarimetric experiment in different polarization states – scaling in $-(x$ dB). The fence is clearly visible in the co-polar data sets. Right-hand side: Difference between individual measurement and MIMO-SAR acquisition – scaling in $(-x)$ dB.

8. Discussion

Running spaceborne SAR missions, like COSMO-SkyMed, TerraSAR-X / TanDEM-X, Radarsat-2 or Sentinel-1 [5–7] suffer under a system-inherent limitation. In a SAR with a single transmit and receive channel, the swath width can only be increased at the cost of azimuth resolution and vice versa [21]. MIMO-SAR is a promising candidate to enhance the performance of follow-on SAR missions significantly. This claim is based on the increased flexibility due to an independent use of multiple channels simultaneously. Also new novel operation and acquisition modes can be realized with MIMO. Until now, MIMO-SAR is in an early stage and a number of challenges have to be dealt with. Since special focus of this dissertation is on MIMO-SAR for spaceborne High-Resolution Wide-Swath (HRWS) imaging, its chapters contribute into the new and innovative aspects of this field.

A straightforward adaption of existing MIMO techniques from the field of communications to SAR is *not possible*. This is mainly caused by different aims, which should be achieved. While in communication the user are usually interested in the information content of the transmitted signal, in SAR applications the information about the full channel is of interest for the given transmitted signals. This key difference leads to the fact, that a strict separation of the radio channels must be ensured. To say it in other words, the used transmit waveforms must be perfectly orthogonal on receive. Since the signal bandwidth of the transmitted waveform determines the range resolution and the used frequency band has an influence on the measured target scattering response, a frequency multiplex technique is not applicable. But also the large time spread of the channel at wide swathes may lead to ambiguities in the SAR image if time multiplex methods are used. Therefore, finding orthogonal waveforms for MIMO-SAR poses a challenge. According to this, the condition for so-called pseudo-orthogonal or Short-Term Shift-Orthogonal (STSO) waveforms has been defined in this dissertation. Such waveforms provide orthogonality for certain limited shifts in time and frequency. For larger shifts, which occur at HRWS-SAR, it was proposed to apply an additional spacial filtering via DBF. This concept is called Space-Time-Frequency

Adaptive Processing (STFAP). But not only the waveform requirements have been derived in this dissertation, but also four different waveform types have been investigated, which fulfill the aforementioned definition of pseudo-orthogonality. These waveforms are known under the designations OFDM waveforms, Multiple Sub-Pulses (MSP), Segmentally-Shifted Chirp (SSC) waveforms, and chirp diverse waveforms. An extensive analysis on various parameters and a comparison between the waveform types was carried out. As a result, it turned out that there is no optimum signal type for HRWS-SAR, instead the best suitable waveform is rather dependent on the specific system specifications and requirements.

To separate the transmitted STSO waveforms, a frequency- and time-variant DBF on receive is required. This allows to place the nulls of the antenna pattern at the angular positions of the interfering frequencies. Therefore, in this dissertation, the STFAP algorithm was derived. In case of a single transmit waveform, this algorithm can be seen as an extended form of the SCan On REceive (SCORE) technique. In principle, SCORE is a time-variant DBF on receive, which tracks the echo signal on ground. The major difference to STFAP is that also long pulse durations and large swath widths for a spherical Earth model are covered by this method, which is detailed in this dissertation. In case of MIMO-SAR, STFAP allows to separate MSP and SSC waveforms in the receiver by using information about their frequency characteristic over time. However, this poses certain requirements on the receive antenna array in terms of aperture height and number of elements. To enable a spatial filtering of the waveforms via DBF, some antenna design requirements have been derived. A final performance analysis revealed, that the other channels can be sufficiently suppressed by STFAP. Apart from that, a concept for a hardware implementation via a filter bank consisting of Finite Impulse Response (FIR) filters was presented. It allows a waveform separation on-board in real-time.

In HRWS DBF-SAR and MIMO-SAR with narrow antenna beams, a lack of a priori knowledge of the topography of the observed area leads to a significant loss of gain. The receive beam, which follows the echo signal, is usually steered by using the relationship between Time of Arrival (ToA) and Angle of Arrival (AoA) based on an ideal spherical Earth model. In presence of topography, this relationship is distorted and an antenna mis-pointing is the result. The overall idea of the new approach of this dissertation is an estimation of the AoA from the raw-data before DBF. This information should be later used for calculation of

the DBF steering weights. As a basis for the topography-adaptive DBF algorithm, the Matrix Pencil (MP) method was employed, which was originally intended to solve linear equation systems [109]. Further improvements, based on averaging techniques and band-pass filtering led finally to a concept, which fulfills the set demands in terms of accuracy. Because the MP method must be applied on-board, a concept for a possible practical implementation was given, which enables a precise and stable topography-adaptive elevation DBF, in real-time.

As part of this work, a ground-based MIMO-SAR demonstrator has been developed. The purpose of this system is the verification of advanced imaging modes of future DBF-SAR and MIMO-SAR systems. A detailed description of the overall hardware design and synchronization strategies between the components was given. The hardware demonstrator is not only modular in order to allow for extensions to include more channels and frequency bands, but is also fully coherent with a single shared oscillator. At present, four transmit and eight receive channels can be operated simultaneously in X-band. To obtain measurement results of a high quality, signal pre-processing and calibration steps have been implemented and summarized serving as a standard routine to *condition* the acquired raw-data for MIMO-SAR imaging.

For proving the concepts, which are presented in this dissertation, four experimental results were shown. The first experiment was about STFAP. Here it was demonstrated, that ambiguities caused by STSO waveforms can be suppressed sufficiently via DBF on receive in order to allow for HRWS MIMO-SAR. In addition, this experiment also shows the use of a reflector antenna with a digital feed array. DBF in azimuth direction with sub-sampled data was successfully verified in another experimental result. A unique and pioneering MIMO mode was used for the detection of multipath propagation effects in SAR-tomography. While steering the transmit and the receive antenna beams in different directions, it was possible to identify dihedral scattering mechanisms. The last measurement result was about *simultaneous* fully polarized SAR imaging with multiple transmit and receive channels. It was shown, that simultaneous fully polarimetric measurements in SAR are possible without any reduction of the swath width or of the resolution in comparison to the conventional single polarized mode.

In summary, the whole chain from the system concept spanning over the signal processing strategy and the system requirements to the experimental verification is treated in this dissertation. To give an outlook, the list of MIMO modes and

application examples for MIMO-SAR, at the end of the second chapter, shows the groundbreaking impact, which could be achieved by further implementation and continuation of this work.

A. Mathematical Solution of the Basic Matrix Pencil

This section mathematically describes the solution of the equation system in Eq. (5.13).

After singular value decomposition of Eq. (5.11) and Eq. (5.12) we get respectively:

$$\boldsymbol{Y}_0 = \boldsymbol{\Lambda}_{\mathrm{L},0} \cdot \boldsymbol{\Xi} \cdot \boldsymbol{\Lambda}_{\mathrm{R},1} \tag{A.1}$$

and

$$\boldsymbol{Y}_1 = \boldsymbol{\Lambda}_{\mathrm{L},0} \cdot \boldsymbol{\Xi} \cdot \boldsymbol{\Psi} \cdot \boldsymbol{\Lambda}_{\mathrm{R},1} \tag{A.2}$$

with

$$\boldsymbol{\Lambda}_{\mathrm{L},0} = \begin{bmatrix} 1 & 1 & \cdots & 1 \\ z_0 & z_1 & \cdots & z_{N_{\mathrm{Tar}}-1} \\ \vdots & \vdots & \ddots & \vdots \\ z_0^{N_{\mathrm{Rx}}-L-1} & z_1^{N_{\mathrm{Rx}}-L-1} & \cdots & z_{N_{\mathrm{Tar}}-1}^{N_{\mathrm{Rx}}-L-1} \end{bmatrix}, \tag{A.3}$$

$$\boldsymbol{\Xi} = \begin{bmatrix} A_0 & 0 & \cdots & 0 \\ 0 & A_1 & \cdots & 0 \\ \vdots & \vdots & \ddots & \vdots \\ 0 & 0 & \cdots & A_{N_{\mathrm{Tar}}-1} \end{bmatrix}, \tag{A.4}$$

$$\boldsymbol{\Lambda}_{\mathrm{R},1} = \begin{bmatrix} 1 & z_0 & \cdots & z_0^{L-1} \\ 1 & z_1 & \cdots & z_1^{L-1} \\ \vdots & \vdots & \ddots & \vdots \\ 1 & z_{N_{\mathrm{Tar}}-1} & \cdots & z_{N_{\mathrm{Tar}}-1}^{L-1} \end{bmatrix} \tag{A.5}$$

and

$$\boldsymbol{\Psi} = \begin{bmatrix} z_0 & 0 & \cdots & 0 \\ 0 & z_1 & \cdots & 0 \\ \vdots & \vdots & \ddots & \vdots \\ 0 & 0 & \cdots & z_{N_{\mathrm{Tar}}-1} \end{bmatrix}. \tag{A.6}$$

The matrix pencil:

$$\boldsymbol{Y}_1 - \eta \cdot \boldsymbol{Y}_0 = \boldsymbol{\Lambda}_{\mathrm{L},0} \cdot \boldsymbol{\Xi} \cdot (\boldsymbol{\Psi} - \eta \cdot \boldsymbol{I}) \cdot \boldsymbol{\Lambda}_{\mathrm{R},1} \tag{A.7}$$

has the rank N_{Tar} if $N_{\mathrm{Tar}} \leq L \leq N_{\mathrm{Rx}} - N_{\mathrm{Tar}}$, while this rank can be reduced to $N_{\mathrm{Tar}} - 1$, if $\eta = z_m$. Noting that $\boldsymbol{I}$ is the identity matrix. Therefore z_m can be denoted as the generalized eigenvalues of $\{\boldsymbol{Y}_1, \boldsymbol{Y}_0\}$. Accordingly, it is also valid to write

$$\boldsymbol{Y}_1 \cdot \boldsymbol{\Gamma}_m = z_m \cdot \boldsymbol{Y}_0 \cdot \boldsymbol{\Gamma}_m, \tag{A.8}$$

where $\boldsymbol{\Gamma}_m$ denotes the generalized eigenvector corresponding to z_m. Eq. (A.8) can be rearranged to the form

$$\left(\boldsymbol{Y}_0^{\dagger} \cdot \boldsymbol{Y}_1 - z_m \cdot \boldsymbol{I}\right) \cdot \boldsymbol{\Gamma}_m = \boldsymbol{0}, \tag{A.9}$$

which shows that the values for z_m can be obtained by calculating the eigenvalues of $\boldsymbol{Y}_0^{\dagger} \cdot \boldsymbol{Y}_1$. Noting that † represents the Moore-Penrose pseudo inverse.

B. Computational Complexity of Angular Estimators

Based on the computational complexity of mathematical operations [119], in the following, the upper run-time limits using the big O notation for the estimators Spectral MUSIC, Root MUSIC, LS-ESPRIT, MP and TLS-MP and FB-MP are derived.

Spectral MUSIC

The estimator MUltiple SIgnal Classification (MUSIC) is a parametric estimator and was first presented by R. O. Schmidt in 1981 [106]. With respect to chapter 5, Spectral MUSIC is implemented in the following way:

1. Computation of the covariance matrix $\boldsymbol{R} = E\{\overline{\boldsymbol{u}} \cdot \overline{\boldsymbol{u}}^{\mathrm{H}}\}$: $\mathcal{O}(N_{\mathrm{sn,sub}} \cdot N_{\mathrm{Rx}}^2)$
2. The Singular Value Decomposition (SVD) of $\boldsymbol{R}$, which leads to the left singular vector $\boldsymbol{R}_0$ of shape $N_{\mathrm{sn,sub}} \times N_{\mathrm{sn,sub}}$: $\mathcal{O}(N_{\mathrm{sn,sub}}^3)$
3. The noise subspace is spanned by $\boldsymbol{R}_{\mathrm{noise}} = \boldsymbol{R}_0[:, N_{\mathrm{Tar}} : N_{\mathrm{Rx}} - 1]$: $\mathcal{O}(0)$
4. Computation of the steering vectors $\overline{\boldsymbol{a}}$ for all possible angles ϑ (e.g. $\Theta = 15° \ldots 42°$ with $\vartheta = \Theta - \Theta_{\mathrm{tilt}}$), which can be calculated in advance: $\mathcal{O}(0)$
5. Calculation of the MUSIC pseudo-spectrum by

$$\xi[\vartheta] = \frac{1}{\overline{\boldsymbol{a}}_0^{\mathrm{H}} \cdot \boldsymbol{R}_{\mathrm{noise}} \cdot \boldsymbol{R}_{\mathrm{noise}}^{\mathrm{H}} \cdot \overline{\boldsymbol{a}}_0}.$$

   $\mathcal{O}\left(N_{\mathrm{Rx}} \cdot N_{\mathrm{sn,sub}}^3 \cdot (N_{\mathrm{Rx}} - N_{\mathrm{Tar}})\right)$
6. The positions of the N_{Tar} largest maximums of $\xi[\vartheta]$ correspond to the estimated angles $\check{\vartheta}_m$.

Finally, the sum of all operations is

$$\mathcal{O}\left(N_{\mathrm{sn,sub}}^3 + N_{\mathrm{sn,sub}}^3 \cdot N_{\mathrm{Rx}} \cdot (N_{\mathrm{Rx}} - N_{\mathrm{Tar}}) + N_{\mathrm{sn,sub}} \cdot N_{\mathrm{Rx}}^2\right). \tag{B.1}$$

Root MUSIC

Root MUSIC is a more efficient version of Spectral MUSIC, suggested by Barabell in [107]. This algorithm is based on an arithmetic solution, which avoids the calculation and analysis of the whole pseudo-spectrum, by direct computation of the signal roots. The computation steps can be listed as follows:

1. Computation of the covariance matrix $\boldsymbol{R} = E\{\overline{\boldsymbol{u}} \cdot \overline{\boldsymbol{u}}^{\mathrm{H}}\}$: $\mathcal{O}(N_{\mathrm{sn,sub}} \cdot N_{\mathrm{Rx}}^2)$
2. The SVD of $\boldsymbol{R}$, which leads to the left singular vector $\boldsymbol{R}_0$ of shape $N_{\mathrm{sn,sub}} \times N_{\mathrm{sn,sub}}$: $\mathcal{O}(N_{\mathrm{sn,sub}}^3)$
3. The noise subspace is spanned by $\boldsymbol{R}_{\mathrm{noise}} = \boldsymbol{R}_0[:, N_{\mathrm{Tar}} : N_{\mathrm{Rx}} - 1]$: $\mathcal{O}(0)$
4. Calculation of the term $\boldsymbol{D} = \overline{\boldsymbol{a}}^{\mathrm{H}} \cdot \boldsymbol{R}_{\mathrm{noise}} \cdot \boldsymbol{R}_{\mathrm{noise}}^{\mathrm{H}} \cdot \overline{\boldsymbol{a}}$: $\mathcal{O}\left(N_{\mathrm{sn,sub}}^2 \cdot (N_{\mathrm{Rx}} - N_{\mathrm{Tar}})\right)$
5. Calculation of the Eigenvalues of $\boldsymbol{D}$: $\mathcal{O}(N_{\mathrm{sn,sub}}^3)$
6. Sorting the Eigenvalues with the Q-Sort algorithm: $\mathcal{O}(N_{\mathrm{Tar}} \cdot \log\{N_{\mathrm{Tar}}\})$
7. Finding the values, which are closest to the unit circle: $\mathcal{O}(1)$

Finally, the sum of all operations is

$$\mathcal{O}\left(4N_{\mathrm{sn,sub}}^3 + N_{\mathrm{sn,sub}}^2 \cdot (N_{\mathrm{Rx}} - N_{\mathrm{Tar}}) + N_{\mathrm{sn,sub}} \cdot N_{\mathrm{Rx}}^2 + N_{\mathrm{Tar}} \cdot \log\{N_{\mathrm{Tar}}\} + 1\right). \quad \text{(B.2)}$$

LS-ESPRIT

An alternative spectral estimation approach, named Least Squares Estimation of Signal Parameters using Rotational Invariance Techniques (LS-ESPRIT), was introduced in [108]. In contrast to MUSIC, this algorithm does not make use of the noise subspace but of the signal subspace to obtain the necessary eigenvalues for AoA estimation. By forming two antenna sub-arrays of equal size from the whole array and estimating the linear phase shift between these via correlation, the AoAs can be determined. In more detail, all relevant steps are listed below:

1. Computation of the covariance matrix $\boldsymbol{R} = E\{\overline{\boldsymbol{u}} \cdot \overline{\boldsymbol{u}}^{\mathrm{H}}\}$: $\mathcal{O}(N_{\mathrm{sn,sub}} \cdot N_{\mathrm{Rx}}^2)$
2. The SVD of $\boldsymbol{R}$, which leads to the left singular vector $\boldsymbol{R}_0$ of shape $N_{\mathrm{sn,sub}} \times N_{\mathrm{sn,sub}}$: $\mathcal{O}(N_{\mathrm{sn,sub}}^3)$
3. The signal subspace is spanned by $\boldsymbol{R}_{\mathrm{signal}} = \boldsymbol{R}_0[:, 0 : N_{\mathrm{Tar}} - 1]$: $\mathcal{O}(0)$
4. The least-squares solution of the equation

$$\boldsymbol{R}_{\mathrm{signal}}[1 : N_{\mathrm{Rx}}, :] = \boldsymbol{R}_{\mathrm{signal}}[0 : N_{\mathrm{Rx}} - 1, :] \cdot \boldsymbol{\Phi}$$

   results in the eigenvalues

$$\boldsymbol{\Phi} = \begin{bmatrix} z_0 & 0 & \cdots & 0 \\ 0 & z_1 & \cdots & 0 \\ \vdots & \vdots & \ddots & \vdots \\ 0 & 0 & \cdots & z_m \end{bmatrix}.$$

   $\mathcal{O}(N_{\mathrm{Tar}}^3)$
5. The AoAs are determined by using Eq. (5.14): $\mathcal{O}(0)$

Finally, the sum of all operations is

$$\mathcal{O}(N_{\mathrm{sn,sub}}^3 + N_{\mathrm{sn,sub}} \cdot N_{\mathrm{Rx}}^2 + N_{\mathrm{Tar}}^3). \tag{B.3}$$

Matrix Pencil

Following the steps of subsection 5.2.2, the total run-time of the Matrix Pencil (MP) is composed of:

1. Calculation of Eq. 5.13: $\mathcal{O}\left(3L^2 \cdot (N_{\mathrm{Rx}} - L) + L^3\right)$
2. Calculation of the Eigenvalues: $\mathcal{O}\left((N_{\mathrm{Rx}} - L)^3\right)$

Finally, the sum of all operations is

$$\mathcal{O}\Big(|3L^2 \cdot (N_{\mathrm{Rx}} - L) + L^3| + |(N_{\mathrm{Rx}} - L)^3|\Big) = \mathcal{O}\Big(|3L^2 \cdot N_{\mathrm{Rx}} - 2L^3| + (N_{\mathrm{Rx}} - L)^3\Big). \quad \text{(B.4)}$$

While we note that according to Eq. (5.10) the following condition is given: $L \leq N_{\mathrm{Rx}}/2$.

Total Least Squares Matrix Pencil

Following the steps of subsection 5.2.3, the total run-time of the Total Least Squares Matrix Pencil (TLS-MP) is composed of:

1. SVD($\boldsymbol{Y}[p]$): $\mathcal{O}(L^3)$
2. Calculation of $\boldsymbol{Y}'$: $\mathcal{O}\Big(3(N_{\mathrm{Rx}} - L) \cdot (N_{\mathrm{Tar}} - 1) \cdot (2 + L)\Big)$
3. Calculation of Eq. 5.13: $\mathcal{O}\Big(3L^2 \cdot (N_{\mathrm{Rx}} - L) + L^3\Big)$
4. Calculation of the Eigenvalues: $\mathcal{O}\Big((N_{\mathrm{Rx}} - L)^3\Big)$

Finally, the sum of all operations is

$$\begin{aligned}&\mathcal{O}\Big(|L^3| + |3(N_{\mathrm{Rx}} - L) \cdot (N_{\mathrm{Tar}} - 1) \cdot (2 + L)| + |3L^2 \cdot (N_{\mathrm{Rx}} - L) + L^3| + |(N_{\mathrm{Rx}} - L)^3|\Big)\\ &\quad = \mathcal{O}\Big(L^3 + |3(N_{\mathrm{Rx}} - L) \cdot (N_{\mathrm{Tar}} - 1) \cdot (2 + L)| + |3L^2 \cdot N_{\mathrm{Rx}} - 2L^3| + |(N_{\mathrm{Rx}} - L)^3|\Big).\end{aligned} \quad \text{(B.5)}$$

Forward-Backward Matrix Pencil

Following the steps of subsection 5.2.4, the total run-time of the Forward-Backward Matrix Pencil (FB-MP) is composed of:

1. Calculation of $\widetilde{\boldsymbol{Y}}$: $\mathcal{O}\Big(2(N_{\mathrm{Rx}} - L)^2 \cdot (L + 1)\Big)$
2. Calculation of Eq. 5.13: $\mathcal{O}\Big(3L^2 \cdot (N_{\mathrm{Rx}} - L) + L^3\Big)$
3. Calculation of the Eigenvalues: $\mathcal{O}\Big((N_{\mathrm{Rx}} - L)^3\Big)$

Finally, the sum of all operations is

$$\begin{aligned}&\mathcal{O}\Big(|2(N_{\mathrm{Rx}}-L)^2\cdot(L+1)|+|3L^2\cdot(N_{\mathrm{Rx}}-L)+L^3|+|(N_{\mathrm{Rx}}-L)^3|\Big)\\&\quad=\mathcal{O}\Big(|2(N_{\mathrm{Rx}}-L)^2\cdot(L+1)|+|3L^2\cdot N_{\mathrm{Rx}}-2L^3|+(N_{\mathrm{Rx}}-L)^3\Big).\end{aligned}\tag{B.6}$$

Bibliography

[1] C. Hülsmeyer, "Verfahren, um entfernte metallische Gegenstände mittels elektrischer Wellen einem Beobachter zu melden," *DE Patent 165 546*, Apr. 1904.

[2] C. Hülsmeyer, "Verfahren zur Bestimmung der Entfernung von metallischen Gegenständen (Schiffen o. dgl.), deren Gegenwart durch das Verfahren nach Patent 165546 festgestellt wird," *DE Patent 169 154*, Nov. 1904.

[3] C. A. Wiley, "Pulsed Doppler Radar Methods and Apparatus," *United States Patent 3196436*, Aug. 1954.

[4] A. Reigber, R. Scheiber, M. Jäger, P. Prats-Iraola, I. Hajnsek, T. Jagdhuber, K. Papathanassiou, M. Nannini, E. Aguilera, S. Baumgartner, R. Horn, A. Nottensteiner, and A. Moreira, "Very-high-resolution airborne synthetic aperture radar imaging: Signal processing and applications," *Proc. IEEE*, vol. 101, no. 3, pp. 1–25, Mar. 2013.

[5] A. Torre, D. Calabrese, and M. Porfilio, "COSMO-SkyMed: Image quality achievements," in *5th International Conference on Recent Advances in Space Technologies (RAST)*, June 2011, pp. 861–864.

[6] G. Krieger, A. Moreira, H. Fiedler, I. Hajnsek, M. Werner, M. Younis, and M. Zink, "TanDEM-X: A Satellite Formation for High-Resolution SAR Interferometry," *IEEE Transactions on Geoscience and Remote Sensing*, vol. 45, no. 11, pp. 3317–3341, Nov. 2007.

[7] A. A. Thompson, A. Luscombe, K. James, and P. Fox, "RADARSAT-2 Mission Status: Capabilities Demonstrated and Image Quality Achieved," in *7th European Conference on Synthetic Aperture Radar (EUSAR)*, June 2008, pp. 1–4.

[8] M. Suess and W. Wiesbeck, "Side looking SAR system," *United States Patent 6870500*, Mar. 2005.

[9] J.-H. Kim, "Multiple-Input Multiple-Output Synthetic Aperture Radar for Multimodal Operation," *Dissertation*, Dec. 2011.

[10] G. Krieger, N. Gebert, and A. Moreira, "Unambiguous SAR signal reconstruction from nonuniform displaced phase center sampling," *IEEE Geoscience and Remote Sensing Letters*, vol. 1, no. 4, pp. 260–264, Oct. 2004.

[11] G. Krieger, N. Gebert, M. Younis, and A Moreira, "Advanced synthetic aperture radar based on digital beamforming and waveform diversity," in *IEEE Radar Conference*, May 2008, pp. 1–6.

[12] J.-R. Ohm and H. D. Lueke, *Signalübertragung: Grundlagen der digitalen und analogen Nachrichtenübertragungssysteme, Ninth Edition*, Springer-Verlag, 2004, ISBN: 978-3540222071.

[13] R. K. Raney, "Considerations for SAR image quantification unique to orbital systems," *IEEE Transactions on Geoscience and Remote Sensing*, vol. 29, no. 5, pp. 754–760, Sep. 1991.

[14] J. Curlander and R. McDonough, *Synthetic Aperture Radar*, John Wiley & Sons, 1991, ISBN: 978-0471857709.

[15] I. G. Cumming and F. H. Wong, *Digital Processing of Synthetic Aperture Radar Data: Algorithms and Implementation*, Artech House Print on Demand, 2005, ISBN: 978-1580530583.

[16] A. Moreira, P. Prats-Iraola, M. Younis, G. Krieger, I. Hajnsek, and K. P. Papathanassiou, "A tutorial on synthetic aperture radar," *IEEE Geoscience and Remote Sensing Magazine*, vol. 1, no. 1, pp. 6–43, Mar. 2013.

[17] C. A. Balanis, *Antenna Theory: Analysis and Design, Third Edition*, John Wiley & Sons, 2005, ISBN: 978-0471667827.

[18] M. Skolnik, *Radar Handbook, Third Edition*, McGraw-Hill Professional, 2008, ISBN: 978-0071589420.

[19] J. Li and P. Stoica, *MIMO Radar Signal Processing*, John Wiley & Sons, 2008, ISBN: 978-0470178980.

[20] M. Soumekh, *Synthetic Aperture Radar Signal Processing with MATLAB Algorithms*, John Wiley, 1999, ISBN: 978-0471297062.

[21] Robert O. Harger, "An Optimum Design of Ambiguity Function, Antenna Pattern, and Signal for Side-Looking Radars," *IEEE Transactions on Military Electronics*, vol. 9, no. 3, pp. 264–278, July 1965.

[22] P. Woodward, "Radar Ambiguity Analysis," *Technical Report RRE, Technical Note 731*, Feb. 1967.

[23] H. D. Luke, "The origins of the sampling theorem," *IEEE Communications Magazine*, vol. 37, no. 4, pp. 106–108, Apr. 1999.

[24] V. A. Kotelnikov, "On the carrying capacity of the ether and wire in telecommunications," in *First All-Union Conference on the technological reconstruction of the communications sector and the development of low-current engineering*, 1933.

[25] A. Freeman, W. Johnson, B. Huneycutt, R. Jordan, S. Hensley, P. Siqueira, and J. Curlander, "The Myth of the minimum SAR antenna area constraint," *IEEE Transactions on Geoscience and Remote Sensing*, vol. 38, no. 1, pp. 320–324, Jan. 2000.

[26] R. Kinsey, "Phased array beam spoiling technique," in *Antennas and Propagation Society International Symposium*, July 1997, vol. 2, pp. 698–701.

[27] A. V. Oppenheim and Schafer R. W., *Discrete-Time Signal Processing, New International Edition*, Pearson, 2013, ISBN: 978-1292025728.

[28] M. Suess and W. Wiesbeck, "Side-Looking Synthetic Aperture Radar System," *European Patent EP 1 241 487*, Sep. 2002.

[29] G. Krieger, S. Huber, M. Villano, M. Younis, T. Rommel, P. Lopez Dekker, F. Q. de Almeida, and A. Moreira, "CEBRAS: Cross Elevation Beam Range Ambiguity Suppression for High-Resolution Wide-Swath and MIMO-SAR Imaging," in *IEEE International Geoscience and Remote Sensing Symposium (IGARSS)*, July 2015, pp. 196–199.

[30] L. M. H. Ulander, H. Hellsten, and G. Stenstrom, "Synthetic-aperture radar processing using fast factorized back-projection," *IEEE Transactions on Aerospace and Electronic Systems*, vol. 39, no. 3, pp. 760–776, July 2003.

[31] J. Ender, "A brief review of compressive sensing applied to radar," in *14th International Radar Symposium (IRS)*, June 2013, vol. 1, pp. 3–16.

[32] J. H. Blythe, "Radar Systems," *United States Patent 4253098*, Sep. 1979.

[33] J. T. Kare, "Moving Receive Beam Method and Apparatus for Synthetic Aperture Radar," *United States Patent 6175326 B1*, Jun. 1998.

[34] A. Freeman, G. Krieger, P. Rosen, M. Younis, W. T. K. Johnson, S. Huber, R. Jordan, and A. Moreira, "SweepSAR: Beam-forming on receive using a reflector-phased array feed combination for spaceborne SAR," in *2009 IEEE Radar Conference*, May 2009, pp. 1–9.

[35] M. Younis, "Digital Beam-Forming for High Resolution Wide Swath Real and Synthetic Aperture Radar," *Dissertation*, Jul. 2004.

[36] G. Krieger, N. Gebert, and A Moreira, "Digital Beamforming Techniques for Spaceborne Radar Remote Sensing," in *6th European Conference on Synthetic Aperture Radar (EUSAR)*, May 2006, pp. 1–4.

[37] F. He, X. Ma, Z. Dong, and D. Liang, "Digital Beamforming on Receive in Elevation for Multidimensional Waveform Encoding SAR Sensing," *IEEE Geoscience and Remote Sensing Letters*, vol. 11, no. 12, pp. 2173–2177, Dec. 2014.

[38] S. Huber, M. Younis, A. Patyuchenko, G. Krieger, and A. Moreira, "Spaceborne Reflector SAR Systems with Digital Beamforming," *IEEE Transactions on Aerospace and Electronic Systems*, vol. 48, no. 4, pp. 3473–3493, Oct. 2012.

[39] P. P. Rosen, S. Hensley, S. Shaffer, W. Edelstein, Y. Kim, R. Kumar, T. Misra, R. Bhan, R. Satish, and R. Sagi, "An update on the NASA-ISRO dual-frequency DBF SAR (NISAR) mission," in *2016 IEEE International Geoscience and Remote Sensing Symposium (IGARSS)*, July 2016, pp. 2106–2108.

[40] I. Hajnsek, M. Shimada, M. Eineder, K. Papathanassiou, T. Motohka, M. Watanabe, M. Ohki, F. De Zan, P. Lopez-Dekker, G. Krieger, and A. Moreira, "Tandem-L: Science Requirements and Mission Concept," in *10th European Conference on Synthetic Aperture Radar, EUSAR*, June 2014, pp. 1255–1258.

[41] G. Krieger, "MIMO-SAR: Opportunities and Pitfalls," *IEEE Transactions on Geoscience and Remote Sensing*, vol. 52, no. 5, pp. 2628–2645, May 2014.

[42] T. Rommel, S. Huber, A. Patyuchenko, P. Laskowski, M. Younis, and G. Krieger, "An Orthogonal Waveform for MIMO-SAR Applications," in *Proceedings of EUSAR; 10th European Conference on Synthetic Aperture Radar*, June 2014, pp. 1–4.

[43] I. Sikaneta, C. H. Gierull, and D. Cerutti-Maori, "Optimum Signal Processing for Multichannel SAR: With Application to High-Resolution Wide-Swath Imaging," *IEEE Transactions on Geoscience and Remote Sensing*, vol. 52, no. 10, pp. 6095–6109, Oct. 2014.

[44] D. Cerutti-Maori, I. Sikaneta, J. Klare, and C. H. Gierull, "MIMO SAR Processing for Multichannel High-Resolution Wide-Swath Radars," *IEEE Transactions on Geoscience and Remote Sensing*, vol. 52, no. 8, pp. 5034–5055, Aug. 2014.

[45] R. Bamler, "A comparison of range-Doppler and wavenumber domain SAR focusing algorithms," *IEEE Transactions on Geoscience and Remote Sensing*, vol. 30, no. 4, pp. 706–713, July 1992.

[46] R. K. Raney, H. Runge, R. Bamler, I. G. Cumming, and F. H. Wong, "Precision SAR processing using chirp scaling," *IEEE Transactions on Geoscience and Remote Sensing*, vol. 32, no. 4, pp. 786–799, July 1994.

[47] E. Attia and B. D. Steinberg, "Self-cohering large antenna arrays using the spatial correlation properties of radar clutter," *IEEE Transactions on Antennas and Propagation*, vol. 37, no. 1, pp. 30–38, Jan. 1989.

[48] G. Farquharson, P. Lopez-Dekker, and S. J. Frasier, "Contrast-Based Phase Calibration for Remote Sensing Systems With Digital Beamforming Antennas," *IEEE Transactions on Geoscience and Remote Sensing*, vol. 51, no. 3, pp. 1744–1754, Mar. 2013.

[49] P. Lopez Dekker, G. Farquharson, and S. J. Frasier, "Entropy based phase calibration of antenna arrays for digital beamforming remote sensing radars," in *Proceedings of the IEEE Radar Conference*, 2002, pp. 445–452.

[50] A. Moreira, G. Krieger, I. Hajnsek, D. Hounam, M. Werner, S. Riegger, and E. Settelmeyer, "TanDEM-X: a TerraSAR-X add-on satellite for single-pass SAR interferometry," in *Proceedings IEEE International Geoscience and Remote Sensing Symposium, IGARSS*, Sep. 2004, vol. 2, pp. 1000–1003.

[51] M. Younis and W. Wiesbeck, "Antenna system for a forward looking SAR using digital beamforming on-receive-only," in *Proceedings IEEE International Geoscience and Remote Sensing Symposium, IGARSS*, 2000, vol. 5, pp. 2343–2345 vol.5.

[52] J. H. G. Ender and J. Klare, "System architectures and algorithms for radar imaging by MIMO-SAR," in *IEEE Radar Conference*, May 2009, pp. 1–6.

[53] G. Krieger, N. Gebert, and A. Moreira, "Multidimensional Waveform Encoding: A New Digital Beamforming Technique for Synthetic Aperture Radar Remote Sensing," *IEEE Transactions on Geoscience and Remote Sensing*, vol. 46, no. 1, pp. 31–46, Jan. 2008.

[54] G. Krieger, I. Hajnsek, K. P. Papathanassiou, M. Younis, and A. Moreira, "Interferometric Synthetic Aperture Radar (SAR) Missions Employing Formation Flying," May 2010, vol. 98, pp. 816–843.

[55] R. C. Heimiller, J. E. Belyea, and P. G. Tomlinson, "Distributed Array Radar," *IEEE Transactions on Aerospace and Electronic Systems*, vol. AES-19, no. 6, pp. 831–839, Nov. 1983.

[56] A. Reigber and A. Moreira, "First demonstration of airborne SAR tomography using multibaseline L-band data," *IEEE Transactions on Geoscience and Remote Sensing*, vol. 38, no. 5, pp. 2142–2152, Sep. 2000.

[57] G. Krieger, T. Rommel, and A. Moreira, "MIMO-SAR Tomography," in *Proceedings of EUSAR 2016: 11th European Conference on Synthetic Aperture Radar*, June 2016, pp. 1–6.

[58] T. Rommel and G. Krieger, "Detection of Multipath Propagation Effects in SAR-Tomography with MIMO Modes," in *Proceedings of EUSAR 2016: 11th European Conference on Synthetic Aperture Radar*, June 2016, pp. 1–5.

[59] O. Ponce, T. Rommel, M. Younis, P. Prats, and A. Moreira, "Multiple-Input Multiple-Output Circular SAR," in *15th International Radar Symposium (IRS)*, June 2014.

[60] O. Ponce, F. Queiroz de Almeida, and T. Rommel, "Multiple-Input Multiple-Output Circular SAR for High Altitude Pseudo-Satellites," in *Space Generation Congress / International Astronautical Congress*, Sep. 2016.

[61] O. Ponce, P. Prats-Iraola, M. Pinheiro, M. Rodriguez-Cassola, Scheiber R., Reigber A., and Moreira A., "Fully Polarimetric High-Resolution 3-D Imaging With Circular SAR at L-Band," *IEEE Transactions on Geoscience and Remote Sensing*, vol. 52, no. 6, pp. 3074–3090, June 2014.

[62] O. Ponce, P. Prats-Iraola, R. Scheiber, A. Reigber, and A. Moreira, "First Airborne Demonstration of Holographic SAR Tomography With Fully Polarimetric Multicircular Acquisitions at L-Band," *IEEE Transactions on Geoscience and Remote Sensing*, vol. 54, no. 10, pp. 6170–6196, Oct. 2016.

[63] F. Dovis, L. Lo Presti, E. Magli, P. Mulassano, and G. Olmo, "Stratospheric platforms: a novel technological support for Earth observation and remote sensing applications," in *Proceedings of SPIE 4540, Sensors, Systems, and Next-Generation Satellites V*, Dec. 2001, pp. 402–411.

[64] N. Basta, A. Dreher, S. Caizzone, M. Sgammini, F. Antreich, G. Kappen, S. Irteza, R. Stephan, M.A. Hein, E. Schafer, A. Richter, M.A. Khan, L. Kurz, and T.G. Noll, "System concept of a compact multi-antenna GNSS receiver," in *7th German Microwave Conference (GeMiC)*, Mar. 2012, pp. 1–4.

[65] A. N. Akansu, P. Duhamel, X. M. Lin, and M. de Courville, "Orthogonal transmultiplexers in communication: a review," *IEEE Transactions on Signal Processing*, vol. 46, no. 4, pp. 979–995, Apr. 1998.

[66] T. Hwang, C. Yang, G. Wu, S. Li, and G. Y. Li, "OFDM and Its Wireless Applications: A Survey," *IEEE Transactions on Vehicular Technology*, vol. 58, no. 4, pp. 1673–1694, May 2009.

[67] D. Garmatyuk, "Cross-Range SAR Reconstruction With Multicarrier OFDM Signals," *IEEE Geoscience and Remote Sensing Letters*, vol. 9, no. 5, pp. 808–812, Sep. 2012.

[68] W. Wiesbeck and L. Sit, "Radar 2020: The future of radar systems," in *International Radar Conference (Radar)*, Oct. 2014, pp. 1–6.

[69] C. Sturm, Y. L. Sit, M. Braun, and T. Zwick, "Spectrally interleaved multi-carrier signals for radar network applications and multi-input multi-output radar," *IET Radar, Sonar Navigation*, vol. 7, no. 3, pp. 261–269, Mar. 2013.

[70] J.-H. Kim, A Ossowska, and W. Wiesbeck, "Investigation of MIMO SAR for interferometry," in *European Radar Conference, EuRAD*, Oct. 2007, pp. 51–54.

[71] G. Krieger, M. Younis, S. Huber, F. Bordoni, A. Patyuchenko, J. Kim, P. Laskowski, M. Villano, T. Rommel, P. Lopez-Dekker, and A. Moreira, "Digital beamforming and MIMO SAR: Review and new concepts," in *9th European Conference on Synthetic Aperture Radar, EUSAR*, Apr. 2012, pp. 11–14.

[72] J. Mittermayer and J. M. Martinez, "Analysis of range ambiguity suppression in SAR by up and down chirp modulation for point and distributed targets," in *Proceedings IEEE International Geoscience and Remote Sensing Symposium, IGARSS*, July 2003, vol. 6, pp. 4077–4079.

[73] W.-Q. Wang, "MIMO SAR OFDM Chirp Waveform Diversity Design With Random Matrix Modulation," *IEEE Transactions on Geoscience and Remote Sensing*, vol. 53, no. 3, pp. 1615–1625, Mar. 2015.

[74] D. Garmatyuk and M. Brenneman, "Adaptive Multicarrier OFDM SAR Signal Processing," *IEEE Transactions on Geoscience and Remote Sensing*, vol. 49, no. 10, pp. 3780–3790, Oct. 2011.

[75] M. Younis, T. Rommel, F. Bordoni, G. Krieger, and A. Moreira, "On the Pulse Extension Loss in Digital Beamforming SAR," *IEEE Geoscience and Remote Sensing Letters*, vol. 12, no. 7, pp. 1436–1440, July 2015.

[76] U. Pillai, Li K. Y., Selesnick I., and Himed B., *Waveform Diversity - Theory & Applications*, McGraw-Hill, 2011, ISBN: 978-0071622899.

[77] J. W. Gibbs, "Fourier's Series," *Nature*, vol. 59, no. 1539, pp. 606, Apr. 1899.

[78] J. S. Chitode, *Digital Signal Processing*, Technical Publications, 2009, ISBN: 978-8184315103.

[79] R. R. Mosier and R. G. Clabaugh, "Kineplex, a bandwidth-efficient binary transmission system," *Transactions of the American Institute of Electrical Engineers, Part I: Communication and Electronics*, vol. 76, no. 6, pp. 723–728, Jan. 1958.

[80] A. H. Ballard, "A New Multiplex Technique for Communication Systems," *IEEE Transactions on Power Apparatus and Systems*, vol. PAS-85, no. 10, pp. 1054–1059, Oct. 1966.

[81] J.-H. Kim, M. Younis, A. Moreira, and W. Wiesbeck, "A Novel OFDM Waveform for Fully Polarimetric SAR Data Acquisition," in *8th European Conference on Synthetic Aperture Radar (EUSAR)*, June 2010, pp. 1–4.

[82] J.-H. Kim, M. Younis, A. Moreira, and W. Wiesbeck, "Spaceborne MIMO Synthetic Aperture Radar for Multimodal Operation," *IEEE Transactions on Geoscience and Remote Sensing*, vol. 53, no. 5, pp. 2453–2466, May 2015.

[83] A. Goldsmith, *Wireless Communications*, Cambridge University Press, 2005, ISBN: 978-0521837163.

[84] T. Rommel, A. Patyuchenko, P. Laskowski, M. Younis, and G. Krieger, "An Orthogonal Waveform Scheme for Imaging MIMO-Radar Applications," in *14th International Radar Symposium (IRS)*, June 2013, vol. 2, pp. 917–922.

[85] W.-Q. Wang, "Space Time Coding MIMO-OFDM SAR for High-Resolution Imaging," *IEEE Transactions on Geoscience and Remote Sensing*, vol. 49, no. 8, pp. 3094–3104, Aug. 2011.

[86] W.-Q. Wang and J. Cai, "MIMO SAR using Chirp Diverse Waveform for Wide-Swath Remote Sensing," *IEEE Transactions on Aerospace and Electronic Systems*, vol. 48, no. 4, pp. 3171–3185, Oct. 2012.

[87] G. San Antonio, D. R. Fuhrmann, and F. C. Robey, "MIMO Radar Ambiguity Functions," *IEEE Journal of Selected Topics in Signal Processing*, vol. 1, no. 1, pp. 167–177, June 2007.

[88] Y. Li, S. A. Vorobyov, and V. Koivunen, "Ambiguity Function of the Transmit Beamspace-Based MIMO Radar," *IEEE Transactions on Signal Processing*, vol. 63, no. 17, pp. 4445–4457, Sep. 2015.

[89] "IEEE Standard Radar Definitions," *IEEE Std 686-1997*, pp. i–, 1998.

[90] Chun-Yang Chen and P. P. Vaidyanathan, "Properties of the MIMO radar ambiguity function," in *IEEE International Conference on Acoustics, Speech and Signal Processing, ICASSP*, Mar. 2008, pp. 2309–2312.

[91] A. Moreira and T. Misra, "On the use of the ideal filter concept for improving SAR image quality," *Journal of Electromagnetic Waves and Applications*, vol. 9, no. 3, pp. 407–420, 1995.

[92] M. C. Wicks, M. Rangaswamy, R. Adve, and T. D. Hale, "Space-time adaptive processing: a knowledge-based perspective for airborne radar," *IEEE Signal Processing Magazine*, vol. 23, no. 1, pp. 51–65, Jan. 2006.

[93] M. Longbrake, "True time-delay beamsteering for radar," in *IEEE National Aerospace and Electronics Conference (NAECON)*, July 2012, pp. 246–249.

[94] C. Schaefer, "Radar System with Synthetic Aperture," *European Patent EP 2 544 022 A1*, Jan. 2013.

[95] H. L. Van Trees, *Optimum Array Processing*, John Wiley & Sons, 2004, ISBN: 978-0471463832.

[96] J. Capon, "High-resolution frequency-wavenumber spectrum analysis," *Proceedings of the IEEE*, vol. 57, no. 8, pp. 1408–1418, Aug. 1969.

[97] F. Bordoni, M. Younis, E. Makhoul Varona, and G. Krieger, "Performance investigation on Scan-On-Receive and Adaptive Digital Beam-Forming for High-Resolution Wide-Swath Synthetic Aperture Radar," in *International ITG Workshop on Smart Antennas - WSA*, Feb. 2009, pp. 114–121.

[98] F. Feng, S. Li, W. Yu, Huang P., and W. Xu, "Echo Separation in Multidimensional Waveform Encoding SAR Remote Sensing Using an Advanced Null-Steering Beamformer," *IEEE Transactions on Geoscience and Remote Sensing*, vol. 50, no. 10, pp. 4157–4172, Oct. 2012.

[99] W. Wang, R. Wang, Y. Deng, T. Balz, F. Hong, and W. Xu, "An Improved Processing Scheme of Digital Beam-Forming in Elevation for Reducing Resource Occupation," *IEEE Geoscience and Remote Sensing Letters*, vol. PP, no. 99, pp. 1–5, 2016.

[100] S. Huber, "Spaceborne SAR Systems with Digital Beamforming and Reflector Antenna," *Dissertation*, Feb. 2014.

[101] D. Schlichthaerle, *Digital Filters: Basics and Design, Second Edition*, Springer-Verlag, 2011, ISBN: 978-3642143243.

[102] F. Feng, S. Li, W. Yu, and S. Wang, "Study on the Processing Scheme for Space-Time Waveform Encoding SAR System Based on Two-Dimensional Digital Beamforming," *IEEE Transactions on Geoscience and Remote Sensing*, vol. 50, no. 3, pp. 910–932, Mar. 2012.

[103] F. Feng, H. Dang, Tan X., G. Li, and Li C., "An improved scheme of Digital Beam-Forming in elevation for spaceborne SAR," in *IET International Radar Conference 2013*, Apr. 2013, pp. 1–6.

[104] A. K. Madanahalli Jai Prakash, "Investigation of OFDM Signals for Imaging Radar Applications," *Master Thesis*, Oct. 2013.

[105] P. Stoica and R. Moses, *Introduction to Spectral Analysis*, Prentice-Hall, 1997, ISBN: 978-0132584197.

[106] R. O. Schmidt, "A Signal Subspace Approach to Multiple Emitter Location and Spectral Estimation," *Dissertation*, Nov. 1981.

[107] A. Barabell, "Improving the resolution performance of eigenstructure-based direction-finding algorithms," in *IEEE International Conference on Acoustics, Speech, and Signal Processing*, Apr. 1983, vol. 8, pp. 336–339.

[108] R. Roy and T. Kailath, "ESPRIT-estimation of signal parameters via rotational invariance techniques," *IEEE Transactions on Acoustics, Speech and Signal Processing*, vol. 37, no. 7, pp. 984–995, July 1989.

[109] Kh. D. Ikramov, "Matrix pencils: Theory, applications, and numerical methods," *Journal of Soviet Mathematics*, vol. 64, no. 2, pp. 783–853, Apr. 1993.

[110] H. Ouibrahim, D. D. Weiner, and T. K. Sarkar, "A Generalized Approach to Direction Finding," in *Military Communications Conference - Communications-Computers: Teamed for the 90's, 1986. MILCOM 1986. IEEE*, Oct. 1986, vol. 3, pp. 41.4.1–41.4.5.

[111] Y. Hua and T. K. Sarkar, "Matrix pencil method for estimating parameters of exponentially damped/undamped sinusoids in noise," *IEEE Transactions on Acoustics, Speech and Signal Processing*, vol. 38, no. 5, pp. 814–824, May 1990.

[112] S. Ozsoy and A.A. Ergin, "Pencil Back-Projection Method for SAR Imaging," *IEEE Transactions on Image Processing*, vol. 18, no. 3, pp. 573–581, Mar. 2009.

[113] R. S. Adve, "Elimination of the Effects of Mutual Coupling in Adaptive Thin Wire Antennas," *Dissertation*, Dec. 1996.

[114] S. U. Pillai and C. S. Burrus, *Array Signal Processing*, Springer-Verlag, 1989, ISBN: 978-1461281863.

[115] J. Binder, K. Murphy, and Russell S., "Space-Efficient Inference in Dynamic Probabilistic Networks," in *Int'l Joint Conf. on Artificial Intelligence*, Aug. 1997, pp. 1–5.

[116] N. W. D. Le Marshall and Tirkel A. Z., "Modified Matrix Pencil Algorithm for Terminite Detection with High Resolution Radar," *Progress in Electromagnetics Research C*, vol. 16, pp. 51–67, Sep. 2010.

[117] F. Hu, T. K. Sarkar, and Y. Hua, "Utilization of Bandpass Filtering for the Matrix Pencil Method," *Signal Processing, IEEE Transactions on*, vol. 41, no. 1, pp. 442–, Jan. 1993.

[118] N. Yilmazer, T. K. Sarkar, and M. Salazar-Palma, "DOA Estimation using Matrix Pencil and ESPRIT methods using single and multiple snapshots," in *2010 URSI International Symposium on Electromagnetic Theory (EMTS)*, Aug. 2010, pp. 215–218.

[119] W. Dahmen and A. Reusken, *Numerik für Ingenieure und Naturwissenschaftler*, Springer-Verlag, 2008, ISBN: 978-3540764922.

[120] A. Patyuchenko, T. Rommel, P. Laskowski, M. Younis, and G. Krieger, "Digital Beam-Forming reconfigurable Radar System demonstrator," in *IEEE International Geoscience and Remote Sensing Symposium (IGARSS)*, July 2012, pp. 1541–1544.

[121] T. Rommel, A. Patyuchenko, P. Laskowski, M. Younis, and G. Krieger, "Development of a MIMO Radar System demonstrator - Calibration and Demonstration of First Results," in *13th International Radar Symposium (IRS)*, May 2012, pp. 113–118.

[122] D. M. Pozar, *Microwave Engineering, Fourth Edition*, John Wiley & Sons, 2011, ISBN: 978-0470631553.

[123] F. G. Stremler, *Introduction to Communications Systems, Second Edition*, Addison-Wesley, 1982, ISBN: 978-0201072594.

[124] A. Reigber, M. Jäger, R. Scheiber, P. Prats, R. Horn, and A. Nottensteiner, "Multispectral, polarimetric and interferometric SAR imaging with the F-SAR airborne SAR instrument," in *14th International Radar Symposium (IRS)*, June 2013, vol. 1, pp. 27–32.

[125] M. Gabele, B. Brautigam, D. Schulze, U. Steinbrecher, N. Tous-Ramon, and M. Younis, "Fore and Aft Channel Reconstruction in the TerraSAR-X Dual Receive Antenna Mode," *IEEE Transactions on Geoscience and Remote Sensing*, vol. 48, no. 2, pp. 795–806, Feb. 2010.

[126] Agilent Technologies, "Signal Source Solutions for Coherent and Phase Stable Multi-Channel Systems," *Application Note*, May 2010.

[127] D. Gabor, "Theory of communication. Part 1: The analysis of information," *Journal of the Institution of Electrical Engineers - Part III: Radio and Communication Engineering*, vol. 93, no. 26, pp. 429–441, Nov. 1946.

[128] H. Breit, T. Fritz, U. Balss, M. Lachaise, A. Niedermeier, and M. Vonavka, "TerraSAR-X SAR Processing and Products," *IEEE Transactions on Geoscience and Remote Sensing*, vol. 48, no. 2, pp. 727–740, Feb. 2010.

[129] S. Huber, T. Rommel, A. Patyuchenko, and P. Laskowski, "A Reflector Based Digital Beamforming Demonstrator," in *10th European Conference on Synthetic Aperture Radar (EUSAR)*, June 2014, pp. 1–4.

[130] T. Rommel, M. Younis, and G. Krieger, "An Orthogonal Waveform for Fully Polarimetric MIMO-SAR," in *IEEE Radar Conference*, May 2014, pp. 0887–0891.

[131] W. H. Press, B. P. Flannery, S. A. Teukolsky, and Vetterling W. T., *Numerical Recipes in C: The Art of Scientific Computing, Second Edition*, Cambridge University Press, 1992, ISBN: 978-0521431088.

[132] S. Samadi, Y. Igarashi, and H. Iwakura, "Design and multiplierless realization of maximally flat FIR digital Hilbert transformers," *IEEE Transactions on Signal Processing*, vol. 47, no. 7, pp. 1946–1953, July 1999.

[133] K. B. Stewart, "Waveform-Diverse Multiple-Input Multiple-Output Radar Imaging Measurements," *Dissertation*, 2016.

List of Figures

1.1. An example for a fully polarimetric SAR image acquired with DLR's F-SAR sensor in X-band. 26

2.1. Illustration of the SAR principle. 33
2.2. As an example, plot of the real-part of $h_{\mathrm{az}}(\acute{t}, t, \boldsymbol{p})$ with $v_{\mathrm{sat}} = 7.6 \cdot 10^6 \, \frac{\mathrm{m}}{\mathrm{s}}$, $\lambda_0 = 3.1$ cm, $h = 514$ km, $l_{\mathrm{ant,az}} = 4.8$ m and $\Theta_{\mathrm{inc}} = 20°$. The curves in red color indicate the weighting by the azimuth antenna pattern over the observation time $T_{\mathrm{ob}} = 455$ ms. 35
2.3. An example of a set of transmit waveforms in base-band with $N_{\mathrm{Tx}} = 4$. 37
2.4. Basic block diagram for two typical transmit and receive channels. 39
2.5. Dependence between swath-with and *PRF* in terms of range ambiguities. 43
2.6. Back folding of Doppler spectra leading to azimuthal ambiguities. 44
2.7. Classical SAR processing chain with multiple receive channels. The variables u_{rec}, u_{rg}, u_{rcm} and u_{az} represent the result of successive processor stages illustrated above. These stages will be detailed on the following pages. 46
2.8. Effective antenna phase centers of three receive antennas in azimuth. 48
2.9. Flow diagram of the MIMO-SAR simulator and processor. 52
2.10. Advanced DBF-SAR and MIMO-SAR modes. 56
2.11. Principle of multipath detection with transmit and receive beams pointing in different directions. The cross at the edge of the tree trunk and the ground indicates the equivalent phase center of the reflection. 57
2.12. Basic MIMO CSAR geometry with transmit antenna beam in red color and multiple receive antenna beams in elevation and azimuth directions in yellow color. 59

2.13. MIMO CSAR with a geostationary satellite as transmitter and multiple HAPS as receiver platforms. 59

3.1. Illustration of the orthogonality problem in MIMO-SAR in the time-frequency plane with a linear frequency modulated transmit signal. 64

3.2. Maximum swath width for the condition of Eq. (3.2) with $h = 700$ km, $\tau_p = 120\,\mu$s, $N_{Tx} = 2$ and $\epsilon = 0$. 66

3.3. Representation of the receive signal due to a down-chirp, in incidence angle, time and frequency. 67

3.4. Standard chirp signal in time- and frequency domain with $\tau_p = 10\,\mu$s and $B = 20$ MHz. 68

3.5. Scheme of the OFDM chirp waveforms for $N_{Tx} = 2$; left-hand side: signal spectrum; right-hand side: time-frequency relation. . 70

3.6. OFDM chirp in time domain with $N_{Tx} = 2$, $\tau_p = 10\,\mu$s, $B = 10$ MHz, $\Delta f = 1.0$ kHz and $f_0 = B/2$. 72

3.7. Illustration of the MSP waveforms with $B = 10$ MHz, $\tau_p = 10\,\mu$s, $\tau_s = 2\,\mu$s, $N_{Tx} = 2$, $f_0 = B/2$. 73

3.8. MSP waveform in the time-frequency plane. 74

3.9. Illustration of the segmentally-shifted chirp waveform in time-domain for $B = 10$ MHz, $\tau_p = 10\,\mu$s, $N_{Tx} = 2$ and $f_0 = B/2$. Upper plot: $s_0(t)$. Lower plot: $s_1(t)$. 77

3.10. Segmentally-shifted chirp waveform in the time-frequency plane. 79

3.11. Illustration of the up-down chirp modulation. 80

3.12. Illustration of the chirp diverse waveforms with $N_{Tx} = 2$ in the time-frequency plane. 81

3.13. Ambiguity Function (Eq. (3.26)) of an up-chirp. 83

3.14. Cross-Ambiguity Functions with corresponding zero-Doppler cuts (Eq. (3.28)) of different waveforms. 87

3.15. Impulse response function of an up-chirp. The green surface indicated the amount of energy within the sidelobes and the blue surface the energy within the main-lobe. The ratio between the two is defined as *ISLR*. 90

3.16. Integrated sidelobe ratios (Eq. (3.31)) with corresponding impulse responses of different waveforms with $B = 300$ MHz, $\tau_p = 120\,\mu$s, $N_{Tx} = 4$ and Hanning windowing. The upper abscissa axis of the impulse response plots is related to the geometrical positions of the interferences on the ground, while the following parameter were used: $\Theta \approx \Theta_{tilt} = 28.5°$ and $h = 700$ km. 96
3.17. Inter-carrier-to-interference ratio with respect to the Doppler frequency normalized to the sub-carrier spacing ($\Delta f_{Dop}/\Delta f$). The dotted line indicates the required ICI ratio. 99

4.1. A planar wave incident at the antenna array with element separation d. In dependence on the AoA, between each two adjacent receive channels the same phase delay can be observed. After down-conversion and A-D conversion, the DBF weights are applied on each receive channel and the output signals are summed up. 107
4.2. Suppression of the signal ambiguities of STSO waveforms with the antenna beam pattern shown for a certain instant of time. . . 110
4.3. Illustration of the radar pulse extent. Due to the pulse duration τ_p at an arbitrary time instance, the echo is received from an angular section simultaneously. 111
4.4. Angular pulse extent in dependence of the steering angle for the pulse durations $\tau_p = 80\,\mu$s, $100\,\mu$s, $120\,\mu$s, $140\,\mu$s and $160\,\mu$s and an orbit height of $h = 700$ km. 112
4.5. Minimum antenna size in elevation to separate the STSO waveforms as function of the pulse duration and steering angles $\Theta = 15°, 25°, 35°, 42°$; $\lambda = 3.16$ cm, $N_{Tx} = 2$, $\epsilon = 0$ and $h = 700$ km. 114
4.6. Tracking the echo via a narrow antenna beam. Left-hand side: Due to $HPBW < \chi_\Theta$ a loss occurs. Right-hand side: Due to $HPBW > \chi_\Theta$ the antenna is not effectively used. 119
4.7. Pulse extension loss for the varying ratio $HPBW/\,\chi_\Theta$. 120
4.8. Pulse extension loss vs. ground range for the antenna aperture heights $l_{ant,el} = 1.3$ m and $l_{ant,el} = 2.5$ m and the parameters $h = 700$ km, $f_0 = 9.6$ GHz and $\tau_p = 120\,\mu$s. 121
4.9. AoA in dependency on the ToA. Linear approximation and true curve. $\Theta_{tilt} = 33.2°$, $\Theta = 15°...42°$. 122

4.10. Upper part: Block diagram of the SCORE filtering process with two receive channels and three band-pass filters per channel. Lower part: Frequency-variant antenna beam following the reflections of an up-chirp. 123

4.11. Block diagram of a FIR filter with 4 taps. 126

4.12. Resulting frequency spectrum after signal reconstruction with five FIR filters of order $M_{\mathrm{FIR}} = 30$; sum signal: blue curve in background. 128

4.13. Pulse extension loss vs. ground range for the parameters $h = 700$ km, $f_0 = 9.6$ GHz, $l_{\mathrm{ant,el}} = 1.3$ m, $\tau_{\mathrm{p}} = 120$ μs, $N_{\mathrm{FIR}} = [2, 3, 4, 6, 8]$, $M_{\mathrm{FIR}} = 100$. 129

4.14. Representation of the receive signal from the MSP waveform in angle, time and frequency. 130

4.15. Plot of the AR versus ground range for the antenna sizes in elevation $l_{\mathrm{ant,el}} = 2.5$ m and $l_{\mathrm{ant,el}} = 4.0$ m and two sub-pulses with the parameters $h = 700$ km and $f_0 = 9.6$ GHz. 134

4.16. Simulated antenna pattern at a certain time instant, which is steered to antenna bore-site direction at $\Theta = 28.5°$. For the case of two MSP waveforms, the blue colored surface indicates the angular pulse extent of the first waveform, while the green colored surface indicates the angular pulse extent of the second waveform. For simulation, the following parameters were used: $h = 700$ km and $f_0 = 9.6$ GHz, $l_{\mathrm{ant,el}} = 2.5$ m, $\tau_{\mathrm{p}} = 120$ μs, $\tau_{\mathrm{s}} = 0$ s. . 135

4.17. Block diagram of the STFAP filtering process for two transmit waveforms with three band-pass filters per channel (just a single receive channel is shown). 136

4.18. Plot of the AR with FIR filtering versus ground range for the antenna sizes in elevation $l_{\mathrm{ant,el}} = 2.5$ m and $l_{\mathrm{ant,el}} = 4.0$ m and for two sub-pulses with the parameters $h = 700$ km, $f_0 = 9.6$ GHz, $N_{\mathrm{FIR}} = 6$ and $M_{\mathrm{FIR}} = 100$. 139

4.19. Simulated antenna pattern, which is steered to the first angular center of the angular pulse extent after band-pass filtering (left blue colored surface) at a certain time instant. For the case of two MSP waveforms, the colors correspond to the individual angular pulse extents after band-pass filtering with $N_{\mathrm{FIR}} = 6$. For simulation, the following parameters were used: $h = 700$ km and $f_0 = 9.6$ GHz, $l_{\mathrm{ant,el}} = 2.5$ m, $\tau_{\mathrm{p}} = 120$ μs, $\tau_{\mathrm{s}} = 0$ s, $B = 300$ MHz. . . 140

4.20. Plot of the *AR* with FIR filtering and LCMV-DBF versus ground range for the antenna sizes in elevation $l_{\mathrm{ant,el}} = 2.5$ m and $l_{\mathrm{ant,el}} = 4.0$ m and for two sub-pulses with the parameters $h = 700$ km, $f_0 = 9.6$ GHz, $N_{\mathrm{FIR}} = 6$, and $M_{\mathrm{FIR}} = 100$. 141

4.21. Representation of the receive signal from the SSC waveform in angle, time and frequency. 143

4.22. Plot of the *AR* with FIR filtering and LCMV-DBF versus ground range for two SSC waveforms with the parameters $h = 700$ km, $f_0 = 9.6$ GHz, $l_{\mathrm{ant,el}} = [2.5\text{ m}, 4.0\text{ m}]$, $\tau_{\mathrm{p}} = 120$ μs, $N_{\mathrm{FIR}} = 6$ and $M_{\mathrm{FIR}} = 100$. 144

4.23. Block diagram of the demodulation process for the OFDM chirp waveforms. 144

4.24. Illustration of the circular-shift addition on a typical receive signal. 146

5.1. Illustration of the antenna mis-pointing due to topographic changes. 149

5.2. Antenna mis-pointing for various terrain heights and steering angles. 150

5.3. Pole diagrams with the estimated eigenvalues $z_m[p]$ using the MP method for different pencil parameters, $N_{\mathrm{Tar}} = 1$, $N_{\mathrm{Rx}} = 32$. 155

5.4. Principle of the Total Least Squares Matrix Pencil on hand of the pole diagram. 156

5.5. At a certain instant of time, the echo signal is received from an angular interval. After band-pass filtering, the chirp is synthetically narrowed and accordingly also the angular pulse extent. With respect to the maximum of each normal distribution after angle estimation, the AoA for each bin can be estimated. . . 160

5.6. Slant range extent for an angular extent of $\chi_\Theta = 0.05°$ in dependence of the steering angle Θ at an orbit height over the Earth's surface of 700 km. 164
5.7. Practical implementation of the Matrix Pencil Method in a DBF-SAR system. 166
5.8. RMSE of the estimated angle with respect to the expectation value over varying *SNR*. 171
5.9. RMSE of the estimated angle with respect to the expectation value over varying antenna length. 172
5.10. RMSE of the estimated angle with respect to the expectation value over varying steering angle. 172
5.11. Estimated angle for two simulated point targets at $\Theta_1 = 30.0°$ and $\Theta_2 = 30.05°$ with varying relative RCS. 173
5.12. Original SAR scene and extracted range profile. 175
5.13. Standard deviation of the estimated angle from the expectation value along the swath. 176
5.14. Standard deviation of the estimated angle from the expectation value along the swath with correction. 176

6.1. Photo of the ground-based MIMO-radar demonstrator. 179
6.2. Simplified block diagram of the MIMO-radar system. 180
6.3. Block diagram of a single transmit channel. 181
6.4. Transmit powers of the individual transmit channels without the cables to the antennas. The mean output powers are: Ch1: 22.5 dBm, Ch2: 22.5 dBm, Ch3: 22.8 dBm, Ch4: 22.8 dBm. Measured with the vector network analyzer ROHDE&SCHWARZ ZVA24. 181
6.5. Block diagram of a single receive channel. 182
6.6. Screenshot of the graphical user interface to control the digitizer. 184
6.7. Block diagram of the ring-buffer implementation in the digitizer. The acquired data is streamed over the ring buffer to the RAM. Once the data stream is exhausted, the data is streamed to a SSD. 185
6.8. Block diagram of the calibration crate. 186
6.9. Photos of the calibration crate. Left-hand side: Upper layer with microwave components; Right-hand side: lower layer with power supply, digital electronics, and microwave couplers. 187

6.10. Concept of the LO and trigger distribution network. 188
6.11. System drift over 5 hours. 189
6.12. Spectrogram plots of calibration chirp signal in loop Tx1 – Rx1 with $B = 300$ MHz and $\tau_p = 10\,\mu$s. 192
6.13. Photo of a single patch antenna. 194
6.14. Receive mode antenna patterns of a microstrip patch antenna at 9.58 GHz. 195
6.15. MIMO-SAR demonstrator during measurement. 196
6.16. Practical implementation of the Hilbert transform by a FIR filter. 198

7.1. Photo of the measurement setup for the DBF experiment with a reflector antenna. Left-hand side: Five corner reflectors on a lawn as point-like targets. Right-hand side: Reflector antenna on the roof of the building. 205
7.2. Photo and antenna pattern of the DBF reflector antenna with eight feed elements. 206
7.3. Range-compressed data of the experiment using Segmentally-Shifted Chirp (SSC) waveforms and a reflector antenna. 207
7.4. Photo of the measurement scene for the azimuth DBF experiment. Five trihedral corner reflectors on a lawn can be seen. 208
7.5. Processed SAR images of the azimuth DBF experiment. After channel reconstruction, both images look almost identical. 210
7.6. Cuts in range and azimuth through a single corner reflector. The impulse responses show strong similarities before and after DBF. 210
7.7. Sketch of the measurement setup used for the multipath propagation detection experiment. 211
7.8. Photo of the measurement setup used for the multipath propagation detection experiment. 212
7.9. Sketch and photo of the antenna array used for the experiment. . 213
7.10. Array factor of the transmit (blue) and receive (green) antenna beams. The orange color indicates the positions of the two metal plates. 214
7.11. Range-compressed and calibrated data set of the first transmit and receive channel: $|u_{\mathrm{rg},1,1}(t)|^2$. 215

7.12. Remaining phase error of the three corner reflectors with respect to the simulation for the first transmit channel. 216
7.13. Range compressed data after DBF: $|u_{\mathrm{DBF}}(t)|^2$. 217
7.14. Photo of the measurement scene: A fence on the lawn as surface target. 220
7.15. Photo of the measurement scene: MIMO-SAR demonstrator with a fence as surface target. 220
7.16. Comparison of calibrated and uncalibrated impulse responses of a corner reflector after DBF on receive. 221
7.17. Acquired raw-data signal of the first receive channel after band-pass filtering with a bank of 10 FIR filters with 100 taps. . . 221
7.18. Left-hand side: Focused SAR images of the simultaneous fully polarimetric experiment in different polarization states – scaling in $-(x$ dB). The fence is clearly visible in the co-polar data sets. Right-hand side: Difference between individual measurement and MIMO-SAR acquisition – scaling in $(-x)$ dB. 223

List of Tables

3.1. Maximum *ISLR* for small observation intervals ($\Delta T < 0.1 \cdot \tau_p$) in dependence on N_{Tx}, window type and waveform. 92
3.2. Overview of the waveform comparison. 101

5.1. Assumed typical parameters of a spaceborne SAR for AoA estimation. 163
5.2. Run-time of the proposed estimators for the assumed system of Tab. 5.1. $L = 3$, $N_{Tar} = 3$ and $N_{subsw} = 1000$. 169

6.1. System parameters of the MIMO-radar demonstrator. 178
6.2. Patch antenna parameters. 193

7.1. Reflector antenna parameters. 206
7.2. Radar instrument settings and system parameters of the azimuth-DBF experiment. 209

Versicherung

Hiermit versichere ich, dass ich die vorliegende Arbeit ohne unzulässige Hilfe Dritter und ohne Benutzung anderer als der angegebenen Hilfsmittel angefertigt habe; die aus fremden Quellen direkt oder indirekt übernommenen Gedanken sind als solche kenntlich gemacht.

Bei der Auswahl und Auswertung des Materials sowie bei der Herstellung des Manuskripts habe ich Unterstützungsleistungen von folgenden Personen erhalten:

keine

Weitere Personen waren an der Abfassung der vorliegenden Arbeit nicht beteiligt. Die Hilfe eines Promotionsberaters habe ich nicht in Anspruch genommen. Weitere Personen haben von mir keine geldwerten Leistungen für Arbeiten erhalten, die im Zusammenhang mit dem Inhalt der vorgelegten Dissertation stehen.

Die Arbeit wurde bisher weder im Inland noch im Ausland in gleicher oder ähnlicher Form einer anderen Prüfungsbehörde vorgelegt.

München, den 16.11.2017

Items of Key Research

1. The use of multiple transmit and multiple receive channels (MIMO) offers an increased flexibility of Synthetic Aperture Radar (SAR) sensors, and the implementation of new imaging modes.
2. In SAR, orthogonal waveforms for all time and Doppler shifts do not exist.
3. To provide a sufficient orthogonality between the waveforms in SAR scenarios, apart from a certain waveform structure, a filtering in space, time and frequency is required.
4. From the current point of view, the most suitable waveform types for High-Resolution and Wide-Swath (HRWS) MIMO-SAR, are the *Sub-Pulses* and the *Segmentally-Shifted Chirp Waveforms*.
5. The choice of the optimum transmit waveforms for MIMO-SAR is fully dependent on the system architecture and the acquisition mode.
6. For large illuminated swath widths, in case of Digital Beam-Forming (DBF) on receive, the Earth curvature leads to strong distortions of the relation between ground-range and steering angle and thus, a linear scanning approach along elevation is not feasible.
7. In each receive channel of a SAR sensor, a bank of band-pass filters can be used to form frequency-variant antenna beams on receive.
8. For channel separation of the *Sub-Pulses* and the *Segmentally-Shifted Chirp Waveforms*, the same algorithm can be used.
9. Significantly, the matrix pencil method can be used to estimate in real-time the angle of the incident echo signal on the antenna array in order to enable a topography-adaptive DBF.
10. Signal harmonics and spurious components generated by hardware components may strongly effect the orthogonality of waveforms.

11. For calibration of a MIMO-SAR sensor, the combined use of internal, external, and raw-data based calibration is required.

12. For MIMO-SAR, not only planar antenna arrays, but also reflector antennas with a digital feed can be used.

13. Interestingly, multipath propagation effects in SAR tomography can be detected via special MIMO acquisition modes.

14. By using MIMO-SAR, simultaneous fully polarimetric SAR imaging is possible without any reduction of the swath width or resolution.

Curriculum Vitae

Personal Details

Name	Tobias Rommel
Date of Birth	16.12.1987
Place of Birth	Bad Kissingen (Germany)
Nationality	German

Education

2007 – 2011	University of Applied Sciences Wuerzburg-Schweinfurt, Electrical Engineering – Communications Engineering
Since 09/2011	Ph.D. student at the Technical University of Chemnitz and the German Aerospace Centre (DLR)
Since 09/2014	Scientist at the Microwaves and Radar Institute – German Aerospace Centre (DLR)
04/2017 – 07/2017	Guest Scientist at the NASA Goddard Space Flight Center

Awards

Certificate of Merit: *Abbildendes MIMO-Radar mit modifizierten Chirp-Signalen*, U.R.S.I. Kleinheubacher Tagung 2013, Germany, Kleinheubach, Sep. 2013.

Outstanding Paper Distinction: *Multiple-Input Multiple-Output Circular SAR*, 15th International Radar Symposium, Poland, Gdansk, June 2014.

Best Paper Award: *MIMO-SAR Tomography*, EUSAR 2016, Germany, Hamburg, June 2016.

Winner of OHB Competition: *HAPS MIMO CSAR Multiple-Input Multiple-Output Circular SAR for High Altitude Pseudo-Satellites*, International Astronautical Congress, Mexico, Guadalajara, Sep. 2016.

Munich, 16.11.2017